Pressure Induced Structural Transformations of Network Forming Glasses

Wezka, Kamil

Award date:
2013

Awarding institution:
University of Bath

Pressure induced structural transformations of network forming glasses

submitted by

Kamil Wezka

for the degree of Doctor of Philosophy

of the

University of Bath

Department of Physics

October 9, 2013

Abstract

The method of *in situ* high pressure neutron diffraction was employed to measure reliable diffraction patterns to help illuminate the density-driven structural transformations in GeO_2, SiO_2, B_2O_3 and $GeSe_2$ glass. The majority of this neutron diffraction work employed the diffractometer D4c at the ILL with a Paris-Edinburgh press which enabled the pressure range from ambient to 8 GPa to be accessed. In the cases of GeO_2 and $GeSe_2$ glass, the neutron diffraction with isotopic substitution (NDIS) protocol was developed to provide benchmark experimental results to test the results obtained from various molecular dynamics simulations using different theoretical schemes.

For GeO_2 glass, from a combination of neutron diffraction and molecular dynamics results, it was found that the increase in density of the glass initially occurs through a reorganisation of corner-shared GeO_4 tetrahedra on an intermediate length scale as the pressure is increased from ambient to 5 GPa. At higher pressures, there is a progression from a tetrahedral to an octahedral glass, via the formation of 5-fold coordinated Ge-atoms which have a predominantly square pyramidal geometry.

In the work on SiO_2 and B_2O_3 glass the pressure range for the *in situ* high pressure neutron diffraction results was extended to 14.5 GPa and 17.5 GPa, respectively, by using the PEARL diffractometer at ISIS. For both materials the neutron diffraction results provide complementary information to pressure x-ray diffraction studies helping to elucidate the mechanism of network collapse. In the case of SiO_2 glass, densification over the measured pressure range occurs predominantly by a reorganisation of corner shared SiO_4 tetrahedra on an intermediate length scale. In the case of B_2O_3 glass, the B-O coordination number changes from 3 to $\sim$ 3.9 at the pressure is increased from $\sim$ 8 to 17.5 GPa.

For $GeSe_2$ glass, from a combination of neutron diffraction and molecular dynamics results, it was found that the density increase from ambient pressure up $\sim$ 8 GPa occurs by a reorganisation of both corner and edge-sharing $GeSe_4$ tetrahedra on an intermediate length scale. Above this pressure, 5- and 6-fold coordinated Ge atoms start to form at

a similar density and homopolar bonds play an intimate role in the formation of these higher coordinated polyhedra.

Acknowledgments

When I arrived in the United Kingdom in August 1999, I never would have dreamt of achieving so much and reaching the current stage of academic qualification. The whole learning experience has been very challenging, but none of this would have been possible without the support of many people.

I am very grateful to my main supervisor Phil Salmon for his support and guidance during my PhD, especially during the writing up stage. I would like to thank my colleagues in the liquid and amorphous materials (LAM) research group Anita Zeidler, Prae Chirawatkul, Dean Whittaker, Keiron Pizzey and Ruth Rowlands for their help during my research, supportive discussions and friendship. Enormous thanks go to Harry Bone (LAM technician) for his help in the laboratory, Phil Jones (glassblower), Paul Reddish (Physics workshop technician), Wendy Lambson (Physics department technician), Bob Draper (Physics workshop technician), Adrian Hooper and Simon Dodd (Physics IT support).

I would like to thank instrument scientist Henry Fischer (D4c, ILL), Stefan Klotz for sharing his expertise on the Paris-Edinburgh press, and Alain Bertoni, Jean-Luc Laborier and Claude Payre (support technicians on D4c) for all their help during ILL experiments. Great thanks also go to instrument scientists Matt Tucker and Craig Bull (Pearl, ISIS), and Chris Barry (instrument technician) for their support during ISIS experiments.

For collaboration, useful discussions and provision of simulation data I would like to thank Dario Marrocchelli (work on glassy GeO_2), Assil Buzid and Carlo Massobrio (work on glassy $GeSe_2$) and Mark Wilson (ongoing work on glassy SiO_2). I would like to thank Alex Hannon for useful discussions and help with the modelling of B_2O_3 glass.

For my work on praseodymium and neodymium gallate glass which is not presented here, I would like to acknowledge Adrian Barnes, Laurie Skinner and Pinit Kidkhunthod for the provision of samples.

I would like to thank the Engineering and Physical Sciences Research Council (EP-

SRC) for their financial support of the work I was involved in, and I would also like to thank all of the contributors to the ISIS neutron training course and Oxford neutron school for the training provided. I would like to thank Mark Connolly from By Word of Mouth Ltd. and Sarah South from Pesto Food and Party Designers for letting me work and financial aid in my final stages of this thesis.

Lastly, big thanks go to my family and friends for their love, support and encouragement. In particular I am infinitely grateful to my girlfriend Magdalena who always supported and encouraged me during my PhD work, especially during the writing up stage.

I dedicate this thesis
to my family and Magdalena.

List of publications

Published articles:

- K. Wezka, P. S. Salmon, A. Zeidler, D. A. J. Whittaker, J. W. E. Drewitt, S. Klotz, H. E. Fischer and D. Marrocchelli. Mechanisms of network collapse in GeO_2 glass: high-pressure neutron diffraction with isotope substitution as arbitrator of competing models. *Journal of Physics: Condensed Matter*, 24:502101, 2012

- P. S. Salmon, J. W. E. Drewitt, D. A. J. Whittaker, A. Zeidler, K. Wezka, C. L. Bull, M. G. Tucker, M. C. Wilding, M. Guthrie and D. Marrocchelli. High pressure neutron diffraction study of GeO_2 glass up to 17.5 GPa. *Journal of Physics: Condensed Matter*, 24:415102, 2012

- K. Wezka, A. Zeidler, P. S. Salmon, P. Kidkhunthod, A. C. Barnes and H. E. Fischer. Structure of praseodymium and neodymium gallate glasses. *Journal of Non-Crystalline Solids*, 357:2511, 2011

Articles being reviewed:

- K. Wezka, A. Bouzid, K. J. Pizzey, P. S. Salmon, A. Zeidler, S. Klotz, H. E. Fischer, C. L. Bull, M. G. Tucker, M. Boero, S. Le Roux, C. Tugène and C. Massobrio. The density-driven defect-mediated network collapse of $GeSe_2$ glass. *Submitted to Physical Review Letters*

Contents

Chapter 1

Introduction

Structural transformations in condensed matter, including amorphous materials, have been a long-standing area of interest in high-pressure research, and are discussed in various textbooks and articles [1–5]. For example, pressure induced so-called poly-amorphic transitions in glasses and liquids can alter substantially their physical properties which is of importance in areas ranging from materials science to geophysics and technology [5–8]. All of this provides motivation to investigate the atomic scale structure in order to provide a microscopic basis for understanding changes in physical properties such as the viscosity, self-diffusion coefficient, electrical resistivity, compressibility, thermal expansion, glass forming ability, crystallisation of glasses and semiconductor-to-metal transitions [2, 5, 8, 9]. However, a fundamental understanding of these various phenomena is still at the early stages of development, and great experimental and theoretical efforts are being made [5].

Structurally, liquids and glasses resemble one another because each phase lacks regular long range atomic ordering. This disorder in liquids and glasses makes them difficult to investigate on the atomic scale. Nonetheless, chemical bonding constraints lead to structural motifs with a high degree of short range order (SRO), while the flexibility in the connectivity of these motifs gives rise to intermediate range ordering (IRO). In this thesis, the glassy materials were obtained by rapidly quenching liquids through their glass transition temperature.

The structural complexity of amorphous materials requires a multi-disciplinary approach that involves contributions from experiment, theory and simulation. Experimentally, information about the atomic distributions in liquids and glasses can be obtained using various diffraction or spectroscopic methods. Information about the structural motifs describing the SRO can be obtained, for example, by using neutron and x-ray

diffraction techniques or by using spectroscopic methods such as magic angle spinning nuclear magnetic resonance (MASNMR) or x-ray absorption spectroscopy (XAS). IRO is more difficult to probe using neutron and x-ray diffraction methods, and usually requires the use of difference function methods [10]. Vibrational spectroscopy methods can give indirect access to IRO as in the case of Raman [11] spectoroscopy experiments on B_2O_3 glass, but often require *a priori* structural information to aid in the interpretation of the results. The work in this thesis focuses on the use of *in situ* high pressure neutron diffraction to provide new information on the nature of density-driven structural transformations.

Neutrons scatter mostly from the atomic nuclei and the scattering cross section is usually dependent on the isotope of a chemical species. X-ray photons, in contrast, scatter from the atomic electrons and the scattering power is directly proportional to the atomic number. In general, the information obtained by these diffraction methods is complementary and often the data sets are compared [10]. The diffraction patterns measured by both techniques are dependent on the magnitude of the scattering vector Q, and for a multi-component system containing n different chemical species, each pattern can be represented by $n(n+1)/2$ overlapping partial structure factors $S_{\alpha\beta}(Q)$, which describe the pair-correlations between atoms of chemical species α and β. The overlap extends to the corresponding real-space partial pair distribution functions $g_{\alpha\beta}(r)$ making it desirable to design experiments to separate the $S_{\alpha\beta}(Q)$ functions. Suitable experimental methods include neutron diffraction with isotopic substitution (NDIS) and anomalous x-ray scattering (AXS) [10].

The aim of this thesis is to provide new information by neutron diffraction to illuminate the mechanisms of density-driven structural trasformations in the glassy materials GeO_2, $GeSe_2$, SiO_2 and B_2O_3. In the cases of GeO_2 and $GeSe_2$ glass, the first application is made of the *in situ* high pressure NDIS method. The NDIS protocol is developed to provide benchmark experimental results to test the validity of various molecular dynamics simulation methods that can be used in the future for the development of accurate models for different classes of materials with novel properties.

Thesis outline

The thesis outline is described in the following:

- In Chapter 2, the essential theory for neutron diffraction by liquids and amorphous materials is presented and the NDIS method is discussed.
- In Chapter 3, the D4c diffractometer at the Institut Laue-Langevin neutron source

is introduced and the incorporation of a Paris-Edinburgh press for high pressure research is outlined. The data correction protocols are also given in this Chapter.

- Chapter 4 presents the first application of the *in situ* high-pressure NDIS method to measure the structure of GeO_2 glass at pressures up to 8 GPa. The results are discussed by reference to newly available computer simulations using the so-called DIPole-Polarisable Ion Model (DIPPIM) [12] in order to reveal the nature of the density-driven network collapse.

- In Chapter 5, the availability of a new monochromator on D4c made it possible to use neutrons of wavelength 0.5 Å to extend the maximum Q-value to $\sim$ 22 Å^{-1}, thereby giving r-space functions with improved resolution. The structural transformations in SiO_2 glass were investigated at pressures up to 8 GPa, and were augmented, following the developments described in reference [13], by results obtained from the PEARL diffractometer at ISIS for pressure up to 14.5 GPa.

- In Chapter 6, B_2O_3 glass is investigated at pressures up to 8 GPa using D4c, and at pressures up to 17.5 GPa using PEARL. At ambient pressure, B_2O_3 glass has a topology that is significantly different to GeO_2 and SiO_2 because B atoms are 3-fold coordinated and form BO_3 units that assemble to form boroxol rings. An attempt is made to quantify the pressure dependent change in the fraction of boroxol rings using a simple model taken from reference [14].

- In Chapter 7, the chalcogenide glass $GeSe_2$ is investigated at pressures up to 8.2 GPa using the *in situ* high-pressure NDIS method. The results are augmented by those obtained from the PEARL diffractometer for pressures up to 16.1 GPa. The experimental work is complemented by first-principles molecular dynamics simulations that employ the Becke-Lee-Yang-Parr functional [15, 16]. The combined experimental and molecular dynamics approach provides new insights into the density-driven structural collapse of $GeSe_2$ glass.

- Finally, in Chapter 8 an overall summary is presented together with suggestions for future work.

Chapter 2

Theory

This chapter describes the basic theory for neutron diffraction experiments, and briefly considers X-ray diffraction experiments on amorphous solids. The formalism is based on the review written by Fischer *et al* [10]. A basic but very accessible account of neutron scattering theory is given by Sivia [17] while a more fundamental quantum mechanical description is given by Squires [18].

2.1 Basic properties of a neutron

The energy of free neutrons may extend over many orders of magnitude. Thermal neutrons with wavelengths of the order of atomic spacings are, however, used to study the structural arrangements of atoms in condensed matter.

The kinetic energy E and momentum $\mathbf{p}$ of a neutron moving with non-relativistic velocity $\mathbf{v}$ are given by

$$E = \frac{m_n v^2}{2} \tag{2.1}$$

and

$$\mathbf{p} = m_n \mathbf{v}, \tag{2.2}$$

where m_n= 1.675·10^{-27} kg is the mass of a neutron. For thermal neutrons the characteristic speed is $|\mathbf{v}|$ = 2.2 km s^{-1}. The de Broglie wavelength of a neutron is defined

by

$$\lambda = \frac{h}{m_n v}, \tag{2.3}$$

where $h = 6.626{\cdot}10^{-34}$ J s is the Planck constant. The magnitude of a wavevector $\mathbf{k}$ in the direction of $\mathbf{v}$ is given by

$$|\mathbf{k}| = k = \frac{2\pi}{\lambda}. \tag{2.4}$$

By using the relation $\hbar = h/2\pi$, the energy E and momentum $\mathbf{p}$ can be re-written as

$$E = \frac{\hbar^2 k^2}{2m} = \frac{h^2}{2m\lambda^2} \tag{2.5}$$

and

$$\mathbf{p} = \hbar\mathbf{k}. \tag{2.6}$$

By inserting values for the elementary constants, the energy of thermal neutrons can be expressed in terms of the wavelength, velocity and temperature as:

$$E = \frac{81.81}{\lambda^2} = 5.227\ v^2 = 0.08617\ T \tag{2.7}$$

where the units are meV for E, Å for λ, km s^{-1} for v and Kelvin for T.

While the typical spacing between atoms requires neutron energies to be on the order of a few hundreds of meV to produce a diffraction pattern, the high energy neutrons produced by most neutron sources have energies on the order of a few MeV and need to be slowed to usable energies via a process called moderation. By choosing a suitable moderator material, neutrons can lose energy by scattering with the nuclei in the moderator and emerge with a Maxwell-Boltzmann distribution of velocities, where the peak velocity depends on the temperature of the moderator.

2.2 Diffraction experiments and the scattering vector

The scattering of a neutron, or an X-ray photon, by a sample results in momentum and energy changes of $\Delta\mathbf{p}$ and ΔE, respectively. The set up is shown schematically in figure 2-1 where an incident particle with wavevector $\mathbf{k}_i$ and energy E_i scatters from the system and leaves with a final wavevector $\mathbf{k}_f$ and energy E_f.

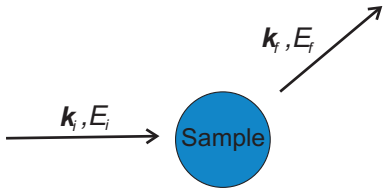

Figure 2-1: Schematic representation of a scattering event.

The momentum transfer in the scattering event is given by

$$\Delta\mathbf{p} = \hbar\mathbf{k}_i - \hbar\mathbf{k}_f = \hbar\mathbf{Q}, \tag{2.8}$$

where $\mathbf{Q}$ is the scattering vector defined as

$$\mathbf{Q} = \mathbf{k}_i - \mathbf{k}_f. \tag{2.9}$$

The energy transferred during such an event is given by:

$$\Delta E = E_i - E_f = \frac{\hbar^2|\mathbf{k}_i|^2}{2m_n} - \frac{\hbar^2|\mathbf{k}_f|^2}{2m_n}. \tag{2.10}$$

In the static approximation it is assumed that $\frac{\Delta E}{E_i} \ll 0$ and it follows from equation 2.10 that

$$|\mathbf{k}_i| = \frac{2\pi}{\lambda_i} \simeq |\mathbf{k}_f| = \frac{2\pi}{\lambda_f}. \tag{2.11}$$

The vector diagram for such an elastic scattering event is shown in figure 2-2, where an incoming quantum is deflected through a scattering angle of 2θ.
By applying a cosine rule to the scattering triangle in figure 2-2

$$Q^2 = k_i^2 + k_f^2 - 2k_ik_f\cos(2\theta), \tag{2.12}$$

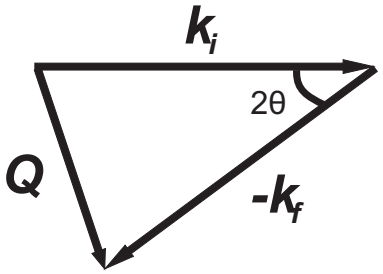

Figure 2-2: The vector diagram for a scattering event.

and using equation 2.11, it follows that the scattering vector is given by

$$Q = \frac{4\pi}{\lambda}\sin(\theta). \tag{2.13}$$

2.3 Differential scattering cross-section

The basic quantity that one aims to measure during a diffraction experiment is the fraction of incident particles that are scattered in a direction as defined by the angles 2θ and φ shown in figure 2-3. Thus when a collimated beam of incident particles (neutrons or X-rays) with flux Φ is scattered by a system centred at the origin of coordinates, all quanta in the direction of $\mathbf{R}$ are counted, irrespectively of their final energy, by a detector of small area dA situated at a distance $|\mathbf{R}|$ from the origin. The differential scattering cross section is defined by

$$\frac{d\sigma}{d\Omega}(2\theta) \equiv \frac{\text{Number of particles scattered into d}\Omega \text{ per second}}{\Phi d\Omega} \tag{2.14}$$

where $d\Omega = dA/|\mathbf{R}|^2$ is the solid angle subtended by the detector. For isotropic scattering, which applies to amorphous materials, the differential scattering cross section is independent of φ. It follows that $d\sigma/d\Omega$ is a function of $|\mathbf{Q}|$ where the relation between Q and 2θ is given by equation 2.13.

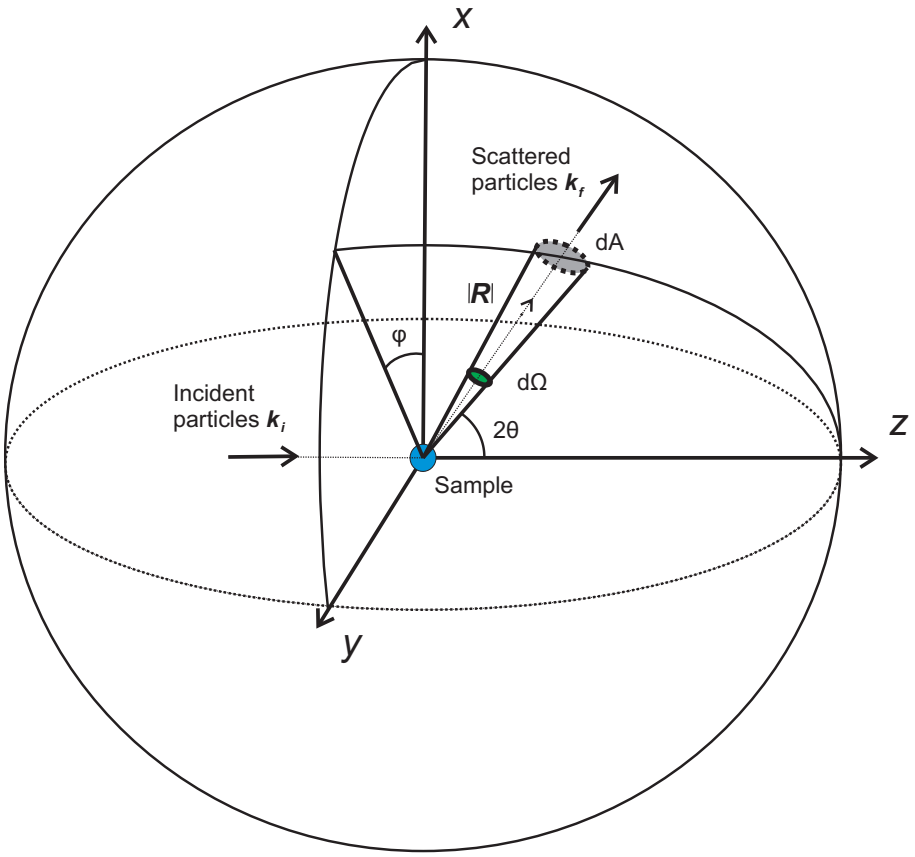

Figure 2-3: Schematic of a scattering experiment. A steady flux of neutrons with wavevector $\mathbf{k}_i$, parallel to the z axis, scatters from a sample placed at the origin of coordinates in the direction $\mathbf{R}$ into solid angle dΩ. The flux of scattered neutrons is measured by a detector of area dA placed at a distance $|\mathbf{R}|$ away from the origin of coordinates.

2.4 Neutron diffraction

Neutrons are scattered from atomic nuclei via the strong force. Due to the short range of the interactions ($\sim 10^{-14}$ m), which is a factor of 10^4 smaller than the de Broglie wavelength of a thermal neutron, the scattering is essentially isotropic. The neutron scattering length b gives a measure of the scattering power of each nucleus, which is not well understood, but the value depends on the makeup of the nucleus and the orientation of the nuclear spin relative to the spin of the incident neutron. This makes for an erratic variation of the scattering lengths between the elements, or even between isotopes of the same element (figure 2-4). One such example is given by the contrast between the

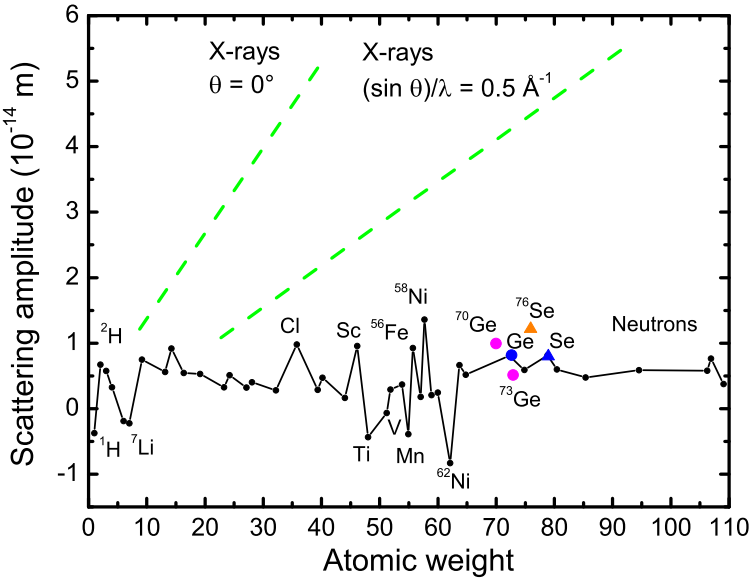

Figure 2-4: The variation with atomic weight of the scattering lengths for X-rays (- - -) $r_e f(\theta)$, where r_e is the classical electron radius of 2.818 fm and $f(\theta)$ is the X-ray form factor at a fixed scattering angle 2θ, and for neutrons (–●–) b, where the latter depends on the isotope [19]. The germanium (●) and selenium (▲) scattering lengths for naturally occurring elements are highlighted along with the specific Ge and Se isotopes used for the diffraction experiments described in Chapters 4 and 7. It is worth noting that in X-ray diffraction the scattering length is dependent on $Q \propto \sin(\theta)/\lambda$.

coherent scattering lengths of hydrogen and deuterium where b(^{1}H)= -3.7406(11) fm and b(^{2}H)= 6.671(4) fm [20].

For an isotropic system of N scattering centres, the differential scattering cross sec-

tion can be written as [10]:

$$\frac{d\sigma}{d\Omega}(Q) = \left\langle \sum_{i=1}^{\mathrm{N}} \sum_{j=1}^{\mathrm{N}} \overline{b_i b_j^*} e^{i\mathbf{Q}\cdot\mathbf{r}_{ij}} \right\rangle \tag{2.15}$$

where $\mathbf{r}_{ij} = \mathbf{r}_i - \mathbf{r}_j$ gives the relative positions of scattering centres i and j, b_i is the bound neutron scattering length of atom i and b_j^* is the complex conjugate of the bound neutron scattering length of atom j. A thermal average is implied by the triangular brackets. The horizontal bar denotes an average of the b_i values over the scattering centre positions, where the scattering length for a site depends on the particular isotope occupying that site and on the relative orientation of the nuclear and neutron spins.

For a system of n different chemical species, the differential scattering cross section is given by [10]:

$$\frac{1}{N}\left(\frac{\mathrm{d}\sigma}{\mathrm{d}\Omega}(Q)\right) = F(Q) + \sum_{\alpha=1}^{n} c_\alpha (b_{\mathrm{coh},\alpha}^2 + b_{\mathrm{inc},\alpha}^2)[1 + P_\alpha(Q)]. \tag{2.16}$$

The total structure factor $F(Q)$ originates from interference of the scattered wavefronts emanating from different nuclear sites and contains useful structural information. The second term on the right hand side of equation 2.16 carries information about the isotropic diffraction from individual atomic sites, where c_α is the atomic fraction of each chemical species α in the system, $b_{\mathrm{coh},\alpha}$ is the coherent scattering length of chemical species α, and $b_{\mathrm{inc},\alpha}$ is the incoherent scattering length of chemical species α. $P_\alpha(Q)$ is the Placzek, or inelasticity, correction [21], which is introduced in equation 2.16 to account for the fact that the static approximation breaks down due to the recoil of nuclei that occurs during a scattering event. The $P_\alpha(Q)$ terms are larger the lighter the element. For very light elements like H there is, at present, no reliable way to calculate the inelasticity corrections.

$F(Q)$ can be written in terms of the Faber-Ziman partial structure factors, denoted by $S_{\alpha\beta}(Q)$, which describe the correlations between pairs of nuclei of chemical species α and β [22]:

$$F(Q) = \sum_{\alpha=1}^{n} \sum_{\beta=1}^{n} c_\alpha c_\beta b_\alpha b_\beta^* [S_{\alpha\beta}(Q) - 1]. \tag{2.17}$$

In general, the imaginary part of the scattering length is sufficiently small that b_β can be treated as a real number. To obtain real space information, the total pair distribution

function $G(r)$ is obtained by taking the sine Fourier transformation of $F(Q)$:

$$\begin{aligned} G(r) &= \frac{1}{2\pi^2 r\rho}\int_0^\infty QF(Q)\sin(Qr)dQ \\ &= \sum_{\alpha=1}^{n}\sum_{\beta=1}^{n} c_\alpha c_\beta b_\alpha b_\beta [g_{\alpha\beta}(r)-1], \end{aligned} \tag{2.18}$$

where ρ is the atomic number density of the sample (in atoms Å^{-3}). The partial pair distribution function, $g_{\alpha\beta}(r)$, is proportional to the probability of finding a nucleus of chemical species β in a spherical shell of radius between r and $r+\delta r$ centred on a nucleus of chemical species α. The relationships between $g_{\alpha\beta}(r)$ and $S_{\alpha\beta}(Q)$ are given by

$$S_{\alpha\beta}(Q) - 1 = \frac{4\pi\rho}{Q}\int_0^\infty r[g_{\alpha\beta}(r)-1]\sin(Qr)dr, \tag{2.19}$$

and

$$g_{\alpha\beta}(r) - 1 = \frac{1}{2\pi^2 r\rho}\int_0^\infty Q[S_{\alpha\beta}(Q)-1]\sin(Qr)dQ. \tag{2.20}$$

In a real neutron experiment, however, it is only possible to the measure the total structure factor, $F(Q)$, up to a finite maximum scattering vector $Q_{\max}$. This often shows itself by a broadening of the real space peaks and by the presence of unphysical 'truncation ripples' after Fourier transformation. These effects are reduced either by (1) applying a cosine modification function or (2) applying a Lorch modification function [23] prior to Fourier transformation. Procedure (1) reduces the severity of un-physical oscillations in r-space that would otherwise be introduced by a sudden truncation of data sets. Procedure (2) gives smoother $G(r)$ functions at all r values but leads to a reduction in resolution of the first peak. This subject will be dealt with in more detail in Chapter 3.

The un-physical oscillations that are present below the minimum atomic radius in $G(r)$ should oscillate symmetrically around the calculated theoretical value of $G(0)$ as defined by

$$G(0) = -\sum_{\alpha=1}^{n}\sum_{\beta=1}^{n} c_\alpha c_\beta b_\alpha b_\beta. \tag{2.21}$$

The sum rule is another constraint that the data sets should be compliant with [24] and is derived from equation 2.18 in the limit as $r \to 0$ to give

$$\int_0^\infty F(Q)Q^2dQ = 2\pi^2\rho G(0). \tag{2.22}$$

The function $g_{\alpha\beta}(r)$ can be used to find the coordination number, $\bar{n}_\alpha^\beta$, which gives the mean number of β species found in a spherical shell of radius between $r = r_1$ and $r = r_2$ centered on an atom of chemical species α:

$$\bar{n}_\alpha^\beta = 4\pi\rho c_\beta \int_{r_1}^{r_2} g_{\alpha\beta}(r)r^2dr \tag{2.23}$$

2.5 Isotopic substitution in neutron diffraction for pressure experiments

The total structure factor that was defined by equation 2.17 comprises $m = (n+1)n/2$ weighted partial structure factors $S_{\alpha\beta}(Q)$. In a pressure experiment, one would like to follow the changes associated with all of the partial structure factors $S_{\alpha\beta}(Q)$. However, a complete determination of the $S_{\alpha\beta}(Q)$ functions requires the measurement of m samples with different isotopic compositions for one or more of the elements [25], for example, $m = 3$ for a binary system composed of two species α and β. Three different total structure factors need therefore to be measured, e.g. $F_1(Q)$, $F_2(Q)$ and $F_3(Q)$, such that in matrix form

$$\begin{pmatrix} F_1(Q) \\ F_2(Q) \\ F_3(Q) \end{pmatrix} = \begin{pmatrix} c_\alpha^2 b_{\alpha 1}^2 & c_\beta^2 b_{\beta 1}^2 & 2c_\alpha c_\beta b_{\alpha 1} b_{\beta 1} \\ c_\alpha^2 b_{\alpha 2}^2 & c_\beta^2 b_{\beta 2}^2 & 2c_\alpha c_\beta b_{\alpha 2} b_{\beta 2} \\ c_\alpha^2 b_{\alpha 3}^2 & c_\beta^2 b_{\beta 3}^2 & 2c_\alpha c_\beta b_{\alpha 3} b_{\beta 3} \end{pmatrix} \begin{pmatrix} S_{\alpha\alpha}(Q) - 1 \\ S_{\beta\beta}(Q) - 1 \\ S_{\alpha\beta}(Q) - 1 \end{pmatrix}, \tag{2.24}$$

or, written is a more succinct way,

$$[F(Q)] = [A][S(Q) - 1], \tag{2.25}$$

where $[F(Q)]$ and $[S(Q) - 1]$ are column vectors and $[A]$ is a matrix. Equation 2.25 can be inverted to solve for the partial structure factors $S_{\alpha\beta}(Q)$ using

$$[S(Q) - 1] = [A]^{-1}[F(Q)]. \tag{2.26}$$

The determinant $|A|$, normalised by dividing each row i (1, 2 or 3) of $[A]$ by $\sum_\alpha \sum_\beta c_\alpha c_\beta b_{\alpha i} b_{\beta i}$, is a measure of the robustness of the determination of the $S_{\alpha\beta}(Q)$ functions [26].

In pressure experiments it is, however, not currently possible to measure the full set of $S_{\alpha\beta}(Q)$ factors because of (i) the poor counting statistics arriving from the small sample size and (ii) scattering from a sample containing gasket and the pressure cell environment (Chapter 3). An alternative strategy is to calculate so-called first difference functions $\Delta F_\alpha(Q)$ or weighted difference functions $\Delta F_\beta(Q)$. For example, if the total structure factors $F_1(Q)$ and $F_2(Q)$ are measured, where the isotopic composition of chemical species α is varied, then $S_{\beta\beta}(Q)$ can be eliminated by forming the first difference function

$$\begin{aligned} \Delta F_\alpha(Q) &\equiv F_1(Q) - F_2(Q) = c_\alpha^2 (b_{\alpha 1}^2 - b_{\alpha 2}^2)[S_{\alpha\alpha}(Q) - 1] \\ &+ 2c_\alpha c_\beta b_\beta (b_{\alpha 1} - b_{\alpha 2})[S_{\alpha\beta}(Q) - 1]. \end{aligned} \tag{2.27}$$

Alternatively, $S_{\alpha\alpha}(Q)$ can be eliminated by forming the weighted difference function

$$\begin{aligned} \Delta F_\beta(Q) &\equiv F_1(Q) - \frac{b_{\alpha 1}^2}{b_{\alpha 2}^2} F_2(Q) = c_\beta^2 (1 - \frac{b_{\alpha 1}^2}{b_{\alpha 2}^2})[S_{\beta\beta}(Q) - 1] \\ &+ 2c_\alpha c_\beta b_\beta b_{\alpha 1} (1 - \frac{b_{\alpha 1}}{b_{\alpha 2}})[S_{\alpha\beta}(Q) - 1]. \end{aligned} \tag{2.28}$$

Thus by eliminating $S_{\alpha\alpha}(Q)$ or $S_{\beta\beta}(Q)$ one reduces the complexity of correlation associated with a single total structure factor and gains access to information that would otherwise be 'hidden' by overlapping partial structure factors.

2.6 X-ray diffraction total structure factor

The information obtained by neutron diffraction is complementary to that obtained by using x-rays and often the data sets from both methods are compared. For an x-ray diffraction experiment the equation for the measured total structure $F_{\mathrm{X}}(Q)$ is obtained by replacing in equation 2.17 the bound coherent scattering length b_α by the Q-dependent atomic form factor $f_\alpha(Q)$ with dispersion terms of chemical species α [27, 28] (also see figure 2-4) such that

$$F_{\mathrm{X}}(Q) = \sum_{\alpha=1}^{n}\sum_{\beta=1}^{n} c_\alpha c_\beta f_\alpha(Q) f_\beta^*(Q)[S_{\alpha\beta}(Q) - 1] \tag{2.29}$$

where the X subscript implies that the function originates from the the x-ray diffraction method.

The $F_{\mathrm{X}}(Q)$ function is usually divided by the factor $\sum_\alpha \sum_\beta c_\alpha c_\beta f_\alpha(Q) f_\beta^*(Q)$ so that the resultant normalised total structure factor $S_{\mathrm{X}}(Q)$ oscillates about unity at high-Q:

$$S_{\mathrm{X}}(Q) = \frac{F_{\mathrm{X}}(Q)}{\sum_\alpha \sum_\beta c_\alpha c_\beta f_\alpha(Q) f_\beta^*(Q)} + 1. \tag{2.30}$$

$S_{\mathrm{X}}(Q)$ can then be compared to the normalised total structure factor $S_{\mathrm{N}}(Q)$ obtained from neutron diffraction as defined by

$$S_{\mathrm{N}}(Q) = \frac{F(Q)}{\sum_\alpha \sum_\beta c_\alpha c_\beta b_\alpha b_\beta^*} + 1. \tag{2.31}$$

Chapter 3

Instrumentation and neutron diffraction data reduction

In this chapter the process of neutron production at a fission reactor source and the instrumentation used to obtain diffraction patterns from amorphous systems under pressure are described. The challenges that the data reduction procedure meets, in order to generate reliable total structure factors $F(Q)$, are also outlined.

3.1 Fission neutron source

Neutrons at the Institut Laue-Langevin (ILL) in Grenoble, France, are produced by a nuclear reactor source. The less common isotope of Uranium ^{235}U, which is fissile, is used as the principal raw material for neutron production at the facility [29]. When a nucleus of ^{235}U captures a neutron n, it forms the unstable ^{235}U* isotope which can break up in a number of different ways to produce an average of 2.4 neutrons per event with energy E as a bi-product. One possible mechanism for such a process is given by

$$n +^{235} \mathrm{U}^* \rightarrow^{236} \mathrm{U}^* \rightarrow^{141} \mathrm{Ba} +^{92} \mathrm{K} + 3n + E. \tag{3.1}$$

Fission neutrons are very energetic but are slowed down through a series of collisions inside the reactor core and within the surrounding moderating material. In the latter, neutrons can lose energy by scattering with the nuclei of the moderator material and emerge with a Maxwell-Boltzmann distribution of velocities, where the peak velocity depends on the temperature of the moderator. A fraction of these thermal neutrons is re-used for self-sustaining the chain reaction, a fraction is absorbed in non-fission events

or escape the nuclear reactor environment, while the remainder allows for research. Neutrons are transported from the moderator using neutron guides, and to achieve collimation neutron absorbing boron-10 carbide ($^{10}B_4C$) can be used.

Figure 3-1 shows a schematic diagram for a typical diffraction experiment at a reactor source. The moderator produces a steady flux of neutrons with a Maxwell-Boltzmann distribution of wavelengths. Some of these are selected by using Bragg reflection at a monochromator. The selected neutrons are scattered by a sample, and the scattered neutrons are then measured as a function of the scattering angle 2θ by a moveable bank of counters, or a position sensitive detector. In Chapter 2 it was shown that the scattering vector $\mathbf{Q}$ for neutrons scattered by a sample is given by $\mathbf{Q} = \mathbf{k}_i - \mathbf{k}_f$ and for elastic scattering $|\mathbf{k}_i| = |\mathbf{k}_f| = 2\pi/\lambda$ such that

$$Q = \frac{4\pi}{\lambda}\sin(\theta) \tag{3.2}$$

where λ is the wavelength of the incident neutrons. Thus, by measuring the scattered

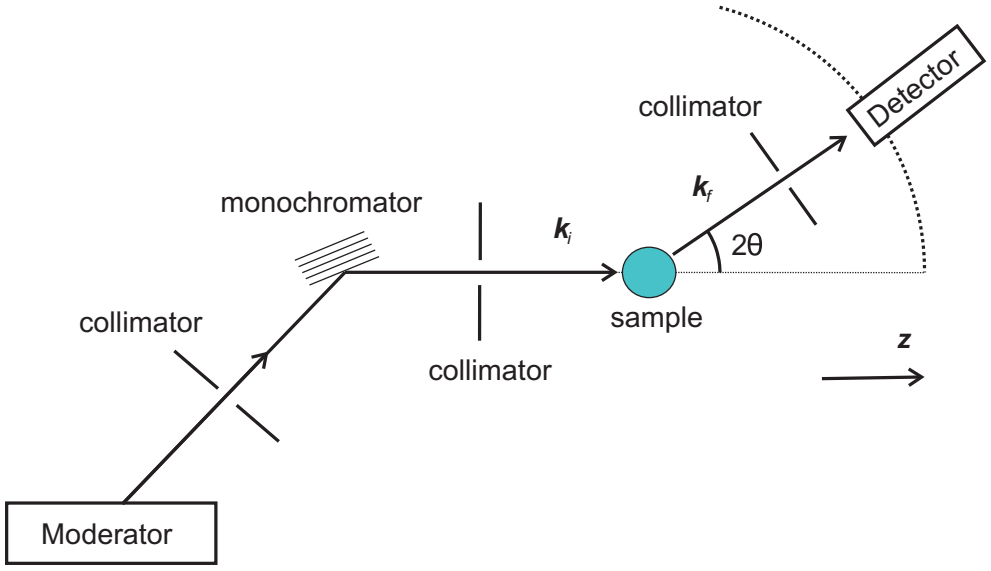

Figure 3-1: Schematic diagram for a diffraction experiment at a fission neutron source. A flux of monochromatic and collimated neutrons with wavevector $\mathbf{k}_i$ is scattered by the sample at the centre of coordinates to produce neutrons with a final wavevector $\mathbf{k}_f$.

intensity for a range of angles the differential scattering cross section $d\sigma/d\Omega$ can be obtained in terms of Q.

3.2 D4c instrument

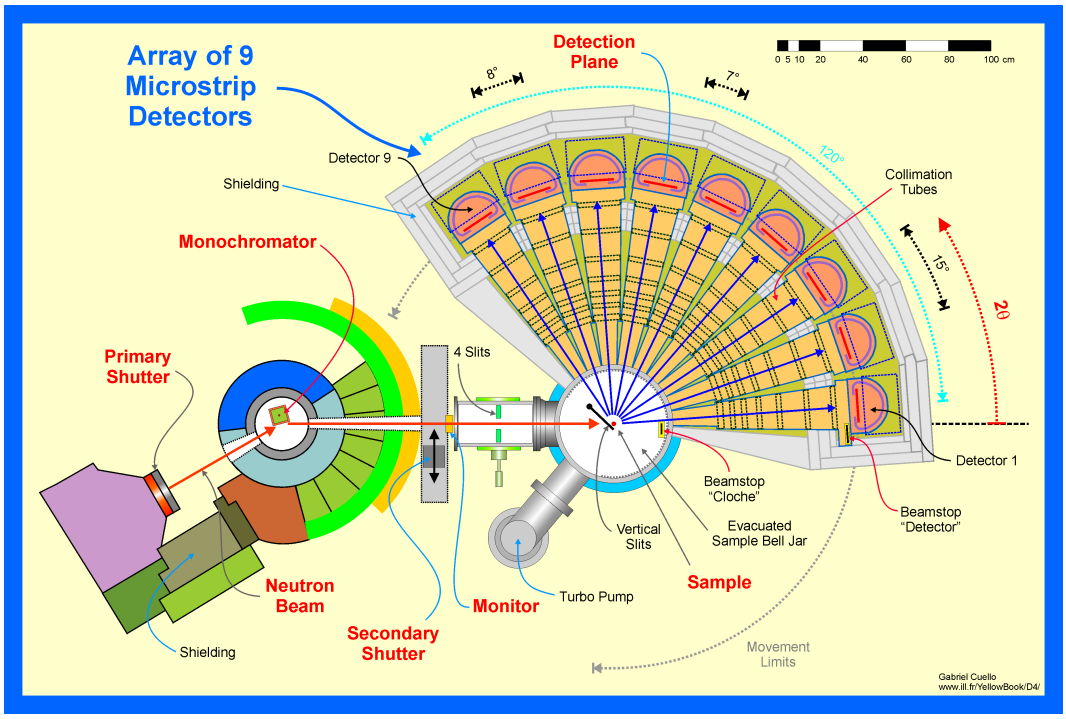

Figure 3-2: Top-view of the D4c instrument [30].

The D4c instrument at the ILL (figure 3-2) is a dedicated high precision diffractometer for disordered materials such as glasses and liquids [29, 30]. The diffractometer uses neutrons from a hot graphite moderator which is kept at 2400 K.

Monochromatic neutrons are selected via Bragg diffraction using the (331), (220) or (200) lateral faces of Cu monocrystals and produce a wavelength of 0.35 Å, 0.5 Å or 0.7 Å, respectively. In addition, Ir or Rh filters are deployed to remove $\lambda/2$ harmonic contamination for $\lambda = 0.5$ Å and $\lambda = 0.7$ Å, respectively. A high-transmission monitor, which is positioned between the monochromator and beam-defining slits, is used for normalising the incident beam intensity. The beam-defining slits allow both vertical and horizontal adjustment of the beam geometry for neutrons that are incident on the sample. The sample is situated within an evacuated aluminium bell jar (diameter = 46 cm, height = 55 cm) with a wide-angle thin aluminum window facing the detectors.

The diffractometer has nine ^{3}He-gas 1D position-sensitive detecting units that are arranged to cover a large area for neutron detection (figure 3-2) with high counting rate stability. Each detector covers a range of 8° in 2θ and there is a 7° gap between adjacent

units. The blind spots are covered by rotating the whole detector assembly to 5 or 6 different angular positions. The final covered 2θ range is 1.5° to 140°. The corresponding Q-range for the three operating wavelengths are $0.5 \leq Q(\text{Å}^{-1}) \leq 33$ for $\lambda = 0.35$ Å, $0.3 \leq Q(\text{Å}^{-1}) \leq 23$ for $\lambda = 0.5$ Å and $0.2 \leq Q(\text{Å}^{-1}) \leq 17$ for $\lambda = 0.7$ Å.

The aluminium bell jar can accommodate various sample environments. Recently much effort has been devoted to the instrumentation and methodology required to make accurate measurements of the neutron diffraction patterns for different glassy systems at pressures ranging from ambient up to ~ 8 GPa. The foundations for experiments on amorphous materials under pressure using neutron diffraction on D4c were laid down by Drewitt *et al* [31] for the 0-8.5 GPa pressure range. The developed protocols were followed in the work presented in this thesis.

3.3 The adaptation and setup of a Paris-Edinburgh press on the D4c instrument for measuring the diffraction patterns for amorphous samples under pressure

The structural transformations in condensed matter, including amorphous materials, have been a long-standing area of interest in high-pressure research [2–4]. In particular, structural information on liquids and amorphous materials provides a microsopic basis for investigating, in materials science and geophysics, various macroscopic physical properties such as viscosity, self-diffusion, electrical resistivity, compressibility and thermal expansion [8]. The possibility of employing the method of neutron diffraction with isotope substitution, which should provide a more direct picture of the pressure driven structural changes, makes neutrons an attractive probe. In neutron diffraction, the Paris-Edinburgh press [32] is often used to allow for the large sample volumes demanded by neutron experiments. The press can be used up to a pressure of ~ 10 GPa for samples of volume ~ 100 mm^3, or up to 25 GPa [33] for samples of volume 35 mm^3.

On D4c, a VX5 variant of the Paris Edinburgh press with two support pillars [34] and standard sintered cubic boron nitride (BN) single toroid anvils [33, 35] is employed to study amorphous materials up to 9 GPa , figure 3-3. Figure 3-4 shows a side view diagram of the anvils that apply pressure to a sample contained within a titanium-zirconium (Ti-Zr) gasket. The boron nitride die, which is a strong neutron absorber, is supported by a binding steel ring, and has a profile with a hemispherical sample chamber and a toroidal groove to accommodate the gasket. The gasket alloy has a Ti:Zr ratio of 0.676:0.324, a composition that gives the gasket a mean coherent neutron scattering

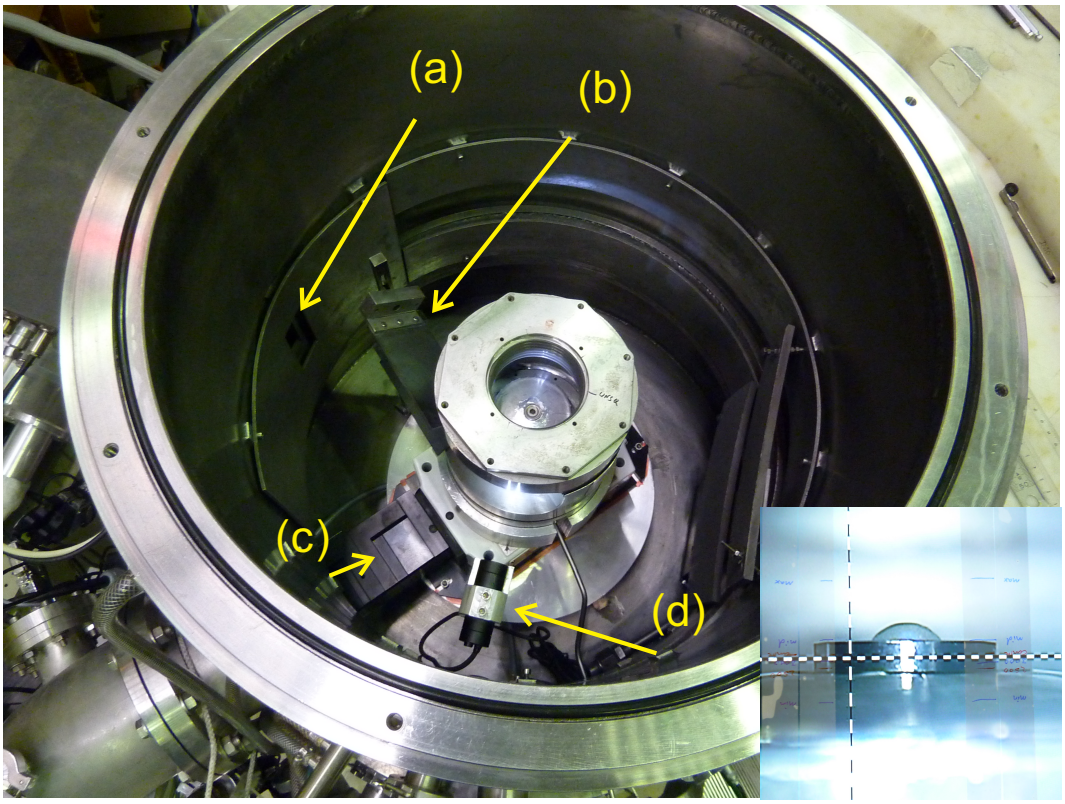

Figure 3-3: A picture showing the experimental set up on D4c used to measure diffractograms of amorphous samples under pressure. The arrows are pointing to (a) a slit through which monochromatic neutrons enter the bell jar, (b) $^{10}B_4C$ flags that help to collimate the incident beam and reduce background scattering from the anvils, (c) a motor driven platform that allows for a vertical repositioning of the PE press, (d) a video camera that is fixed inside the belljar and which allows the sample to be centered in the incident beam. An image from the camera is shown in the inset.

length of zero.

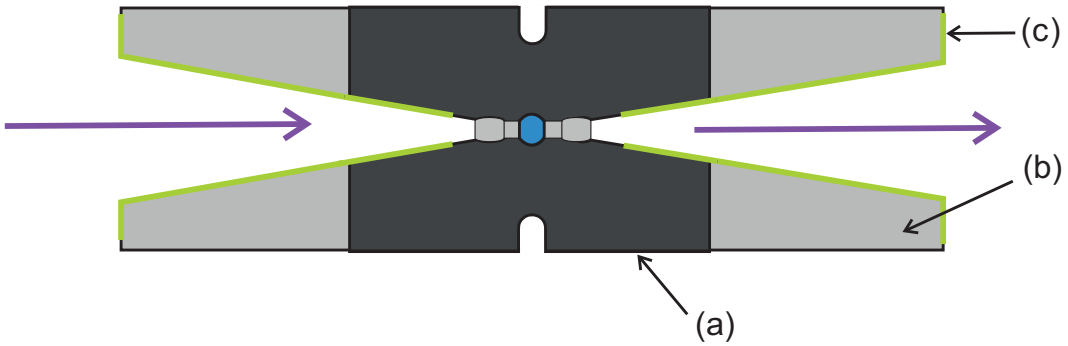

Figure 3-4: (Drawing not to scale) A side view of the single toroid anvils used on D4c in transmission geometry. The incident neutron beam impinges on the edge of a Ti-Zr gasket, which encloses a sample, and scatters from the sample and gasket in the direction of the detectors. The sample and gasket are held in a boron nitride insert (a). In order to reduce background scattering from the steel binding ring (b) cadmium plating is used (c).

A neutron beam of 11 mm width and 4 mm height is usually chosen to fully illuminate the sample within the anvils in the D4c pressure setup. Background scattering is reduced by using (i) neutron absorbing $^{10}B_4C$ flag placed a few cm upstream of the sample (figure 3-3) and (ii) neutron absorbing cadmium metal to cover the anvils (figure 3-4). The neutron beam is further collimated by the BN anvils defining a near cylindrical sample geometry for the incident and scattered beams. At ambient conditions, the sample height and diameter are 1.6 mm and 6 mm, respectively, as shown in figure 3-5 which also shows the typical dimensions of Ti-Zr gaskets at ambient pressure. The volume of the sample is given by

$$V_S = 2V_{\text{cap}} + V_{\text{cylinder}} = \frac{1}{3}\pi t_{\text{cap}}(3{r'_g}^2 + t_{\text{cap}}^2) + \pi {r'_g}^2 t_g, \tag{3.3}$$

where V_{cap} is the volume of a cap, V_{cylinder} is the volume of the middle section, t_{cap} is the height of a cap and r'_g is the gasket inner radius. At ambient pressure $V_S = 91.18$ mm^3.

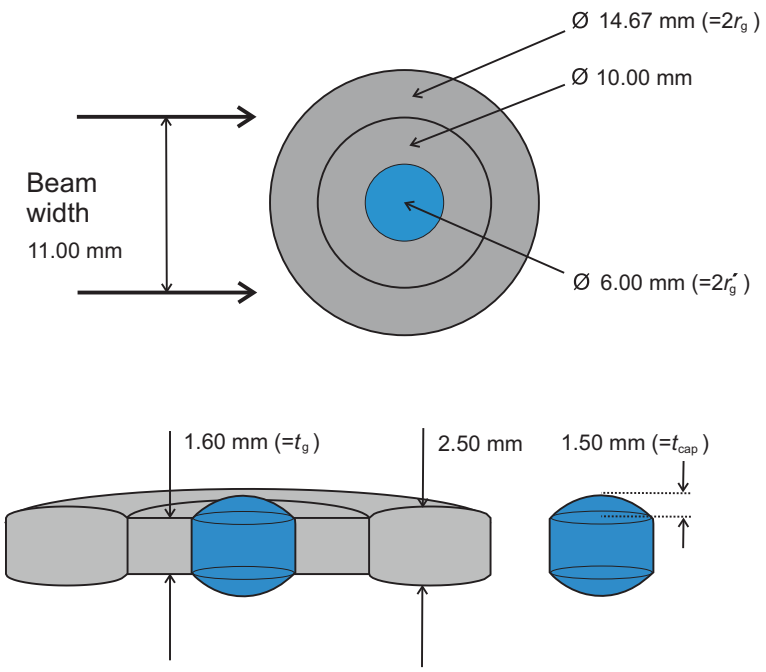

Figure 3-5: (Drawings not to scale) Typical dimensions of the sample (blue) and gasket (grey) used on D4c to study amorphous materials under pressure.

3.3.1 Pressure at the sample position

Pressure is applied to the anvils using a hydraulic pump and, as pressure is increased, the gasket assembly deforms into the grooves of the anvils, thus providing inward radial support. The force F on an anvil is given by

$$F = PA = Lg, \tag{3.4}$$

where P is the oil pressure in the hydraulic system, $A = 66.5$ cm^2 is the area of the anvil supporting piston for the VX5 variant PE press, L is the applied load and $g = 9.80665$ m s^{-2}. The pressure at the sample position is determined from the load L applied to the anvils through a calibration curve based on many neutron-diffraction experiments. The calibration curve used in this thesis in shown in figure 3-6 which was deduced from (i) a run in which a pellet made from a 1:3 mixture of NaCl and glassy $GeSe_2$ was compressed in BN anvils, a Rietveld refinement was made of the NaCl Bragg peaks, and the pressure was obtained from the NaCl equation of state [36]; (ii) by measuring the recovered gasket radius r_g from various sample runs to estimate the average pressure at the sample position (see below); and (iii) compression of GeO_2 glass pellets using sintered diamond anvils where a Rietveld refinement was made of the diamond Bragg peaks and the unit cell volume to pressure conversion was made on the basis of previous experiments made on crystalline ice VII [37].

Method (ii), which is described in reference [31], assumes a parabolic profile for the pressure distribution $P(r)$ on the sample and gasket assembly at a distance r from the centre of the sample (see figure 3-7) as given by

$$P(r) = -ar^2 + P_0, \tag{3.5}$$

where P_0 is the maximum pressure at the centre of symmetry and a is a constant. The boundary conditions are $P(r = 0) = P_0$ and $P(r = r_g) = P_0 - ar_g^2 = 0$, where r_g is the outer radius of the gasket, so that the constant becomes $a = P_0/r_g^2$. The total force that the sample and gasket assembly experiences is given by

$$F(r_g) = 2\pi \int_0^{r_g} rP(r)dr = \frac{\pi P_0 r_g^2}{2}. \tag{3.6}$$

By using equations 3.4 and 3.6 the relationship between load L and the maximum

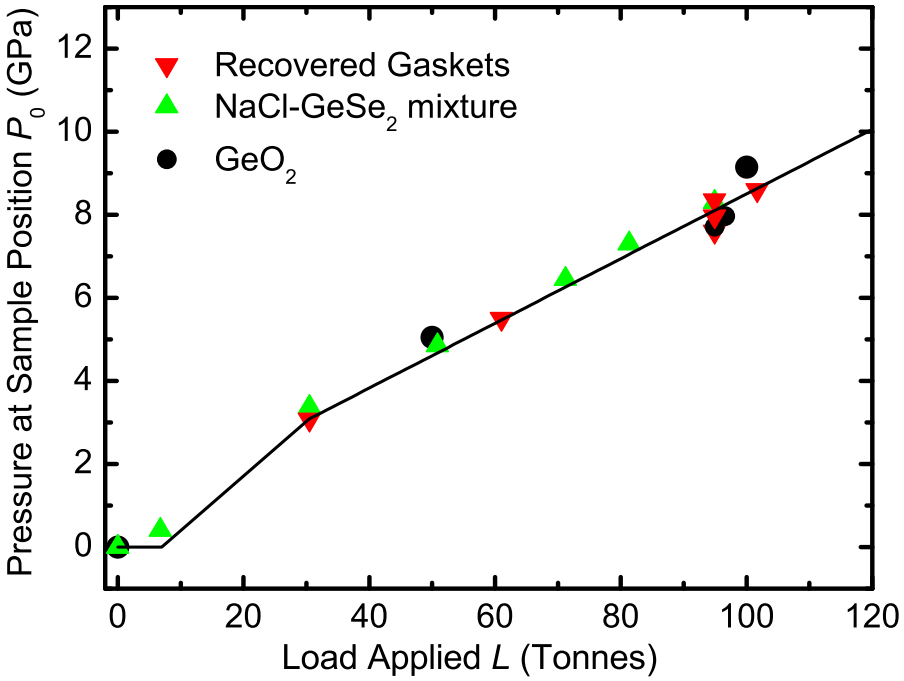

Figure 3-6: Load L applied to the piston of a VX5 variant PE press versus the pressure P at the sample position for single toroid anvils at a temperature of $\simeq$ 300 K. The data points are for standard Ti-Zr gaskets and correspond to (i) a calibration run using a mixture of NaCl and glassy $GeSe_2$ (▲); (ii) measurement of the dimensions of recovered gaskets after various samples were compressed using different loads (•); and (iii) consideration of the diamond Bragg peaks measured when various GeO_2 glass pellets were compressed in sintered diamond anvils (▼). The solid curve (—) was obtained by assuming that no pressure is applied to the sample for $0 \leqslant L$ (tonne) $\lesssim 7$, as the gasket assembly deforms into the grooves of the anvils.

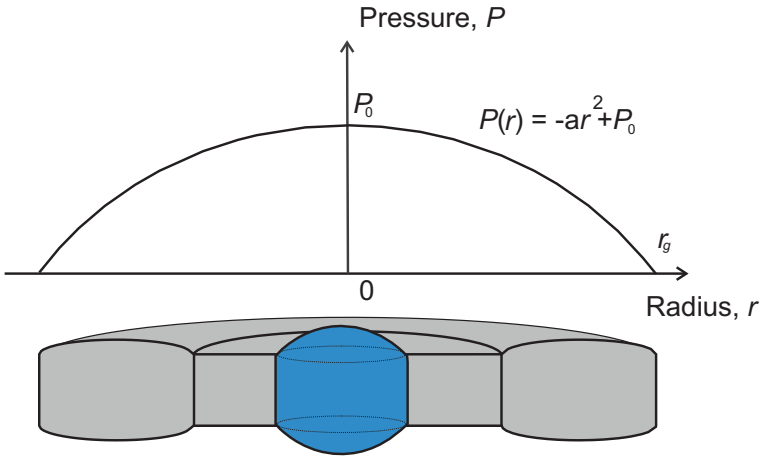

Figure 3-7: A schematic showing the parabolic pressure profile assumed for a sample within a Ti-Zr gasket in the Paris-Edinburgh press.

pressure at the sample position P_0 is obtained using

$$P_0 = \frac{2F(r_g)}{A_g} = \left(\frac{2g}{\pi r_g^2}\right) L, \tag{3.7}$$

where $A_g = \pi r_g^2$ is the total area of the sample and gasket system.

3.3.2 Pressure across gasket

The effective pressure across the gasket and its effective density can be expressed as a function of P_0. The force applied across the Ti-Zr gasket is given by

$$F_g = F(r_g) - F(r'_g), \tag{3.8}$$

where r'_g is the inner radius of the gasket and the total force $F(r'_g)$ up to radius r'_g is

$$F(r'_g) = \int_0^{r'_g} 2\pi r P(r) r dr = \pi P_0 r_g^2 \left[\left(\frac{r'_g}{r_g}\right)^2 - \frac{1}{2}\left(\frac{r'_g}{r_g}\right)^4\right]. \tag{3.9}$$

Thus by combining equations 3.6 and 3.9, F_g is given by

$$F_g = \pi P_0 r_g^2 \left[\frac{1}{2} - \left(\frac{r'_g}{r_g}\right)^2 + \frac{1}{2}\left(\frac{r'_g}{r_g}\right)^4\right] \tag{3.10}$$

Given that the total annular surface area is

$$A_g = \pi(r_g^2 - {r'_g}^2), \tag{3.11}$$

the average pressure exerted over the gasket can be written as

$$P_g = \frac{F_g}{A_g} = \frac{P_0 {r_g}^2}{{r_g}^2 - {r'_g}^2}\left[\frac{1}{2} - \left(\frac{r'_g}{r_g}\right)^2 + \frac{1}{2}\left(\frac{r'_g}{r_g}\right)^4\right]. \tag{3.12}$$

The values for r_g and r'_g at each pressure point P_0 were estimated by assuming a linear relationship between the measured values for uncompressed and recovered gaskets. The thickness t_g of the gasket also decreased linearly with load after the initial deformation took place (figure 3-8). The vertical displacement with applied load of the centre of the sample and gasket system with respect to the centre of the beam makes it necessary to reposition the press at each pressure point. This was done by supporting the PE press on a piezoelectric motor driven platform, and using a video camera to ensure alignment

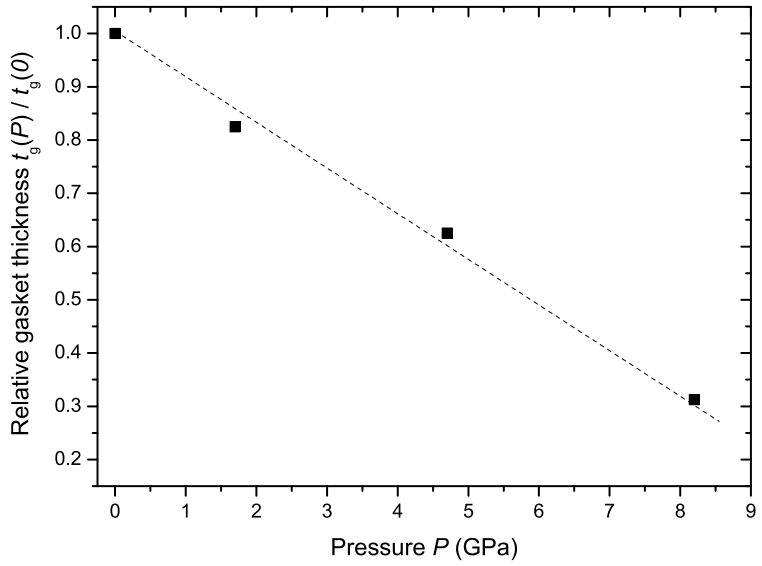

Figure 3-8: Plot of the relative thickness (■) of a Ti-Zr gasket recovered from various pressure points. The broken black line (- - -) is shown to aid visualisation

of the sample and the gasket system in the incident beam at each pressure point (see figure 3-3).

The equation of state for the null scattering alloy $Ti_{0.676}Zr_{0.324}$ has not been measured as a function of pressure. However, the elements Ti [38, 39] and Zr [40–43], and the equiatomic alloy TiZr [44, 45], have been studied. Under ambient conditions, titanium forms a hexagonal close-packed α-phase which transforms at ambient temperature to a hexagonal ω-phase at 7.4-9 GPa. Similarly, zirconium transforms from an α to an ω-phase at 5.5-6.7 GPa, while for the equiatomic alloy TiZr, the same transformation between phases occurs at 11.0 ± 1.5 GPa. Vegard's law can be used to calculate the number density of a Ti-Zr alloy by first using a linear combination of the volume per atom of the individual components i.e.

$$V(\mathrm{Ti}_{c_{\mathrm{Ti}}}\mathrm{Zr}_{c_{\mathrm{Zr}}}) = c_{\mathrm{Ti}}V(\mathrm{Ti}) + c_{\mathrm{Zr}}V(\mathrm{Zr}), \tag{3.13}$$

where $c_{\mathrm{Ti}} + c_{\mathrm{Zr}} = 1$ and then converting to number density using

$$\rho(\mathrm{Ti}_{c_{\mathrm{Ti}}}\mathrm{Zr}_{c_{\mathrm{Zr}}}) = \frac{\rho(\mathrm{Ti})\rho(\mathrm{Zr})}{c_{\mathrm{Ti}}\rho(\mathrm{Zr}) + c_{\mathrm{Zr}}\rho(\mathrm{Ti})} \tag{3.14}$$

As shown in figure 3-9, where the data for α-Zr is extrapolated from 6 to 9 GPa, Vegard's law reproduces the measured density of α-TiZr across the same pressure range

to within 2%. The null scattering Ti-Zr number density was also calculated using Vegard's law by assuming distinct α and ω phases. The ambient pressure number density of $\rho(\mathrm{Ti}_{0.676}\mathrm{Zr}_{0.324})$= 0.0511(5) Å^{-3} was measured in ref. [31] and is reproduced by using Vegard's law to within 2%.

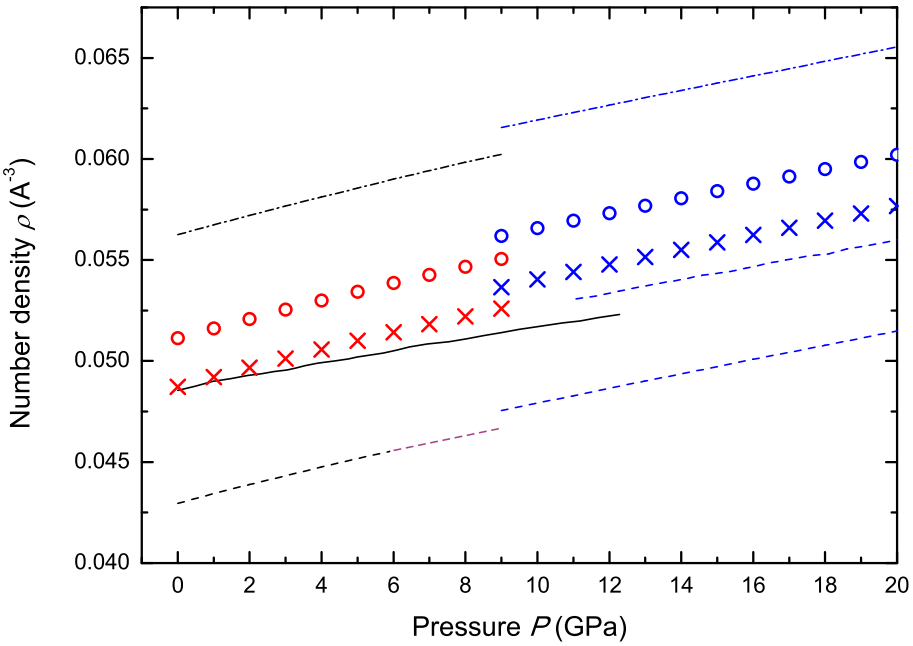

Figure 3-9: The relationship between the number density n_0 and pressure at room temperature for α-Ti [38] (-·-·-), α-Zr [43] (- - -) and the equiatomic alloy α-TiZr (——) [44]. The broken purple curve (- - -) shows an extrapolation for α-Zr into the 6–9 GPa range. The number density for the equiatomic alloy α-TiZr (×) and the null scattering alloy α-$\mathrm{Ti}_{0.676}\mathrm{Zr}_{0.324}$ (○) as calculated by Vegard's rule. The blue curves or symbols represent ω phases.

3.4 Neutron diffraction data treatment

The scattered intensities measured by the D4c detectors are normalised with respect to the monitor count. As shown in the previous section, a pressure experiment requires the sample to be contained within a Ti-Zr gasket enclosed by the anvils of the press. The measured intensity, denoted by $I^E_{SC}(\theta)$, therefore contains a non-negligible contribution from gasket and anvil scattering. To correct for this, the scattered intensities are also measured for an empty gasket $I^E_C(\theta)$ and the empty anvils $I^E_B(\theta)$. In addition, the beam intensities are affected by absorption and multiple scattering events, and further challenges arise as the sample and gasket geometry changes with increasing pressure. These issues are addressed in this section which describes the procedure that is required for the extraction of a total structure factor $F(Q)$.

3.4.1 Attenuation, multiple scattering and Placzek corrections

The anvils define a nearly cylindrical sample geometry which is shown in figure 3-10. The absorption or scattering events will lead to attenuation of the incident and scattered beams. The calculated attenuation coefficients, which are dependent on the scattering angle 2θ, are denoted by $A_{i,j}(\theta)$ [46] where the subscripts refer to neutrons scattered in medium i and attenuated in medium j. Additional corrections are also required for (i) neutrons that undergo multiple scattering events prior to detection and (ii) deviations from the static approximation if the energy exchanged between an incident neutron and target nucleus is non-negligible, i.e. if $\frac{\Delta E}{E_i} \ll 1$ does not hold.

Let us consider the ideal case of a containerless sample with a cylindrical geometry, say a silica rod. The background corrected intensity for the sample is then given by

$$\begin{aligned} I'_S(\theta) &= I^E_S(\theta) - I^E_B(\theta) \\ &= A_{S,S} I_S(\theta) + a(\theta) M_S(\theta), \end{aligned} \tag{3.15}$$

where $a(\theta)$ is the diffractometer calibration factor which is measured by reference to a vanadium standard [47]. $M_S(\theta)$ is the multiple-scattering cross and is calculated using the quasi-isotropic approximation [48] such that

$$M_S(\theta) = N_S A_{S,S}(\theta) \frac{\sigma_S}{4\pi} \Delta_S(\theta)(1 + P_S(\theta)), \tag{3.16}$$

where N_S is the number of illuminated sample scattering centres, $\Delta_S(\theta)$ is the ratio of multiple to single scattering, $\sigma_S = 4\pi(b^2_{\text{coh}} + b^2_{\text{inc}})$ is the total scattering cross section and

$P_S(\theta)$ is the Placzek [21] or inelasticity correction for the sample.

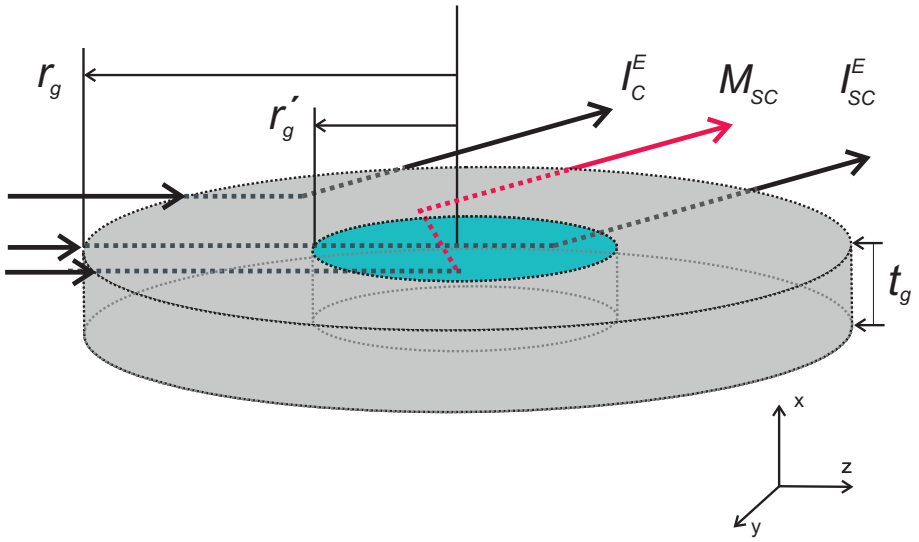

Figure 3-10: Possible paths of neutrons that are incident on the edge of a Ti-Zr gasket of inner radius r_g', outer radius r_g and thickness t_g. The measured intensity $I_{SC}^E(\theta)$ has a significant contribution from the background and gasket scattering. It is also affected by attenuation in the sample and gasket environments and by multiple scattering events $M_{SC}(\theta)$ which need to be corrected for. The scattered gasket intensity $I_C^E(\theta)$ needs to be measured separately without the presence of a sample.

The background corrected intensity for the sample in a Ti-Zr gasket is given by:

$$\begin{aligned} I'_{SC}(\theta) &= I_{SC}^E(\theta) - I_B^E(\theta) \\ &= A_{S,SC}(\theta)I_S(\theta) + A_{C,SC}(\theta)I_C(\theta) + a(\theta)M_{SC}(\theta). \end{aligned} \tag{3.17}$$

In equation 3.17, $I_S(\theta)$ and $I_C(\theta)$ denote the single scattered intensities for the sample and container, respectively. Similarly, the background corrected intensity for an empty Ti-Zr gasket is given by

$$\begin{aligned} I'_C(\theta) &= I_C^E(\theta) - I_B^E(\theta) \\ &= A_{C,C}(\theta)I_C(\theta) + a(\theta)M_C(\theta). \end{aligned} \tag{3.18}$$

It follows that the single scattered intensities are given by

$$I_S(\theta) = \frac{1}{A_{S,SC}(\theta)}\left\{I'_{SC}(\theta) - A_{C,SC}I_C(\theta) - a(\theta)M_{SC}(\theta)\right\} \tag{3.19}$$

and

$$I_C(\theta) = \frac{1}{A_{C,C}(\theta)}\left\{I'_C(\theta) - a(\theta)M_C(\theta)\right\}, \tag{3.20}$$

where $I_S(\theta)$ is related to the differential scattering cross section via

$$I_S(\theta) \;=\; a(\theta)N_S\left[\frac{d\sigma}{d\Omega}\right]_S. \tag{3.21}$$

By using equations 3.19, 3.20 and 3.21 and rearranging, the differential scattering cross section can be re-expressed in terms of the measured intensities as

$$\left[\frac{d\sigma}{d\Omega}\right]_S \;=\; \frac{1}{N_S A_{S,SC}(\theta)}\left\{\left[\frac{I'_{SC}(\theta)}{a(\theta)} - M_{SC}(\theta)\right] - \frac{A_{C,SC}(\theta)}{A_{C,C}(\theta)}\left[\frac{I'_C(\theta)}{a(\theta)} - M_C(\theta)\right]\right\}. \tag{3.22}$$

In the case of high-pressure experiments it is difficult to measure exactly the contribution to the scattering from the gasket and background at each pressure point. For example, an empty gasket in the press under a given applied load will not replicate a gasket under the same load with the sample present because the mechanical properties of the sample will affect the gasket deformation. Nonetheless, the intensities measured for the empty uncompressed gasket $I^E_C(\theta)$, an empty gasket $I^E_{C'}(\theta)$ recovered from high pressure and the empty anvils $I^E_B(\theta)$ can be used to find the gasket and background scattering for a sample under load by linear interpolation [31] such that

$$\left[\frac{d\sigma}{d\Omega}\right]_S \;=\; \frac{1}{N_S A_{S,SC}(\theta)}\left\{\frac{I^*_{SC}(\theta)}{a(\theta)} - \left[M_{SC}(\theta) - \frac{A_{C,SC}(\theta)}{A_{C,C}(\theta)}M_C(\theta)\right]\right\}. \tag{3.23}$$

In this equation, the sample intensity corrected for background and container scattering is given by

$$\begin{aligned} I^*_{SC}(\theta) &= [I^E_{SC}(\theta) - I^E_B(\theta)] - \\ &- \frac{A_{C,SC}(\theta)}{A_{C,C}(\theta)}\Big\{x[I^E_C(\theta) - I^E_B(\theta)] + (1-x)[I^E_{C'}(\theta) - I^E_B(\theta)]\Big\} \\ &\equiv I^E_{SC}(\theta) - A_1(\theta,x)I^E_C(\theta) - A_2(\theta,x)I^E_{C'}(\theta) - A_3(\theta)I^E_B(\theta) \end{aligned} \tag{3.24}$$

where $A_1(\theta,x) = xA_{C,CS}(\theta)/A_{C,C}(\theta)$, $A_2(\theta,x) = (x-1)A_{C,CS}(\theta)/A_{C,C}(\theta)$ and $A_3(\theta) = 1 - A_{C,CS}(\theta)/A_{C,C}(\theta)$. The coefficient x $(0 \le x \le 1)$ is used to weight the background corrected container scattering and is unity for an ambient-pressure experiment.

Figure 3-11 shows an example of the intensity $I^E_{SC}(\theta)$ measured for an SiO_2 sample (Chapter 5) under ambient conditions and at a pressure of $P = 3.9$ GPa, along with the intensities measured for an uncompressed gasket $I^E_C(\theta)$, a recovered gasket $I^E_{C'}(\theta)$ and the empty anvils $I^E_B(\theta)$. The sample intensities corrected for the empty anvil and gasket scattering $I^*_{SC}(\theta)$ are also given. Figure 3-12 shows the various calculated attenuation coefficients for a glassy SiO_2 sample in a Ti-Zr gasket under ambient conditions.

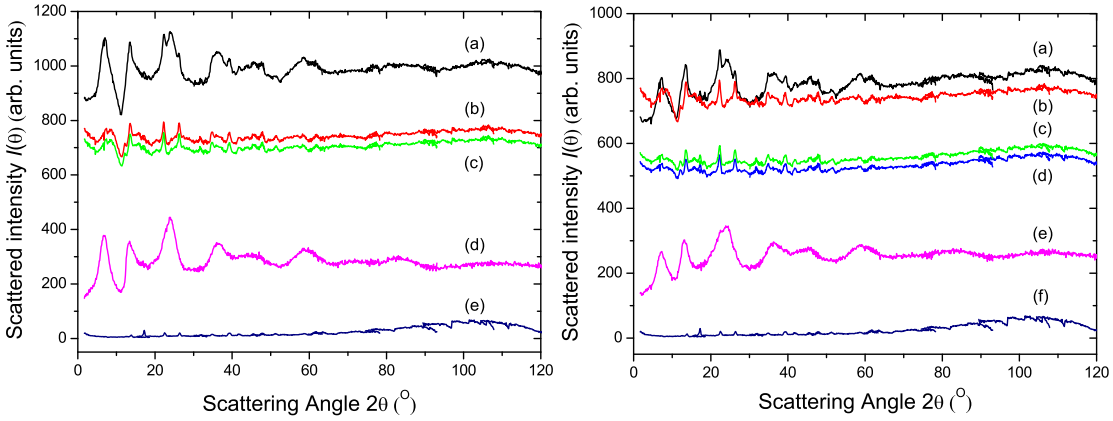

(I) Ambient *(II)* 3.9 GPa

Figure 3-11: A plot of the measured intensities for (I) (a) a glassy SiO_2 sample in a Ti-Zr gasket at ambient pressure, (b) an empty Ti-Zr gasket at ambient pressure, (c) the empty gasket at ambient pressure when multiplied by the ratio of attenuation coefficients $A_{C,SC}(\theta)/A_{C,C}(\theta)$, (d) the sample corrected for the empty anvil and gasket scattering and (e) the empty anvils; (II) (a) a glassy SiO_2 sample in a Ti-Zr gasket under an applied pressure of 3.9 GPa, (b) an empty Ti-Zr gasket at ambient pressure, (c) an effective gasket as constructed from the ambient and recovered empty gasket scattered intensities and weighted by $A_{C,SC}(\theta)/A_{C,C}(\theta)$, (d) an empty Ti-Zr gasket recovered from 5.5 GPa, (e) the sample corrected for gasket and empty anvil scattering and (f) the empty anvils.

To test the validity of the linear approximation made in equation 3.24, measurements were made on a selection of empty Ti-Zr gaskets in the PE press during an experiment on SiO_2 (see Chapter 3). As shown in figure 3-13, an intensity $I'_C(\theta)$ was measured for an empty Ti-Zr gasket at ambient pressure, an intensity $I'_{C'}(\theta)$ was measured for an empty Ti-Zr gasket recovered from 3 GPa, an intensity $I'_{C''}(\theta)$ was measured for an empty Ti-Zr gasket recovered from 5.5 GPa, and an intensity $I'_{C'''}(\theta)$ was measured for an empty Ti-Zr gasket recovered from 8.2 GPa. The reconstruction of $I'_{C'}(\theta)$ from the linear combination $I_{\mathrm{rec},C'}(\theta) = 0.49I'_C(\theta) + 0.52I'_{C''}(\theta) - 0.16I^{\mathrm{E}}_B$ reproduces almost all of

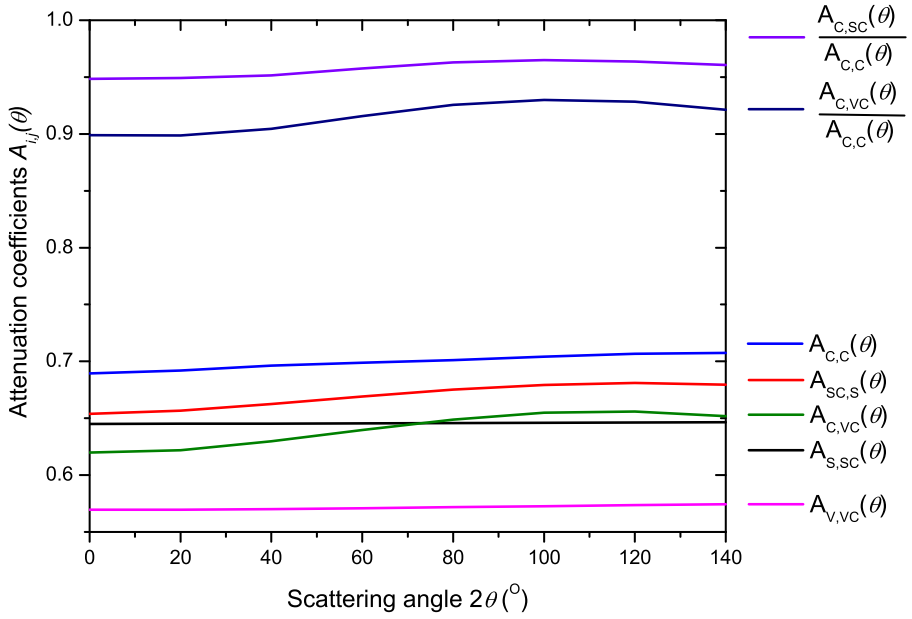

Figure 3-12: An example of the attenuation coefficients calculated using the GUDRUN program [49] for a pellet of SiO_2 or a pellet of vanadium in a Ti-Zr container under ambient conditions.

the features and gives $R_\chi = 0.012$ [50] where the goodness-of-fit parameter is defined by

$$R_\chi = \left\{ \frac{\sum_i [I'_X(\theta_i) - I_{\mathrm{rec,X}}(\theta_i)]^2}{\sum_i {I'_X}^2(\theta_i)} \right\}^{\frac{1}{2}} . \tag{3.25}$$

The reconstruction of $I'_{C''}(\theta)$ from the linear combination $I_{\mathrm{rec},C''}(\theta) = 0.35I'_{C'}(\theta) + 0.70I'_{C'''}(\theta)$ is even better giving $R_\chi = 0.010$ and results from the general observation that the low 2θ features in the Ti-Zr gasket are smoothed out at higher pressures.

It should be noted that the diffraction pattern for the Ti-Zr gasket under ambient conditions is sensitive to the history of the gasket material e.g. the way in which it is machined. Also, XRD experiments [51] show that the gasket material becomes more uniform with increasing pressure so that it shows less preferred orientation.

3.4.2 Vanadium normalisation

The normalisation factor $a(\theta)$ which converts cross-sections to intensities can be measured by reference to a vanadium standard [47]. Vanadium is chosen because it acts as an isotropic elastic scatterer of thermal neutrons and its coherent scattering cross section $\sigma_{\mathrm{coh,V}} \equiv 4\pi b^2_{\mathrm{coh}} = 0.01838(12)$ barn is small by comparison with its incoherent

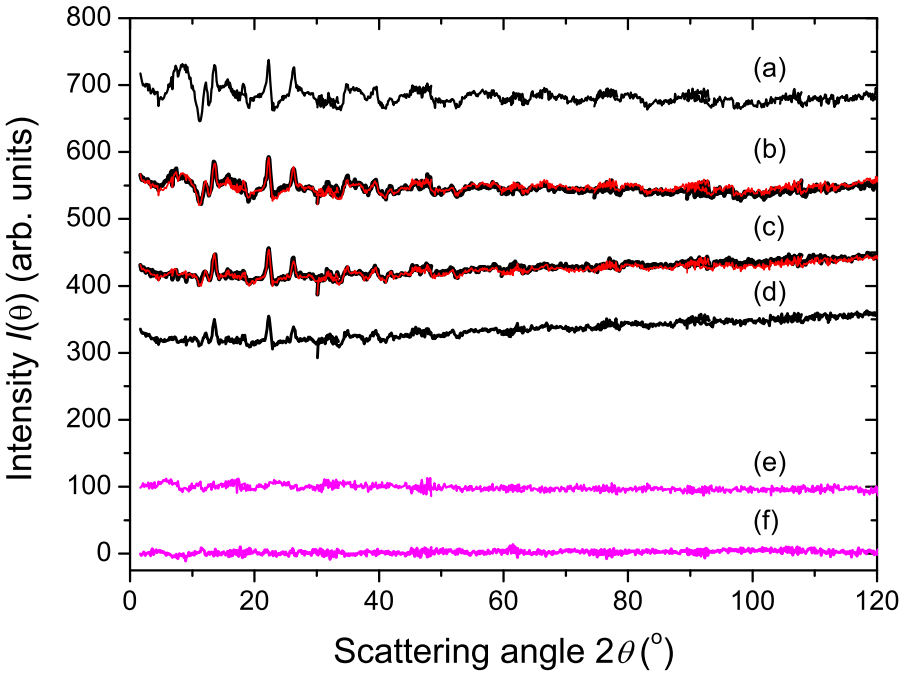

Figure 3-13: A plot of the measured intensity $I(\theta)$ for various empty Ti-Zr gaskets in the PE press that were used to correct the SiO_2 data sets in Chapter 5. The black solid curve (—) corresponds in (a) to the intensity $I'_C(\theta)$ measured for an empty Ti-Zr gasket at ambient pressure, (b) to the intensity $I'_{C'}(\theta)$ measured for an empty Ti-Zr gasket recovered from 3 GPa and (c) to the intensity $I'_{C''}(\theta)$ measured for an empty Ti-Zr gasket recovered from 5.5 GPa, (d) to the intensity $I'_{C'''}(\theta)$ measured for an empty Ti-Zr gasket recovered from 8.2 GPa. The red solid curve (—) gives the reconstruction (a) of $I'_{C'}(\theta)$ from the linear combination $I_{\mathrm{rec},C'}(\theta) = 0.49I'_C(\theta) + 0.52I'_{C''}(\theta) - 0.16I^E_B$ and (c) $I'_{C''}(\theta)$ from the linear combination $I_{\mathrm{rec},C''}(\theta) = 0.35I'_{C'}(\theta) + 0.70I'_{C'''}(\theta)$. The solid magenta curves give the difference (e) $I_{C'}(\theta) - I_{\mathrm{rec},C'}(\theta)$, which is displaced vertically for clarity of presentation, or the difference (f) $I_{C''}(\theta) - I_{\mathrm{rec},C''}(\theta)$.

scattering cross section $\sigma_{\mathrm{inc,V}} \equiv 4\pi b_{\mathrm{inc}}^2 = 5.08(6)$ barn i.e. the scattering is mostly incoherent. In pressure experiments, the diffraction pattern for a solid vanadium pellet of comparable dimensions to the sample is normally used to normalise the neutron diffraction data. When a vanadium pellet is used in place of the sample, equation 3.23 is re-written as

$$\left[\frac{d\sigma}{d\Omega}\right]_V = \frac{1}{N_V A_{V,VC}(\theta)} \left\{ \frac{I^*_{VC}(\theta)}{a(\theta)} - \left[M_{VC}(\theta) - \frac{A_{C,VC}(\theta)}{A_{C,C}(\theta)} M_C(\theta) \right] \right\}, \quad (3.26)$$

where N_V is the number of vanadium nuclei illuminated by the neutron beam and the intensity $I^*_{VC}(\theta)$ is given by

$$I^*_{VC}(\theta) = I^E_{VC}(\theta) - A_1(\theta, x) I^E_C(\theta) - A_2(\theta, x) I^E_{C'}(\theta) - A_3(\theta) I^E_B(\theta). \quad (3.27)$$

Given that the coherent scattering from vanadium is negligible, the differential scattering cross section can be written as

$$\left[\frac{d\sigma}{d\Omega}\right]_V \simeq \frac{\sigma_{\mathrm{inc,V}}}{4\pi}[1 + P_V(\theta)]. \quad (3.28)$$

By rearranging equation 3.26, and substituting in equation 3.28, the normalisation factor is given by

$$a(\theta) = \frac{I^*_{VC}(\theta)}{N_V A_{V,VC}(\theta) \frac{\sigma_{\mathrm{inc,V}}}{4\pi}[1 + P_V(\theta)] + M_{VC}(\theta) - \frac{A_{C,VC}(\theta)}{A_{C,C}(\theta)} M_C(\theta)}. \quad (3.29)$$

Again, since the sample geometry is not explicitly known for *in situ* high pressure measurements, $a(\theta)$ is calculated at intermediate pressures by assuming a linear combination of the ambient pressure diffraction patterns taken for a 'large' vanadium pellet matching the ambient pressure sample geometry, and a 'small' vanadium pellet that approximates the sample geometry at higher pressures. Figure 3-14 shows an example of the measured diffraction patterns for 'large' and 'small' vanadium pellets.

The attenuation factors $A_{i,j}(\theta)$, the multiple scattering cross sections $M_i(\theta)$ for the sample, vanadium and container, and the number of nuclei N_S and N_V in the neutron beam, are all dependent on the gasket geometry.

The attenuation coefficients for the experimental geometry were calculated using the GUDRUN program [49], while the CYLMULTOF program was used to obtain the multiple scattering cross sections [48].

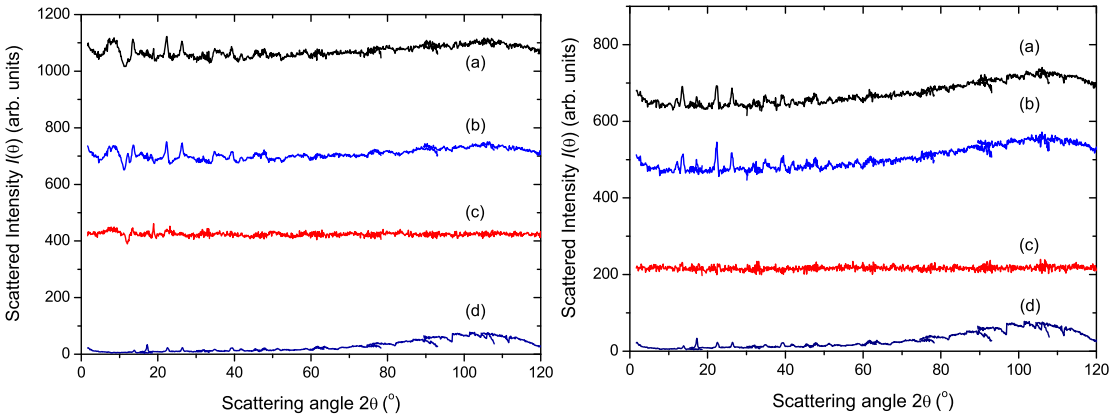

(I) Ambient *(II)* 3.9 GPa

Figure 3-14: A plot of the measured intensities for (I) (a) a 'large' vanadium sample in a Ti-Zr gasket at ambient pressure, (b) an empty Ti-Zr gasket at ambient pressure, (c) the vanadium sample corrected for empty anvil and gasket scattering and (d) the empty anvils; (II) (a) a 'small' vanadium sample in a recovered Ti-Zr gasket at ambient pressure, (b) an empty Ti-Zr gasket recovered from 8.2 GPa and measured at ambient pressure, (c) the vanadium sample corrected for gasket and empty anvil scattering and (d) the empty anvils.

3.4.3 The effect of a finite Q window on the Fourier transformation of F(Q)

By using equation 2.16, the total structure factor $F(Q)$ for a multicomponent glass can be extracted from the differential scattering cross section $[d\sigma/d\Omega]_S$ using

$$F(Q) = \left[\frac{d\sigma}{d\Omega}\right]_S - \sum_{\alpha=1}^{n} c_\alpha (b_{\mathrm{coh},\alpha}^2 + b_{\mathrm{inc},\alpha}^2)(1 + P_\alpha(Q)). \tag{3.30}$$

In isotopic substitution experiments, a difference function $\Delta F(Q)$ obtained from the total structure factors is defined e.g. by using equation 2.27 or 2.28.

The real space functions associated with $F(Q)$ and $\Delta F(Q)$ are obtained from the Fourier transform relations

$$\begin{aligned} G(r) &= \frac{1}{2\pi^2 r\rho}\int_0^\infty QF(Q)M(Q)\sin(Qr)\mathrm{dQ} \\ \Delta G(r) &= \frac{1}{2\pi^2 r\rho}\int_0^\infty Q\Delta F(Q)M(Q)\sin(Qr)\mathrm{dQ}, \end{aligned} \tag{3.31}$$

where $M(Q)$ is a modification function defined by $M(Q) = 1$ for $Q \leq Q_{\max}$, $M(Q) = 0$ for $Q > Q_{\max}$ which is introduced because a diffractometer can measure only over a finite Q range up to maximum value $Q_{\max}$. To provide smoother real space data sets,

$M(Q)$ is often adjusted such that

(1) $M(Q) = 1$ for $Q < Q_{\min}$, $M(Q) = [1 + \cos(X)]/2$ for $Q_{\min} \leq Q \leq Q_{\max}$ and $M(Q) = 0$ for $Q > Q_{\max}$ where $X = \pi Q/(Q_{\max} - Q_{\min})$ and $Q_{\min}$ is a chosen point in the diffractogram where $M(Q) = [1 + \cos(X)]/2$ starts taking effect

or

(2) it is given by the Lorch modification function $M(Q) = \sin(\pi Q/Q_{\max})$ [23].

Procedure (1) reduces the severity of unphysical oscillations in r-space that would otherwise be introduced by a sudden truncation of the data sets. Procedure (2) gives smoother $G(r)$ or $\Delta G(r)$ functions at all r values but leads to a reduction in the resolution of the first r-space peak. Harwell spline fitting [52] is often applied to the measured structure factors $F(Q)$ or difference functions $\Delta F(Q)$ prior to Fourier transformation, in order to reduce the effects of noise and to smooth out any sharp artifacts that are not fully corrected when subtracting the gasket and background scattering.

Self consistency checks are performed on the data sets to ensure that each measured $F(Q)$ or $\Delta F(Q)$ function obeys the sum rule relation (equation 2.22), the low-r features in $G(r)$ or $\Delta G(r)$ oscillate about the theoretical $G(r \to 0)$ or $\Delta G(r \to 0)$ limit, respectively, and that the back Fourier transforms of $G(r)$ or $\Delta G(r)$, after their low-r features are set to the calculated $G(r \to 0)$ or $\Delta G(r \to 0)$ limit, are in agreement with the original $F(Q)$ or $\Delta F(Q)$ functions [53].

3.4.4 Data analysis flow diagram

The data analysis procedure for obtaining structural information from diffraction data measured for amorphous materials under pressure can be summarised by the flow diagram shown in figure 3-15.

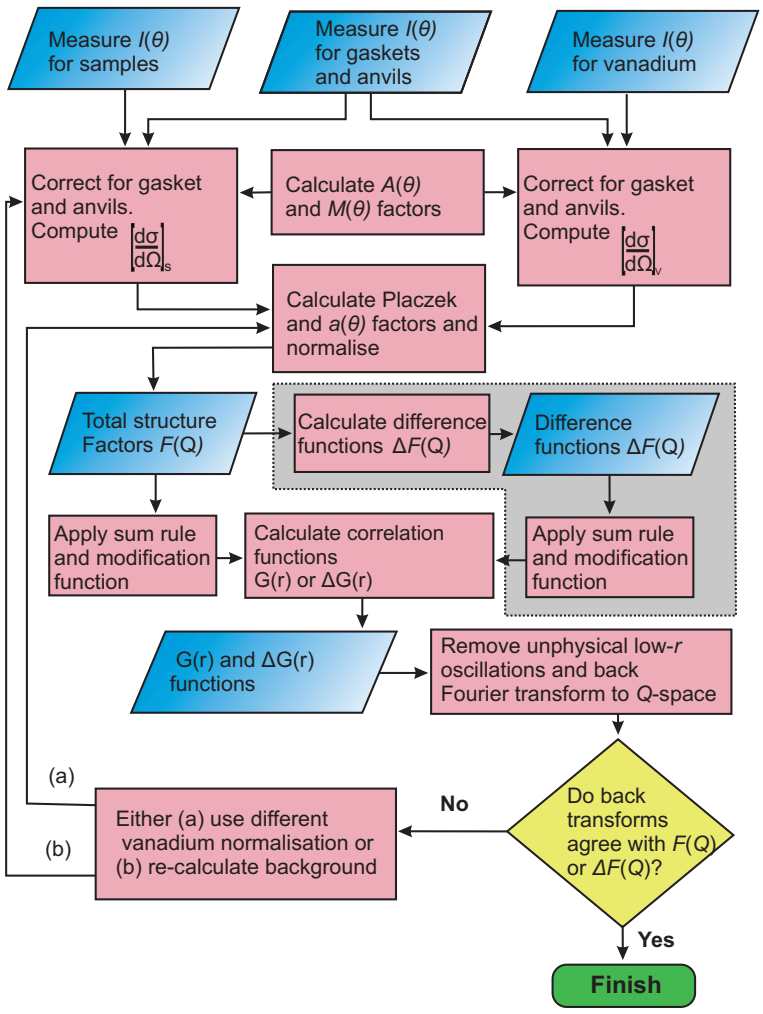

Figure 3-15: A flow diagram representing the procedure used for data analysis at the D4c instrument for diffraction work under pressure. The grey area shows the additional steps used in isotopic substitution experiments.

Chapter 4

Mechanisms of network collapse in GeO_2 glass

4.1 Introduction

The structural changes in glasses and liquids induced by high-pressure and/or high-temperature conditions can alter substantially their dynamical and transport properties [5–8]. A notable example is provided by so-called polyamorphic transitions where the variation of a state parameter such as pressure of temperature leads to an abrupt transformation between two phases having the same composition but different densities [5–8, 54, 55]. Unravelling the mechanisms by which these transformations occur is, however, a formidable task owing to the nature of structural disorder [5, 56] and the experimental difficulties associated with the investigation of materials under extreme conditions [31, 57–61]. Notwithstanding these challenges, structural transformations offer an excellent opportunity for testing the efficacy of models used to predict the physical properties of glasses and liquids.

In this chapter, these issues are addressed by making the first use of the method of *in situ* neutron diffration with isotope substitution (NDIS) to measure the high-pressure structure of a glass, chosen to be GeO_2 on account of its scientific interest and the availability of suitable germanium isotopes [20]. Like silica, which is studied in Chapter 5, and BeF_2, GeO_2 is a prototypical 'strong' network glass-forming system [6, 62] for which significant structural changes occur as the material transforms to a high density polyamorph, often regarded as a more 'fragile' counterpart to the ambient-pressure material [6, 31, 57, 63–70]. The transformations in GeO_2 occur at lower pressures by comparison with silica, making them more amenable to study by *in situ* high-pressure

experiments [64, 67, 71], which are necessary to avoid relaxation of the glass on recovery to ambient conditions [31, 57, 72]. Furthermore, the pressure and temperature-driven structural transformations in Mg_2GeO_4 have been investigated to reveal, for example, the phase transformations between the olivine and spinel structures and the mechanical properties of these polymorphs [73–77]. The germanate Mg_2GeO_4 is an analogue of forsterite Mg_2SiO_4 which is the Mg rich member of the olivine solid solution series $(Mg, Fe)_2SiO_4$, important constituents of the Earth's upper mantle [78].

The real-space results obtained from conventional neutron diffraction [13, 31] and extended x-ray absorption fine structure (EXAFS) spectroscopy [63, 68, 70] are limited to a description of the Ge-O nearest neighbours, although x-ray diffraction experiments also provide some information on the Ge-Ge correlations [31, 57, 69]. It is therefore necessary to have more detailed and unambiguous structural information on e.g. the O-O correlations in this oxide glass in order to test the veracity of the various models that have been proposed for the mechanisms of pressure-driven network collapse [57, 79–85]. The NDIS method has played a key role in revealing the structure of multi-component glasses and liquids [10, 24, 56].

Recently, much effort has been devoted to the instrumentation and methodology required to make accurate measurements of the neutron diffraction patterns for glasses and liquids at pressures within the 1-20 GPa regime [13, 31]. The progress made has facilitated the present *in situ* NDIS experiment which is designed to resolve the nearest-neighbour Ge-Ge and O-O correlations and hence provide previously unknown information on e.g. the intra-polyhedral O-Ge-O and inter-polyhedral Ge-O-Ge bond-angle distributions. It is found that, of the various models available, the NDIS results are in agreement only with molecular dynamics simulations based on the method described by Marrocchelli *et al* [12, 85]. Additional quantitative information is thereby gained on the nature of the structural transformations that occur.

4.2 Theory

As shown in Chapter 2, the coherent scattered intensity measured in a neutron diffraction experiment on a multicomponent glassy system is proportional to the total structure factor:

$$F(Q) = \sum_{\alpha=1}^{n} \sum_{\beta=1}^{n} c_\alpha c_\beta b_\alpha b_\beta [S_{\alpha\beta}(Q) - 1], \tag{4.1}$$

where n is the number of chemical species α or β, c_α and b_α are the concentration and coherent scattering length of species α, respectively, while $S_{\alpha\beta}(Q)$ is a Faber-Ziman

partial structure factor and Q is the magnitude of the scattering vector. Suppose that diffraction patterns are measured for three samples $^{70}GeO_2$, $^{N}GeO_2$ and $^{73}GeO_2$ that are identical in every way apart from the isotopic abundance of germanium where N denotes the natural isotopic abundance of Ge while ^{70}Ge and ^{73}Ge denote highly enriched Ge isotopes ($\geq 96\%$). The resultant total structure factors, denoted by $^{70}F(Q)$, $^{N}F(Q)$ and $^{73}F(Q)$,respectively, can be represented in matrix notation by

$$\begin{pmatrix} ^{70}F(Q) \\ ^{N}F(Q) \\ ^{73}F(Q) \end{pmatrix} = \begin{pmatrix} 0.1102(4) & 0.2569(5) & 0.1497(4) \\ 0.0744(25) & 0.2111(22) & 0.1497(4) \\ 0.0294(9) & 0.1328(10) & 0.1497(4) \end{pmatrix} \begin{pmatrix} S_{\mathrm{GeGe}}(Q)-1 \\ S_{\mathrm{GeO}}(Q)-1 \\ S_{\mathrm{OO}}(Q)-1 \end{pmatrix} \tag{4.2}$$

where the weighing coefficients for $S_{\alpha\beta}(Q)$ are in units of barns (10^{-28} m^2) and are tabulated for coherent scattering length values of $b_{^{70}\mathrm{Ge}} = 9.965(98)$, $b_{^{73}\mathrm{Ge}} = 5.148(39)$, $b_{^{N}\mathrm{Ge}} = 8.185(20)$ and $b_{\mathrm{O}} = 5.803(4)$ fm, which correspond to the isotopic enrichments used in this experiment and where the values for the scattering lengths are taken from Sears [86]. The atomic concentrations of Ge and O are $c_{\mathrm{Ge}} = 1/3$ and $c_{\mathrm{O}} = 2/3$, respectively.

The complexity of correlations associated with a single total structure factor can be reduced, for example, by removing the O-O correlations thus forming a first order difference function such as $\Delta F^{(1)}_{\mathrm{Ge}}(Q)$ written as:

$$\begin{aligned} \Delta F^{(1)}_{\mathrm{Ge}}(Q) &\equiv {}^{70}F(Q) - {}^{73}F(Q) = \\ &= c^2_{\mathrm{Ge}}(b^2_{^{70}\mathrm{Ge}} - b^2_{^{73}\mathrm{Ge}})[S_{\mathrm{GeGe}}(Q)-1] + \\ &+ 2c_{\mathrm{Ge}}c_{\mathrm{O}}b_{\mathrm{O}}(b_{^{70}\mathrm{Ge}} - b_{^{73}\mathrm{Ge}})[S_{\mathrm{GeO}}(Q)-1], \end{aligned} \tag{4.3}$$

where the $S_{\mathrm{GeGe}}(Q)$ and $S_{\mathrm{GeO}}(Q)$ weighting factors take values of 0.0809(11) and 0.1243(27) barns respectively. Equivalent expressions follow for $\Delta F^{(2)}_{\mathrm{Ge}}(Q) \equiv {}^{70}F(Q) - {}^{N}F(Q)$ and $\Delta F^{(3)}_{\mathrm{Ge}}(Q) \equiv {}^{N}F(Q) - {}^{73}F(Q)$. The coefficients are summarised in the following matrix:

$$\begin{pmatrix} \Delta F^{(1)}_{\mathrm{Ge}}(Q) \\ \Delta F^{(2)}_{\mathrm{Ge}}(Q) \\ \Delta F^{(3)}_{\mathrm{Ge}}(Q) \end{pmatrix} = \begin{pmatrix} 0.0809(11) & 0.1243(27) & 0.0000(3) \\ 0.0450(3) & 0.0783(11) & 0.0000(3) \\ 0.0359(11) & 0.0459(26) & 0.0000(3) \end{pmatrix} \begin{pmatrix} S_{\mathrm{GeGe}}(Q)-1 \\ S_{\mathrm{GeO}}(Q)-1 \\ S_{\mathrm{OO}}(Q)-1 \end{pmatrix}. \tag{4.4}$$

The Ge-Ge correlations can be eliminated by forming a weighted first order difference function such as $\Delta F^{(1)}_{\mathrm{O}}(Q)$ written as:

$$\begin{aligned}
\Delta F_{\mathrm{O}}^{(1)}(Q) &\equiv {}^{70}F(Q) - \frac{b_{^{70}\mathrm{Ge}}^2}{b_{^{70}\mathrm{Ge}}^2 - b_{^{73}\mathrm{Ge}}^2}\Delta F_{\mathrm{Ge}}^{(1)}(Q) = \\
&= \frac{b_{^{70}\mathrm{Ge}}^2\ {}^{73}F(Q) - b_{^{73}\mathrm{Ge}}^2\ {}^{70}F(Q)}{b_{^{70}\mathrm{Ge}}^2 - b_{^{73}\mathrm{Ge}}^2} \\
&= c_{\mathrm{O}}^2 b_{\mathrm{O}}^2[S_{\mathrm{OO}}(Q) - 1] \\
&+ \frac{2c_{\mathrm{Ge}}c_{\mathrm{O}}b_{\mathrm{O}}\ b_{^{73}\mathrm{Ge}}b_{^{70}\mathrm{Ge}}}{b_{^{70}\mathrm{Ge}} + b_{^{73}\mathrm{Ge}}}[S_{\mathrm{GeO}}(Q) - 1], \qquad (4.5)
\end{aligned}$$

where the Ge-O and O-O coefficients are 0.0875(4) and 0.1497(4) barns, respectively. Equivalent expressions follow for $\Delta F_{\mathrm{O}}^{(2)}(Q) \equiv^{\mathrm{N}} F(Q) - b_{^{\mathrm{N}}\mathrm{Ge}}^2/\left(b_{^{\mathrm{N}}\mathrm{Ge}}^2 - b_{^{73}\mathrm{Ge}}^2\right)\Delta F_{\mathrm{Ge}}^{(2)}(Q)$ and $\Delta F_{\mathrm{O}}^{(3)}(Q) \equiv^{70} F(Q) - b_{^{70}\mathrm{Ge}}^2/\left(b_{^{70}\mathrm{Ge}}^2 - b_{^{\mathrm{N}}\mathrm{Ge}}^2\right)\Delta F_{\mathrm{Ge}}^{(3)}(Q)$. The coefficients are summarised in the following matrix:

$$\begin{pmatrix} \Delta F_{\mathrm{O}}^{(1)}(Q) \\ \Delta F_{\mathrm{O}}^{(2)}(Q) \\ \Delta F_{\mathrm{O}}^{(3)}(Q) \end{pmatrix} = \begin{pmatrix} 0.0000(3) & 0.0875(5) & 0.1497(4) \\ 0.0000(3) & 0.0815(2) & 0.1497(4) \\ 0.0000(3) & 0.0700(8) & 0.1497(4) \end{pmatrix} \begin{pmatrix} S_{\mathrm{GeGe}}(Q) - 1 \\ S_{\mathrm{GeO}}(Q) - 1 \\ S_{\mathrm{OO}}(Q) - 1 \end{pmatrix}. \qquad (4.6)$$

Also, the Ge-O correlations can be eliminated using another set of weighted first order difference functions such as:

$$\begin{aligned}
\Delta F_{\mathrm{O}'}^{(1)}(Q) &\equiv {}^{70}F(Q) - \frac{b_{^{70}\mathrm{Ge}}}{b_{^{70}\mathrm{Ge}} - b_{^{73}\mathrm{Ge}}}\Delta F_{\mathrm{Ge}}^{(1)}(Q) = \\
&= \frac{b_{^{70}\mathrm{Ge}}\ {}^{73}F(Q) - b_{^{73}\mathrm{Ge}}\ {}^{70}F(Q)}{b_{^{70}\mathrm{Ge}} - b_{^{73}\mathrm{Ge}}} \\
&= c_{\mathrm{O}}^2 b_{\mathrm{O}}^2[S_{\mathrm{OO}}(Q) - 1] \\
&- c_{\mathrm{Ge}}^2 b_{^{73}\mathrm{Ge}}\ b_{^{70}\mathrm{Ge}}[S_{\mathrm{GeGe}}(Q) - 1], \qquad (4.7)
\end{aligned}$$

where the $S_{\mathrm{GeGe}}(Q)$ and $S_{\mathrm{OO}}(Q)$ weighting factors are -0.0570(80) and 0.1497(4) barns, respectively. Equivalent expressions follow for $\Delta F_{\mathrm{O}'}^{(2)}(Q) \equiv^{\mathrm{N}} F(Q) - b_{^{\mathrm{N}}\mathrm{Ge}}/(b_{^{\mathrm{N}}\mathrm{Ge}} - b_{^{73}\mathrm{Ge}})\Delta F_{\mathrm{Ge}}^{(2)}(Q)$ and $\Delta F_{\mathrm{O}'}^{(3)}(Q) \equiv^{70} F(Q) - b_{^{70}\mathrm{Ge}}/(b_{^{70}\mathrm{Ge}} + b_{^{\mathrm{N}}\mathrm{Ge}})\Delta F_{\mathrm{Ge}}^{(3)}(Q)$. The coefficients are summarised in the following matrix:

$$\begin{pmatrix} \Delta F_{\mathrm{O}'}^{(1)}(Q) \\ \Delta F_{\mathrm{O}'}^{(2)}(Q) \\ \Delta F_{\mathrm{O}'}^{(3)}(Q) \end{pmatrix} = \begin{pmatrix} -0.0570(80) & 0.0000(4) & 0.1497(4) \\ -0.0468(40) & 0.0000(2) & 0.1497(4) \\ -0.0906(189) & 0.0000(4) & 0.1497(4) \end{pmatrix} \begin{pmatrix} S_{\mathrm{GeGe}}(Q) - 1 \\ S_{\mathrm{GeO}}(Q) - 1 \\ S_{\mathrm{OO}}(Q) - 1 \end{pmatrix}. \qquad (4.8)$$

The real space functions $G(r)$, $\Delta G_{\mathrm{O}}^{(i)}(r)$ and $\Delta G_{\mathrm{O}'}^{(i)}(r)$, with $i = 1,\ 2,\ 3$, are obtained by Fourier transforming of the corresponding reciprocal space functions:

$$G(r) = \frac{1}{2\pi^2 r\rho}\int_0^\infty QF(Q)\sin(Qr)M(Q)dQ \tag{4.9}$$

$$\Delta G_{\mathrm{Ge}}^{(i)}(r) = \frac{1}{2\pi^2 r\rho}\int_0^\infty Q\Delta F_{\mathrm{Ge}}^{(i)}(Q)\sin(Qr)M(Q)dQ \tag{4.10}$$

$$\Delta G_{\mathrm{O}}^{(i)}(r) = \frac{1}{2\pi^2 r\rho}\int_0^\infty Q\Delta F_{\mathrm{O}}^{(i)}(Q)\sin(Qr)M(Q)dQ \tag{4.11}$$

$$\Delta G_{\mathrm{O}'}^{(i)}(r) = \frac{1}{2\pi^2 r\rho}\int_0^\infty Q\Delta F_{\mathrm{O}'}^{(i)}(Q)\sin(Qr)M(Q)dQ \tag{4.12}$$

where ρ is the atomic number density, $g_{\alpha\beta}(r)$ is a partial pair distribution function, r is a real space distance and $M(Q)$ is a modification function defined by $M(Q)$=1 for $Q \leq Q_{\max}$, $M(Q)$=0 for $Q > Q_{\max}$ that has been introduced because a diffractometer can measure over only a limited Q range up to a maximum value $Q_{\max}$. Provided the structure in reciprocal space function has decayed by $Q_{\max}$, expressions for $G(r)$, $\Delta G_{\mathrm{Ge}}^{(i)}(r)$, $\Delta G_{\mathrm{O}}^{(i)}(r)$ and $\Delta G_{\mathrm{O}'}^{(i)}(r)$ can be obtained from the equations for $F(Q)$, $\Delta F_{\mathrm{Ge}}^{(i)}(Q)$, $\Delta F_{\mathrm{O}}^{(i)}(Q)$ and $\Delta F_{\mathrm{O}'}^{(i)}(Q)$, respectively, by replacing $S_{\alpha\beta}(Q)$ by $g_{\alpha\beta}(r)$.

The theoretical low-r limits of these these functions are given by the sum of the weighting coefficients of the $g_{\alpha\beta}(r)$ functions presented in table 4.1.

Table 4.1: Weighting factors for the $g_{\alpha\beta}(r)$ partials (in barns) for the $G(r)$, $\Delta G^{(i)}_{\mathrm{Ge}}(r)$, $\Delta G^{(i)}_{\mathrm{O}}(r)$ and $\Delta G^{(i)}_{\mathrm{O'}}(r)$ functions. The theoretical low r limits (in barns) are also given.

	$g_{\mathrm{GeO}}(r)$	$g_{\mathrm{GeGe}}(r)$	$g_{\mathrm{OO}}(r)$	r=0 limit
${}^{70}G(r)$	0.1102(4)	0.2569(5)	0.1497(4)	-0.517(3)
${}^{\mathrm{N}}G(r)$	0.074(3)	0.211(2)	0.1497(4)	-0.4352(8)
${}^{73}G(r)$	0.0294(9)	0.133(1)	0.1497(4)	-0.312(1)
$\Delta G^{(1)}_{\mathrm{Ge}}(r)$	0.081(1)	0.124(3)	0.0000(3)	-0.205(4)
$\Delta G^{(2)}_{\mathrm{Ge}}(r)$	0.0450(3)	0.078(1)	0.0000(3)	-0.123(2)
$\Delta G^{(3)}_{\mathrm{Ge}}(r)$	0.036(1)	0.046(3)	0.0000(3)	-0.0818(3)
$\Delta G^{(1)}_{\mathrm{O}}(r)$	0.0000(3)	0.0875(5)	0.1497(4)	-0.237(6)
$\Delta G^{(2)}_{\mathrm{O}}(r)$	0.0000(1)	0.0815(2)	0.1497(4)	-0.231(2)
$\Delta G^{(3)}_{\mathrm{O}}(r)$	0.0000(3)	0.0700(8)	0.1497(4)	-0.27(1)
$\Delta G^{(1)}_{\mathrm{O'}}(r)$	0.0000(4)	-0.0570(5)	0.1497(4)	-0.093(8)
$\Delta G^{(2)}_{\mathrm{O'}}(r)$	0.0000(2)	-0.0470(4)	0.1497(4)	-0.103(4)
$\Delta G^{(3)}_{\mathrm{O'}}(r)$	0.0000(4)	-0.0910(2)	0.1497(4)	-0.06(2)

4.3 Experimental procedure

4.3.1 Sample preparation

Glassy samples were prepared by heating powdered $^{N}GeO_2$ (99.9999%, Alfa Aesar), $^{70}GeO_2$ (^{70}Ge 97.71%, ^{72}Ge 2.23%, ^{73}Ge 0.02%, ^{74}Ge 0.03%, ^{72}Ge 0.01%, Isoflex USA) or $^{73}GeO_2$ (^{70}Ge 0.04%, ^{72}Ge 2.84%, ^{73}Ge 96.07%, ^{74}Ge 1.03%, ^{72}Ge 0.02%, Isoflex USA) contained in platinum crucibles at 1400 °C for half an hour [13]. The samples were heated in air in order to prevent any change of sample stoichiometry. After the dwelling time, the crucibles were placed quickly on a liquid nitrogen precooled copper block to bring them to room temperature. Since the GeO_2 samples are hygroscopic, they were stored under dry conditions.

4.3.2 The neutron diffraction experiment

The experiments were made at ambient temperature (T ~300 K) and used the diffractometer D4c at the Institut Laue-Langevin [30]. The high-pressure diffraction experiment employed a VX5/180 type Paris-Edinburgh press (Chapter 3) with cubic BN anvils having a single-toroid profile. Since the sample position changes with piston displacement upon increasing the applied load, the press was mounted on a platform that could be translated vertically (z-axis drive) so that the sample could be centred in the incident beam at each pressure point with the aid of an optical camera.

The background scattering was minimized by optimizing the setup given in Chapter 3. The sample pellets for the high-pressure runs were prepared by using an identical procedure in which finely powdered glass was compacted in a pellet press. They were held in gaskets made from a $Ti_{0.676}Zr_{0.324}$ alloy which has a zero coherent neutron scattering length. The sample masses, as measured at the end of the high-pressure runs, showed that the number of scattering centres for the $^{70}GeO_2$ and $^{73}GeO_2$ samples matched the number for the $^{N}GeO_2$ sample to within 3.5%, while the masses of the gaskets were matched to within 1.1% as shown in table 4.2.

Table 4.2: Masses of the recovered GeO_2 glassy pellets and their corresponding Ti-Zr gaskets.

Sample	Sample mass (g)	Gasket mass (g)
$^{N}GeO_2$	0.229(1)	1.4510(1)
$^{73}GeO_2$	0.222(1)	1.4346(1)
$^{70}GeO_2$	0.230(1)	1.4414(1)

The incident neutron wavelength of $\lambda = 0.6947(1)$ Å and zero scattering angle for the detectors were measured using Ni powder contained within an encapsulated $Ti_{0.676}Zr_{0.324}$ gasket [87] mounted in the Paris-Edinburgh press with no applied load. Higher order ($\lambda/2$) scattering was suppressed by placing an Ir filter after the Cu(200) monochromator, upstream of the sample position.

For a given sample, the diffraction pattern for an empty Ti-Zr gasket was first measured with a small applied load. The sample was then mounted in the gasket and the load on the anvils was always increased during the course of a high-pressure run. Diffraction patterns were also measured for (a) several empty Ti-Zr gaskets that had been recovered from different high pressures in order to estimate the gasket scattering under load, and (b) the empty anvils with different anvil separations in order to help in estimating the background scattering. To assist in the data normalization at different pressures, where the anvils have different separations, additional diffraction patterns were measured at ambient pressure for large and small vanadium pellets contained in unsquashed and recovered (i.e. previously squashed) Ti-Zr gaskets, respectively. The data analysis followed the procedure described in Chapter 3.

The sample pressure P was deduced from the load applied to the anvils of the press by using a calibration curve that has been extensively checked (Chapter 3). At several of the pressure points, in order to assess the sensitivity of the results to the applied load, the latter was varied about its desired value by up to 3.4 tonnes (corresponding to a change in sample pressure of 0.3 GPa) and diffraction patterns were measured. For a given pressure point, this variation of load did not give rise to a notable change in the diffraction patterns within the counting statistics.

The ambient-pressure diffraction experiment used a different experimental setup in which powdered glass samples were held in a vanadium container of inner diameter 4.8 mm and 0.1 mm wall thickness. The incident neutron wavelength was 0.6950(1) Å. Diffraction patterns were taken for each sample in its container, the empty container, the empty instrument, and a cylindrical vanadium rod of diameter 6.072(6) mm for normalisation purposes. A diffraction pattern was also measured for a bar of neutron absorbing $^{10}B_4C$ of dimensions comparable to the sample to account for the effect of the sample's attenuation on the background signal at small scattering angles. As for the high-pressure experiment, each complete diffraction pattern was built up from the intensities measured for different positions of D4c's group of nine microstrip detectors. These intensities were saved at regular intervals to check the sample and diffractometer stabilities. The data were analysed by using a standard procedure (Chapter 3).

The supporting pillars of the Paris-Edinburgh press restrict the maximum accessible

scattering angle as compared to the vanadium container experiment which did not employ high-pressure apparatus. The maximum cutoff value Q_{max} was therefore 15.3 Å^{-1} for the high-pressure experiment as compared to 16.9 Å^{-1} for the ambient-pressure experiment.

The pressure P dependence of the number density of GeO_2 glass, as obtained from several *in situ* studies [65, 66, 69, 88], is shown in figure 4-1.

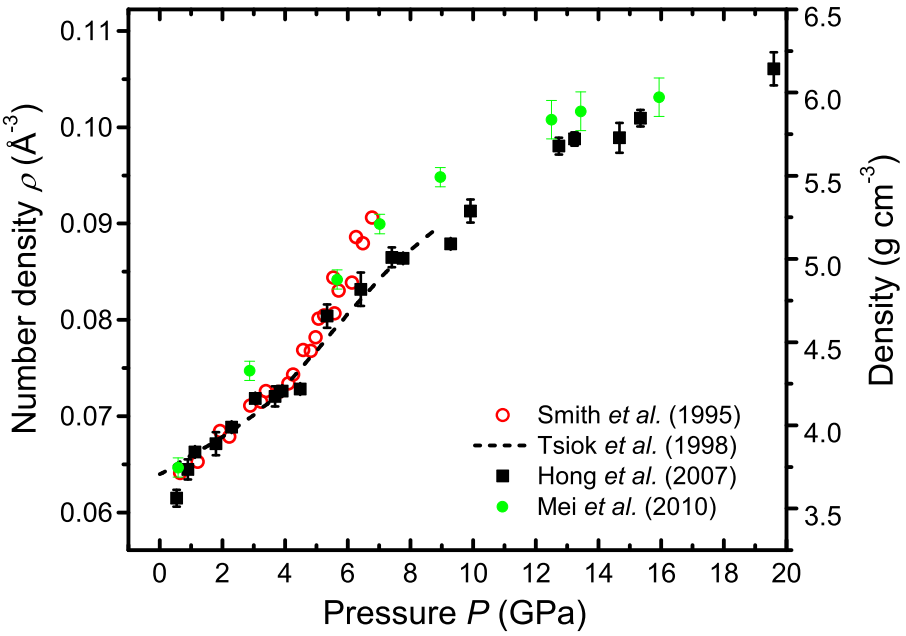

Figure 4-1: The number density ρ and mass density for GeO_2 glass as measured on compression from the *in situ* studies of Hong *et al* [88](■, no pressure transmitting medium), Smith *et al* [65](○, 1:1 mixture of pentane and isopentane used as a pressure transmitting medium), Tsiok *et al* [66] (- - -), 4:1 mixture of methanol:ethanol used as a pressure transmitting medium with a coated glass sample to avoid reaction with this medium), and Mei *et al* [69] (● with vertical error bars, He pressure transmitting medium)

The final results at ambient pressure and at pressures of 4.0(5), 5.9(5), 6.8(5) and 8.0(5) GPa correspond to reduced sample number densities ρ/ρ_0 of 1, 1.156, 1.304, 1.343 and 1.378, respectively, where $\rho_0 = 0.0629$ Å^{-3} is the ambient-pressure value [88–90].

4.4 Molecular dynamics simulations

The molecular dynamics simulations were made using the so-called DIPole-Polarisable Ion Model (DIPPIM) where the interaction potentials include dipole-polarization effects. The potentials were parameterized by using *ab initio* simulations as opposed to

experimental results and are therefore largely unbiased in their predictions of the glass structure [12]. The DIPPIM is the only model currently available that gives, for a single set of parameters, a good account of both the structural and vibrational properties of glassy GeO_2 at ambient pressue along with the dynamical properties of liquid GeO_2 at elevated temperatures [12]. The simulations of the glass were made at $T = 300$ K using a system of $N = 432$ atoms in the NVT ensemble where V denotes the volume of the system. The equations of motion were integrated using a time step of 1 fs, and the polarization energy at each time step was minimized using a conjugate gradient method. An in-house code called PIMAIM was used for the calculations.

To obtain the glass at ambient pressure, GeO_2 was first liquefied at high temperature (5000-10000 K), and a 1 ns long simulation was made at 4000 K. The system was then cooled down to room temperature at a rate of 3.7 K ps^{-1}. A high-pressure state was susequently obtained by using a cold-compression procedure [91] in which the cell lengths and particle positions were rescaled to the new density, a 1 ns long simulation was made to equilibrate the system, and data were collected during a further 1 ns run. A limited timescale is associated with the glass preparation procedure in the molecular dynamics simulations, in common with all standard simulation techniques, such that the equation of state for GeO_2 glass was not reproduced [85]. The simulations were therefore made with the glass density set at the value used to analyse the diffraction results. Where necessary, a density-to-pressure conversion was made using the data of Hong *et al* [88] (figure 4-1).

4.5 Results

4.5.1 Total structure factors

The measured and simulated total structure factors ${}^{70}F(Q)$, ${}^{\mathrm{N}}F(Q)$ and ${}^{73}F(Q)$ at various pressures are plotted in figures 4-2, 4-4 and 4-6 respectively. The corresponding Fourier transforms ${}^{70}G(r)$, ${}^{\mathrm{N}}G(r)$ and ${}^{73}G(r)$ are shown in figures 4-3, 4-5 and 4-7, respectively. The Fourier transformations were performed on Harwell spline fitted $F(Q)$ functions [52] whose high-Q data points were multiplied by a cosine function in the region of $Q = 14.1$–15.3 $Å^{-1}$ so as to remove possible truncation steps. The simulated total structure factors were truncated at the same $Q_{\max}$ as in experiment and multiplied by the same cosine function before Fourier transformation.

As shown in figures 4-2, 4-4 and 4-6 there is good agreement between the data taken for the glassy samples measured in a vanadium can and in the pressure cell environment,

where in the first case a conventional diffraction setup was used with a much larger sample volume (see § 4.3.2). In general there is good agreement between the experimental data and the new molecular dynamics results obtained by using the DIPPIM interaction potentials.

The measured total structure factors show systematic changes with increasing pressure. For example, each function has a first sharp diffraction peak at $\simeq 1.55$ Å^{-1} under ambient conditions which moves to higher Q values and decreases in magnitude with increasing density, indicating a significant alteration to the intermediate range order [92]. In comparison, the principal peak at $\simeq 2.64$ Å^{-1} under ambient conditions, which is associated with extended-range ordering [93, 94], sharpens with increasing pressure. These changes are consistent with a competition between the intermediate and extended-range ordering which is won by the latter with increasing density as the glass transforms to a more 'fragile' material [92, 94].

In real space the $^{70}G(r)$, $^{\mathrm{N}}G(r)$ and $^{73}G(r)$ functions have their the first peak attributable to Ge-O correlations and, for each pressure point, the various functions yield the same Ge-O bond length r_{GeO} and coordination number $\bar{n}^{\mathrm{O}}_{\mathrm{Ge}}$ for oxygen around germanium, within the experimental uncertainty.

The positions of the leading peaks in the $F(Q)$ and $G(r)$ functions, together with the coordination number $\bar{n}^{\mathrm{O}}_{\mathrm{Ge}}$ which was calculated by integrating over the first peak up to the first minimum in $G(r)$, are summarised in table 4.3.

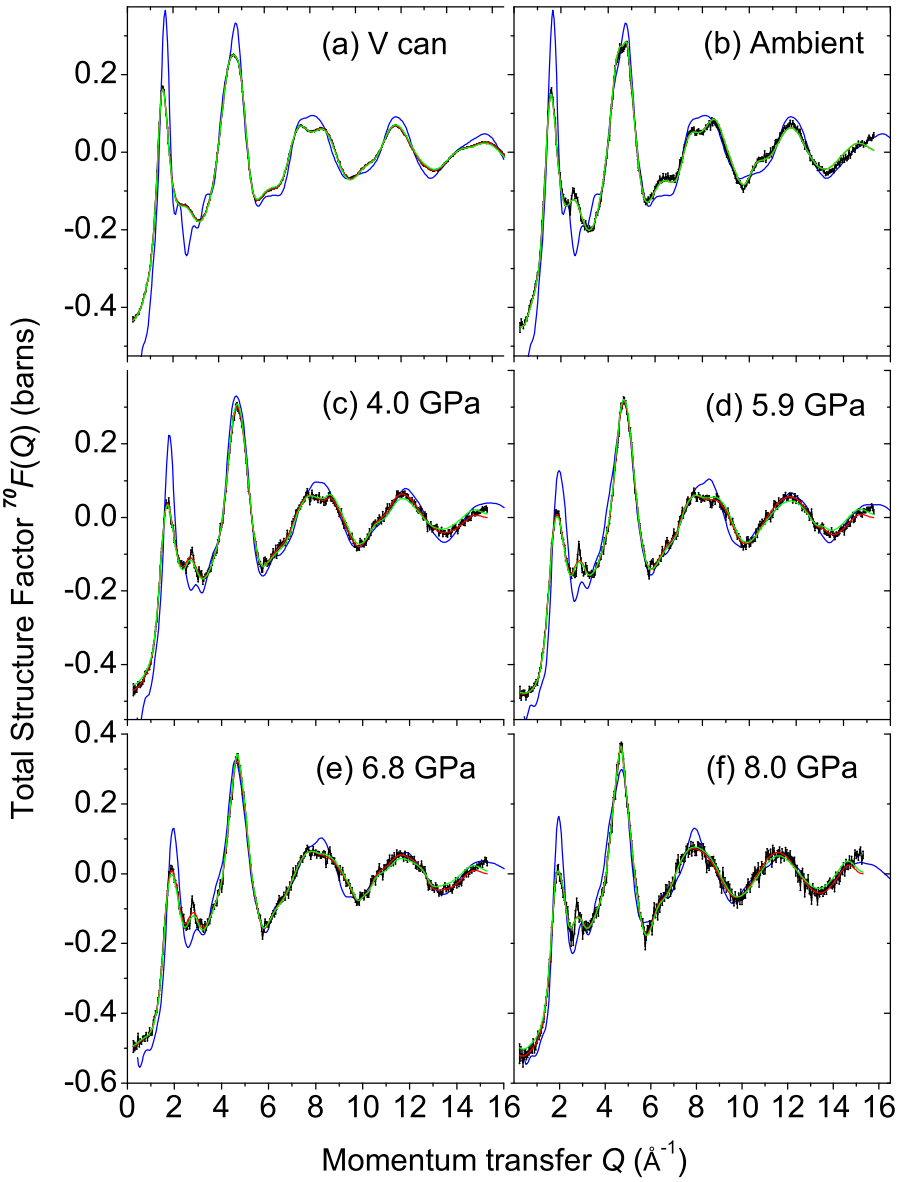

Figure 4-2: Total structure factors $^{70}F(Q)$ measured for a $^{70}GeO_2$ glassy sample (a) in a vanadium can or (b)–(f) in the PE press for applied pressures of 0–8 GPa. The black solid curves (—) with vertical error bars represent the unsmoothed total structure factors, the solid red curves (—) represent Harwell spline fitted data sets after a cosine window function has been applied over the Q range from 14.1–15.3 Å^{-1}, and the solid green curves (—) represent the Fourier back transforms of the $^{70}G(r)$ functions shown in figure 4-3 after the unphysical oscillations at $r \leq$ 1.1 Å have been set to the calculated $^{70}G(0)$ limit. For comparison, the solid blue curves (—) give the molecular dynamics results.

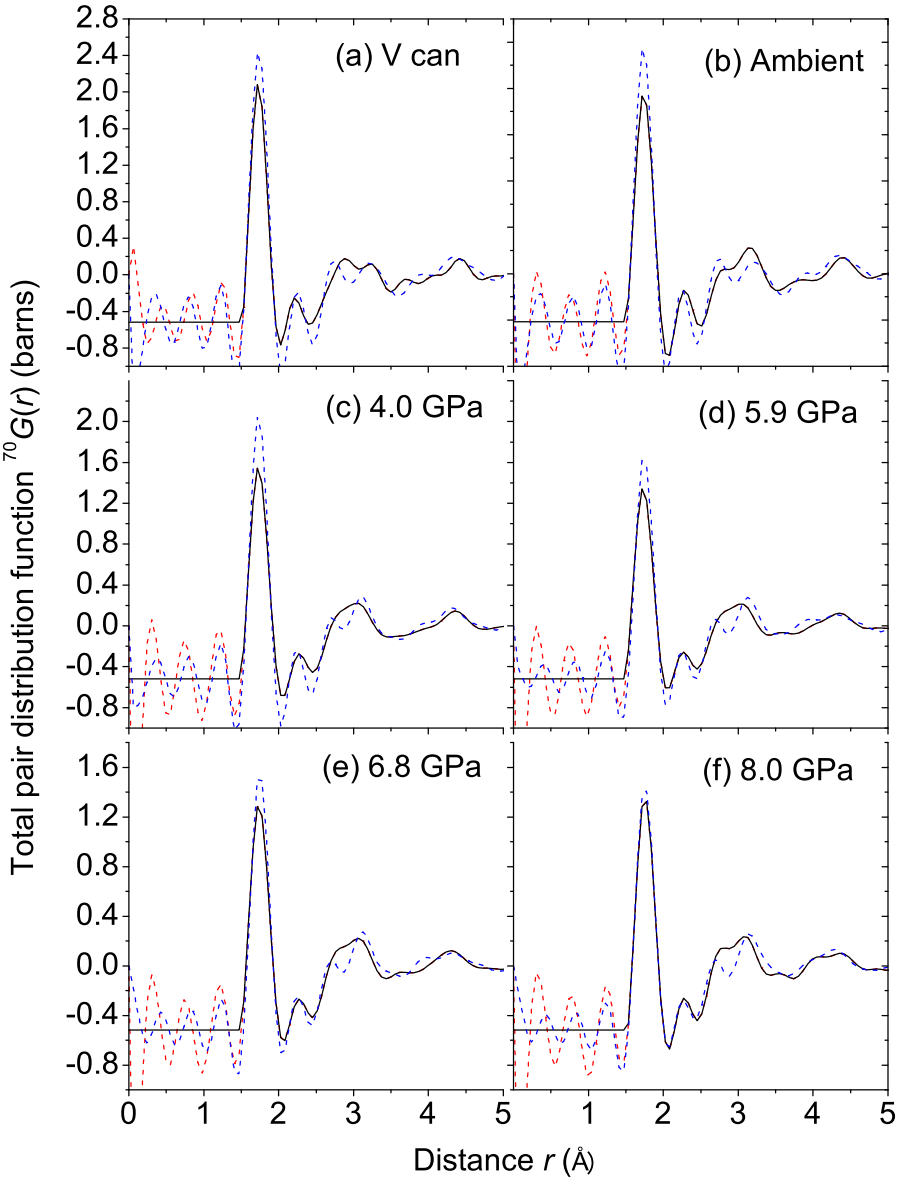

Figure 4-3: Total pair distribution functions $^{70}G(r)$ as obtained by Fourier transforming the total structure factors $^{70}F(Q)$ shown by the solid red curves (——) in Figure 4-2. The broken red curves (- - -) show the extent of the low r oscillations and the horizontal black curves (——) at low r give the calculated $^{70}G(0)$ limit. For comparison, the broken blue curves (- - -) give the molecular dynamics results.

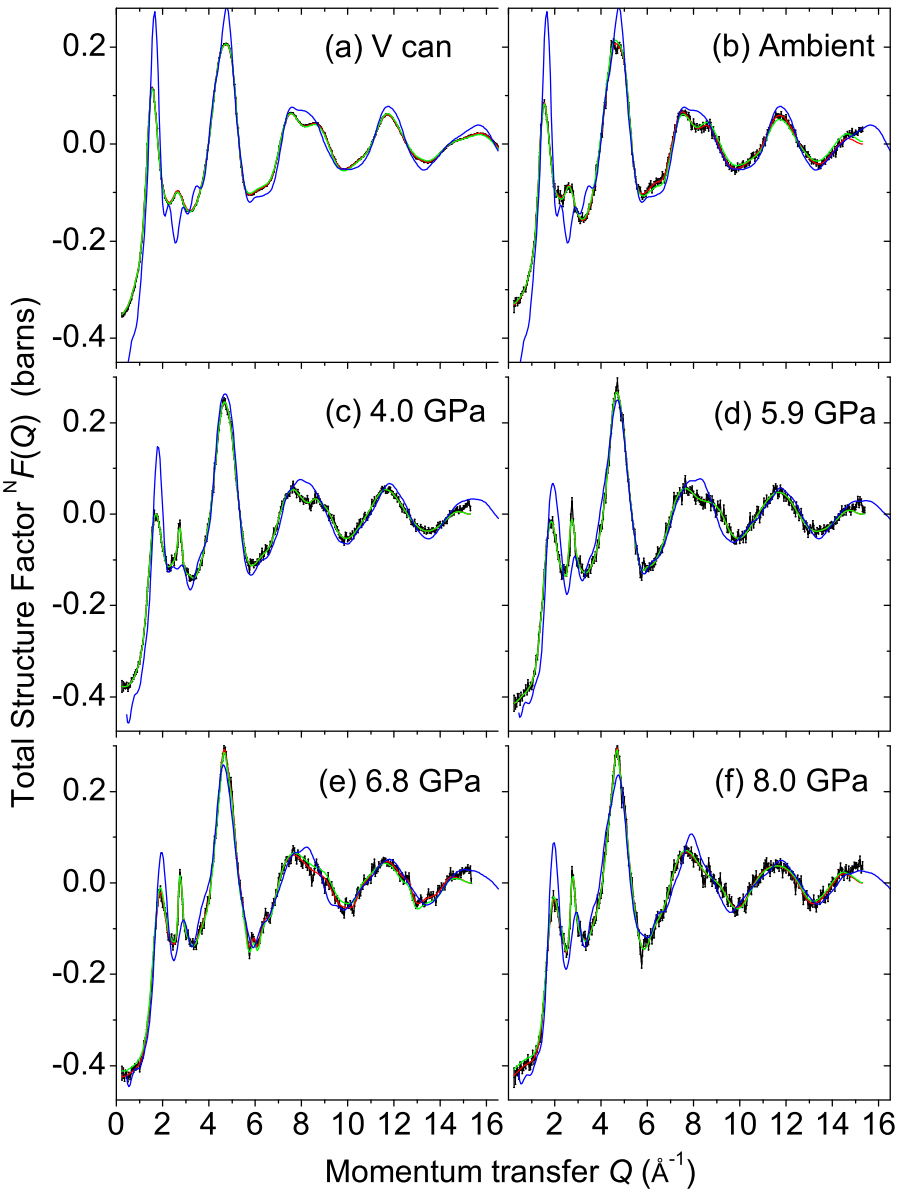

Figure 4-4: Total structure factors $^{N}F(Q)$ measured for a $^{N}GeO_2$ glassy sample (a) in a vanadium can or (b)–(f) in the PE press for applied pressures of 0–8 GPa. The black solid curves (——) with vertical error bars represent the unsmoothed total structure factors, the solid red curves (——) represent Harwell spline fitted data sets after a cosine window function has been applied over the Q range from 14.1–15.3 Å^{-1}, and the solid green curves (——) represent the Fourier back transforms of the $^{N}G(r)$ functions shown in figure 4-5 after the unphysical oscillations at $r \leq 1.1$ Å have been set to the calculated $^{N}G(0)$ limit. For comparison, the solid blue curves (——) give the molecular dynamics results.

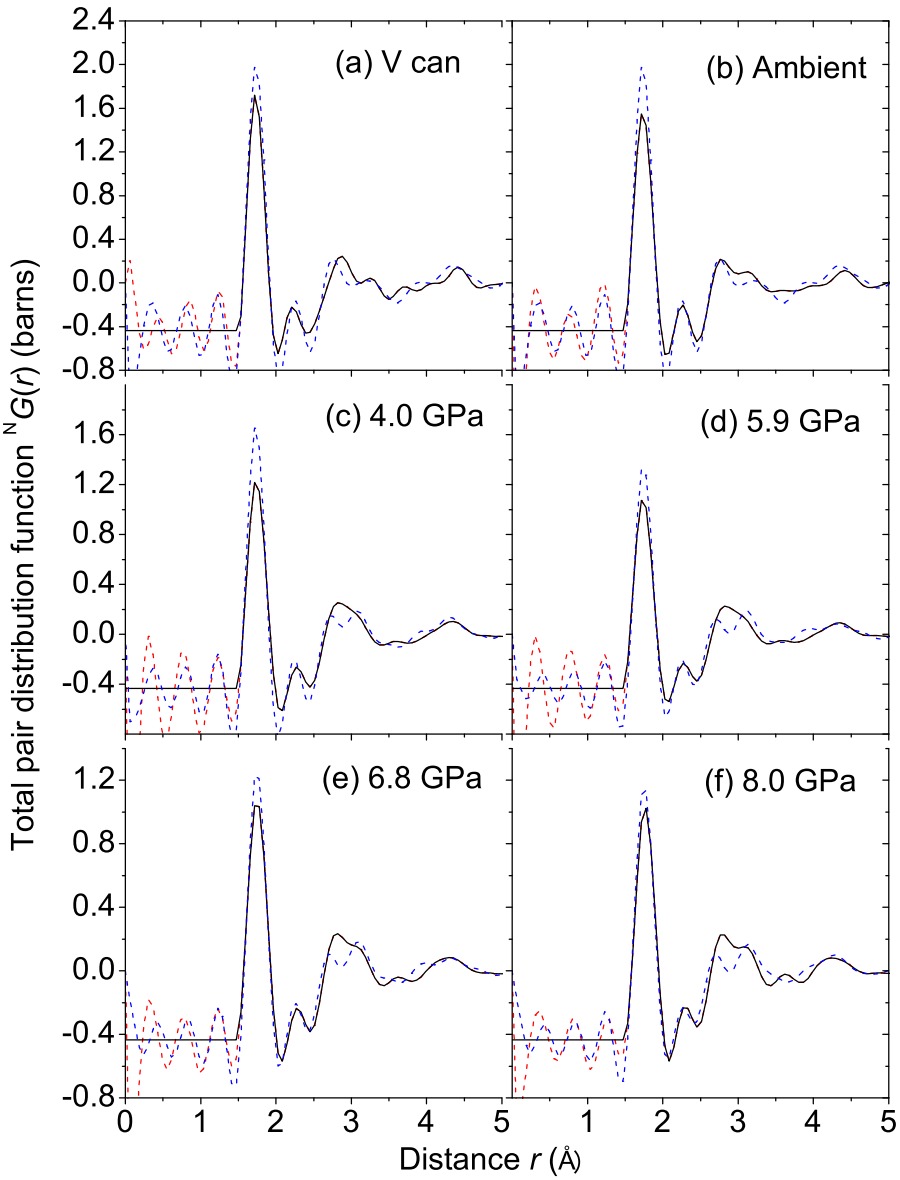

Figure 4-5: Total pair distribution functions $^{N}G(r)$ as obtained by Fourier transforming the total structure factors $^{N}F(Q)$ shown by the solid red curves (——) in Figure 4-4. The broken red curves (- - -) show the extent of the low r oscillations and the horizontal black curves (——) at low r give the calculated $^{N}G(0)$ limit. For comparison, the broken blue curves (- - -) give the molecular dynamics results.

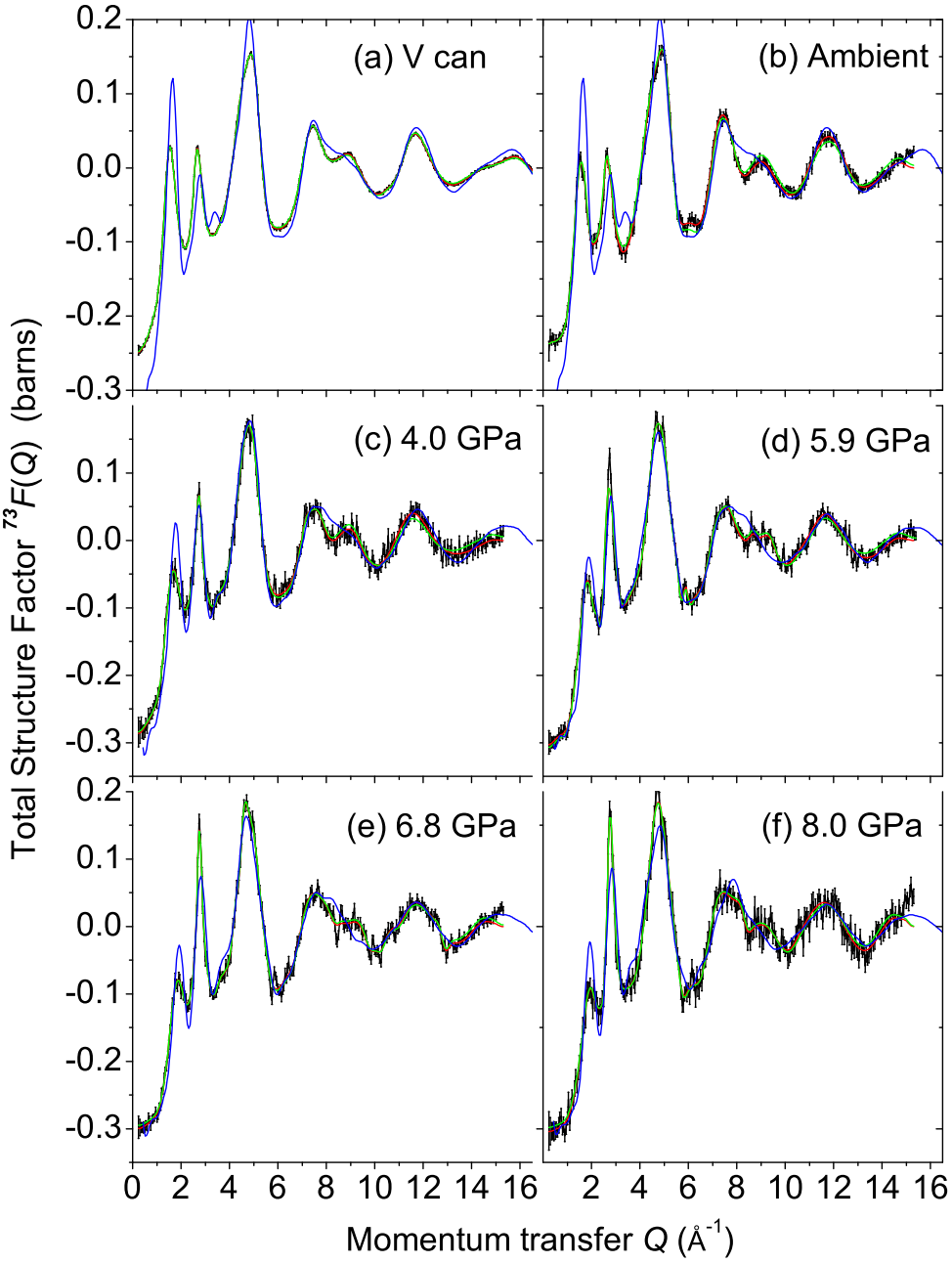

Figure 4-6: Total structure factors $^{73}F(Q)$ measured for a $^{73}GeO_2$ glassy sample (a) in a vanadium can or (b)–(f) in the PE press for applied pressures of 0–8 GPa. The black solid curves (——) with vertical error bars represent the unsmoothed total structure factors, the solid red curves (——) represent Harwell spline fitted data sets after a cosine window function has been applied over the Q range from 14.1–15.3 Å^{-1}, and the solid green curves (——) represent the Fourier back transforms of the $^{73}G(r)$ functions shown in figure 4-7 after the unphysical oscillations at $r \leq$ 1.1 Å have been set to the calculated $^{73}G(0)$ limit. For comparison, the solid blue curves (——) give the molecular dynamics results.

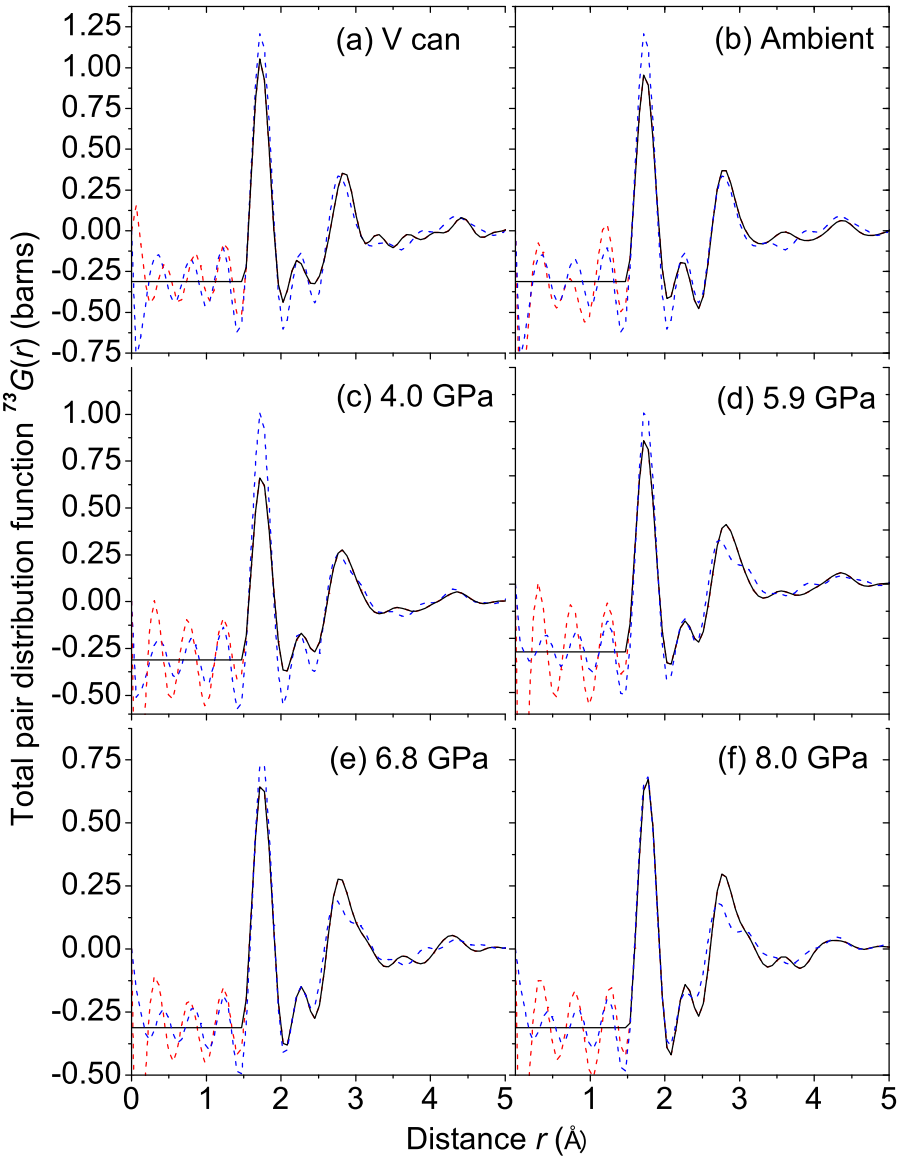

Figure 4-7: Total pair distribution functions $^{73}G(r)$ as obtained by Fourier transforming the total structure factors $^{73}F(Q)$ shown by the solid red curves (——) in Figure 4-6. The broken red curves (- - -) show the extent of the low r oscillations and the horizontal black curves (——) at low r give the calculated $^{73}G(0)$ limit. For comparison, the broken blue curves (- - -) give the molecular dynamics results.

Table 4.3: The leading peak positions Q_1, Q_2 and Q_3 in the measured total structure factors ${}^{70}F(Q)$, ${}^{\mathrm{N}}F(Q)$ and ${}^{73}F(Q)$ plotted in figures 4-2, 4-4 and 4-6 for GeO_2 glass at pressures of 0–8 GPa. The leading peak position r_1 from the corresponding $G(r)$ functions plotted in figures 4-3, 4-5, 4-7 and the coordination number $\bar{n}^{\mathrm{O}}_{\mathrm{Ge}}$ are also listed.

	${}^{70}F(Q)$			${}^{70}G(r)$	
P (GPa)	Q_1 (Å^{-1})	Q_2 (Å^{-1})	Q_3 (Å^{-1})	r_1 (Å)	$\bar{n}^{\mathrm{O}}_{\mathrm{Ge}}$
V can	1.56(2)	2.55(3)	4.64(3)	1.73(2)	4.0(1)
0.0	1.55(2)	2.53(3)	4.75(3)	1.74(2)	4.1(1)
4.0(5)	1.71(2)	2.66(3)	4.67(3)	1.73(2)	4.0(1)
5.9(5)	1.83(2)	2.79(3)	4.67(3)	1.74(2)	4.2(1)
6.7(5)	1.89(2)	2.81(3)	4.67(3)	1.74(2)	4.3(1)
8.0(5)	1.93(2)	2.82(3)	4.69(3)	1.76(2)	4.4(1)
	${}^{\mathrm{N}}F(Q)$			${}^{\mathrm{N}}G(r)$	
P (GPa)	Q_1 (Å^{-1})	Q_2 (Å^{-1})	Q_3 (Å^{-1})	r_1 (Å)	$\bar{n}^{\mathrm{O}}_{\mathrm{Ge}}$
V can	1.56(2)	2.68(3)	4.67(3)	1.73(2)	4.0(1)
0.0	1.55(2)	2.61(3)	4.63(3)	1.74(2)	4.1(1)
4.0(5)	1.71(2)	2.74(3)	4.67(3)	1.73(2)	4.0(1)
5.9(5)	1.85(2)	2.72(3)	4.67(3)	1.74(2)	4.2(1)
6.7(5)	1.89(2)	2.76(3)	4.67(3)	1.74(2)	4.3(1)
8.0(5)	1.97(2)	2.78(3)	4.69(3)	1.76(2)	4.4(1)
	${}^{73}F(Q)$			${}^{73}G(r)$	
P (GPa)	Q_1 (Å^{-1})	Q_2 (Å^{-1})	Q_3 (Å^{-1})	r_1 (Å)	$\bar{n}^{\mathrm{O}}_{\mathrm{Ge}}$
V can	1.55(2)	2.68(3)	4.89(3)	1.73(2)	4.1(1)
0.0	1.58(2)	2.65(3)	4.91(3)	1.74(2)	4.1(1)
4.0(5)	1.69(2)	2.74(3)	4.80(3)	1.73(2)	4.2(1)
5.9(5)	1.83(2)	2.72(3)	4.76(3)	1.74(2)	4.3(1)
6.7(5)	1.89(2)	2.76(3)	4.67(3)	1.74(2)	4.4(1)
8.0(5)	1.96(2)	2.78(3)	4.76(3)	1.76(2)	4.5(1)

4.5.2 Difference functions

As shown in figures 4-8, 4-10 and 4-12, the measured and simulated difference functions $\Delta F^{(i)}_{\mathrm{Ge}}(Q)$ $(i = 1,\ 2,\ 3)$ show very similar features, in accordance with the relative weighting factors of the partial structure factors summarised in equation (4.4). The corresponding Fourier transforms $\Delta G^{(i)}_{\mathrm{Ge}}(Q)$ $(i = 1,\ 2,\ 3)$ are shown in figures 4-9, 4-11 and 4-13, respectively. The simulated difference functions were truncated at the same Q_{max} as in experiment and multiplied by the same cosine function before Fourier transformation.

As in the case of total structure factors, the FSDP persists in the difference functions as a feature at about ≈ 1.55 Å^{-1} at ambient conditions but it decreases in intensity as it shifts towards higher Q values as pressure is increased. The principal peak PP, in comparison, is reduced to a trough whose depth increases and sharpens with increasing pressure. It is also observed that the smaller the contrast between structure factors, the more the resultant difference functions are prone to systematic errors.

Like in the case of the total correlation functions, the first peak in the $\Delta G^{(i)}_{\mathrm{Ge}}(Q)$ $(i = 1,\ 2,\ 3)$ functions is attributable to Ge-O correlations. For each pressure point, the $\Delta G^{(i)}_{\mathrm{Ge}}(Q)$ $(i = 1,\ 2)$ functions yield the same Ge-O bond length r_{GeO} and coordination number $\bar{n}^{\mathrm{O}}_{\mathrm{Ge}}$ for oxygen around germanium, within the experimental uncertainty. The scattering length contrast between the Ge isotopes in the $\Delta G^{(3)}_{\mathrm{Ge}}(Q)$ function is, unfortunately, too small to give reliable measured parameters. The second peak is attributed to Ge-Ge correlations from which the nearest-neighbour Ge-Ge distance r_{GeGe} is found. However, it is not possible to calculate an accurate coordination number $\bar{n}^{\mathrm{Ge}}_{\mathrm{Ge}}$ as there exists a small but non-neglieglable overlap between $g_{\mathrm{GeGe}}(r)$ and $g_{\mathrm{GeO}}(r)$ [94].

The positions of the leading peaks in the $\Delta F^{(i)}_{\mathrm{Ge}}(Q)$ and $\Delta G^{(i)}_{\mathrm{Ge}}(r)$ functions, together with the coordination number $\bar{n}^{\mathrm{O}}_{\mathrm{Ge}}$ which was calculated by integrating over the first peak in $\Delta G_{\mathrm{Ge}}(r)$ up to the first minimum, are summarised in table 4.4.

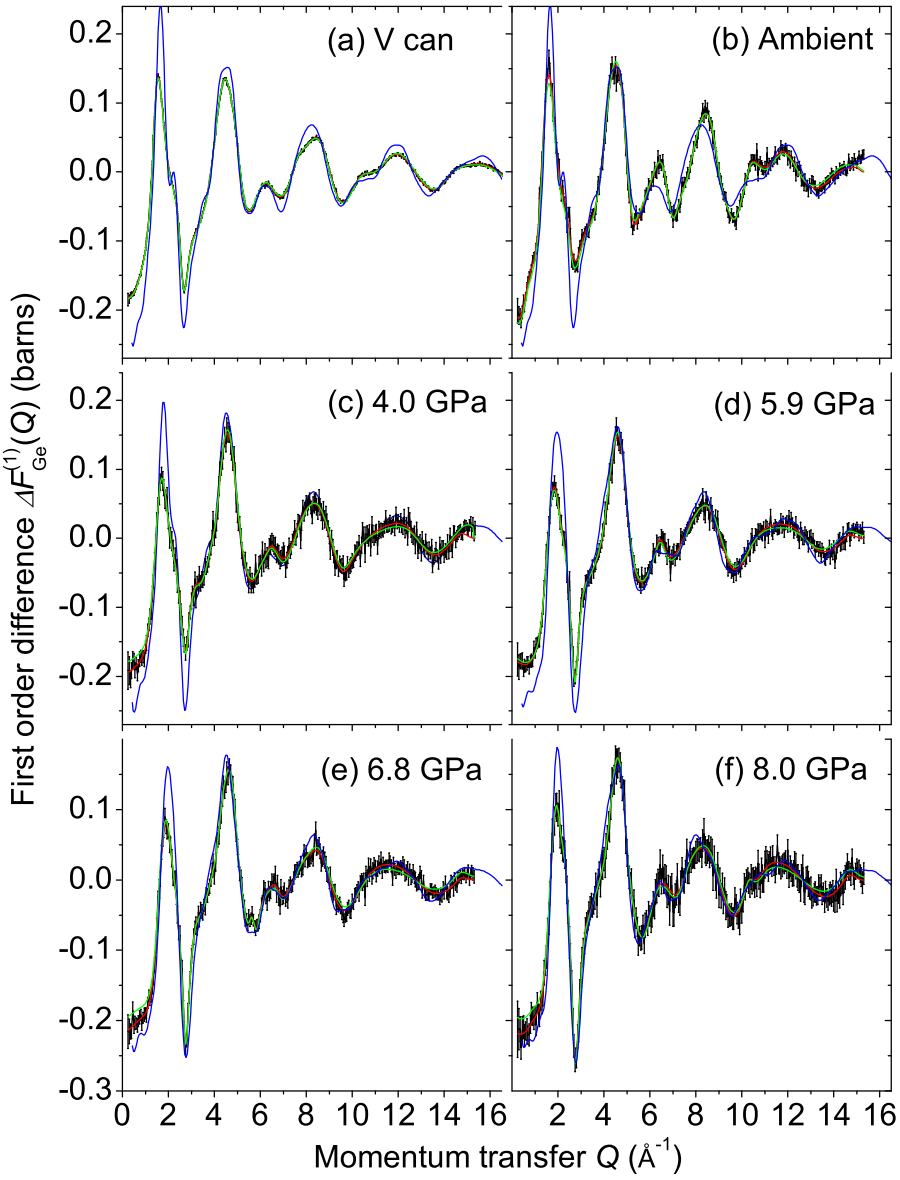

Figure 4-8: Difference functions $\Delta F^{(1)}_{\mathrm{Ge}}(Q)$ as measured for samples (a) in a vanadium can or (b)–(f) in the PE press for applied pressures of 0–8 GPa. The black solid curves (—) with vertical error bars represent the unsmoothed difference functions, the solid red curves (—) represent Harwell spline fitted data sets after a cosine window function has been applied over the Q range from 14.1–15.3 Å^{-1}, and the solid green curves (—) represent the Fourier back transforms of the $\Delta G^{(1)}_{\mathrm{Ge}}(r)$ functions shown in figure 4-9 after the unphysical oscillations at $r \leq 1.1$ Å have been set to the calculated $\Delta G^{(1)}_{\mathrm{Ge}}(0)$ limit. For comparison, the solid blue curves (—) give the molecular dynamics results.

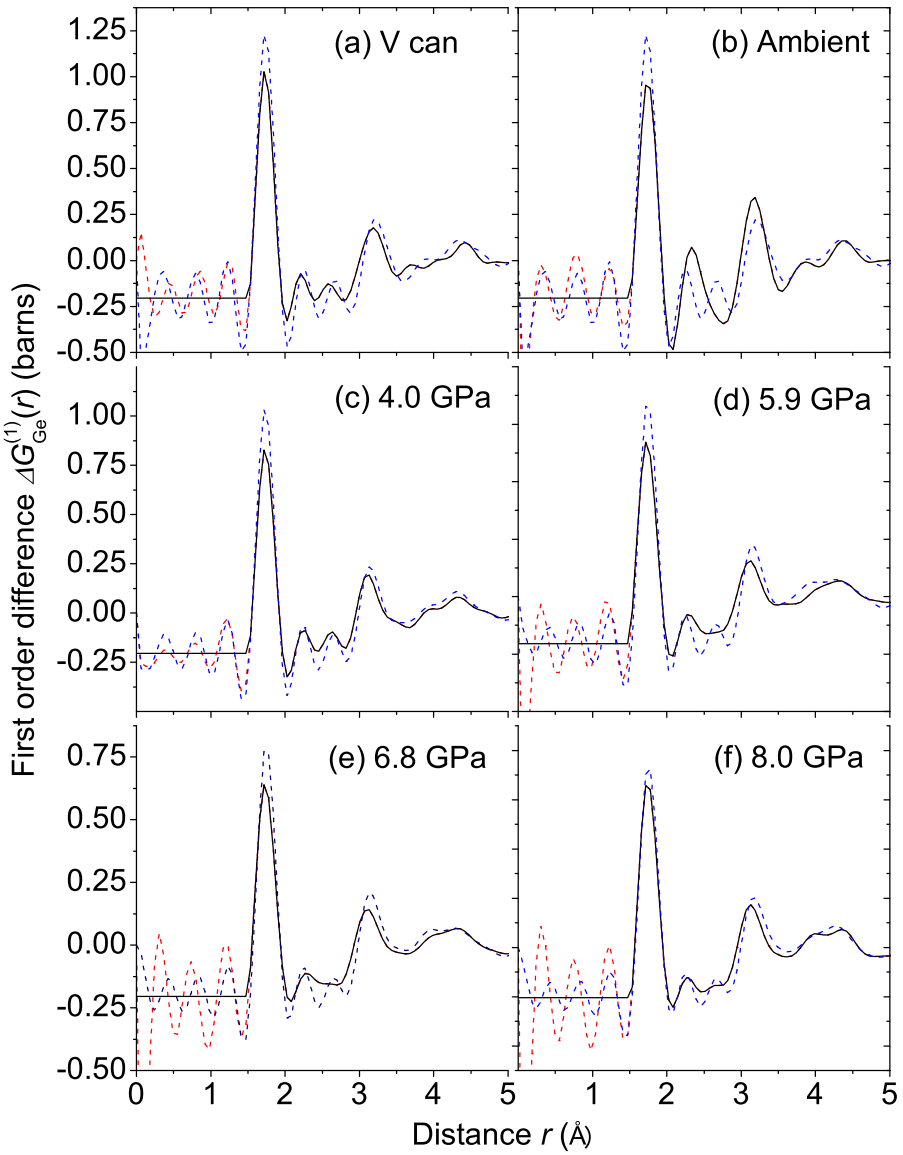

Figure 4-9: The pair distribution functions $\Delta G^{(1)}_{\mathrm{Ge}}(r)$ as obtained by Fourier transforming the difference functions $\Delta F^{(1)}_{\mathrm{Ge}}(Q)$ shown by the solid red curves (——) in figure 4-8. The broken red curves (- - -) show the extent of the low r oscillations and the horizontal black curves (——) at low r give the calculated $\Delta G^{(1)}_{\mathrm{Ge}}(0)$ limit. For comparison, the broken blue curves (- - -) give the molecular dynamics results.

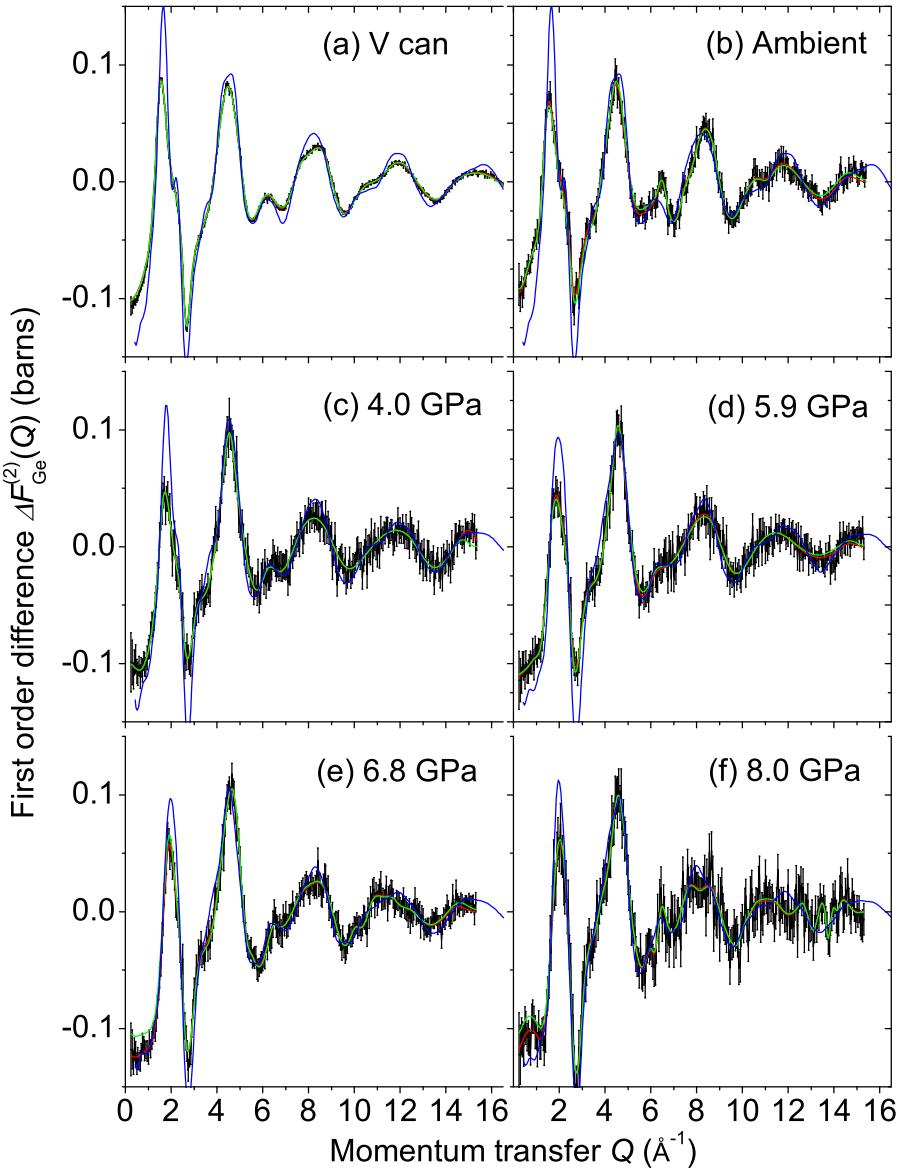

Figure 4-10: Difference functions $\Delta F^{(2)}_{\mathrm{Ge}}(Q)$ as measured for samples (a) in a vanadium can or (b)–(f) in the PE press for applied pressures of 0–8 GPa. The black solid curves (—) with vertical error bars represent the unsmoothed difference functions, the solid red curves (—) represent Harwell spline fitted data sets after a cosine window function has been applied over the Q range from 14.1–15.3 Å^{-1}, and the solid green curves (—) represent the Fourier back transforms of the $\Delta G^{(2)}_{\mathrm{Ge}}(r)$ functions shown in figure 4-11 after the unphysical oscillations at $r \leq 1.1$ Å have been set to the calculated $\Delta G^{(2)}_{\mathrm{Ge}}(0)$ limit. For comparison, the solid blue curves (—) give the molecular dynamics results.

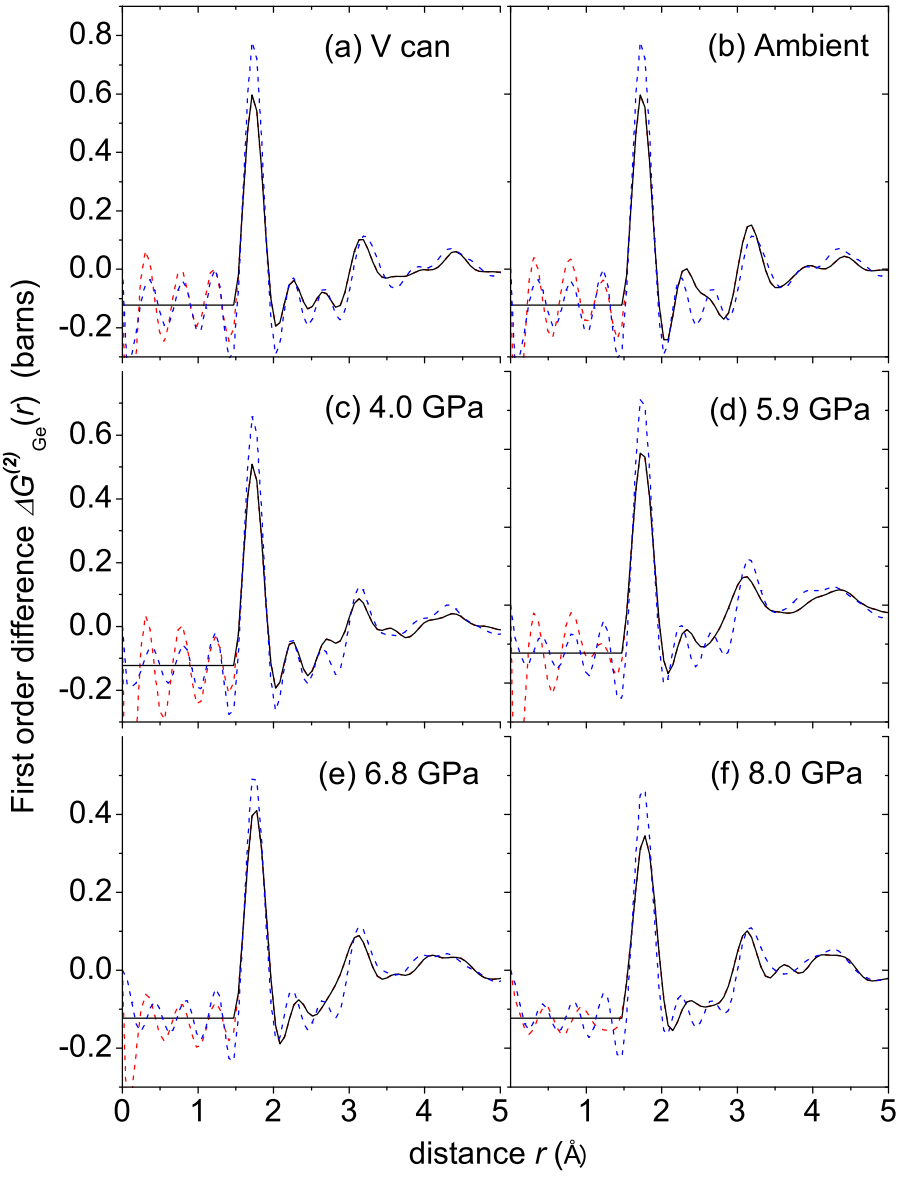

Figure 4-11: The pair distribution functions $\Delta G^{(2)}_{\mathrm{Ge}}(r)$ as obtained by Fourier transforming difference functions $\Delta F^{(2)}_{\mathrm{Ge}}(Q)$ shown by the solid red curves (——) in figure 4-10. The broken red curves (- - -) show the extent of the low r oscillations and the horizontal black curves (——) at low r give the calculated $\Delta G^{(2)}_{\mathrm{Ge}}(0)$ limit. For comparison, the broken blue curves (- - -) give the molecular dynamics results.

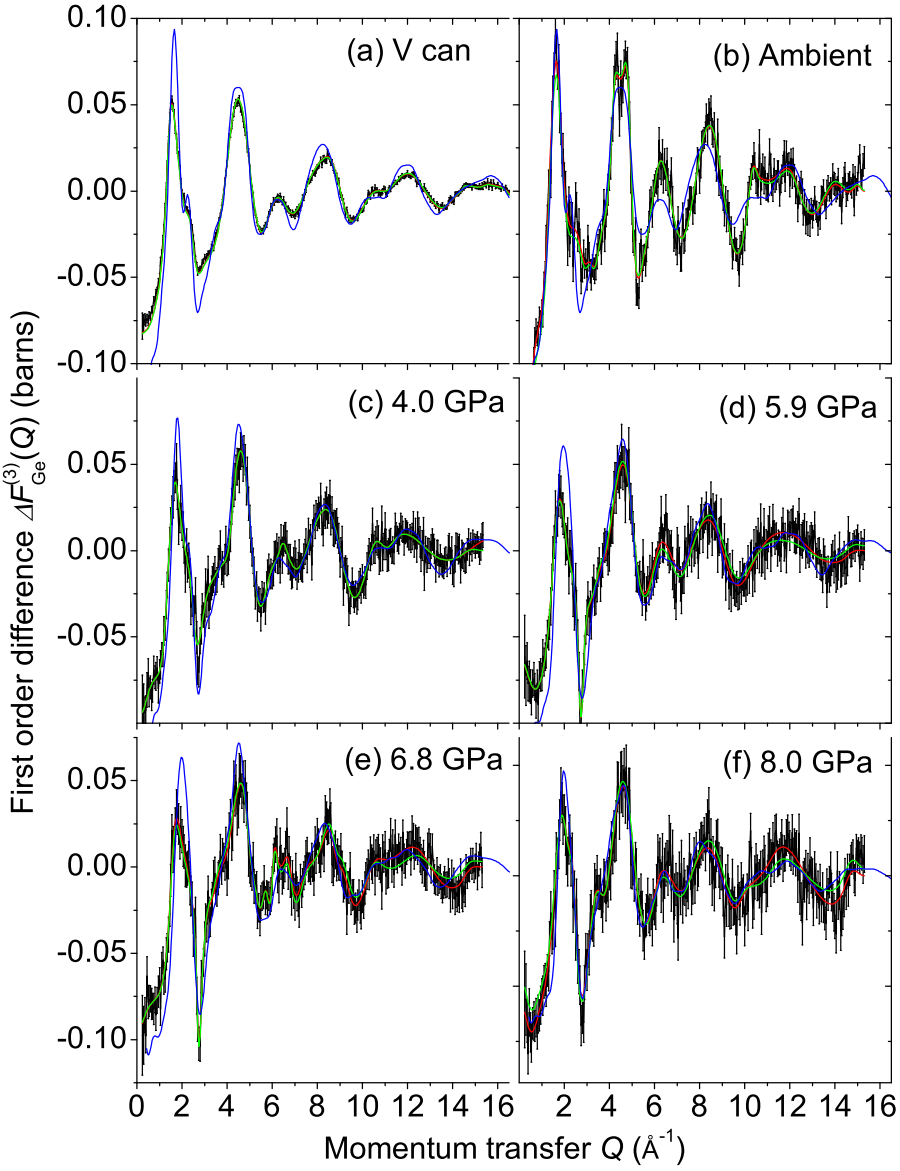

Figure 4-12: Difference functions $\Delta F^{(3)}_{\mathrm{Ge}}(Q)$ as measured for samples (a) in a vanadium can or (b)–(f) in the PE press for applied pressures of 0–8 GPa. The black solid curves (—) with vertical error bars represent the unsmoothed difference functions, the solid red curves (—) represent Harwell spline fitted data sets after a cosine window function has been applied over the Q range from 14.1–15.3 Å^{-1}, and the solid green curves (—) represent the Fourier back transforms of the $\Delta G^{(3)}_{\mathrm{Ge}}(r)$ functions shown in figure 4-13 after the unphysical oscillations at $r \leq 1.1$ Å have been set to the calculated $\Delta G^{(3)}_{\mathrm{Ge}}(0)$ limit. For comparison, the solid blue curves (—) give the molecular dynamics results.

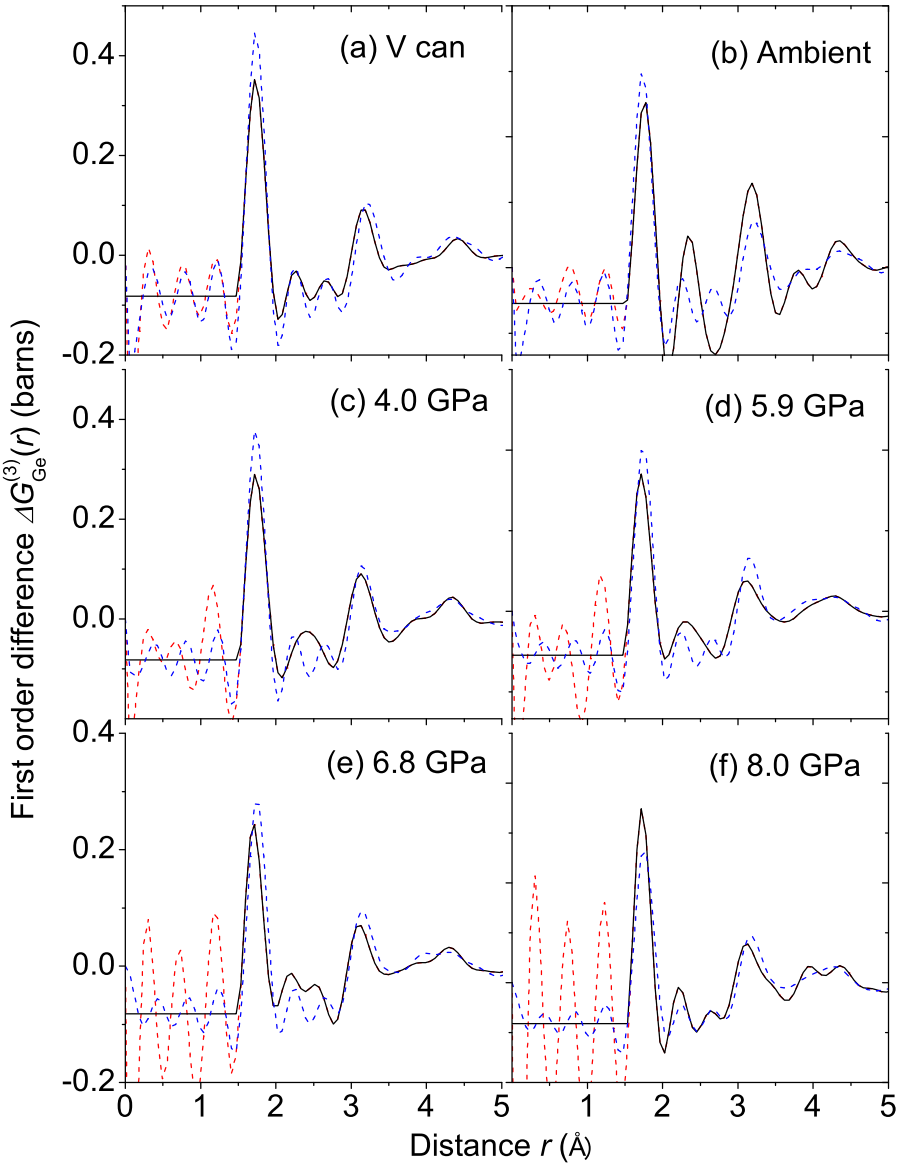

Figure 4-13: The pair distribution functions $\Delta G^{(3)}_{\mathrm{Ge}}(r)$ as obtained by Fourier transforming the difference functions $\Delta F^{(3)}_{\mathrm{Ge}}(Q)$ shown by the solid red curves (——) in figure 4-12. The broken red curves (- - -) show the extent of the low r oscillations and the horizontal black curves (——) at low r give the calculated $\Delta G^{(3)}_{\mathrm{Ge}}(0)$ limit. For comparison, the broken blue curves (- - -) give the molecular dynamics results.

Table 4.4: The leading peak positions Q_1, Q_2 and Q_3 in the first order difference functions $\Delta F^{(1)}_{\mathrm{Ge}}(Q)$, $\Delta F^{(2)}_{\mathrm{Ge}}(Q)$ and $\Delta F^{(3)}_{\mathrm{Ge}}(Q)$ plotted in figures 4-8, 4-10 and 4-12 for GeO_2 glass for ambient pressure and for pressures up to 8 GPa. The leading peak positions r_1 and r_2 from the corresponding $\Delta G^{(i)}_{\mathrm{Ge}}(r)$ functions plotted in figures 4-9, 4-11, 4-13 and the coordination number $\bar{n}^{\mathrm{O}}_{\mathrm{Ge}}$ are also listed.

	$\Delta F^{(1)}_{\mathrm{Ge}}(Q)$			$\Delta G^{(1)}_{\mathrm{Ge}}(r)$		
P (GPa)	Q_1 (Å^{-1})	Q_2 (Å^{-1})	Q_3 (Å^{-1})	r_1 (Å)	r_2 (Å)	$\bar{n}^{\mathrm{O}}_{\mathrm{Ge}}$
V can	1.55(2)	-	4.64(3)	1.74(2)	3.19(2)	3.9(1)
0.0	1.61(2)	-	4.52(3)	1.73(2)	3.17(2)	4.0(1)
4.0(5)	1.72(2)	-	4.57(3)	1.73(2)	3.11(2)	3.9(1)
5.9(5)	1.83(2)	-	4.61(3)	1.73(2)	3.12(2)	4.1(1)
6.7(5)	1.89(2)	-	4.63(3)	1.73(2)	3.11(2)	4.2(1)
8.0(5)	1.94(2)	-	4.60(3)	1.75(2)	3.13(2)	4.4(1)
	$\Delta F^{(2)}_{\mathrm{Ge}}(Q)$			$\Delta G^{(2)}_{\mathrm{Ge}}(r)$		
P (GPa)	Q_1 (Å^{-1})	Q_2 (Å^{-1})	Q_3 (Å^{-1})	r_1 (Å)	r_2 (Å)	$\bar{n}^{\mathrm{O}}_{\mathrm{Ge}}$
V can	1.56(2)	-	4.67(3)	1.73(2)	3.19(2)	3.9(1)
0.0	1.56(2)	-	4.49(3)	1.73(2)	3.17(2)	3.9(1)
4.0(5)	1.73(2)	-	4.55(3)	1.73(2)	3.13(2)	3.9(1)
5.9(5)	1.85(2)	-	4.61(3)	1.74(2)	3.11(2)	4.1(1)
6.7(5)	1.92(2)	-	4.65(3)	1.76(2)	3.11(2)	4.4(1)
8.0(5)	2.05(2)	-	4.57(3)	1.77(2)	3.13(2)	4.5(1)
	$\Delta F^{(3)}_{\mathrm{Ge}}(Q)$			$\Delta G^{(3)}_{\mathrm{Ge}}(r)$		
P (GPa)	Q_1 (Å^{-1})	Q_2 (Å^{-1})	Q_3 (Å^{-1})	r_1 (Å)	r_2 (Å)	$\bar{n}^{\mathrm{O}}_{\mathrm{Ge}}$
V can	1.55(2)	-	4.89(3)	1.73(2)	3.19(2)	4.0(1)
0.0	1.65(2)	-	4.71(3)	1.74(2)	3.18(2)	4.2(1)
4.0(5)	1.70(2)	-	4.60(3)	1.73(2)	3.12(2)	4.0(1)
5.9(5)	1.83(2)	-	4.60(3)	1.73(2)	3.11(2)	4.1(1)
6.7(5)	1.76(2)	-	4.61(3)	1.76(2)	3.11(2)	4.0(1)
8.0(5)	1.90(2)	-	4.61(3)	1.73(2)	3.11(2)	4.4(1)

As shown in figures 4-14, 4-16 and 4-18, the measured or simulated difference functions $\Delta F_{\mathrm{O}}^{(i)}(Q)$ $(i = 1, 2, 3)$ show very similar features, in accordance with the relative weighting factors of the partial structure factors summarised in equation (4.6). The corresponding Fourier transforms $\Delta G_{\mathrm{O}}^{(i)}(Q)$ $(i = 1, 2, 3)$ are shown in figures 4-15, 4-17 and 4-19, respectively.

The FSDP appears as a much weaker feature in the $\Delta F_{\mathrm{O}}^{(i)}(Q)$ functions in comparison to the $\Delta F_{\mathrm{Ge}}^{(i)}(Q)$ functions at about $\simeq 1.55$ Å^{-1} under ambient conditions. As in the case of the $\Delta F_{\mathrm{Ge}}^{(i)}(Q)$ functions, the peak's intensity decreases and shifts towards higher Q with increasing pressure. In contrast, the principal peak at $\simeq 2.64$ Å^{-1} shows a sharp increase in intensity with increasing pressure and, given the relatively strong contribution from the O-O partial structure factor [94], these changes are associated with the rearrangement of oxygen atoms on an extended length scale.

In the real space functions $\Delta G_{\mathrm{O}}^{(i)}(r)$ $(i = 1, 2, 3)$, the first peak is attributable to Ge-O correlations. For each pressure point, the $\Delta G_{\mathrm{O}}^{(i)}(r)$ $(i = 1, 2)$ functions yield, within experimental uncertainty, the same Ge-O bond length r_{GeO} and coordination number $\bar{n}_{\mathrm{Ge}}^{\mathrm{O}}$ as the total correlation functions or the $\Delta G_{\mathrm{Ge}}^{(i)}(r)$ $(i = 1, 2)$ difference functions. The scattering length contrast between the Ge isotopes in the $\Delta G_{\mathrm{Ge}}^{(3)}(r)$ function is, unfortunately, too small to give reliable parameters. The second peak in the $\Delta G_{\mathrm{O}}^{(i)}(r)$ functions arises predominantly from $g_{\mathrm{OO}}(r)$ [94] and its maximum gives the average O-O distance r_{OO}. The coordination number $\bar{n}_{\mathrm{O}}^{\mathrm{O}}$ is found by integrating over the second peak in $\Delta G_{\mathrm{O}}^{(i)}(Q)$ and assuming a minimal contribution from $g_{\mathrm{GeO}}(r)$.

The positions of the leading peaks in the $\Delta F_{\mathrm{O}}^{(i)}(Q)$ and $\Delta G_{\mathrm{O}}^{(i)}(r)$ functions, together with the coordination numbers $\bar{n}_{\mathrm{Ge}}^{\mathrm{O}}$ and $\bar{n}_{\mathrm{O}}^{\mathrm{O}}$, are summarised in table 4.4.

The parameters that are common to the $\Delta G_{\mathrm{Ge}}^{(i)}(Q)$ $(i = 1,\ 2)$ and $\Delta G_{\mathrm{O}}^{(i)}(Q)$ $(i = 1,\ 2)$ functions are averaged and compared in figure 4-27 to those obtained from previous neutron diffraction work [13, 31] and the simulation studies using the DIPPIM interaction potentials.

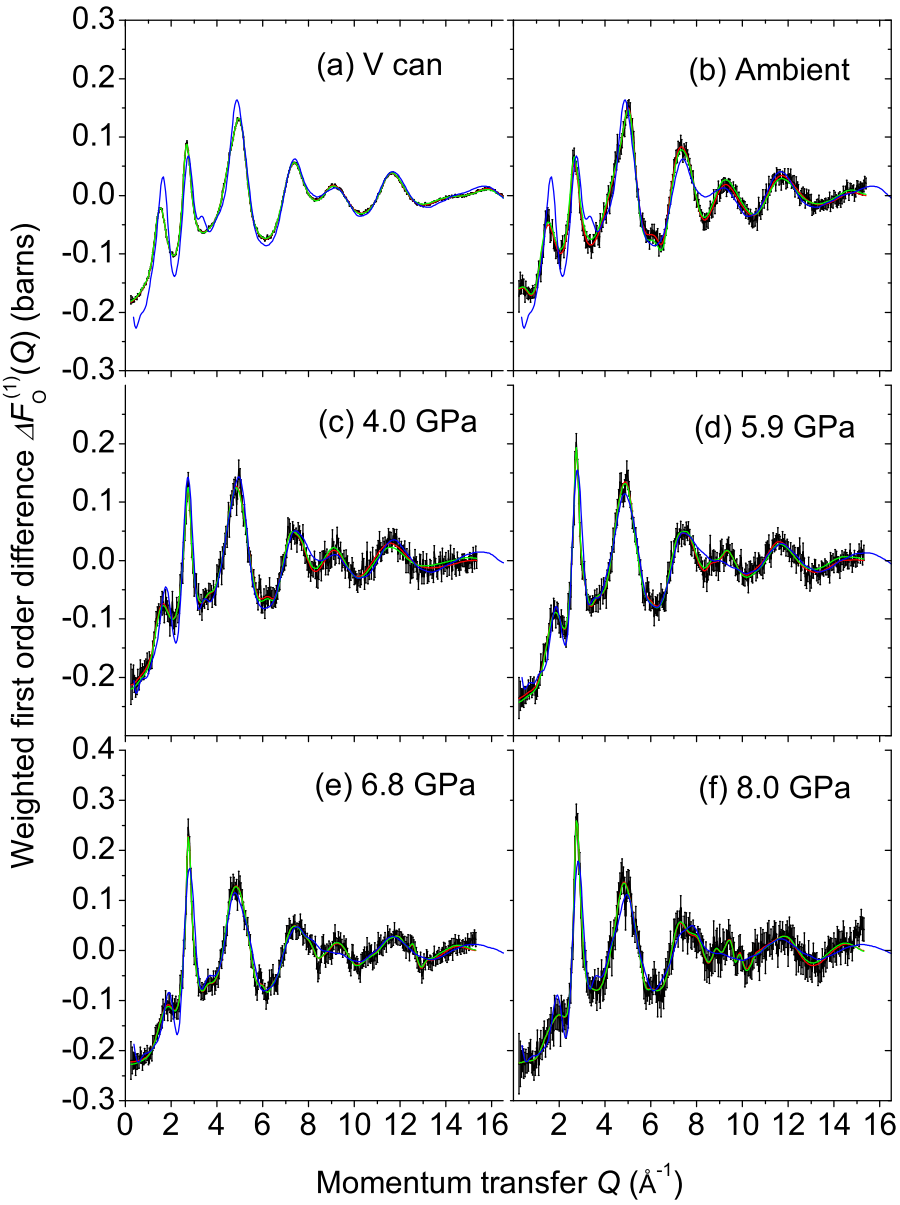

Figure 4-14: Difference functions $\Delta F_{\mathrm{O}}^{(1)}(Q)$ as measured for samples (a) in a vanadium can or (b)–(f) in the PE press for applied pressures of 0–8 GPa. The black solid curves (—) with vertical error bars represent the unsmoothed difference functions, the solid red curves (—) represent Harwell spline fitted data sets after a cosine window function has been applied over the Q range from 14.1–15.3 Å^{-1}, and the solid green curves (—) represent the Fourier back transforms of the $\Delta G_{\mathrm{O}}^{(1)}(r)$ functions shown in figure 4-15 after the unphysical oscillations at $r \leq 1.1$ Å have been set to the calculated $\Delta G_{\mathrm{O}}^{(1)}(0)$ limit. For comparison, the solid blue curves (—) give the molecular dynamics results.

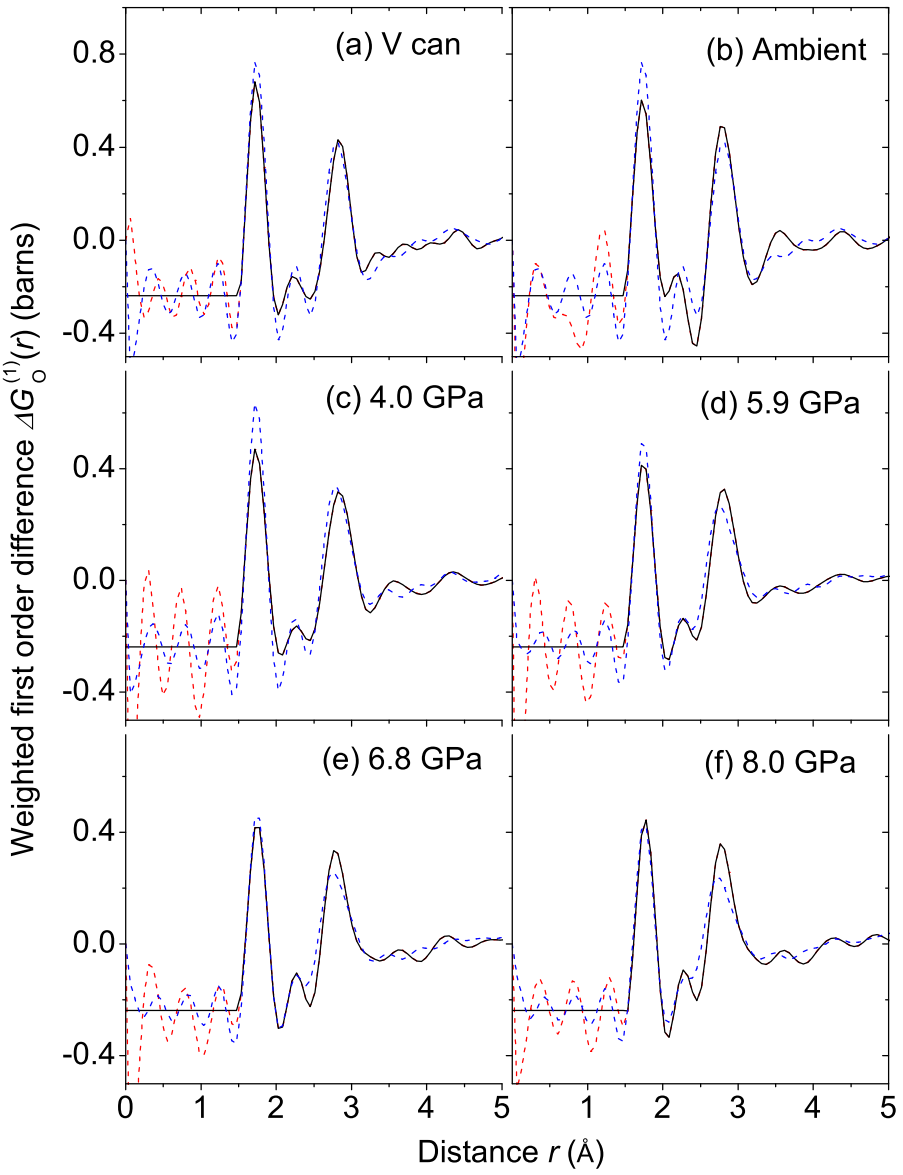

Figure 4-15: The pair distribution functions $\Delta G_{\mathrm{O}}^{(1)}(r)$ as obtained by Fourier transforming the difference functions $\Delta F_{\mathrm{O}}^{(1)}(Q)$ shown by the solid red curves (——) in figure 4-14. The broken red curves (- - -) show the extent of the low r oscillations and the horizontal black curves (——) at low r give the calculated $\Delta G_{\mathrm{O}}^{(1)}(0)$ limit. For comparison, the broken blue curves (- - -) give the molecular dynamics results.

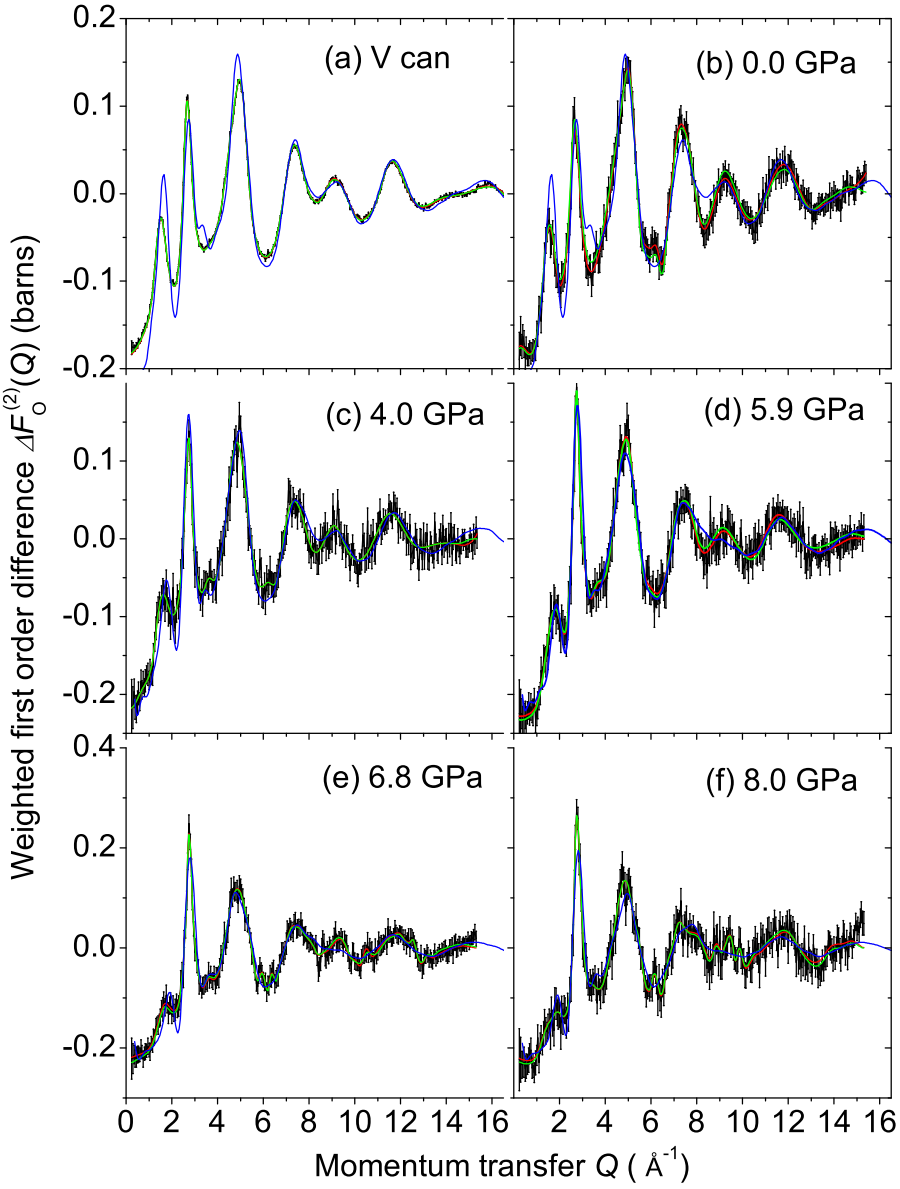

Figure 4-16: Difference functions $\Delta F_O^{(2)}(Q)$ as measured for samples (a) in a vanadium can or (b)–(f) in the PE press for applied pressures of 0–8 GPa. The black solid curves (—) with vertical error bars represent the unsmoothed difference functions, the solid red curves (—) represent Harwell spline fitted data sets after a cosine window function has been applied over the Q range from 14.1–15.3 Å^{-1}, and the solid green curves (—) represent the Fourier back transforms of the $\Delta G_O^{(2)}(r)$ functions shown in figure 4-17 after the unphysical oscillations at $r \leq 1.1$ Å have been set to the calculated $\Delta G_O^{(2)}(0)$ limit. For comparison, the solid blue curves (—) give the molecular dynamics results.

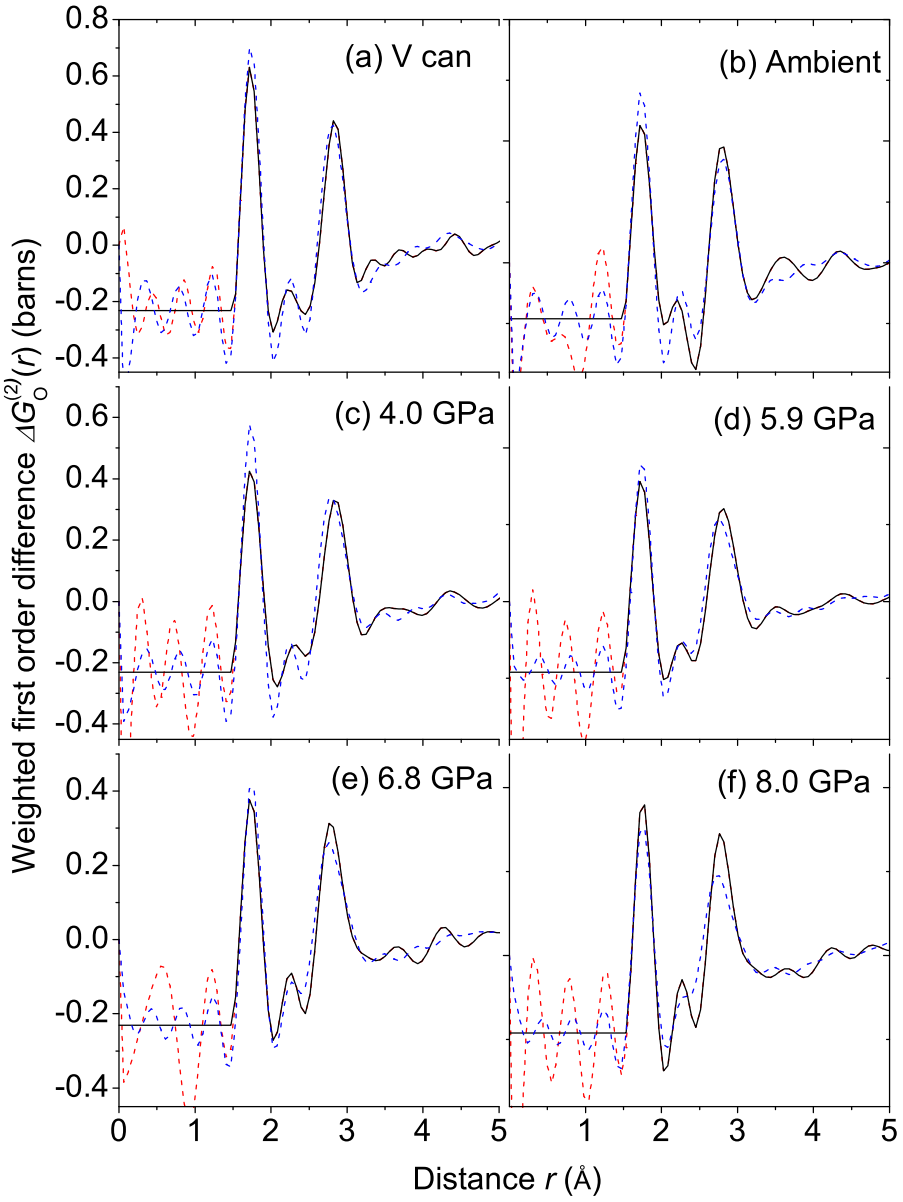

Figure 4-17: The pair distribution functions $\Delta G_O^{(2)}(r)$ as obtained by Fourier transforming the difference functions $\Delta F_O^{(2)}(Q)$ shown by the solid red curves (——) in figure 4-16. The broken red curves (- - -) show the extent of the low r oscillations and the horizontal black curves (——) at low r give the calculated $\Delta G_O^{(2)}(0)$ limit. For comparison, the broken blue curves (- - -) give the molecular dynamics results.

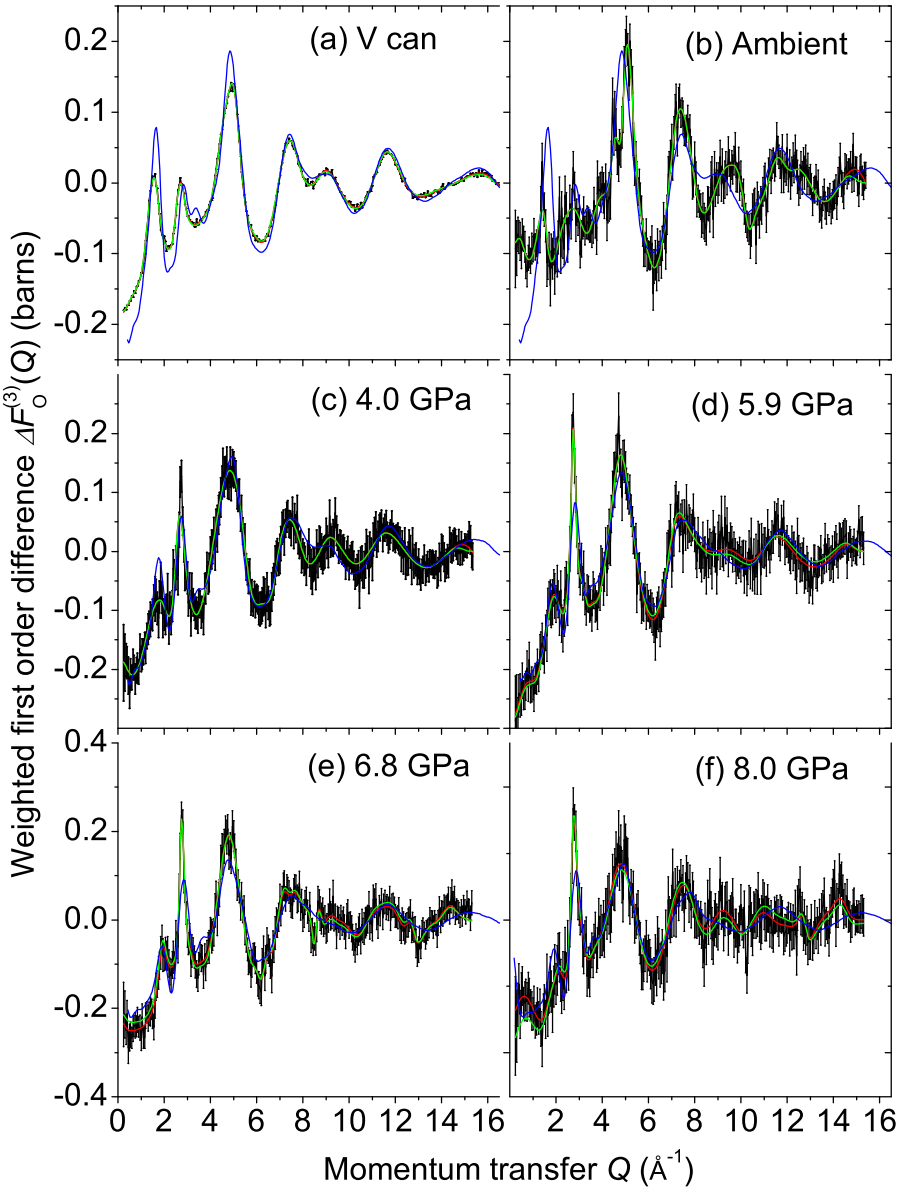

Figure 4-18: Difference functions $\Delta F_O^{(3)}(Q)$ as measured for samples (a) in a vanadium can or (b)–(f) in the PE press for applied pressures of 0–8 GPa. The black solid curves (—) with vertical error bars represent the unsmoothed difference functions, the solid red curves (—) represent Harwell spline fitted data sets after a cosine window function has been applied over the Q range from 14.1–15.3 Å^{-1}, and the solid green curves (—) represent the Fourier back transforms of the $\Delta G_O^{(3)}(r)$ functions shown in figure 4-19 after the unphysical oscillations at $r \leq 1.1$ Å have been set to the calculated $\Delta G_O^{(3)}(0)$ limit. For comparison, the solid blue curves (—) give the molecular dynamics results.

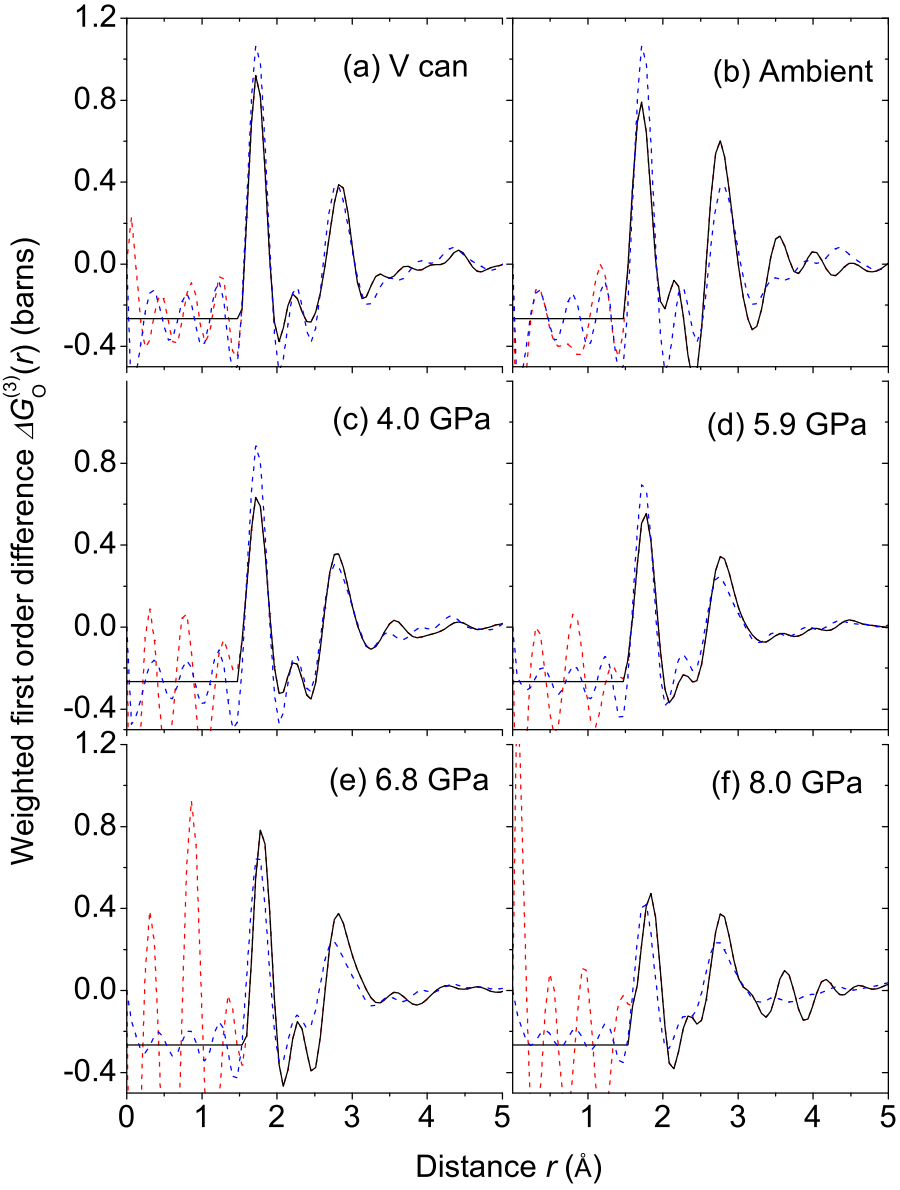

Figure 4-19: The pair distribution functions $\Delta G_O^{(3)}(r)$ as obtained by Fourier transforming the difference functions $\Delta F_O^{(3)}(Q)$ shown by the solid red curves (——) in figure 4-18. The broken red curves (- - -) show the extent of the low r oscillations and the horizontal black curves (——) at low r give the calculated $\Delta G_O^{(3)}(0)$ limit. For comparison, the broken blue curves (- - -) give the molecular dynamics results.

Table 4.5: The leading peak positions Q_1, Q_2 and Q_3 in the weighted first order difference functions $\Delta F_{\mathrm{O}}^{(1)}(Q)$, $\Delta F_{\mathrm{O}}^{(2)}(Q)$ and $\Delta F_{\mathrm{O}}^{(3)}(Q)$ plotted in figures 4-14, 4-16 and 4-18 for GeO_2 glass for pressures of 0–8 GPa. The leading peak positions r_1 and r_2 from the corresponding $\Delta G_{\mathrm{O}}^{(i)}(r)$ functions plotted in figures 4-15, 4-17, 4-19 and the Ge-O and O-O coordination numbers, $\bar{n}_{\mathrm{O}}^{\mathrm{O}}$ and $\bar{n}_{\mathrm{Ge}}^{\mathrm{O}}$, respectively, are also listed.

	$\Delta F_{\mathrm{O}}^{(1)}(Q)$			$\Delta G_{\mathrm{O}}^{(1)}(r)$			
P (GPa)	Q_1 (Å^{-1})	Q_2 (Å^{-1})	Q_3 (Å^{-1})	r_1 (Å)	r_2 (Å)	$\bar{n}_{\mathrm{Ge}}^{\mathrm{O}}$	$\bar{n}_{\mathrm{O}}^{\mathrm{O}}$
V can	1.53(2)	2.68	4.96(3)	1.73(2)	2.83(2)	3.9(1)	6.7(3)
0.0	1.52(2)	2.67	5.02(3)	1.73(2)	2.79(2)	4.2(1)	7.3(4)
4.0(5)	1.65(2)	2.74	4.84(3)	1.73(2)	2.84(2)	4.2(1)	8.0(4)
5.9(5)	1.83(2)	2.75	4.92(3)	1.74(2)	2.80(2)	4.4(1)	9.2(4)
6.7(5)	1.89(2)	2.76	4.86(3)	1.75(2)	2.78(2)	4.4(1)	9.7(4)
8.0(5)	1.91(2)	2.77	4.87(3)	1.77(2)	2.78(2)	4.3(1)	10.4(4)
	$\Delta F_{\mathrm{O}}^{(2)}(Q)$			$\Delta G_{\mathrm{O}}^{(2)}(r)$			
P (GPa)	Q_1 (Å^{-1})	Q_2 (Å^{-1})	Q_3 (Å^{-1})	r_1 (Å)	r_2 (Å)	$\bar{n}_{\mathrm{Ge}}^{\mathrm{O}}$	$\bar{n}_{\mathrm{O}}^{\mathrm{O}}$
V can	1.52(2)	2.68(3)	4.96(3)	1.73(2)	2.83(2)	4.0(1)	6.6(3)
0.0	1.57(2)	2.67(3)	4.99(3)	1.73(2)	2.79(2)	4.2(1)	7.2(4)
4.0(5)	1.63(2)	2.74(3)	4.84(3)	1.73(2)	2.85(2)	4.3(1)	7.8(4)
5.9(5)	1.85(2)	2.75(3)	4.92(3)	1.73(2)	2.81(2)	4.4(1)	8.5(4)
6.7(5)	1.73(2)	2.76(3)	4.86(3)	1.74(2)	2.78(2)	4.3(1)	9.5(4)
8.0(5)	1.91(2)	2.77(3)	4.87(3)	1.76(2)	2.78(2)	4.9(1)	10.3(4)
	$\Delta F_{O}^{(3)}(Q)$			$\Delta G_{O}^{(3)}(r)$			
P (GPa)	Q_1 (Å^{-1})	Q_2 (Å^{-1})	Q_3 (Å^{-1})	r_1 (Å)	r_2 (Å)	$\bar{n}_{\mathrm{Ge}}^{\mathrm{O}}$	$\bar{n}_{\mathrm{O}}^{\mathrm{O}}$
V can	1.56(2)	2.72(3)	4.93(3)	1.73(2)	2.83(2)	4.0(1)	7.1(3)
0.0	1.40(2)	2.72(3)	5.10(3)	1.71(2)	2.76(2)	3.9(1)	7.9(4)
4.0(5)	1.80(2)	2.67(3)	4.85(3)	1.74(2)	2.79(2)	4.1(1)	8.8(4)
5.9(5)	1.83(2)	2.75(3)	4.80(3)	1.77(2)	2.78(2)	4.3(1)	10.0(4)
6.7(5)	1.95(2)	2.76(3)	4.79(3)	1.78(2)	2.77(2)	–(–)	10.6(4)
8.0(5)	2.17(2)	2.78(3)	4.77(3)	1.83(2)	2.76(2)	–(–)	11.3(4)

The difference functions $\Delta F^{(i)}_{O'}(Q)$ $(i = 1, 2, 3)$ shown in figures 4-20, 4-22 and 4-24, respectively, have very similar features, in accordance with the relative weighting factors of the partial structure factors summarised in equation (4.8). The corresponding Fourier transforms $\Delta G^{(i)}_{O'}(r)$ $(i = 1, 2, 3)$ are shown in figures 4-21, 4-23 and 4-25, respectively.

The FSDP is not clearly defined in the $\Delta F^{(i)}_{O'}(Q)$ functions but, interestingly, the principal peak shows a sharp increase of intensity and shifts towards higher Q values. With increasing pressure, given that $S_{GeGe}(Q)$ has a small negative weighting in the difference functions, the intensity increase must arise predominantly from a rearrangement of the relative positions of the oxygen atoms on extended-range.

In contrast to the previous real space total and difference functions, the peak, which arises solely from Ge-O correlations [94], has been completely removed in all of the $\Delta G^{(i)}_{O'}(r)$ functions. Instead, the first peak is mostly due to O-O correlations and its position agrees with the position r_{OO} measured from the second peak in the $\Delta G^{(i)}_{O}(r)$ functions. However, overlap between the $g_{OO}(r)$ and $g_{GeGe}(r)$ functions means that it is not possible to extract accurate values for $\bar{n}^{O}_{O}$.

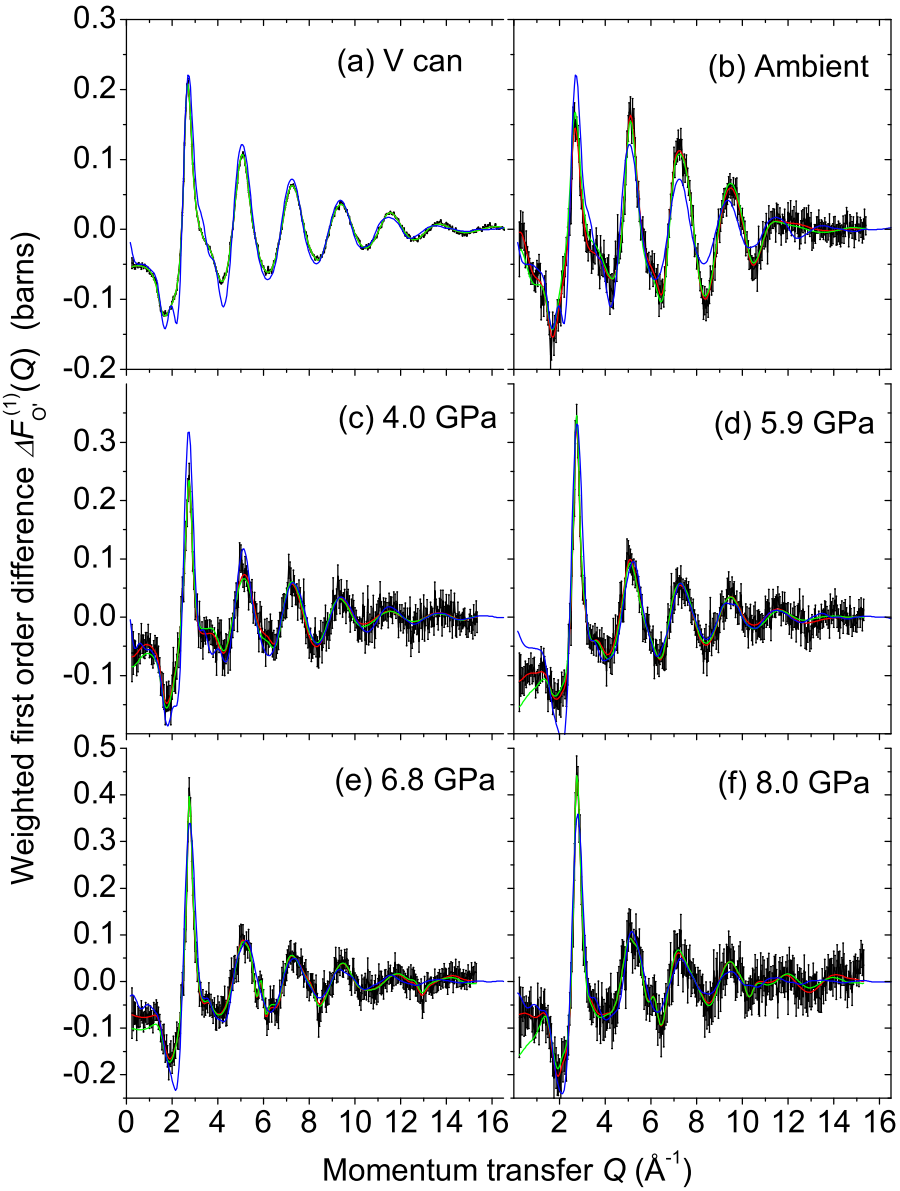

Figure 4-20: Difference functions $\Delta F^{(1)}_{O'}(Q)$ as measured for samples (a) in a vanadium can or (b)–(f) in the PE press for applied pressures of 0–8 GPa. The black solid curves (—) with vertical error bars represent the unsmoothed difference functions, the solid red curves (—) represent Harwell spline fitted data sets after a cosine window function has been applied over the Q range from 14.1–15.3 Å^{-1}, and the solid green curves (—) represent the Fourier back transforms of the $\Delta G^{(1)}_{O'}(r)$ functions shown in figure 4-21 after the unphysical oscillations at $r \leq 1.1$ Å have been set to the calculated $\Delta G^{(1)}_{O'}(0)$ limit. For comparison, the solid blue curves (—) give the molecular dynamics results.

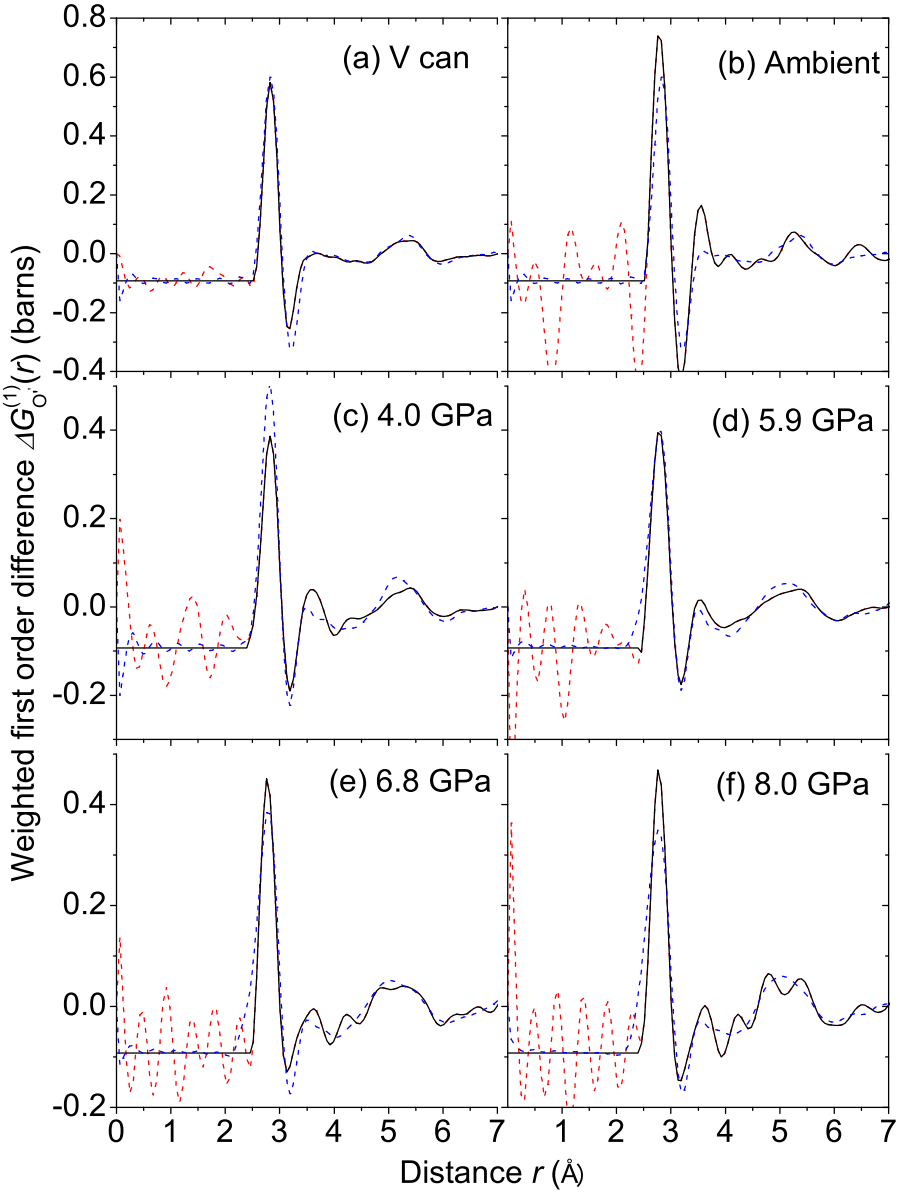

Figure 4-21: The pair distribution functions $\Delta G^{(1)}_{O'}(r)$ as obtained by Fourier transforming the difference functions $\Delta F^{(1)}_{O'}(Q)$ shown by the solid red curves (——) in figure 4-20. The broken red curves (- - -) show the extent of the low r oscillations and the horizontal black curves (——) at low r give the calculated $\Delta G^{(1)}_{O'}(0)$ limit. For comparison, the broken blue curves (- - -) give the molecular dynamics results.

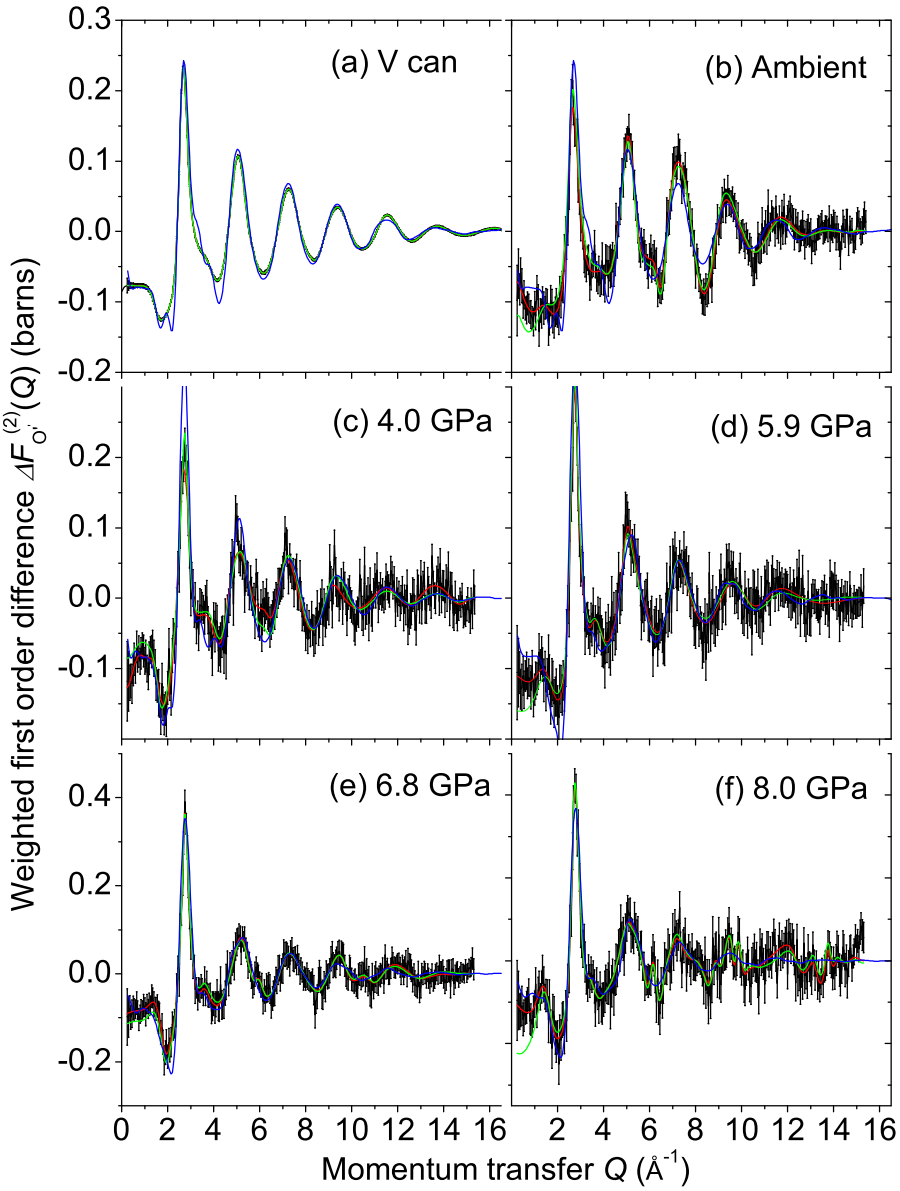

Figure 4-22: Difference functions $\Delta F^{(2)}_{O'}(Q)$ as measured for samples (a) in a vanadium can or (b)–(f) in the PE press for applied pressures of 0–8 GPa. The black solid curves (—) with vertical error bars represent the unsmoothed difference functions, the solid red curves (—) represent Harwell spline fitted data sets after a cosine window function has been applied over the Q range from 14.1–15.3 Å^{-1}, and the solid green curves (—) represent the Fourier back transforms of the $\Delta G^{(2)}_{O'}(r)$ functions shown in figure 4-23 after the unphysical oscillations at $r \leq 1.1$ Å have been set to the calculated $\Delta G^{(2)}_{O'}(0)$ limit. For comparison, the solid blue curves (—) give the molecular dynamics results.

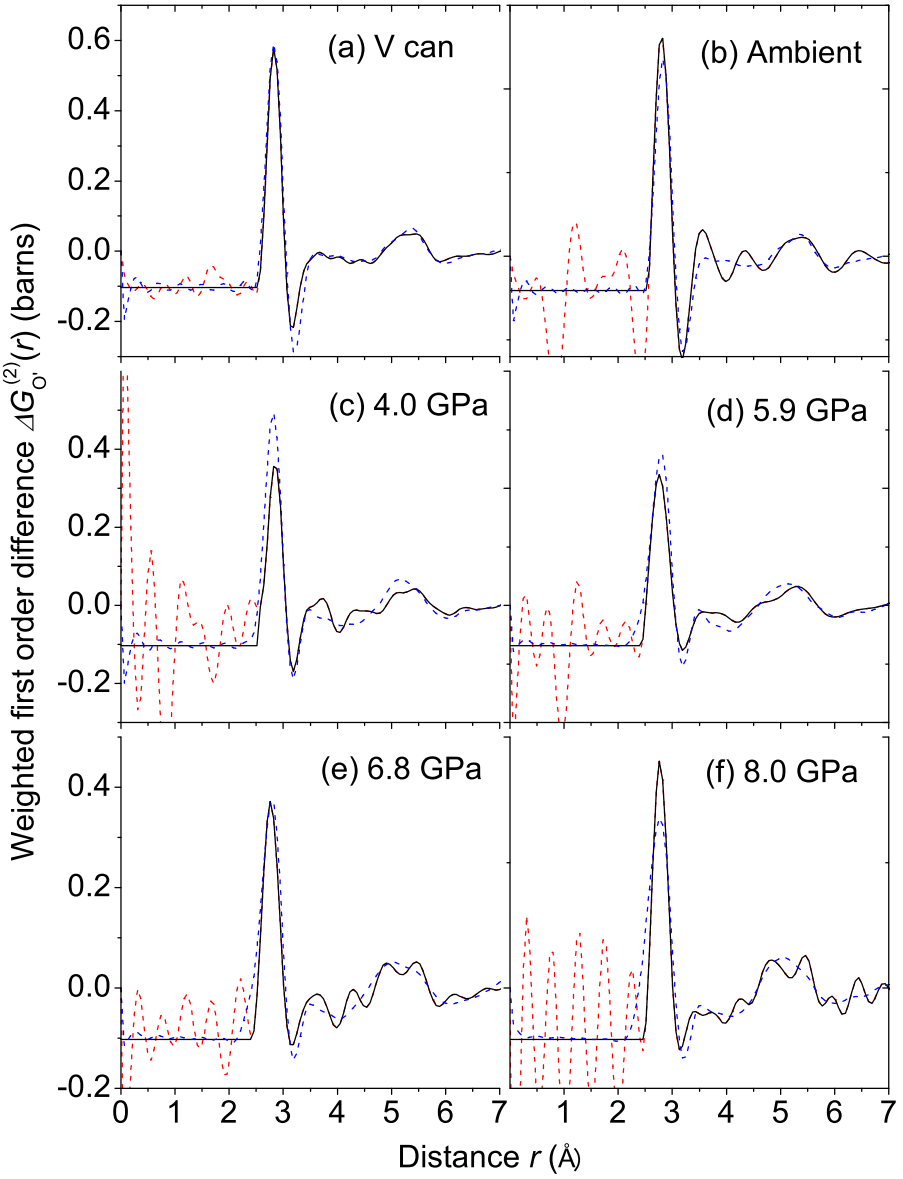

Figure 4-23: The pair distribution functions $\Delta G^{(2)}_{O'}(r)$ as obtained by Fourier transforming the difference functions $\Delta F^{(2)}_{O'}(Q)$ shown by the solid red curves (——) in figure 4-22. The broken red curves (- - -) show the extent of the low r oscillations and the horizontal black curves (——) at low r give the calculated $\Delta G^{(2)}_{O'}(0)$ limit. For comparison, the broken blue curves (- - -) give the molecular dynamics results.

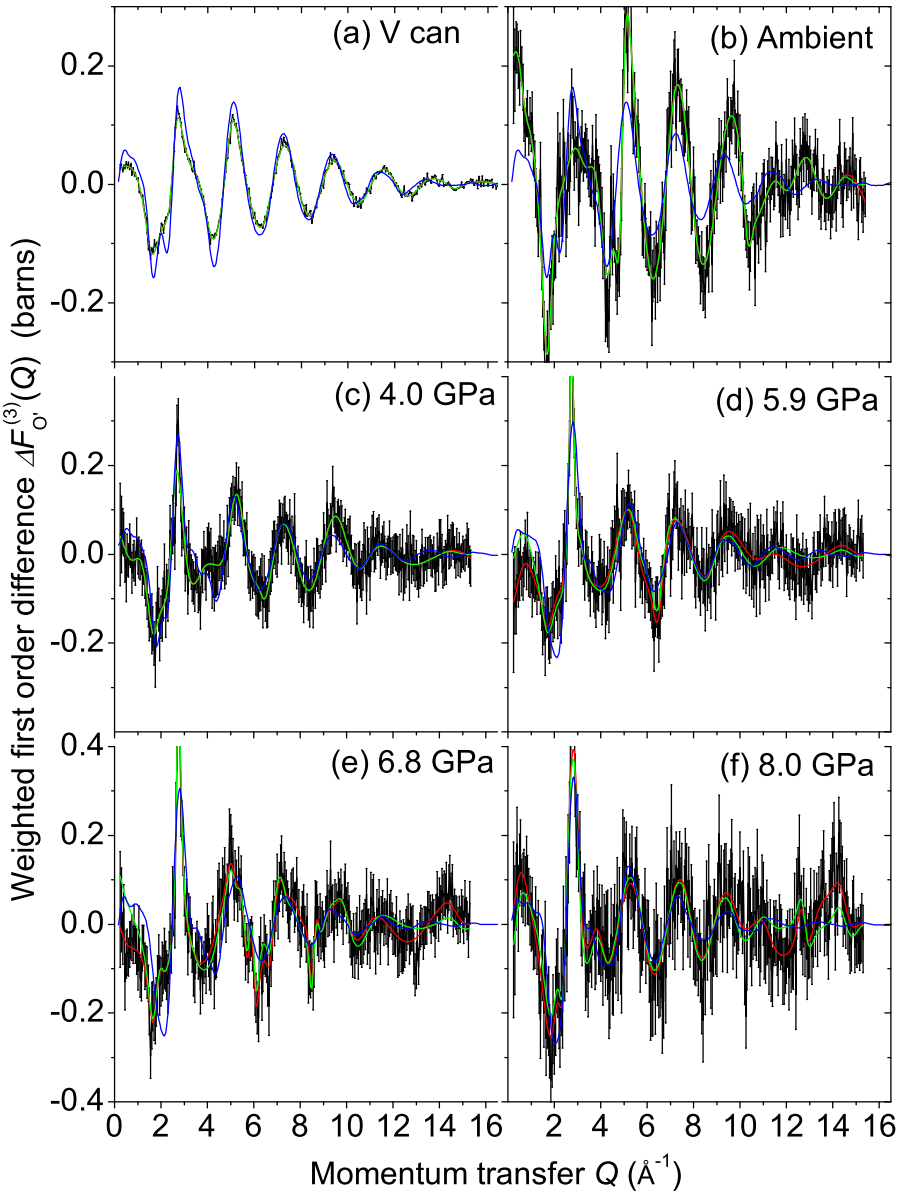

Figure 4-24: Difference functions $\Delta F^{(3)}_{O'}(Q)$ as measured for samples (a) in a vanadium can or (b)–(f) in the PE press for applied pressures of 0–8 GPa. The black solid curves (—) with vertical error bars represent the unsmoothed difference functions, the solid red curves (—) represent Harwell spline fitted data sets after a cosine window function has been applied over the Q range from 14.1–15.3 Å^{-1}, and the solid green curves (—) represent the Fourier back transforms of the $\Delta G^{(3)}_{O'}(r)$ functions shown in figure 4-25 after the unphysical oscillations at $r \leq 1.1$ Å have been set to the calculated $\Delta G^{(3)}_{O'}(0)$ limit. For comparison, the solid blue curves (—) give the molecular dynamics results.

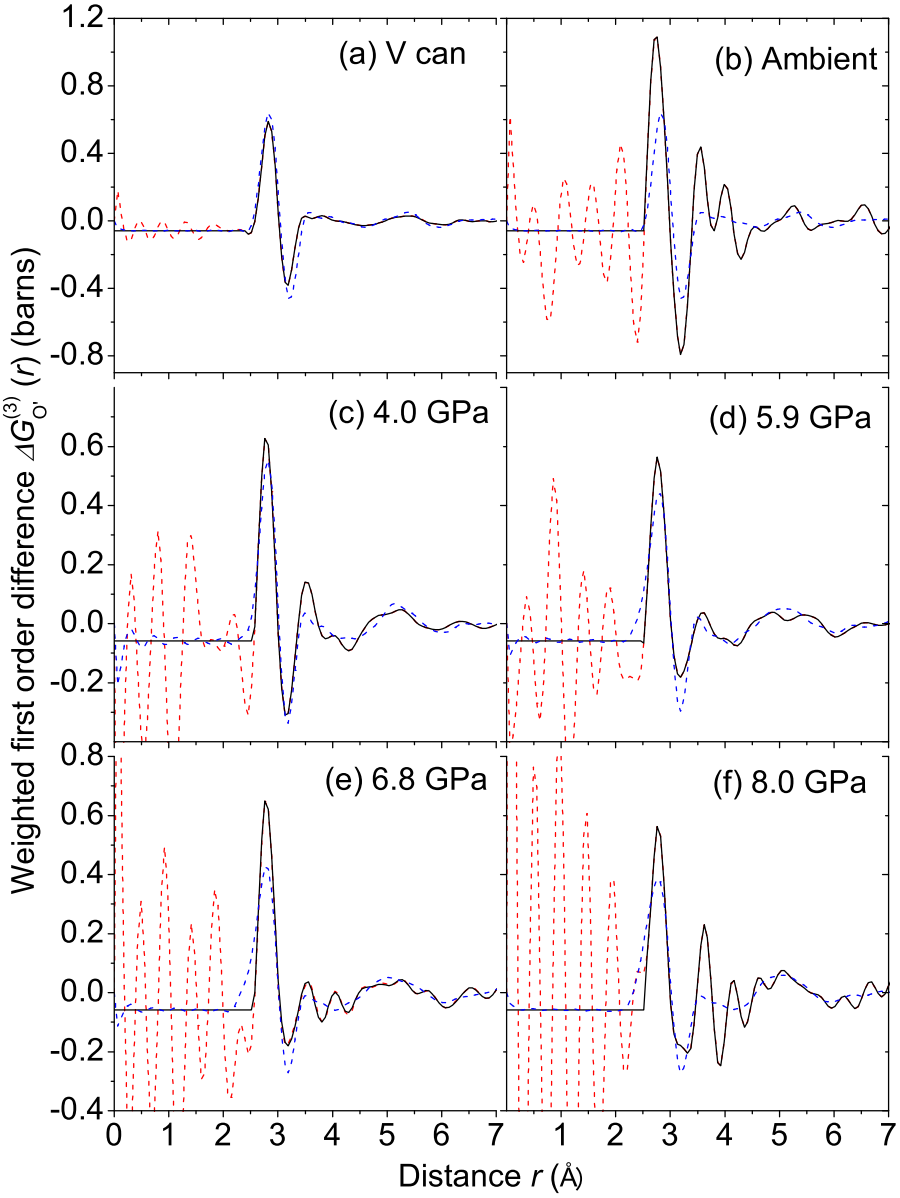

Figure 4-25: The pair distribution functions $\Delta G^{(3)}_{O'}(r)$ as obtained by Fourier transforming the difference functions $\Delta F^{(3)}_{O'}(Q)$ shown by the solid red curves (——) in figure 4-24. The broken red curves (- - -) show the extent of the low r oscillations and the horizontal black curves (——) at low r give the calculated $\Delta G^{(3)}_{O'}(0)$ limit. For comparison, the broken blue curves (- - -) give the molecular dynamics results.

Table 4.6: The leading peak positions Q_1, Q_2 and Q_3 in the first order weighted difference functions $\Delta F^{(1)}_{O'}(Q)$, $\Delta F^{(2)}_{O'}(Q)$ and $\Delta F^{(3)}_{O'}(Q)$ plotted in figures 4-20, 4-22 and 4-24 for GeO_2 glass for ambient pressure and for pressures up to 8 GPa. The leading peak position r_1 from the corresponding $\Delta G^{(i)}_{O'}(Q)$ functions plotted in figures 4-21, 4-23, 4-25 is also given. Due to overlap between $g_{OO}(r)$ and $g_{GeGe}(r)$ [94] it is not possible to extract reliable O-O coordination numbers $\bar{n}^{O}_{O}$.

	$\Delta F^{(1)}_{O'}(Q)$			$\Delta G^{(1)}_{O'}(r)$
P (GPa)	Q_1 (Å^{-1})	Q_2 (Å^{-1})	Q_3 (Å^{-1})	r_1 (Å)
V can	-	2.68(3)	5.07(3)	2.83(3)
0.0	-	2.68(3)	5.11(3)	2.78(3)
4.0(5)	-	2.69(3)	5.16(3)	2.81(3)
5.9(5)	-	2.74(3)	5.08(3)	2.76(3)
6.7(5)	-	2.75(3)	5.10(3)	2.77(3)
8.0(5)	-	2.77(3)	5.08(3)	2.77(3)
	$\Delta F^{(2)}_{O'}(Q)$			$\Delta G^{(2)}_{O'}(r)$
P (GPa)	Q_1 (Å^{-1})	Q_2 (Å^{-1})	Q_3 (Å^{-1})	r_1 (Å)
V can	-	2.68(3)	5.06(3)	2.83(3)
0.0	-	2.67(3)	5.07(3)	2.81(3)
4.0(5)	-	2.70(3)	5.09(3)	2.81(3)
5.9(5)	-	2.75(3)	5.06(3)	2.79(3)
6.7(5)	-	2.76(3)	5.19(3)	2.77(3)
8.0(5)	-	2.76(3)	5.10(3)	2.76(3)
	$\Delta F^{(3)}_{O'}(Q)$			$\Delta G^{(3)}_{O'}(r)$
P (GPa)	Q_1 (Å^{-1})	Q_2 (Å^{-1})	Q_3 (Å^{-1})	r_1 (Å)
V can	-	2.73(3)	5.08(3)	2.83(3)
0.0	-	2.90(3)	5.15(3)	2.74(3)
4.0(5)	-	2.69(3)	5.26(3)	2.81(3)
5.9(5)	-	2.75(3)	5.15(3)	2.79(3)
6.7(5)	-	2.76(3)	5.00(3)	2.78(3)
8.0(5)	-	2.83(3)	5.21(3)	2.78(3)

4.6 Discussion

The FSDP is associated with intermediate-range order of periodicity $2\pi/Q_{\mathrm{FSDP}}$, where Q_{FSDP} is the peak position, with a correlation length related to the inverse peak width ΔQ_{FSDP} [92]. The pressure dependence of the FSDP from the current neutron experiment is compared in figure 4-26 to that measured in the previous *in situ* neutron diffraction studies of Drewitt *et al* [31] and Salmon *et al* [13], and in the *in situ* x-ray diffraction studies of Guthrie *et al* [57], Hong *et al* [88], and Mei *et al* [69]. The linear increase of Q_{FSDP} with pressure up to 8.0 GPa found in the present work is consistent with previous neutron investigations. As pointed out in reference [13], the digression of the x-ray results by Mei *et al* [69] from the other studies is probably due to the use of He as a pressure transmission medium. The measurement by Mei *et al* [69] of larger Q_{FSDP} values contrasts to studies made on SiO_2 glass where He can penetrate the voids in the network and reduce the glass compressibility [95, 96].

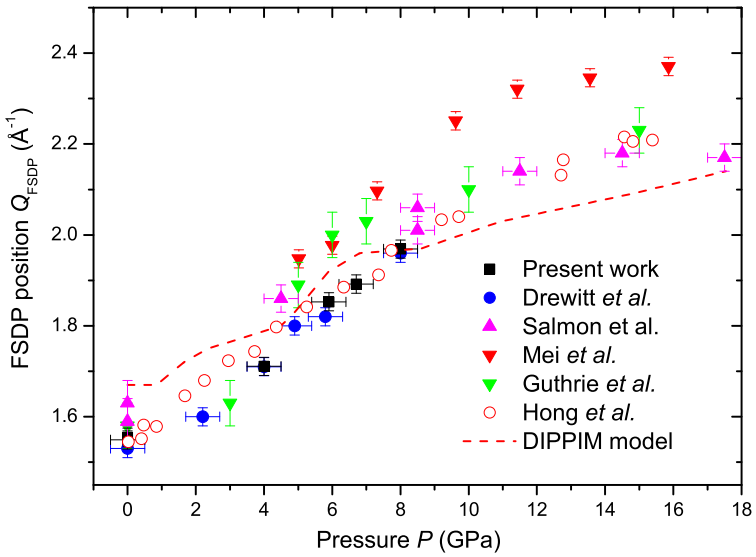

Figure 4-26: The pressure dependence of the FSDP position, Q_{FSDP}, for GeO_2 glass as measured in the *in situ* neutron diffraction work of the present study (■), Drewitt *et al.* [31] (●) and Salmon *et al.* [13] (▲). Also shown are the values obtained from the *in situ* x-ray diffraction studies of Mei *et al.* (▼) [69], Guthrie *et al.* (▼) [57] and Hong *et al.* (○) [88]. The broken curve (- - -) shows the molecular dynamics results obtained by using the DIPPIM interaction potentials.

The Ge-O bond distance for r_{GeO} and coordination number $\bar{n}^{\mathrm{O}}_{\mathrm{Ge}}$, as obtained by averaging the values from the $G(r)$, $\Delta G^{(i)}_{\mathrm{Ge}}(r)$ and $\Delta G^{(i)}_{\mathrm{O}}(r)$ functions with $i = 1,\ 2$ are plotted in figure 4-27. These results are compared to those obtained from previous neutron diffraction work [13, 31] and from an inelastic X-ray scattering (IXS) study

[97]. Importantly, the NDIS method also allows the nearest-neighbour Ge-Ge and O-O correlations to be resolved, as manifested by the second peaks in $\Delta G^{(i)}_{\rm Ge}(r)$ and $\Delta G^{(i)}_{\rm O}(r)$, respectively. The corresponding distances $r_{\rm GeGe}$ and $r_{\rm OO}$ are plotted in figure 4-27 along with the O-O coordination number $\bar{n}^{\rm O}_{\rm O}$, obtained by assuming minimal overlap with the Ge-O correlations as observed under ambient conditions [94].

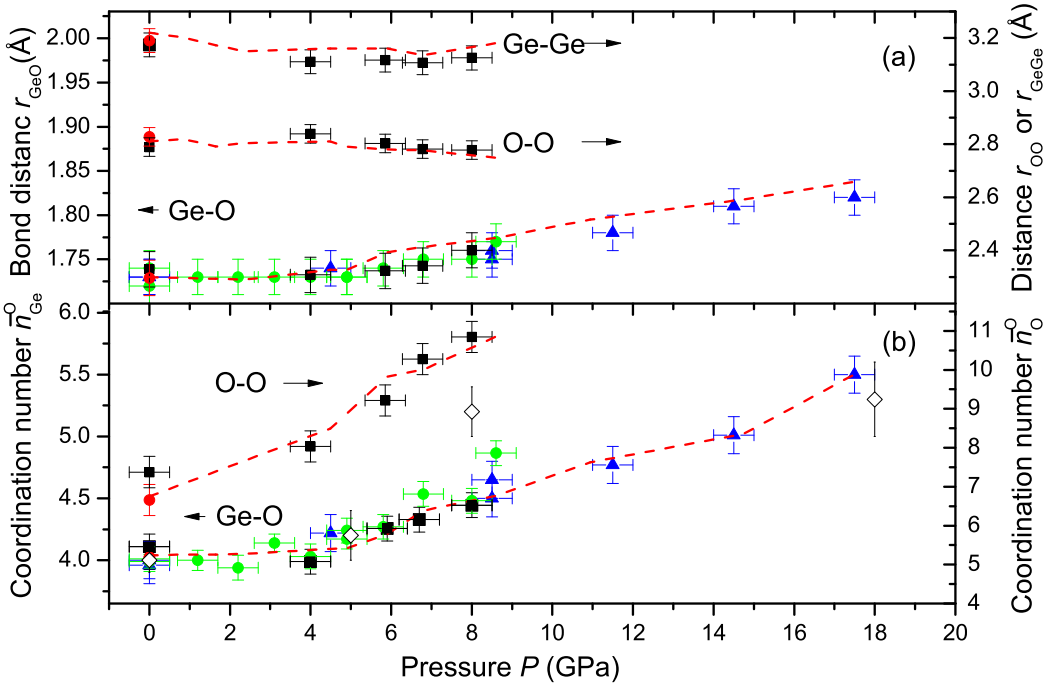

Figure 4-27: The pressure dependence of (a) the Ge-O, O-O and Ge-Ge bond distances and (b) and the Ge-O and O-O coordination numbers. The results of the present neutron diffraction experiment in a pressure cell (■) and in a vanadium can (●) are compared to the neutron results of Drewitt *et al.* [31] (●) and Salmon *et al.* (▲) and with molecular dynamics simulations (- - -) made using the DIPPIM potentials. The distances were taken from the peak positions in the real-space functions, except for the molecular dynamics Ge-O distance which was found using $< r_{\rm GeO} > = \int dr r g_{\rm GeO}(r) / \int dr g_{\rm GeO}(r)$. The molecular dynamics $\bar{n}^{\rm O}_{\rm O}$ values were found by integrating $g_{\rm OO}(r)$ up to $r_{\rm max}$ as found from the second peak in the measured $\Delta G^{(i)}_{\rm O}(r)$ $(i = 1,\ 2)$ functions. In (b) the Ge-O coordination numbers from IXS experiments [97] are also shown (◇).

The mean O-Ge-O and Ge-O-Ge bond angles, deduced from the measured nearest-neighbour distances, are compared in figure 4-30 with those measured for the α-quartz polymorph of GeO_2 [98, 99]. Because of a large difference in density between crystalline and amorphous GeO_2, it is more useful to plot the data as a function of the reduced density ρ/ρ_0 where ρ_0 is the ambient value. The evolution of the bond angle distributions with reduced density from simulations using the DIPPIM potentials are shown in figures 4-28 and 4-29. The positions of the peak maxima in the bond angle distributions

are also compared to the experimental results in figure 4-30.

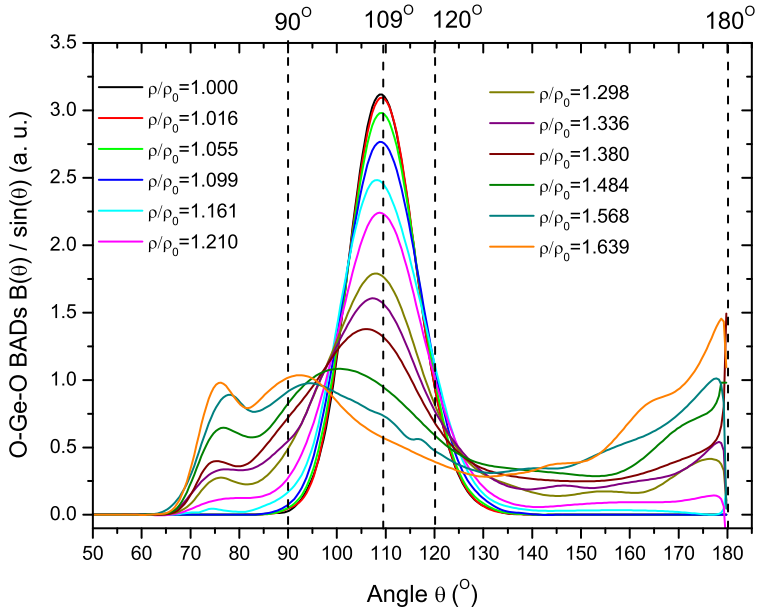

Figure 4-28: Evolution of the O-Ge-O bond angle distributions (BADs) with increasing reduced density as calculated for GeO_2 glass by molecular dynamics simulations with the DIPPIM interaction potentials.

As shown in figures 4-27 and 4-30, there is excellent overall agreement between the experimental results and the new molecular dynamics results obtained by using the DIPPIM interaction potentials. By contrast, other models for the pressure-induced structural changes in GeO_2, as obtained by using the Oeffner-Elliott potentials [100] in classical molecular dynamics simulations [79–83] or by using first principles molecular dynamics simulations [84], do not reproduce basic features such as the pressure dependence of the measure Ge-O bond lengths and coordination number (see figure 4-31).

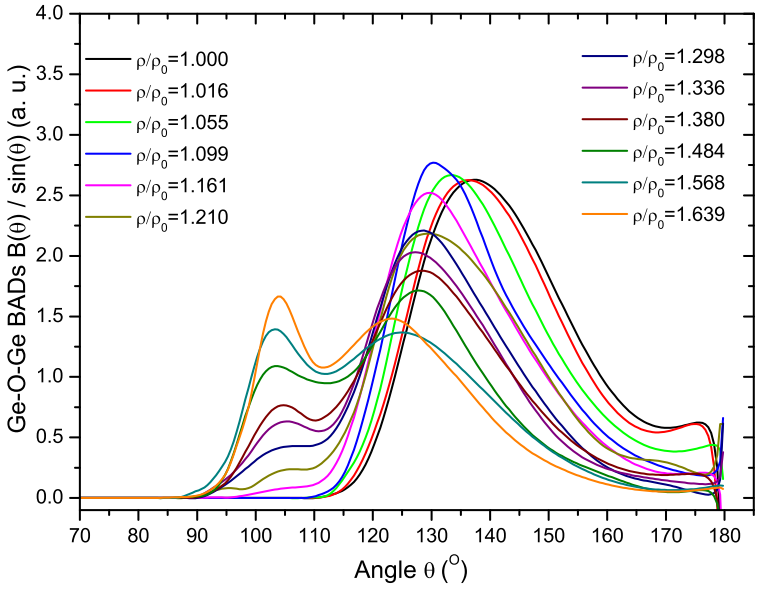

Figure 4-29: Evolution of the Ge-O-Ge bond angle distributions (BADs) with increasing reduced density as calculated for GeO_2 glass by molecular dynamics simulations with the DIPPIM interaction potentials.

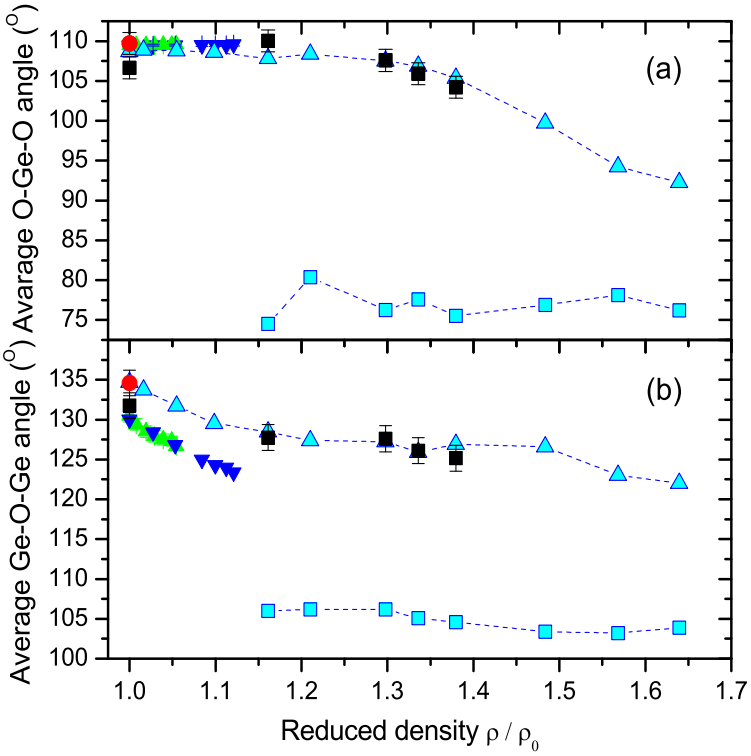

Figure 4-30: The reduced density ρ /ρ_0 dependence of (a) the O-Ge-O and (b) the Ge-O-Ge bond angles as measured in the present neutron diffraction study (■) on the glass, in the neutron diffraction study by Jorgensen *et al.* (▲) [98] and in the x-ray diffraction study by Glinnemann *et al.* (▼) [99] on the α-quartz polymorph of crystalline GeO_2. Also shown are the molecular dynamics results for the glass where two branches appear, corresponding to a shoulder or peak in the bond-angle distributions. One branch originates at ambient density from tetrahedral GeO_4 motifs (-▲-) and the other appears at higher densities (-■-) as these motifs are replaced by GeO_5 and GeO_6 units.

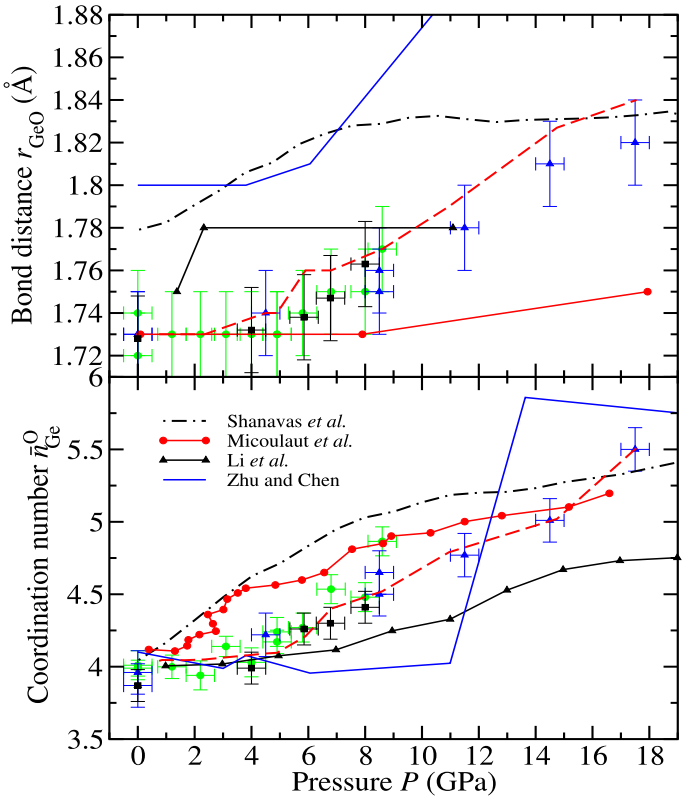

Figure 4-31: The pressure dependence of the Ge-O bond distance and coordination number in GeO_2 glass. The data points with error bars from neutron diffraction are defined in the figure 4-27 caption. The curves give the results obtained from various molecular dynamics simulations where those using the DIPPIM interaction potentials of Marrocchelli *et al* [85] are given by the broken red curves (- - -) and are in agreement with the experimental data. By comparison, the molecular dynamics results of Micoulaut *et al* [79, 80] (–●–), Shanavas *et al* [81] (-·-·-) and Li *et al* [83] (–▲–) using the Oeffner-Elliott interaction potentials [100], and the first principles molecular dynamics results of Zhu and Chen [84] (——), are not consistent with the measured data sets.

The following picture thus emerges for the structural evolution of compressed GeO_2 glass. When $\rho/\rho_0 < 1.16$ (or $P < 4.5$ GPa) there is little change in r_{GeO} or $\bar{n}^{O}_{Ge}$ (figure 4-27). Compaction proceeds via a reorganization of distorted corner-sharing tetrahedral GeO_4 units in which there is a reduction of the mean Ge-O-Ge bond angle, supporting an interpretation of Raman scattering results [64, 71], and an increase in $\bar{n}^{O}_{O}$. The rate of decrease of this bond angle with ρ/ρ_0 is similar to the α-quartz polymorph (figure 4-30(b)). On further densification, r_{GeO} and $\bar{n}^{O}_{Ge}$ both increase and a second branch appears in both the O-Ge-O and Ge-O-Ge bond-angle distributions (figures 4-28, 4-29 and 4-30).

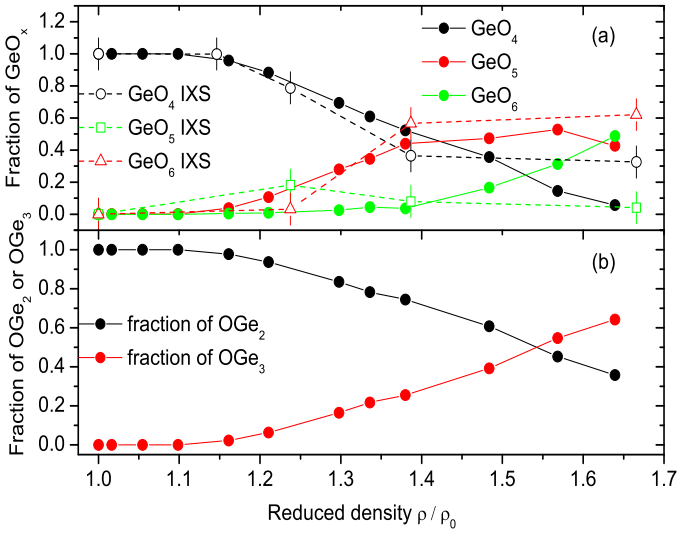

Figure 4-32: Molecular dynamics results using the DIPPIM interaction potentials for the density dependence of (a) the fractions of GeO_x species, where $x = 4$ (–●–), 5 (–●–) or 6 (–●–), and (b) the fractions of OGe_x species, where x=2 (–●–) or $x = 3$ (–●–). In (a), the fraction of GeO_x species from IXS experiments [97] are also shown where $x = 4$ (···○···), 5 (···□···) or 6 (···△···).

Initially, these changes correspond to a replacement of GeO_4 tetrahedra by GeO_5 units (figure 4-32(a)) and, to maintain the glass stoichiometry, threefold coordinated oxygen atoms must form (figure 4-32(b)). Signatures associated with the appearance of GeO_5 units are an increase and decrease in the rate of change with pressure of the O-Ge-O and Ge-O-Ge bond angles, respectively (figure 4-30), and an increase in the rate of change with pressure of the measured density [13, 88]. Subsequently, when $\rho/\rho_0 \gtrsim 1.4$ ($P \gtrsim 8.5$ GPa), the tetrahedra are also replaced by octahedral GeO_6 units, the fraction of GeO_5 units reaching a maximum when $\rho/\rho_0 \simeq 1.57$ ($P \simeq 14.5$ GPa). In comparison, $\rho/\rho_0 = 1.45$ for the ambient-temperature transformation of crystalline GeO_2 at $P >$ 6 GPa from the α-quartz to the monoclinic polymorph built from chains of edge-sharing

GeO_6 octahedra [101]. It is noted that, when GeO_5 units first appear at a reduced density $\rho/\rho_0 \simeq 1.16$, the first peak in the simulated partial pair-distribution function $g_{\mathrm{GeO}}(r)$ develops a high r tail (figure 4-33). This is not, however, seen as an obvious feature in the $\Delta G^{(i)}_{\mathrm{Ge}}(r)$ and $\Delta G^{(i)}_{\mathrm{O}}(r)$ functions plotted in figures 4-8, 4-10, 4-14 and 4-16 because the molecular dynamics data have been treated in the same way as the experimental results in order to respect the finite Q_{max} value (see equation 4.12).

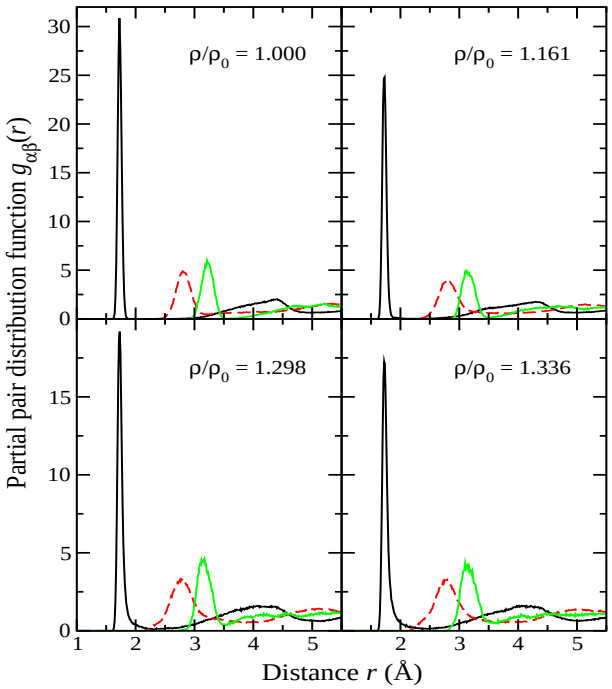

Figure 4-33: Evolution of the Ge-O (——), Ge-Ge (——) and O-O (- - -) partial pair-distribution functions from molecular dynamics simulations using the DIPPIM interaction potentials at different reduced densities.

The GeO_5 units found from the molecular dynamics simulations range from trigonal bipyramids, as seen in crystalline germanates [98, 99], to square pyramids where interconversion can be achieved via a minimal distortion of the intra-polyhedral O-Ge-O bond angles [102]. As indicated by figure 4-30(a), the O-Ge-O bond-angle distributions calculated for the GeO_5 units at the various pressures do not, however, show a peak or obvious shoulder at $\simeq 120^\circ$ (figure 4-28) as anticipated for a significant fraction of triagonal bipyramids. Inspection of the GeO_5 conformations shows that most have a distorted square pyramidal geometry described by $\tau \sim 40\%$ at all pressures, where τ is a parameter that ranges from 0% for regular square pyramids to 100% for regular trigonal bypyramids [102] (see figure 4-34).

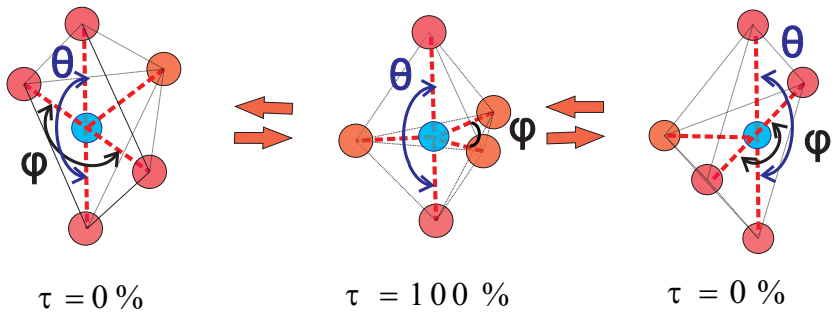

Figure 4-34: An illustration of the parameter $\tau = (\theta - \phi)/60\times\ 100\%$ where θ and ϕ are O-Ge-O angles. The twist mechanism, from left to right, shows the reorientation of the main axis of a square pyramidal configuration by pseudorotation via a trigonal bipyramidal configuration [102]. The atoms in the plane of the trigonal bipyramid are all candidates for becoming apical atoms in a square pyramid.

Thus, with increasing density, there is initially a progression from tetrahedral to predominantly square pyramidal units, where the vacancy at the base of latter anticipates the eventual formation of octahedral (i.e. square bipyramidal) units. The density dependence of GeO_x units (x = 4, 5 or 6) found from the present work contrasts with recent inelastic x-ray scattering (IXS) experiments (figure 4-32(a)), perhaps due to use of data from crystalline standards containing trigonal bipyramidal GeO_5 units to analyse the IXS spectra measured for the glass [97]. The corresponding Ge-O coordination numbers are compared to the neutron diffraction results in figure 4-27(b).

To gain further insight into the nature of the pressure-driven network collapse, the

configurations generated from the molecular dynamics simulations were analysed by making a shortest path search for rings containing either n Ge atoms or n O atoms by employing the Rigorous Investigation of Networks Generated using Simulation (RINGS) code [103, 104]. These searches were initiated either from Ge atoms or from O atoms and were restricted to looking for successive neighbours of unlike chemical species. In the RINGS analysis $R_c(n)$ is the number of n-fold rings normalized to the total number of atoms in the model. $P_{\mathrm{N}}(n)$ is the number of Ge (or O) atoms used in finding at least one ring containing n atoms, normalized to the total number of Ge (or O) atoms. $P_{\mathrm{max}}(n)$ and $P_{\mathrm{min}}(n)$ are the probabilities that, for a given Ge (or O) atom in an n-fold ring, the ring is either the longest or shortest closed path that can be found by using this same atom to initiate a search, respectively.

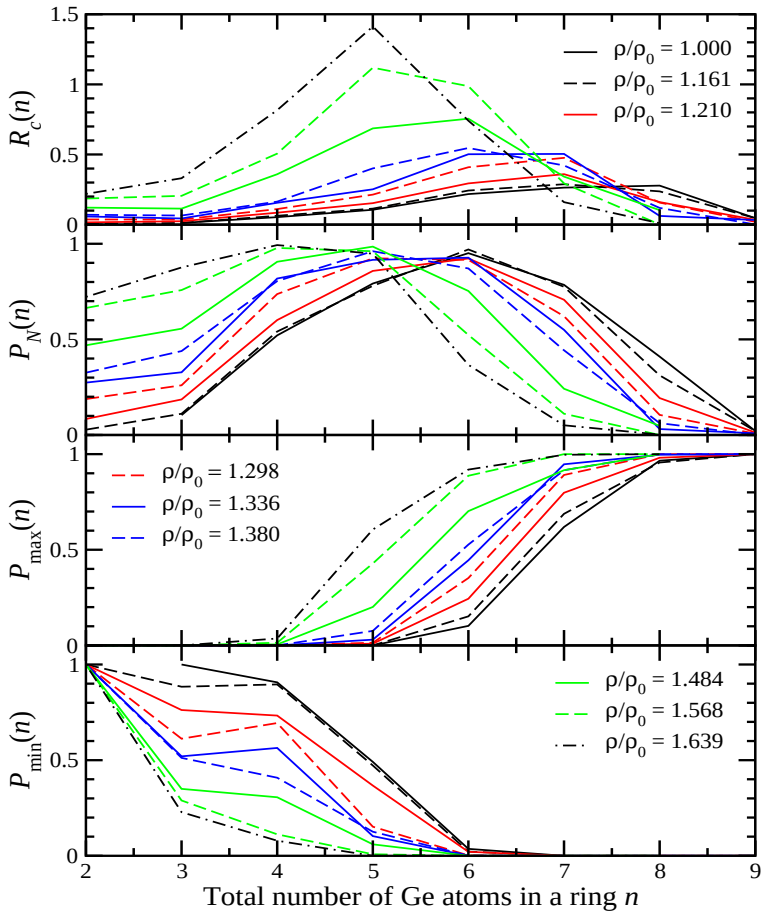

Figure 4-35: The connectivity profiles $R_{\mathrm{c}}(n)$, $P_{\mathrm{N}}(n)$, $P_{\mathrm{max}}(n)$ and $P_{\mathrm{min}}(n)$ as calculated for the molecular dynamics configurations for GeO_2 glass at different reduced densities by using the RINGS code [103, 104]. The searches were initiated from Ge atoms and were restricted to looking for successive neighbours of unlike chemical species.

The dependence on reduced density of the connectivity profiles obtained when using Ge atoms to initiate shortest path searches is shown in figure 4-35. The maximum in $R_c(n)$ at $n = 8$ for $\rho/\rho_0 = 1$ compares to a maximum at n = 6-7 from other molecular dynamics simulations [82, 105]. The formation of edge-sharing GeO_5 polyhedra at $\rho/\rho_0 \simeq 1.16$ manifests itself by the appearance of $n = 2$ rings and, as their number increases with ρ/ρ_0, there is a shift in the distribution of rings to smaller sizes. When $\rho/\rho_0 > 1.16$ the increase in number of $n = 3$ rings, attributed to the D_2 band at $\simeq 520$ cm^{-1} in Raman spectra [105, 106], is consistent with the measured density dependence of this feature [64, 71, 80]. The peak in $P_N(n)$ shows that the ring size for the majority of Ge atoms changes from $n = 6$ at ambient density to $n = 4$ at ρ/ρ_0 = 1.64. The dependence on reduced density of the connectivity profiles obtained with using oxygen atoms to initiate shortest path searches is shown in figure 4-36. When GeO_5 units appear at $\rho/\rho_0 \simeq 1.16$, threefold coordinated oxygen atoms also appear and there is a change in the values of $P_{min}(n)$ and $P_{max}(n)$ from unity i.e. the increased connectivity of the oxygen atoms leads to the possibility that they will be involved in more than one type of ring.

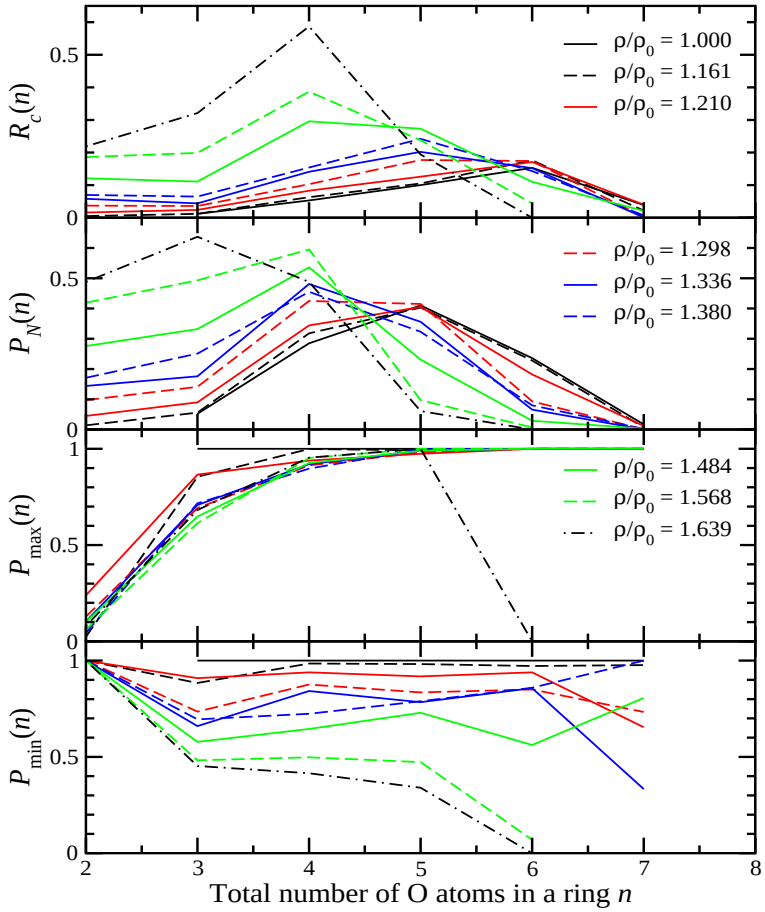

Figure 4-36: The connectivity profiles $R_c(n)$, $P_N(n)$, $P_{max}(n)$ and $P_{min}(n)$ as calculated for the molecular dynamics configurations for GeO_2 glass at different reduced densities by using the RINGS code [103, 104]. The searches were initiated from O atoms and were restricted to looking for successive neighbours of unlike chemical species.

4.7 Conclusions

In summary, it has been shown that the NDIS method can be used to help disentangle the structural complexity of GeO_2 glass *in situ* under high-pressure conditions, thus providing detailed experimental information to test the efficacy of different structural models. In the case of GeO_2 glass, quantitative agreement is found between the NDIS measurements and molecular dynamics simulations made by using transferable interatomic potentials that include dipole-polarization effects, an agreement that spans self-consistently a good number of structural parameters. These include the nearest neighbour Ge-O bond distances and coordination numbers, the nearest neighbour O-O distance and the peaks in the Ge-O-Ge and O-Ge-O bond length distributions. At elevated densities, the interplay between GeO_4, GeO_5 and GeO_6 polyhedra shows that two-state models [5, 8, 63, 65] will not provide a reliable account of pressure-induced structural transformations.

Chapter 5

Structure of glassy SiO_2 at pressures up to 14.5 GPa

5.1 Introduction

Silica is well known as a prototypical network glass-forming system whose behaviour under pressure has been of long standing interest [1]. The glass, under ambient conditions, forms an open network made from 4-fold coordinated tetrahedra SiO_4 motifs connected by their corners [107, 108]. Moreover the compressibility of SiO_2 glass is small, $\kappa = 0.0270$ GPa^{-1} [109], relative to many other network glass-forming systems [110] such as GeO_2 with $\kappa = 0.0420$ GPa^{-1} [65] (Chapter 4), $GeSe_2$ with $\kappa = 0.0625$ GPa^{-1} [111] (Chapter 5) and B_2O_3 with $\kappa = 0.0725$ GPa^{-1} [66] (Chapter 6), and there is an anomalous compressibility maximum at a pressure of $\simeq 2$ GPa [66, 112, 113] which is the subject of debate, there being competing models based on network rigidity arguments [114] or mechanisms associated with the rotation of Si-O-Si bonds in six-membered rings [115, 116]. After compaction at pressures above 10 GPa, the glasses recovered to ambient conditions are permanently densified [1, 117–120].

X-ray diffraction patterns show relatively small changes in the structure until pressures in excess of $\simeq 15$ GPa are attained, whereupon SiO_4 tetrahedra are gradually replaced by SiO_5 and/or SiO_6 polyhedra [13, 121]. *In situ* Raman spectroscopy experiments have been interpreted in terms of a reduction in width and shift of the Si-O-Si bond angle distribution for pressures below 8 GPa, followed by a change in the ring statistics at pressures in the range 8–30 GPa [122]. Raman spectroscopy studies of permanently densified SiO_2 glass have been interpreted in terms of a reduction [123] or not [124] in the mean Si-O-Si bond angle with increasing density, where different descrip-

tions may result from the use of different sample preparation procedures. Support for a reduction with pressure in the mean Si-O-Si bond angle in permanently densified glass is found from ^{29}Si magic-angle spinning nuclear magnetic resonance experiments [125].

High-pressure neutron diffraction has the potential for offering a new perspective on the structure of silica glass since it is more sensitive to the oxygen correlations by comparison with x-ray diffraction: the relative weighting factors for the Si-Si, Si-O and O-O correlations are 0.0694:0.3880:0.5427 for neutron diffraction versus 0.2178:0.4978:0.2844 for x-ray diffraction at a scattering vector $Q = 0$. High-pressure neutron diffraction experiments will therefore yield complementary information on the mechanisms of network collapse. Progress has been hampered, however, by the inherent difficulties associated with the necessary employment of small samples, the use of high-pressure apparatus which leads to detrimental background scattering, and the flux-limitations associated with neutron diffraction by comparison with x-ray diffraction [57, 58]. Therefore, the maximum pressure values that can be attained in neutron diffraction studies are still much lower than in x-ray diffraction studies.

The work presented in this chapter takes advantage of recent developments in high-pressure neutron diffraction as applied to amorphous materials [13, 31, 126] to measure the structure factor of SiO_2 glass *in situ* at pressures increasing from ambient to 14.5 GPa using the D4c [30] and PEARL [127] diffractometers. The neutron experiment on D4c also takes advantage of the new monochromator which increases the flux of neutrons by a factor of two for neutrons of wavelength $\lambda = 0.5$ Å. In contrast to x-ray diffraction, much larger changes are observed in the neutron diffraction patterns over this pressure range. It is thus possible to probe, with particular sensitivity to the O-O correlations, the structural changes that take place on compressing SiO_2 at constant network topology i.e. as corner-sharing SiO_4 tetrahedra reorganise with increasing density without breaking and re-making bonds.

5.2 Theory

In a neutron diffraction experiment the total structure factor

$$F(Q) = \sum_{\alpha=1}^{n} \sum_{\beta=1}^{n} c_\alpha c_\beta b_\alpha b_\beta [S_{\alpha\beta}(Q) - 1] \tag{5.1}$$

is measured where α and β denote the chemical species, n is the number of different chemical species, c_α and b_α represent the atomic fraction and bound coherent scattering

length of chemical species α, $S_{\alpha\beta}(Q)$ is a Faber-Ziman partial structure factor and Q is the magnitude of the scattering vector [10]. The corresponding real space information is represented by the total pair-distribution function $G(r)$ which is obtained from $F(Q)$ by using the Fourier transform relation

$$G(r) = \frac{1}{2\pi^2\rho r}\int_0^\infty F(Q)M(Q)\sin(Qr)QdQ \tag{5.2}$$

where ρ is the atomic number density of the glass and $M(Q)$ is a modification function defined by $M(Q) = 1$ for $Q \leq Q_{\max}$, $M(Q) = 0$ for $Q > Q_{\max}$. The latter is introduced because a diffractometer can measure only over a finite Q range up to a maximum value $Q_{\max}$. However, if $Q_{\max}$ is sufficiently large that $F(Q)$ no longer shows structure at high Q, then $G(r)$ follows from equation 5.1 by replacing each $S_{\alpha\beta}(Q)$ by its corresponding partial pair-distribution function $g_{\alpha\beta}(r)$.

5.3 Experimental procedure

The high-pressure neutron diffraction experiments were made at ambient temperature ($T \sim 300$ K) using a Paris-Edinburgh (PE) press mounted either on the diffractometer D4c at the steady-state reactor source of the Institut Laue-Langevin [30] or the time-of-flight diffractometer PEARL at the ISIS pulsed neutron source. The samples were in the form of solid pieces of silica glass (GE 214 type fused quartz, impurity content < 25 ppm) that had been ground to the geometry required for the anvils of the press by using a rotary tool.

The sample masses were close to the ideal values as defined by the anvil and gasket geometry (for D4c see Chapter 3, for PEARL see reference [128]). By using a Quantachrome gas pycnometer, the measured density of SiO_2 was found to be 2.195(5) g cm^{-3} from which the ideal sample masses were calculated to be 0.2024 g for D4c and 0.07397 g for PEARL. The actual pellet masses were 0.2040 g for D4c and 0.0638 g for PEARL. The samples were held in gaskets made from a $Ti_{0.676}Zr_{0.324}$ alloy which has a zero coherent neutron scattering length. The load on the anvils was always increased during the course of a given high-pressure run. The pressure dependence of the number density of SiO_2 glass, as obtained from several *in situ* studies [66, 129, 130], is shown in figure 5-1. Also given is a fit of the data to a third order Birch-Murnaghan equation of

state given by [131]

$$P = \frac{3B_0}{2}\left[\left(\frac{V}{V_0}\right)^{-7/3} - \left(\frac{V}{V_0}\right)^{-5/3}\right]\left[1 + \frac{3}{4}(B_1 - 4)\left(\left(\frac{V}{V_0}\right)^{-2/3} - 1\right)\right] \tag{5.3}$$

where V is the volume at pressure P and V_0 is the volume under ambient conditions. The fit parameters were found to be $B_0 = 26.5(6)$ GPa and $B_1 = 2.85(8)$, where B_0 is the bulk modulus under ambient conditions. In comparison, the bulk modulus is $B_0 = 37$ GPa from reference [109].

The coherent neutron scattering lengths are b_{Si}= 4.1491(10) fm and b_O= 5.803(4) fm [86].

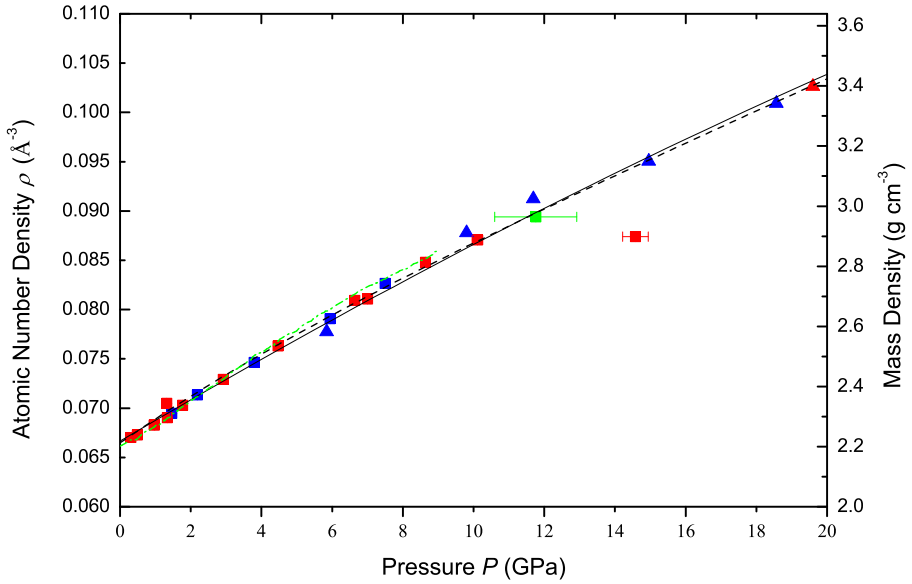

Figure 5-1: The density of SiO_2 glass as measured with increasing pressure in the experiments by Meade and Jeanloz (■) [129], Sato and Funomari (▲) [130] and Tsiok *et al* (-·-·-) [66]. The black curve (——) shows a fit made to the experimental data sets using a second order polynominal and the broken black curve (- - -) shows a fit to the data sets using a third order Birch-Murnaghan equation of state [131].

5.3.1 D4c high-pressure diffraction experiment

The D4c experiment employed a VX5/180 type PE press (piston area of 66.5 cm^2) with cubic BN anvils having a single-toroid profile [132] (Chapter 3) giving reliable access to pressures up to $\sim$ 8 GPa. The press was mounted so that the incident and scattered beams were in the same plane, perpendicular to the axis along which load

is applied to the anvils. Upon increasing the applied load, the sample position changes with piston displacement. The PE press was therefore mounted on a platform that could be translated vertically (z-axis drive) in order to centre the sample in the incident beam at each pressure point with the aid of an optical camera (Chapter 3). The background scattering was minimised by optimising the setup given in [31] (Chapter 3). The incident neutron wavelength of $\lambda = 0.4951(1)$ Å and zero scattering angle for the detectors were measured using Ni powder contained within an encapsulated $Ti_{0.676}Zr_{0.324}$ gasket [87] mounted in the PE press with no applied load. Higher order ($\lambda/2$) scattering was supressed by placing a Ir filter after the Cu(220) monochromator, upstream of the sample position.

Diffraction patterns were measured for (a) the sample in its Ti-Zr gasket at different pressures, (b) an unsquashed empty Ti-Zr gasket, (c) several empty Ti-Zr gaskets that had been recovered from different high pressures in order to estimate the gasket scattering under load, and (d) the empty anvils. To assist in the data normalisation at different pressures, where the anvils have different separations, additional diffraction patterns were measured at ambient pressure for large and small vanadium pellets contained in unsquashed and recovered (i.e. previously squashed) Ti-Zr gaskets, respectively.

An ambient-pressure diffraction experiment was also made on a solid silica rod of 6 mm diameter using a different experimental setup. Here diffraction patterns were measured for an incident beam height of 3.8 cm for the silica rod, the empty instrument and a cylindrical rod of vanadium of diameter 6.072(6) mm for normalisation purposes. The data analysis followed the procedure described in Chapter 3. The sample pressure was deduced from the load applied to the anvils of the press using a calibration curve that has been extensively checked (figure 3-6, Chapter 3) [13, 31].

5.3.2 PEARL high-pressure diffraction experiment

The PEARL experiment employed a V3 variant PE press [32] (piston area of 102 cm^2) with sintered diamond anvils having a double-toroid profile that enables pressures in excess of 8 GPa to be reliably obtained. The press was mounted using a transverse geometry such that the incident beam was directed along the compression axis through the anvil mounted on the breach of the press, and the scattered beam was observed by detectors mounted at a scattering angle $2\theta \simeq 90°$. Upon increasing the applied load, the sample position relative to the detectors changes with piston displacement. The press assembly for each pressure point was therefore moved using a motorized system to ensure that the sample was correctly centered in the diffractometer. The background

scattering was minimised by using the setup described in [13].

Diffraction patterns were measured for an empty Ti-Zr gasket with a small applied load and for the sample in its gasket at several different pressures. To normalise the data sets, diffraction patterns were also measured for a piece of vanadium contained in a Ti-Zr gasket at comparable loads to the sample in order to match the sample geometry at each pressure point. The measurement protocol and data analysis procedure, including the use a Lorentzian function to extrapolate the measured $F(Q)$ functions to $Q = 0$ for use in equation 5.2, are described in detail in reference [13]. The sample pressure was determined from the load applied to the anvils by constructing a calibration curve based on the results obtained from several independent neutron diffraction experiments [13].

5.4 Results

The total structure factors $F(Q)$ for SiO_2 glass measured on the D4c and PEARL instruments at pressures up to 14 GPa are plotted in figure 5-2. The corresponding Fourier transforms, the total pair correlation functions $G(r)$, are plotted in figure 5-3. The Fourier transformations were performed on Harwell spline fitted $F(Q)$ functions [52]. The key parameters describing the $F(Q)$ and $G(r)$ functions are given in table 5.1.

As shown in figure 5-2, there is good agreement between the diffraction patterns taken for the silica rod and for the samples measured in the pressure cell environment under ambient conditions, where in the first case a setup was used with a much larger sample volume. With increasing pressure, there is a reduction in height and shift of the first sharp diffraction peak (FSDP) at $\simeq 1.5$ Å^{-1} to higher Q-values, accompanied by an increase in intensity of the principal peak (PP) at $\simeq 2.9$ Å^{-1}. The latter is anticipated to be less broad in the case of the PEARL data because the Q-space resolution is $\Delta Q/Q = 0.85\%$ as compared to $\Delta Q/Q = 2.5\%$ for D4c at $Q = 2.9$ Å^{-1}. However, a comparison of the $F(Q)$ function, measured for GeO_2 glass (see figure 8 in reference [13]), using both instruments at different pressures does not show any major differences in the PP region.

Over the measured pressure range, the mean Si-O coordination number does not vary from its ambient value of $\bar{n}^{O}_{Si} = 4.0(1)$ and the mean Si-O bond length remains constant at $r_{SiO} = 1.60(2)$ Å. Also, if the second peak in $G(r)$ at r_2 is attributed primarily to nearest-neighbour O-O correlations, then the ratio r_2/r_{SiO} does not vary within the experimental error and the results listed in table 5.1 are comparable to the value of $\sqrt{8/3} = 1.633$ expected for regular tetrahedra. While the width of the first peak remains constant, the width of the second peak appears to broaden above 1.7 GPa (the half width at half

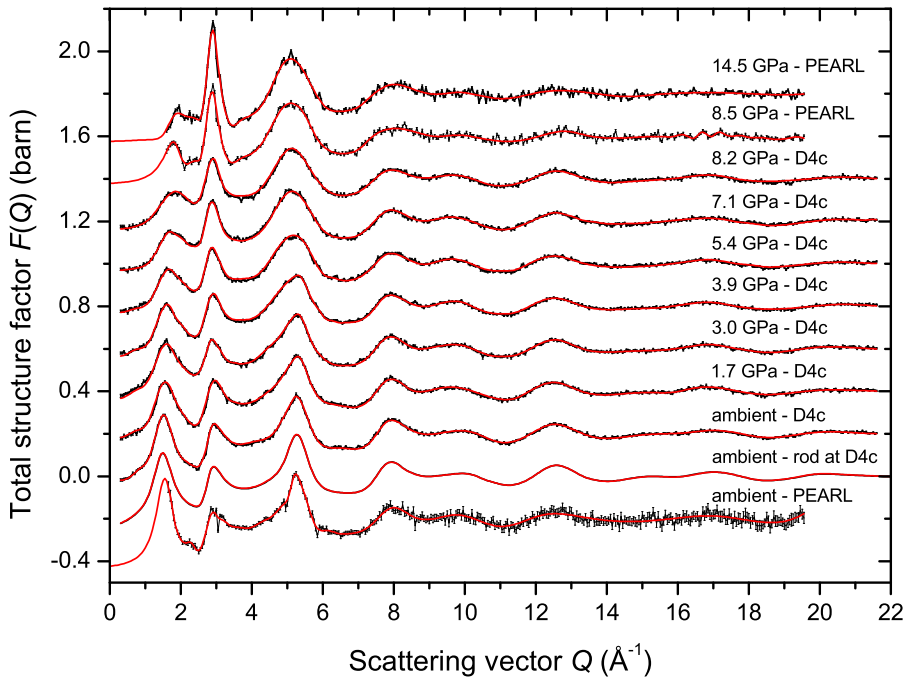

Figure 5-2: The pressure dependence of the total structure factor $F(Q)$ for SiO_2 glass as measured using the D4c or PEARL diffractometer for samples held in a Paris-Edinburgh press. The results are compared to $F(Q)$ as measured for a solid silica rod using D4c. The solid black curves (——) with vertical error bars represent the unsmoothed total structure factors and the solid red curves (——) represent Harwell spline fitted data sets. For the PEARL experiments, the region $Q \leq 1.55$ Å^{-1} was not accessible and the solid red curves (——) for this region correspond to fitted Lorentzian functions (see reference [13]). The data sets measured using the PE press have been shifted vertically for clarity of presentation.

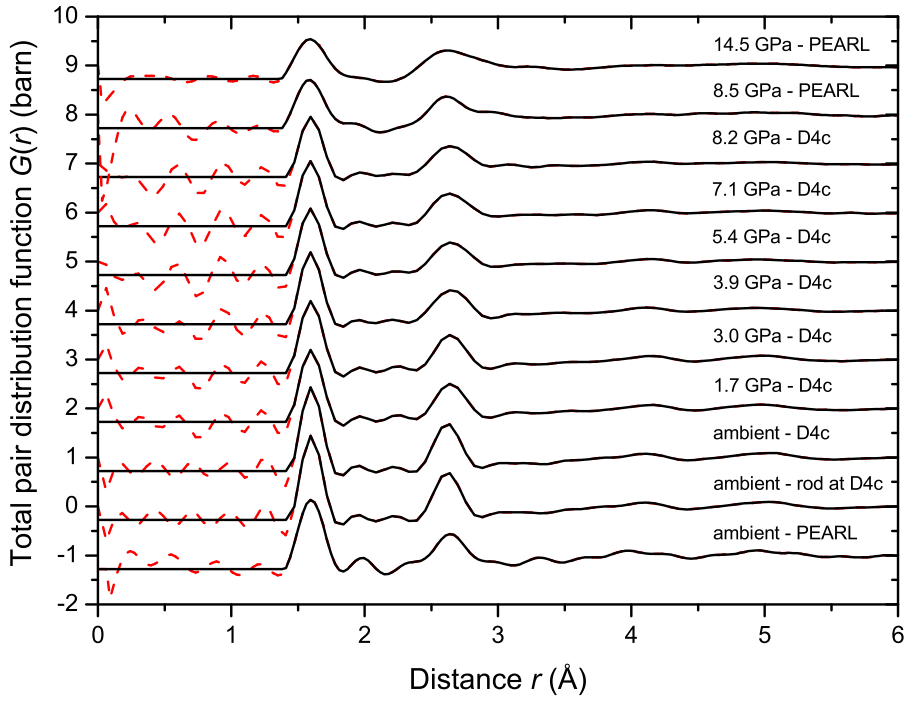

Figure 5-3: The pressure dependence of the total pair-distribution function $G(r)$ for SiO_2 glass as measured using the D4c or PEARL diffractometer. The $G(r)$ functions were obtained by Fourier transforming the total structure factors $F(Q)$ show by the solid red curves (——) in figure 5-2. The broken red curves (- - -) show the extent of the low r oscillations and the horizontal black curves (——) at low r give the calculated $G(0)$ limit.

maximum HWHM = 0.248 Å at ambient cf. HWHM = 0.329 Å at 8.2 GPa), which suggests deformation of the tetrahedra as the pressure is increased.

Table 5.1: Parameters describing the pressure dependence of the structure of SiO_2 glass as measured using the D4c or PEARL diffractometer. The number density ρ of the glass is given (figure 5-1) together with the position Q_{FSDP} of the first sharp diffraction peak, the position Q_{PP} of the principal peak, the Si-O bond distance r_{SiO} as taken from the position of the first peak in $G(r)$, the mean Si-O coordination number $\bar{n}^{\mathrm{O}}_{\mathrm{Si}}$, and the ratio r_2/r_{SiO} where r_2 is the position of the second peak in $G(r)$.

P (GPa)	Instrument	ρ (Å^{-3})	Q_{FSDP} (Å^{-1})	Q_{PP} (Å^{-1})	r_{SiO} (Å)	$\bar{n}^{\mathrm{O}}_{\mathrm{Si}}$	r_2/r_{SiO}
Ambient	D4c−rod	0.0665	1.49(2)	2.92(2)	1.60(2)	4.1(1)	1.640
Ambient	D4c	0.0665	1.52(2)	2.93(2)	1.60(2)	4.0(1)	1.633
Ambient	PEARL	0.0665	1.55(2)	2.90(2)	1.60(2)	4.0(1)	1.652
1.7(5)	D4c	0.070(1)	1.55(2)	2.91(2)	1.60(2)	4.0(1)	1.657
3.0(5)	D4c	0.073(1)	1.60(2)	2.87(2)	1.60(2)	4.1(1)	1.651
3.9(5)	D4c	0.075(1)	1.59(2)	2.90(2)	1.60(2)	4.0(1)	1.659
5.4(5)	D4c	0.078(1)	1.66(2)	2.88(2)	1.60(2)	4.0(1)	1.660
7.1(5)	D4c	0.081(1)	1.74(2)	2.89(2)	1.59(2)	4.0(1)	1.655
8.2(5)	D4c	0.083(1)	1.83(2)	2.89(2)	1.60(2)	4.0(1)	1.648
8.5(5)	PEARL	0.085(1)	1.78(2)	2.90(2)	1.59(2)	4.0(1)	1.652
14.5(5)	PEARL	0.095(1)	1.93(2)	2.90(2)	1.59(2)	4.0(1)	1.647

5.5 Discussion

The evolution of the position of the FSDP Q_{FSDP} with pressure from the studies made on the D4c and PEARL instruments is shown in figure 5-4. These data points are compared to the results from x-ray diffraction experiments made using a diamond anvil cell by Benmore *et al.* [121], Sato *et al.* [130, 133], Meade *et al.* [134], and to the x-ray diffraction experiments made using a cubic-type multianvil apparatus by Inamura *et al.* [120]. A comparison is also made with the MD simulation results from Huang *et al.* [115] and Wilson [128, 135, 136]. There is consistency between the rate of change of the peak position Q_{FSDP} with pressure as measured in both the neutron and x-ray diffraction experiments. However, the intensity decrease in the FSDP as seen by neutron diffraction up to 8.2 GPa is larger than the intensity decrease seen by x-ray diffraction over the same pressure range [120, 121].

In the molecular dynamics work by Huang [137] a charge-transfer three-body potential was employed, as parameterised for tetrahedrally coordinated Si, which was developed to reflect the charge redistribution in a situation when bonds are being broken and reformed beyond 20 GPa. Although the simulations reflect the change in gradient $\Delta Q_{\mathrm{FSDP}}/\Delta P$ up to $\sim$ 10 GPa, the rate of change of Q_{FSDP} is steeper than in the experimental measurements. The simulations made by Wilson [135], which used the potentials of Tangney and Scandolo [136] obtained from *ab initio* force field calculations, give better agreement with the experimental Q_{FSDP} values at pressures up to $\sim$ 15 GPa. At the present time the simulation work by Wilson is still in progress and further results will not, therefore, be presented.

Given that the weighting factor for the $S_{\mathrm{SiSi}}(Q)$ partial is small in neutron diffraction as compared to x-ray diffraction, the changes in the FSDP in the neutron diffraction work will be more sensitive to the rearrangements of oxygen atoms on an intermediate range. A sharpening of the principal peak in $F(Q)$ with increasing pressure, as seen in figure 5-2, accompanied by a decrease in height of the FSDP as it moves to higher Q values, is consistent with other tetrahedral glass forming systems such as GeO_2 [13, 31] (Chapter 4), $GeSe_2$ [138] (Chapter 7) and GeS_2 [126] and is a signature of increasing glass fragility [90]. The growth in importance of the principal peak leads to enhanced extended range ordering [89, 139] but it is not, however, evident from the x-ray diffraction experiments [121] because the weighting coefficients for the partial structure factors lead to a cancellation of the principal peaks in $S_{\mathrm{SiSi}}(Q)$ and $S_{\mathrm{OO}}(Q)$ with the principal peak trough in $S_{\mathrm{SiO}}(Q)$ (see figure 4 in reference [107]).

The pressure dependence of the mean Si-O bond distances and coordination numbers

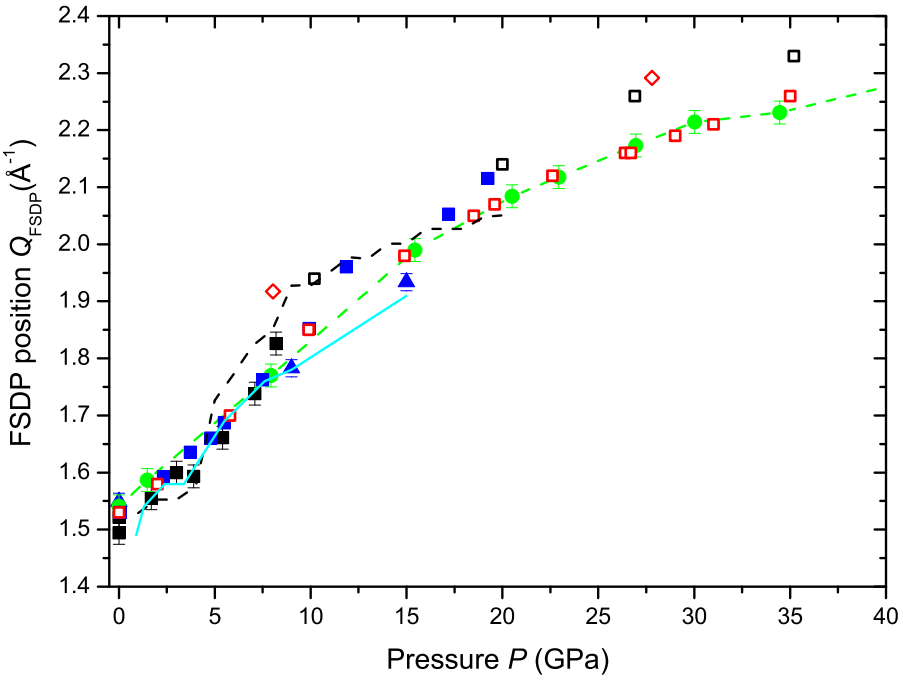

Figure 5-4: The position of the first sharp diffraction peak Q_{FSDP} in the total structure factor for SiO_2 glass as measured using neutron and x-ray diffraction. The results from the D4c (■) and PEARL (▲) diffractometers are compared to those obtained from the x-ray diffraction experiments made by Benmore *et al.* (– ● –) [121], Inamura *et al.* (■) [120], Sato *et al.* (□) [130] and (□) [133], Meade *et al.* (◇) [134] and those obtained from the molecular dynamics work of Huang *et al.* (- - -) [115]. The preliminary molecular dynamics results of Wilson *et al.* (——) [128, 135, 136] are also shown.

$\bar{n}^{O}_{Si}$ as measured using D4c and PEARL are shown in figure 5-5. The results are compared to the parameters obtained from the x-ray diffraction work by Benmore *et al.* [121], Meade *et al.* [134] and Sato *et al.* [130, 133] as well from the MD simulations by Huang *et al.* [115] and Tse *et al.* [140]. In general there is good agreement, accounting for the experimental uncertainty, between the neutron and x-ray diffraction parameters. The larger Si-O distances measured by Sato *et al.* [133] are, according to these authors, probably caused by the effects of differential stress. The neutron data does not show any evidence of tetrahedral shrinkage at pressures up to 14.5 GPa. As seen from the x-ray diffraction data [121, 130, 133, 134], a gradual coordination change appears to be taking place for pressures beyond 16 GPa, as the tetrahedral structural motifs start to gradually transform, leading to an octahedral glass at a pressure of $\sim$ 40 GPa. At the present time, neutron diffraction is limited to a maximum pressure of $\sim$ 20 GPa due to anvil limitations and the requirement for small sample volumes to attain large pressures (see pp.76-80 [3]). As will be seen in Chapter 5, a similar transformation from a tetrahedral to an octahedral glass occurs for GeO_2 but the transformation starts at a much lower pressure threshold of 5 GPa.

As shown in figure 5-5 the molecular dynamics simulations by Tse *et al.* [140] and Huang *et al.* [115], reproduce the measured peak positions r_{SiO} and coordination numbers $\bar{n}^{O}_{Ge}$, to within the experimental uncertainty, in the pressure region below $\sim$ 14 GPa. The Tse *et al.* [140] results fall short, however, at pressures beyond this point. For pressures below 8 GPa, the simulations suggest that densification proceeds via a reduction of the Si-O-Si bond angle and a broadening of the O-Si-O bond angle distribution. Huang *et al.* [115] also see a shift in the distribution of ring sizes formed by corner sharing tetrahedra, such that larger rings are generated at pressure beyond 8 GPa. This process is somewhat counter-intuitive and is opposite to the behaviour observed for glassy GeO_2 under pressure (see the discussion section in Chapter 4) where the rings decrease in size with increased applied pressure. Recent molecular dynamics simulations by Mark Wilson at Oxford University will bring a fresh view to the densification of SiO_2 glass in the region of constant network topology and beyond. It is anticipated that the present neutron diffraction results, together with the results obtained from the x-ray diffraction study by Benmore *et al.* [121], will provide a comprehensive test for the validity of these new molecular dynamics simulations.

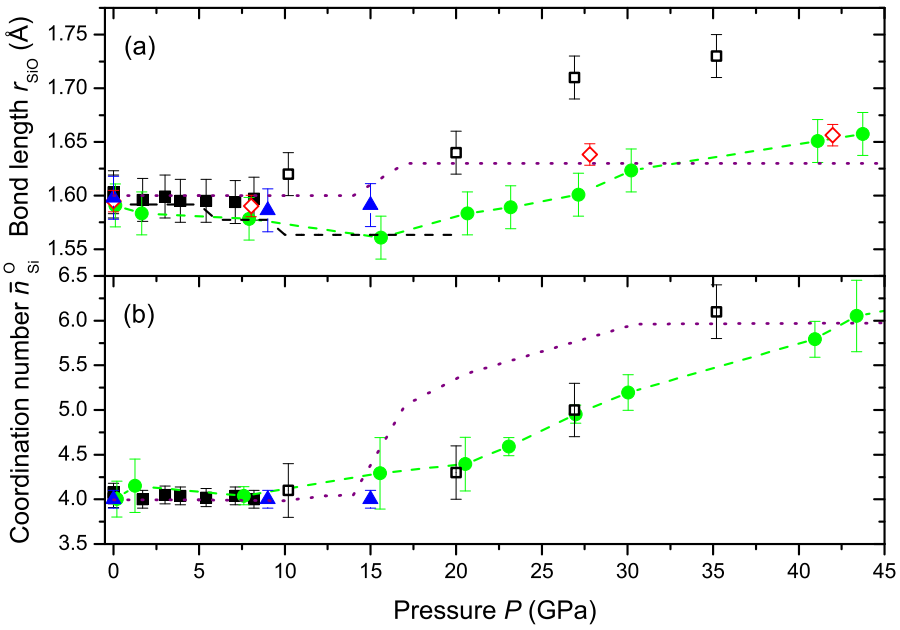

Figure 5-5: The pressure dependence of (a) the bond length r_{SiO} (b) the mean Si-O coordination number $\bar{n}^{O}_{Si}$. The results of the D4c (■) and PEARL (▲) experiments are compared to the x-ray diffraction results of Benmore *et al.* (–●–) [121], Meade *et al.* (◇) [134] and Sato *et al.* (□) [133], and to the molecular dynamics results of Huang *et al.* (- - -) [115] and Tse *et al.* (···) [140].

5.6 Conclusion

Accurate neutron total structure factors $F(Q)$ have been measured for glassy SiO_2 at pressures up to 14.5 GPa using two variants of the Paris-Edinburgh press. The pressure dependence of the first sharp diffraction peak Q_{FSDP}, the mean nearest neighbour Si-O bond distances and coordination number $\bar{n}_{\mathrm{Si}}^{\mathrm{O}}$ are in agreement with the x-ray diffraction work by Benmore *et al.* [121] in the measured pressure range.

The principal mechanism for the densification of SiO_2 glass at pressures up to $\sim$ 15 GPa, as seen by both neutron and x-ray diffraction, is a change in the intermediate range ordering of the tetrahedra. This is manifested by a shift of the FSDP towards larger Q values and the sharpening of the PP in the measured total structure factors $F(Q)$. Recent molecular dynamics simulations by Wilson [135] will help to illuminate the densification processes in SiO_2 glass for region of constant network topology and beyond. All of this will help to distinguish the mechanisms of structural collapse in SiO_2 and related glasses to those found in other network glass forming materials.

Chapter 6

Structural transformations in glassy B_2O_3 at pressures up to 17.5 GPa

6.1 Introduction

B_2O_3 is a prototypical glass forming oxide material and is an essential component in many industrial glasses [11, 141–149]. Unlike SiO_2 and GeO_2 its structure under ambient conditions in not based on tetrahedral units but is instead based on corner shared BO_3 planar triangles [150, 151]. The network topology of B_2O_3 is, therefore, very different to silica and germania and there has been much debate on the glass structure [142, 152, 153], in particular on the role played by B_3O_6 boroxol rings which are planar motifs formed by connecting three corner-sharing BO_3 triangles [11, 141–144, 147] (see also figure 6-1). Boroxol rings promote the formation of a low density network [147] and the fraction of B atoms belonging to these rings is thought to be as high as 75% [144]. In view of the importance of B_2O_3 as an archetypical oxide glass and the openness of the network under ambient conditions, there is considerable interest in the behaviour of B_2O_3 glass under pressure [145, 146]. There is not, however, any consensus on the nature of the network collapse but the most recent *in situ* x-ray scattering experiments show a considerable change in the intermediate range order [146] and in the coordination number of B at pressures above $\sim$ 8 GPa [145, 146].

High-pressure neutron diffraction has the potential for offering a new perspective on the structure of boron oxide glass since the neutron scattering lengths are $b(^{11}\mathrm{B}) = 6.65(4)$ and $b(\mathrm{O}) = 5.803$ fm [86] whereas the x-ray form factors are $f(\mathrm{B}) = 5$ and $f(\mathrm{O}) = 8$

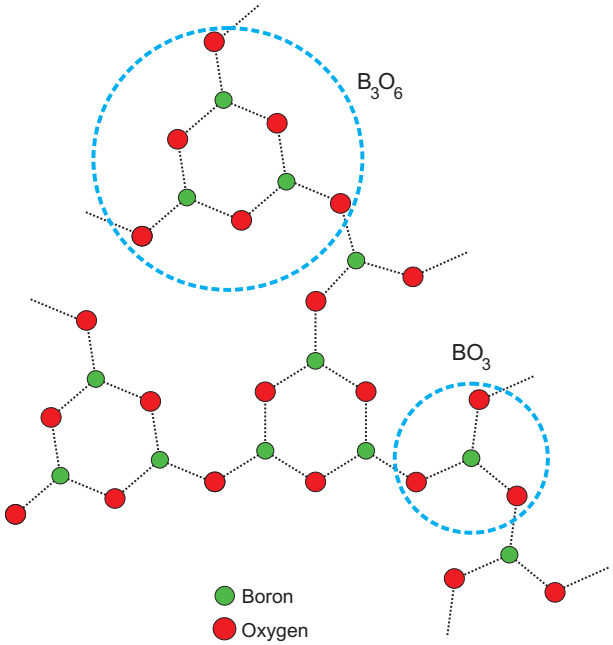

Figure 6-1: The structure of the B_2O_3 glassy network under ambient conditions where the BO_3 planar triangles and boroxol B_3O_6 groups have been highlighted. The green atoms represent B and the red atoms O.

electron units at a scattering vector $Q = 0$. The weighting functions for the B-B, B-O and O-O correlations are therefore 0.1876:0.4910:0.3214 for neutron diffraction versus 0.0865:0.4152:0.4983 for x-ray diffraction at $Q = 0$. High-pressure neutron diffraction experiments will therefore yield complementary information on the mechanisms of network collapse. Progress has been hampered, however, by the inherent difficulties associated with the necessary employment of small samples, the use of high-pressure apparatus which leads to detrimental background scattering, and the flux limitations associated with neutron diffraction by comparison with x-ray diffraction [57, 58]. The maximum pressure values that can be attained in neutron diffraction studies are still much lower than in complementary x-ray studies.

The work in this chapter takes advantage of developments in high-pressure neutron diffraction as applied to amorphous materials [13, 31, 154] to measure the structure factor of B_2O_3 glass *in situ* at pressures increasing from ambient to 17.5 GPa.

6.2 Theory

In a neutron diffraction experiment the total structure factor

$$F(Q) = \sum_{\alpha=1}^{n}\sum_{\beta=1}^{n} c_\alpha c_\beta b_\alpha b_\beta [S_{\alpha\beta}(Q) - 1] \tag{6.1}$$

is measured where α and β denote the chemical species, n is the number of different chemical species, c_α and b_α represent the atomic fraction and bound coherent scattering length of chemical species α, $S_{\alpha\beta}(Q)$ is a Faber-Ziman partial structure factor and Q is the magnitude of the scattering vector [10]. The corresponding real space information is represented by the total pair-distribution function $G(r)$ which is obtained from $F(Q)$ by using the Fourier transform relation

$$G(r) = \frac{1}{2\pi^2\rho r}\int_0^\infty F(Q)M(Q)\sin(Qr)QdQ \tag{6.2}$$

where ρ is the atomic number density of the glass and $M(Q)$ is a modification function defined by $M(Q) = 1$ for $Q \leq Q_{\max}$, $M(Q) = 0$ for $Q > Q_{\max}$. The latter is introduced because a diffractometer can measure only over a finite Q range up to a maximum value $Q_{\max}$. However, if $Q_{\max}$ is sufficiently large that $F(Q)$ no longer shows structure at high Q, then $G(r)$ follows from equation 6.1 by replacing each $S_{\alpha\beta}(Q)$ by its corresponding partial pair-distribution function $g_{\alpha\beta}(r)$.

6.3 Experimental procedure

B_2O_3 glassy samples were prepared from isotopically enriched (99.62 % ^{11}B and 0.38% ^{10}B, Ceradyne Inc.) in order to minimise the content of highly absorbing ^{10}B; ^{10}B has an absorption cross section of 3835 barn at a neutron wavelength of 1.798 Å as compared to ^{11}B which has an absorption cross section of 0.0055(33) barn [86]. To prepare glassy $^{11}B_2O_3$ approximately 5 g of $^{11}B_2O_3$ was first heated in a Pt (10 % Rh) crucible for 2 h at 200 °C in order to remove any moisture. The powder was then melted in air at 1000 °C for 45 min. To make samples for the D4c experiment, the melt was poured into the bottom part of a mould (kept at room temperature) made from P20 stainless tool steel (figure 6-2) and the top part was quickly closed while the melt was still soft. Usually the glass solidified quicker than we could fully close the mould which produced sample pellets with well shaped spherical caps but with a glassy sheet from the excess poured glass fused to the cylindrical part. Furthermore, because the melt was poured

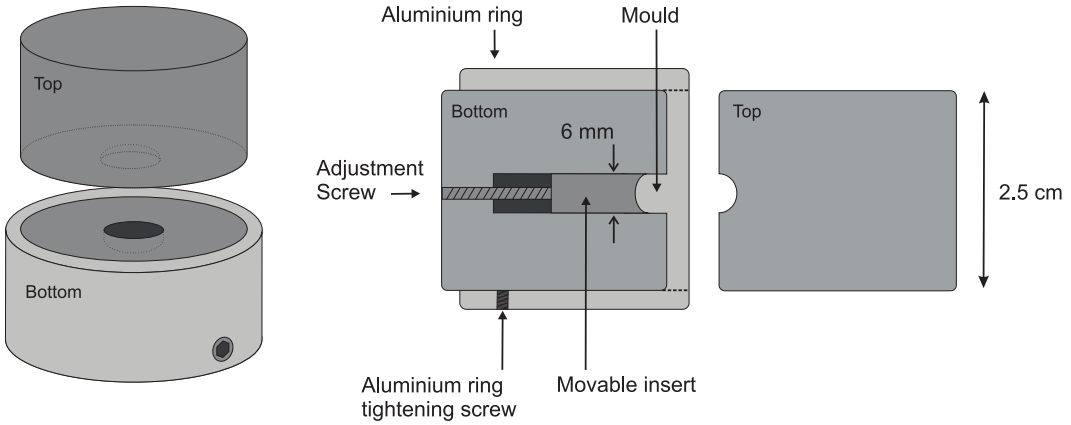

Figure 6-2: (Left and not to scale) A side representation of the mould. (Right and not to scale) Cross section of the stainless steel mould designed to make glassy pellets for single toroid geometry. The aluminium ring that encapsulates the bottom part of the stainless steel mould, and whose position can be adjusted, ensures that the top and bottom parts are in alignment. Once the glassy melt is poured over the bottom part of the mould both parts of the mould are quickly pushed together.

in excess, the heights of the pellets were usually larger than desired. The upper part of the spherical cap of the glassy sample had therefore to be shaped, and the glassy sheet removed by grinding with a rotary tool in an Ar filled glovebag in order to protect the sample from atmospheric moisture. The samples made for the PEARL experiment used a smaller type of stainless steel mould suited to the double toroid geometry [128]. The manufactured B_2O_3 pellets were always kept dry in an Ar filled glovebox.

The sample masses were close to the ideal values as defined by the anvil and gasket geometry (for D4c see Chapter 3, for PEARL see reference [128]). By using a Quantachrome gas pycnometer, the measured density of $^{11}B_2O_3$ glass was found to be 1.800(4) g cm^{-3} from which the ideal sample masses were calculated to be 0.1641 g for D4c and 0.06066 g for PEARL. The actual masses of the pellets were 0.1645(2) g for D4c and 0.06038(2) g for PEARL. The samples were held in gaskets made from a $Ti_{0.676}Zr_{0.324}$ alloy which has a zero coherent neutron scattering length. The load on the anvils was always increased during the course of a given high-pressure run. The pressure dependence of the number density of B_2O_3 glass, as obtained from several *in situ* studies [1, 7, 137, 146], is shown in figure 6-3. Also given is a fit to the data [146] using a third order Birch-Murnaghan equation of state given by [131]

$$P = \frac{3B_0}{2}\left[\left(\frac{V}{V_0}\right)^{-7/3} - \left(\frac{V}{V_0}\right)^{-5/3}\right]\left[1 + \frac{3}{4}(B_1 - 4)\left(\left(\frac{V}{V_0}\right)^{-2/3} - 1\right)\right] \qquad (6.3)$$

where V is the volume at pressure and V_0 is the volume under ambient conditions. The fitted parameters were found to be $B_0 = 12.31(7)$ GPa and $B_1 = 3.28(3)$, where B_0 is the bulk modulus at ambient conditions. This B_0 value compares to a measured value of $B_0 = 13.8$ GPa from reference [146].

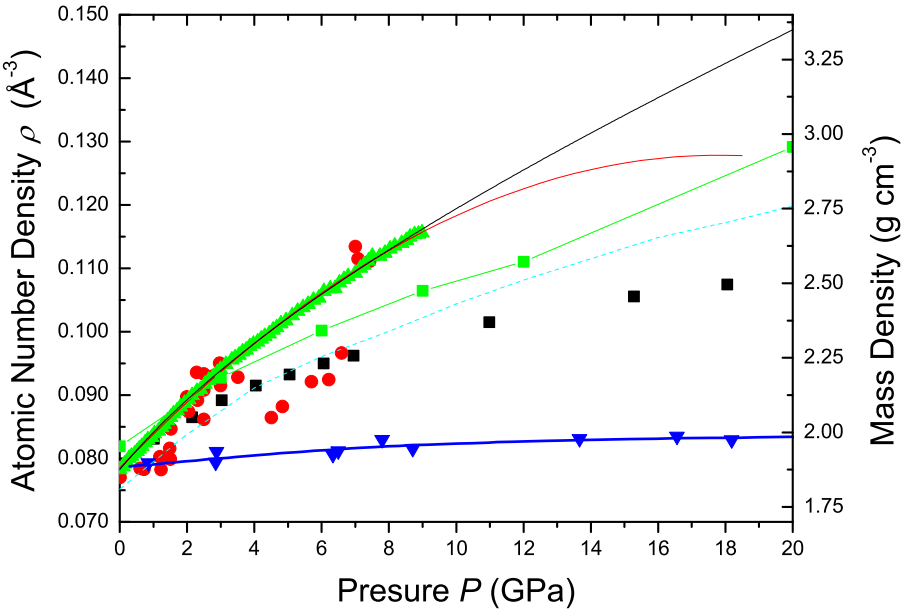

Figure 6-3: The density of B_2O_3 glass as (i) measured with increasing pressure in the experiments by Brazhkin *et al.* [146] (▲), or [155, 156] (●) using volumetric measurements for a small sample in a single toroid cell with a methanol-ethanol pressure transmitting medium or (ii) calculated from simulations (■) [146]; taken from the sound velocity measurements of Huang *et al.* [149] (■); taken from uniaxial measurements on a thin disk of B_2O_3 by Bridgman and Simon (▼) [1]; and taken from the simulations made by Takada *et al.* (- - -)[148]. The solid red (——) and black (——) curves are fits to the Brazhkin *et al.* data (▲) using a second order polynominal or a third order Birch-Murnaghan equation of state [131], respectively. The solid blue curve (——) shows a fit to the Bridgman and Simon (▼) data points [1].

The coherent neutron scattering lengths for the neutron diffraction experiments reported in this chapter are b_B= 6.624(4) fm and b_O= 5.803(4) fm [86] where the former takes into account the isotopic enrichment of the boron in the samples.

6.3.1 D4c high-pressure diffraction experiment

The D4c experiment employed a VX5/180 type PE press (piston area of 66.5 cm^2) with cubic BN anvils having a single-toroid profile [132] (Chapter 3) giving reliable access to pressures up to $\sim$ 8 GPa. The press was mounted so that the incident and scattered beams were in the same plane, perpendicular to the axis along which load

is applied to the anvils. Upon increasing the applied load, the sample position changes with piston displacement. The PE press was therefore mounted on a platform that could be translated vertically (z-axis drive) in order to centre the sample in the incident beam at each pressure point with the aid of an optical camera (Chapter 3). The background scattering was minimised by optimising the setup given in [31] (Chapter 3). The incident neutron wavelength of $\lambda = 0.4951(1)$ Å and zero scattering angle for the detectors were measured using Ni powder contained within an encapsulated $Ti_{0.676}Zr_{0.324}$ gasket [87] mounted in the PE press with no applied load. Higher order ($\lambda/2$) scattering was supressed by placing a Rh filter after the Cu(220) monochromator, upstream of the sample position.

Diffraction patterns were measured for (a) the sample in its Ti-Zr gasket at different pressures, (b) an unsquashed empty Ti-Zr gasket, (c) several empty Ti-Zr gaskets that had been recovered from different high pressures in order to estimate the gasket scattering under load (Chapter 3), and (d) the empty anvils. To assist in the data normalisation at different pressures, where the anvils have different separations, additional diffraction patterns were measured at ambient pressure for large and small vanadium pellets contained in unsquashed and recovered (i.e. previously squashed) Ti-Zr gaskets, respectively.

An ambient-pressure diffraction experiment was also made on a bulk sample of $^{11}B_2O_3$ glass. The sample was in the form of small glassy lumps and had a total mass of 0.96184 g. It was held in a vanadium can of diameter 5 mm and wall thickness 0.1 mm. The incident beam height was 5.0 cm and the neutron wavelength $\lambda = 0.49876$ Å. Diffraction patterns were taken for the sample in the can, the empty can, the empty instrument, and a cylindrical vanadium rod of diameter 6.072(6) mm for normalisation purposes. The data analysis followed the procedure described in Chapter 3. The sample pressure was deduced from the load applied to the anvils of the press using a calibration curve that has been extensively checked (figure 3-6, Chapter 3) [13, 31].

6.3.2 PEARL high-pressure diffraction experiment

The PEARL experiment employed a V3 variant of the PE press [32] (piston area of 102 cm^2) with sintered diamond anvils having a double-toroid profile that enables pressures in excess of 8 GPa to be reliably obtained. The press was mounted in a transverse geometry such that the incident beam was directed along the compression axis through the anvil mounted on the breach of the press, and the scattered beam was observed by detectors mounted at a scattering angle $2\theta \simeq 90°$. Upon increasing the applied load,

the sample position relative to the detectors changes with piston displacement. The press assembly for each pressure point was therefore moved using a motorized system to ensure that the sample was correctly centred in the diffractometer. The background scattering was minimised by using the setup described in [13].

Diffraction patterns were measured for an empty Ti-Zr gasket with a small applied load and for the sample in its gasket at several different pressures. To normalise the data sets, diffraction patterns were also measured for a piece of vanadium contained in a Ti-Zr gasket at comparable loads to the sample in order to match the sample geometry at each pressure point. The measurement protocol and data analysis procedure, including the use a Lorentzian function to extrapolate the measured $F(Q)$ functions to $Q = 0$ for use in equation 6.2, are described in detail in reference [13]. The sample pressure was determined from the load applied to the anvils by constructing a calibration curve based on the results obtained from several independent neutron diffraction experiments [13].

6.4 Results

The total structure factors $F(Q)$ for B_2O_3 glass measured using the D4c or PEARL instrument at pressures up to 17.5 GPa are plotted in figure 6-4. The corresponding Fourier transforms, the total pair distribution functions $G(r)$, are plotted in figure 6-5. The Fourier transformations were performed on Harwell spline fitted $F(Q)$ functions [52]. The key parameters describing the $F(Q)$ and $G(r)$ functions are given in table 6.1.

As seen in figure 6-4 there is good agreement between the patterns taken for the $^{11}B_2O_3$ glass sample in a vanadium can and for the samples measured in the pressure cell environment under ambient conditions. With increasing pressure, there is a reduction in height and shift of the first sharp diffraction peak (FSDP) initially at $\simeq 1.6$ Å^{-1} to a Q-value of $\simeq 2.1$ Å^{-1} at 8.2 GPa, which is seen using both the D4c and PEARL instruments. The principal peak (PP), which manifests itself as a weak broad feature in $F(Q)$ at $\simeq 3$ Å^{-1} under ambient conditions, does not grow to be a sharp feature with increasing pressure, but it does merge with the FSDP.

The B-O bond distance r_{BO} and coordination number $\bar{n}_B^O$, shown in figure 6-10, take values of 1.35(2) Å and 3.0(1) at ambient pressure. These values do not change until a pressure of 7.1 GPa is reached. Beyond this pressure point, the B-O distance r_{BO} increases to 1.37(2) Å at 8.2 GPa and continues to increase to 1.41(2) Å at 17.5 GPa. Meanwhile the coordination number $\bar{n}_B^O$ increases to 3.3(1) at 8.5 GPa and increases further to 3.9(1) at 17.5 GPa. The second peak in $G(r)$ at $r_2 = 2.37(2)$ Å under

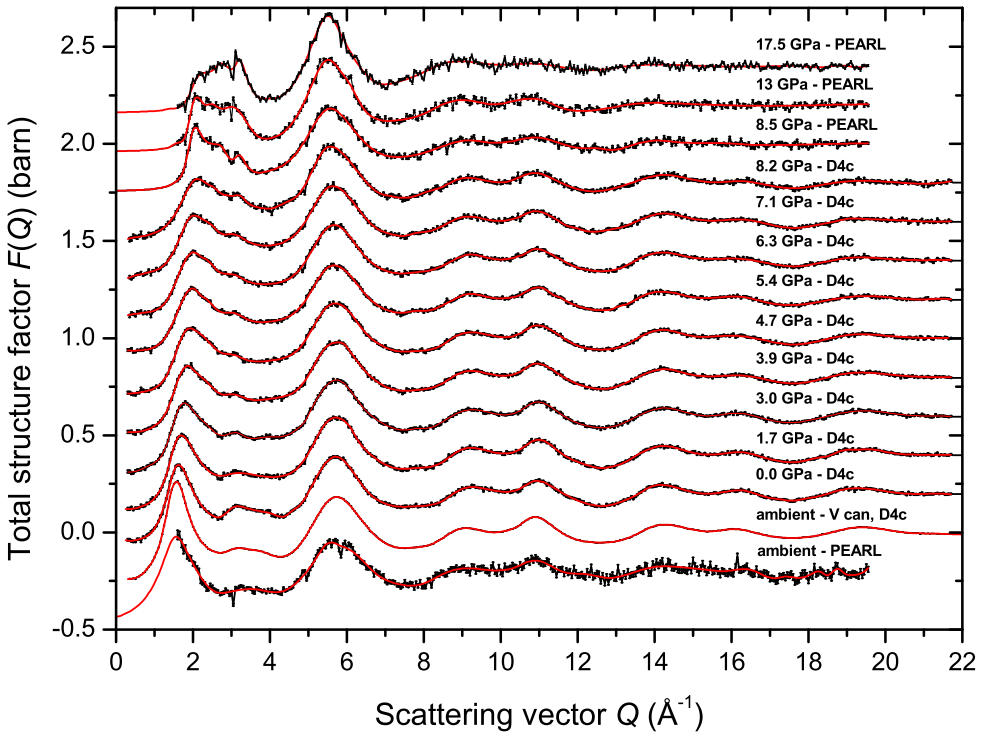

Figure 6-4: The pressure dependence of the total structure factor $F(Q)$ for B_2O_3 glass as measured using the D4c or PEARL diffractometer for samples held in a Paris-Edinburgh press. The results are compared to $F(Q)$ as measured for B_2O_3 glass in a vanadium can using D4c. The solid black curves (—) with vertical error bars represent the unsmoothed total structure factors, and the solid red curves (—) represent Harwell spline fitted data sets. For the PEARL experiments, the region $Q \leq 1.55$ Å^{-1} was not accessible and the solid red curves (—) for this region correspond to fitted Lorentzian functions (see reference [13]). The data sets measured using the PE press have been shifted vertically for clarity of presentation.

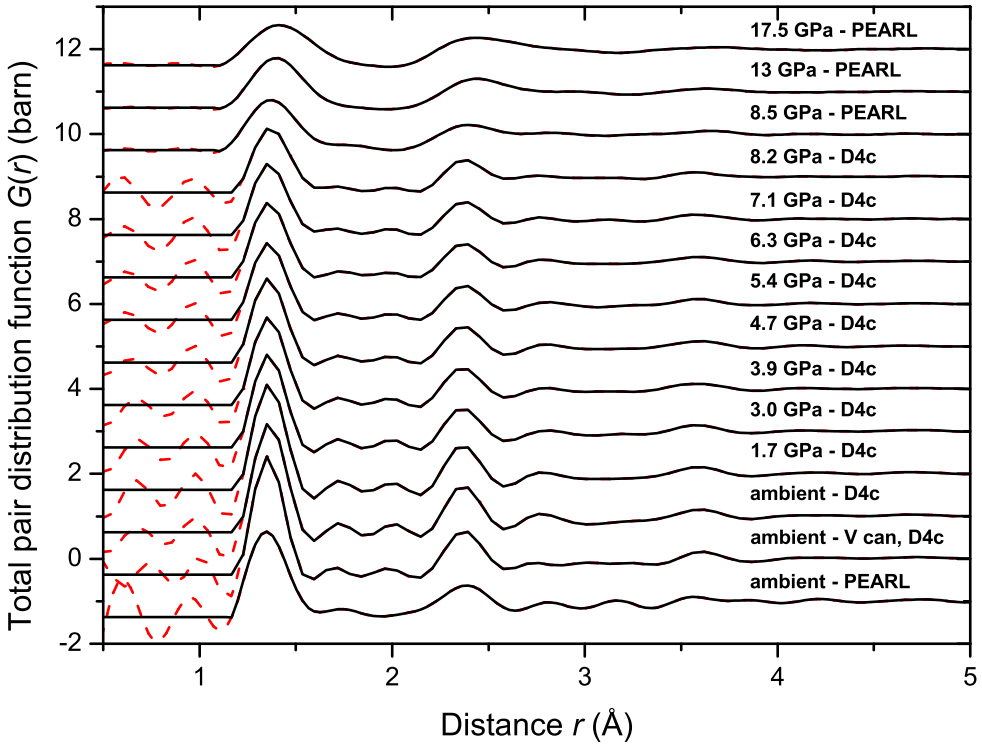

Figure 6-5: The pressure dependence of the total pair-distribution function $G(r)$ for B_2O_3 glass as measured using the D4c or PEARL diffractometer. The $G(r)$ functions were obtained by Fourier transforming the total structure factors $F(Q)$ shown by the solid red curves (——) in figure 6-4. The broken red curves (- - -) show the extent of the low r oscillations and the horizontal black curves (——) at low r give the calculated $G(0)$ limit.

ambient conditions is attributed primarily to nearest-neighbour O-O correlations. The ratio $r_2/r_{BO} = 1.74$ at ambient is consistent with the BO_3 units forming an equilateral triangle for which $r_2/r_{BO} = \sqrt{3} = 1.732$ is expected (table 6.1). This ratio does not vary to a great extent until the highest pressure of 17.5(5) GPa is attained, when its value of 1.70 gets closer to the value $r_2/r_{BO} = \sqrt{8/3} = 1.633$ expected for a regular tetrahedron.

A diffraction pattern was also taken for the B_2O_3 pellet recovered from a pressure of 8.2 GPa in the D4c experiment and the results are shown in figure 6-6. In reciprocal space the FSDP has been shifted to $Q = 1.86(2)$ Å^{-1} while the PP appears to have been completely removed. By plotting the FSDP position Q_{FSDP} against density ρ in figure 6-7, the density of the recovered sample can be estimated to be 0.0944 (Å^{-3}) which is 21% higher than the ambient pressure value. In the study by Brazhkin *et al.* [146], however, the density ρ of the recovered glass from $\sim$ 9 GPa was 6% higher than the ambient pressure value [146] as measured using *in situ* volumetric studies. The latter value for the density ρ was used to calculate the total pair distribution function $G(r)$ which is also shown in figure 6-6. The peak position r_{BO} and coordination number $\bar{n}_B^O$ for the recovered sample are the same as for the ambient pressure glass.

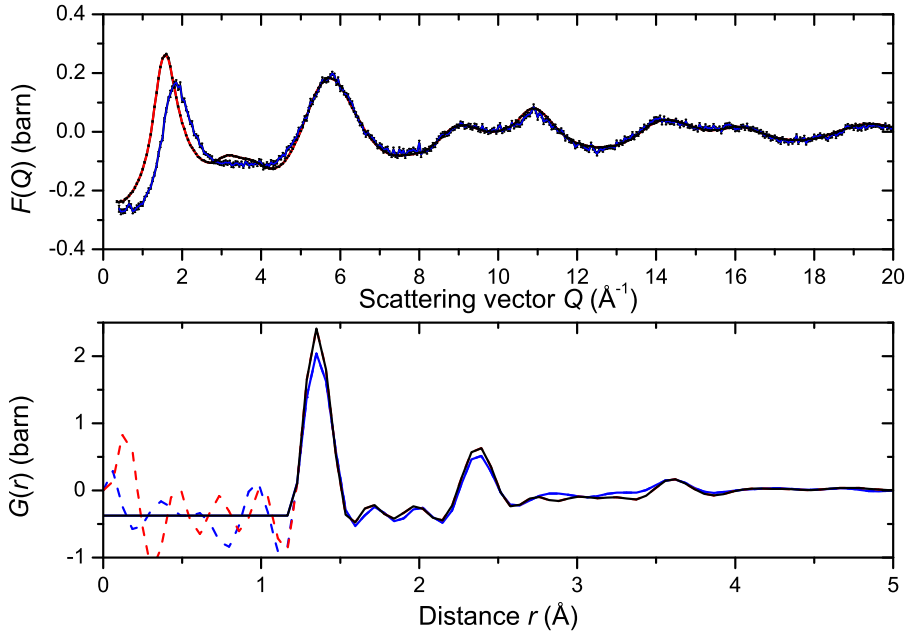

Figure 6-6: (a) The total structure factor $F(Q)$ for B_2O_3 glass as measured using the D4c diffractometer for a sample held in a vanadium can at ambient pressure (—) and a sample recovered from 8.2 GPa (—) measured in the Paris-Edinburgh press for one hour after pressure release. The solid black curves (—) with vertical error bars represent the unsmoothed total structure factors. (b) The total pair-distribution function $G(r)$ for B_2O_3 glass as measured using D4c. The $G(r)$ functions were obtained by Fourier transforming the total structure factors $F(Q)$ shown by the solid red (—) or solid blue (—) curve in (a). The solid red (- - -) or blue (- - -) curves show the extent of the low r oscillations and the horizontal red curve (—) at low r gives the calculated $G(0)$ limit.

Table 6.1: Parameters describing the pressure dependence of the structure of B_2O_3 glass as measured using the D4c or PEARL diffractometer. The number density ρ of the glass is given (fig. 6-4) together with the position Q_{FSDP} of the first sharp diffraction peak, the B-O bond distance r_{BO} as taken from the position of the first peak in $G(r)$, the mean B-O coordination number $\bar{n}_{\mathrm{B}}^{\mathrm{O}}$, the ratio r_2/r_{BO} where r_2 is the position of the second peak in $G(r)$, and the position of the third peak r_3. The density of the recovered sample was assumed to be 6% higher as found in the volumetric study by Brazhkin *et al.* [146]

P	Instrument	ρ	Q_{FSDP}	r_{BO}	r_2	r_3	r_2/r_{BO}	$\bar{n}_{\mathrm{B}}^{\mathrm{O}}$
GPa		Å^{-3}	Å^{-1}	Å	Å	Å		
Ambient	D4c V can	0.0782(1)	1.57(2)	1.35(2)	2.37(2)	3.61(1)	1.754(30)	3.0(1)
Ambient	D4c	0.0782(1)	1.62(2)	1.36(2)	2.37(2)	3.62(1)	1.741(30)	2.9(1)
Ambient	PEARL	0.0785(1)	1.56(2)	1.35(2)	2.39(2)	–	1.773(30)	3.0(1)
1.7(5)	D4c	0.0876(1)	1.70(2)	1.36(2)	2.37(2)	3.59(2)	1.741(30)	3.1(1)
3.0(5)	D4c	0.0938(1)	1.78(2)	1.36(2)	2.37(2)	3.58(2)	1.742(30)	3.0(1)
3.9(5)	D4c	0.0977(1)	1.86(2)	1.36(2)	2.36(2)	3.58(2)	1.741(30)	3.0(1)
4.7(5)	D4c	0.1010(1)	1.92(2)	1.36(2)	2.37(2)	3.60(2)	1.746(30)	3.0(1)
5.4(5)	D4c	0.1040(1)	1.99(2)	1.36(2)	2.38(2)	3.59(2)	1.750(30)	3.0(1)
6.3(5)	D4c	0.1067(1)	2.01(2)	1.36(2)	2.37(2)	3.60(2)	1.747(30)	3.0(1)
7.1(5)	D4c	0.1096(1)	2.03(2)	1.36(2)	2.38(2)	3.58(1)	1.748(30)	3.0(1)
8.2(5)	D4c	0.1134(1)	2.12(2)	1.37(2)	2.38(2)	3.57(2)	1.739(30)	3.0(1)
8.5(5)	PEARL	0.1145(1)	2.09(2)	1.37(2)	2.40(2)	–	1.750(30)	3.3(1)
13.0(5)	PEARL	0.1166(1)	–	1.40(2)	2.43(2)	–	1.735(30)	3.7(1)
17.5(5)	PEARL	0.1279(1)	–	1.41(2)	2.43(2)	–	1.704(30)	3.9(1)
Recovered	D4c	0.0829(1)	1.82(2)	1.36(2)	2.38(2)	3.61(2)	1.750(30)	3.0(1)

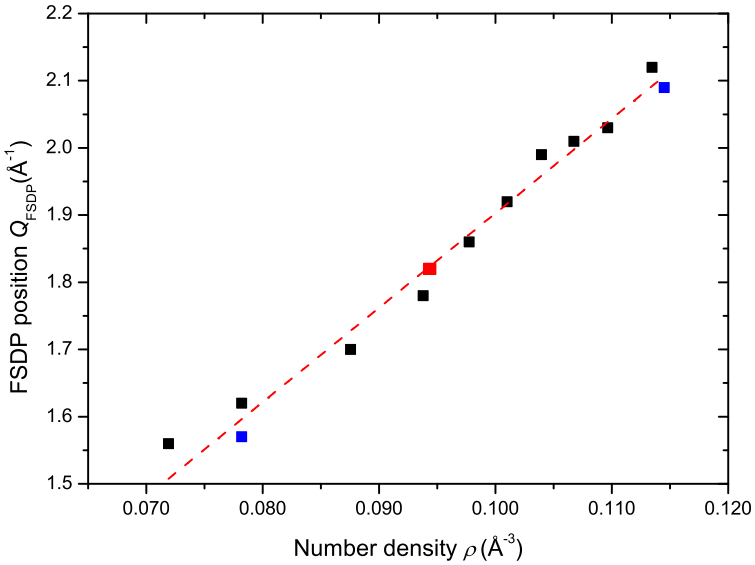

Figure 6-7: The FSDP position Q_{FSDP} as a function of B_2O_3 glass density as measured using the D4c (■) and PEARL (■) diffractometers. An estimate for the recovered sample density ρ (■) is found from the straight line fit (- - -) and corresponds to the measured position $Q_{\mathrm{FSDP}} = 1.82(2)$ Å^{-1}.

6.5 Discussion

The evolution in the position of the FSDP Q_{FSDP} with pressure is shown in figure 6-8, where the data points from D4c and PEARL are compared to the x-ray diffraction results of Brazhkin *et al.* [146] who used a cubic-type multi-anvil press. The FSDP merges with the PP at high pressures and beyond $\sim$ 8.5 GPa it is difficult to distinguish between them in both the neutron figure 6-4 and x-ray (figure 6-9) diffraction work. The values of Q_{FSDP} seen by neutron and x-ray diffraction are different at each pressure point, but each data set shows a linear increase with pressure with $dQ_{\mathrm{FSDP}}/dP = 0.062(3)$ (Å GPa)$^{-1}$ for the neutron diffraction data and $dQ_{\mathrm{FSDP}}/dP = 0.081(5)$ (Å GPa)$^{-1}$ for the x-ray diffraction data.

A sharpening of the principal peak in the total x-ray structure factor at $\sim$ 3 Å^{-1} with increasing pressure is seen in figure 6-9 [146], and is accompanied by a decrease in height of the FSDP as it moves to higher Q values. A decrease in height of the FSDP peak is also seen in the present neutron diffraction work. This behaviour is similar to that observed for tetrahedral glass forming systems such as GeO_2 [13, 31] (Chapter 4), SiO_2 [121] (Chapter 5), $GeSe_2$ [138] (Chapter 7) and GeS_2 [126] and is a signature that the glass fragility increases with pressure [90].

The dependence of the coordination number $\bar{n}_{\mathrm{B}}^{\mathrm{O}}$ and bond distance r_{BO} on pressure is shown in figure 6-10 where the present neutron diffraction results are compared to the x-ray diffraction results of Brazhkin *et al.* [146] and to the inelastic x-ray scattering results of Lee *et al.* where the sample was held in a diamond anvil cell [145]. The results from the D4c experiment show that $\bar{n}_{\mathrm{B}}^{\mathrm{O}}$ and r_{BO} do not change at pressures below 8 GPa within the experimental error. The onset of a coordination number change at 8.5 GPa is seen from the PEARL results. In the experiment by Lee *et al.* [145] changes in the absorption spectra were interpreted in terms of a sharp increase in the B-O coordination number, with $\bar{n}_{\mathrm{B}}^{\mathrm{O}} = 3.5(2)$ at a pressure of 7 GPa, but no data was collected by these authors in the range 4-7 GPa. The pressure at which the structural motifs in B_2O_3 glass become fully tetrahedral was estimated by Lee *et al.* [145] to be around $\sim$23 GPa. The molecular dynamics simulations made by Brazhkin *et al.* [146] and Takada *et al.* [148] reproduce the measured $\bar{n}_{\mathrm{B}}^{\mathrm{O}}$ values in the pressure regime below 8 GPa but do not reproduce the change this coordination number sees by both neutron and x-ray scattering at pressures $\gtrsim$ 8 GPa. Moreover, these simulations do not reproduce the pressure-volume equation of state for B_2O_3 as shown in figure 6-3. Simulations of B_2O_3 under pressure are difficult because the high quench rates used in the simulations prevent the formation of glassy structures with a substantial fraction of boroxol rings.

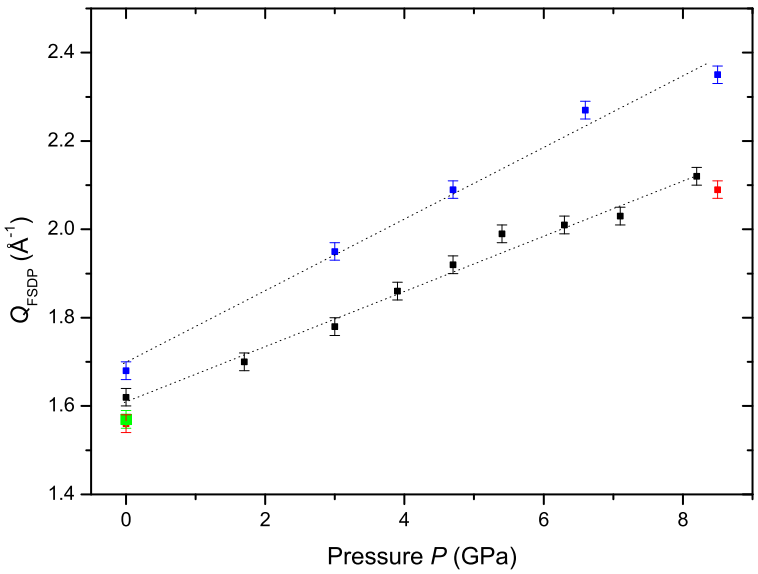

Figure 6-8: The pressure dependence of the position of the first sharp diffraction peak Q_{FSDP} in the total structure factor for B_2O_3 glass as measured using neutron and X-ray diffraction. The results from the D4c (■) and PEARL (■) diffractometers are compared to those obtained from the x-ray diffraction experiments made by Brazhkin *et al.* (■) [146]. The black dotted curves $(\cdots)$ show fitted straight lines, having a gradient $dQ_{\mathrm{FSDP}}/dP = 0.062(3)$ (Å GPa)$^{-1}$ for the neutron diffraction data and $dQ_{\mathrm{FSDP}}/dP = 0.081(5)$ (Å GPa)$^{-1}$ for the x-ray diffraction data. Note that for pressures beyond 8.5 GPa it is difficult to determine the position Q_{FSDP} as the FSDP merges with the principal peak in both the neutron (figure 6.1) and x-ray (figure 6-9) diffraction studies.

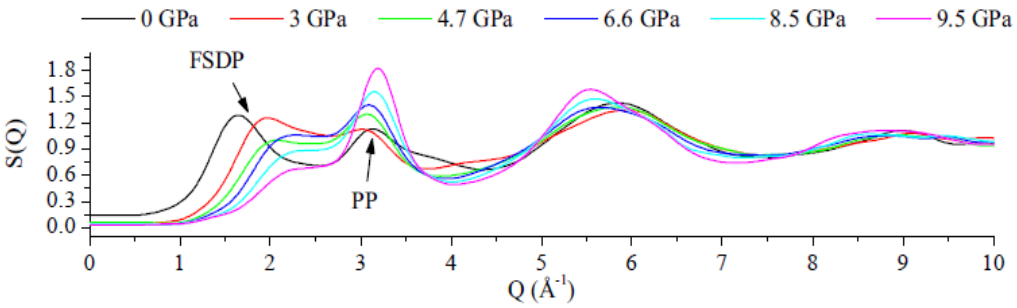

Figure 6-9: The pressure dependence of the total x-ray structure factor $S(Q)$ as measured by Brazhkin *et al.* using cubic-type multi-anvil press [146].

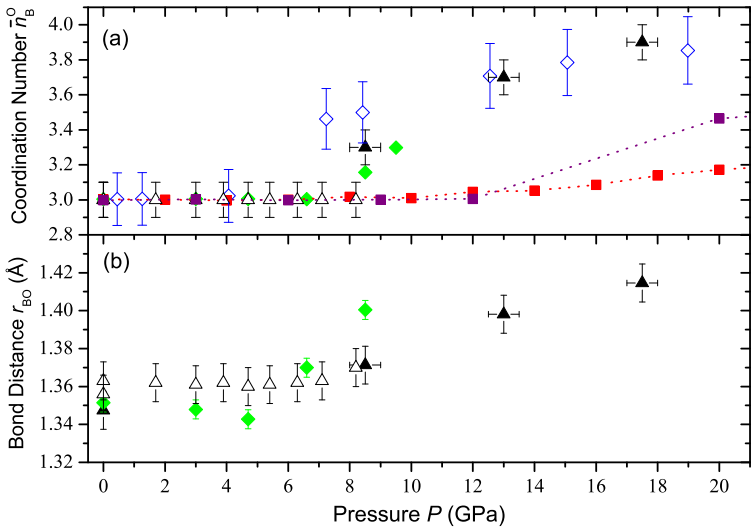

Figure 6-10: The pressure dependence of (a) the mean B-O coordination number $\bar{n}_B^O$ and (b) the bond length r_{BO} as measured in the present neutron diffraction work using the D4c (△) or PEARL (▲) diffractometers, in the x-ray diffraction work of Brazkin *et al.* (–♦–) [146], or in the inelastic x-ray diffraction experiments made by Lee *et al.* (◇) [145]. Results are also given for the molecular dynamics simulations made by Brazhkin *et al.* (–■–) [146], and Takada *et al.* (–■–) [148].

The present neutron diffraction study, and the x-ray diffraction work by Brazhkin *et al.* [146], support a two stage densification process for B_2O_3 glass (see figure 6-10). First, at pressures from ambient to 8 GPa structural changes occur on an intermediate range that involve a rearrangement of planar BO_3 motifs. Second, as the pressure is increased beyond 8 GPa, there is an increase in the B-O coordination number $\bar{n}_B^O$ accompanied by an increase in the nearest neighbour B-O distance. For the first pressure range *in situ* Raman and Brillouin investigations by Nicolas *et al.* [143] and *in situ* Raman investigations by Grimsditch *et al.* [11] associate, in each study, the densification mechanism with a collapse of boroxol rings in the glass network as indicated by the disappearance of the boroxol ring breathing mode at a wavenumber of 808 cm^{-1} in the Raman spectra.

A closer inspection of the evolution of the D4c measured $G(r)$ functions in the region beyond the first peak at ambient and at a pressure of 8.2 GPa, is given in figures 6-11 and 6-12. D4c data is preferred for this type of comparison because it covers a larger Q range ($Q_{max} \sim 22$ Å^{-1}) and it has better counting statistics, leading to better r space resolution as compared to the $G(r)$ functions obtained from the PEARL instrument. The observed changes between ambient pressure and 8.2 GPa are subtle. Simple geometrical considerations reveal that it is difficult to distinguish/resolve between those

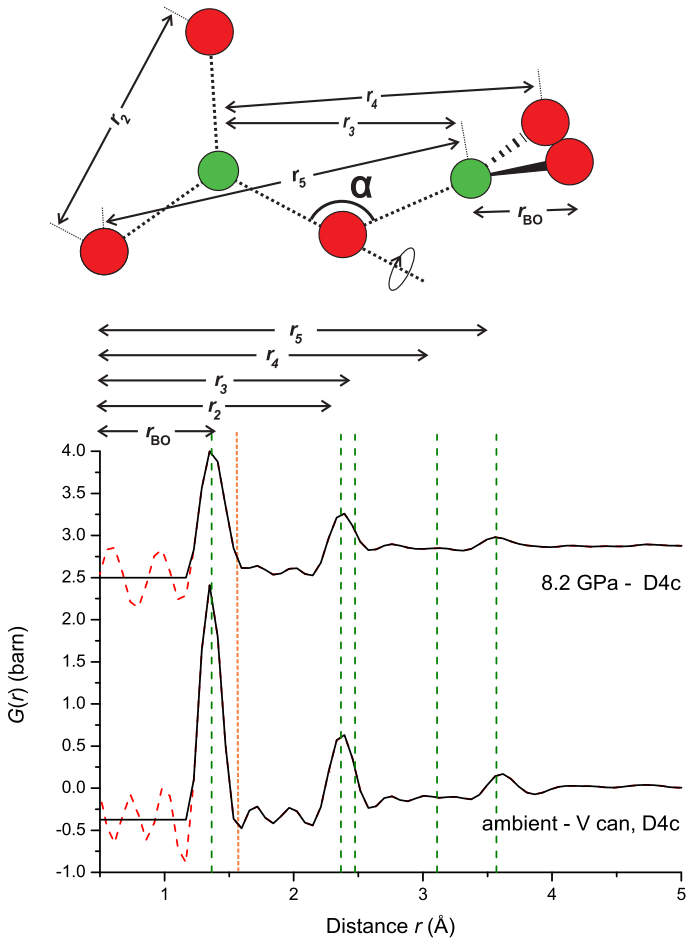

Figure 6-11: A schematic representing possible r_i atomic distances between two adjacent BO_3 units as aligned to make a ∠ BOB angle of $\alpha = 130°$ [14, 152]. The ↻ symbol indicates that the adjacent BO_3 unit can can be rotated freely around the B-O bond. The corresponding features in the measured $G(r)$ functions at ambient pressure and at a pressure of 8.2 GPa are indicated by the vertical green dashed lines (- - -). A vertical orange dashed line (- - -) corresponds to the largest distance $r_{BO} = 1.512$ Å belonging to a disordered BO_4 tetrahedron in a crystalline sample of B_2O_3-II [157].

atomic correlations that occur between planar BO_3 triangles connected via a bridging oxygen atom figure 6-11 and those that occur within a B_3O_6 boroxol ring (figure 6-12) because the average distances are very similar. The B-O, O-O and B-B distances r_k were calculated for one case of freely connected BO_3 units by assuming that the adjacent units are normal to one another and that the bridging oxygen subtends an angle $\angle$ BOB of 130° [14, 152]. The calculated distances are given in table 6.2 where they are compared to equivalent distances obtained for boroxol rings. The largest distance

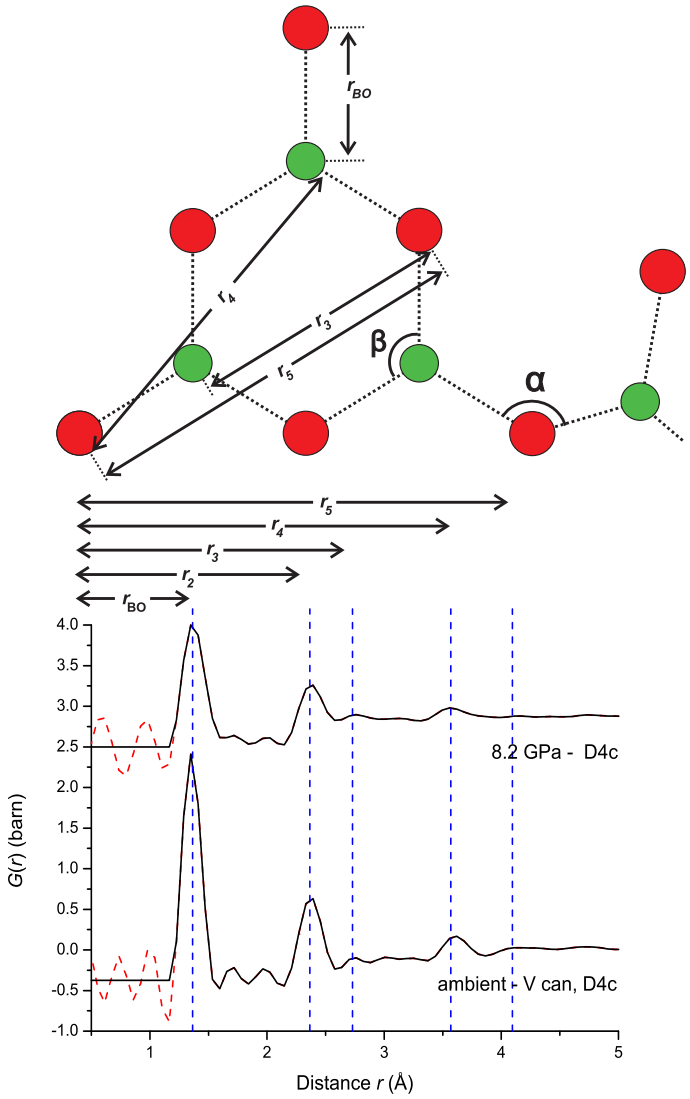

Figure 6-12: A schematic representing possible r_i atomic distances within a boroxol ring unit. The corresponding features in the measured $G(r)$ functions at ambient pressure and at a pressure of 8.2 GPa are indicated by the vertical blue dashed lines (- - -).

r_{BO} = 1.512 Å belonging to a disordered BO_4 tetrahedron in crystalline B_2O_3-II [157] is also indicated in figure 6-11 for comparison with the $G(r)$ functions.

Table 6.2: The calculated distances shown in figures 6-11 and 6-12 at ambient pressure. The distances marked with a star * corresponds to one of the possible configurations in which the planes of adjacent BO_3 triangles are normal to one other and the angle $\angle$ BOB subtended by the bridging oxygen atom is 130° [14, 152].

Adjacent BO_3 units			
Distance r_k	Type $i-j$	r_k/r_{BO}	r_k (Å)
r_1	B-O	1	1.365
r_2	O-O	$\sqrt{3}$	2.364
r_3	B-B	$2\sin(\alpha/2)$	2.474
r_4	O-O	–	3.106*
r_5	B-O	–	3.569*
Boroxol ring			
Distance r_k	Type $i-j$	r_{ij}/r_{BO}	r_k (Å)
r_1	B-O	1	1.365
r_2	B-B	$\sqrt{3}$	2.364
	O-O		
r_3	B-O	2	2.730
r_4	B-O	$\sqrt{7}$	3.611
r_5	O-O	3	4.095

To try to deduce the fraction f of boron atoms in boroxol groups the $QF(Q)$ functions measured using D4c were fitted using the approach described by Hannon *et al.* [14]. However, the data sets did not show a large variation with pressure in the $5 \leq Q(\text{Å}^{-1}) \leq 20$ region where the data are predicted to be most sensitive to the fraction f of boroxol rings in the glass (see figure 6-13).

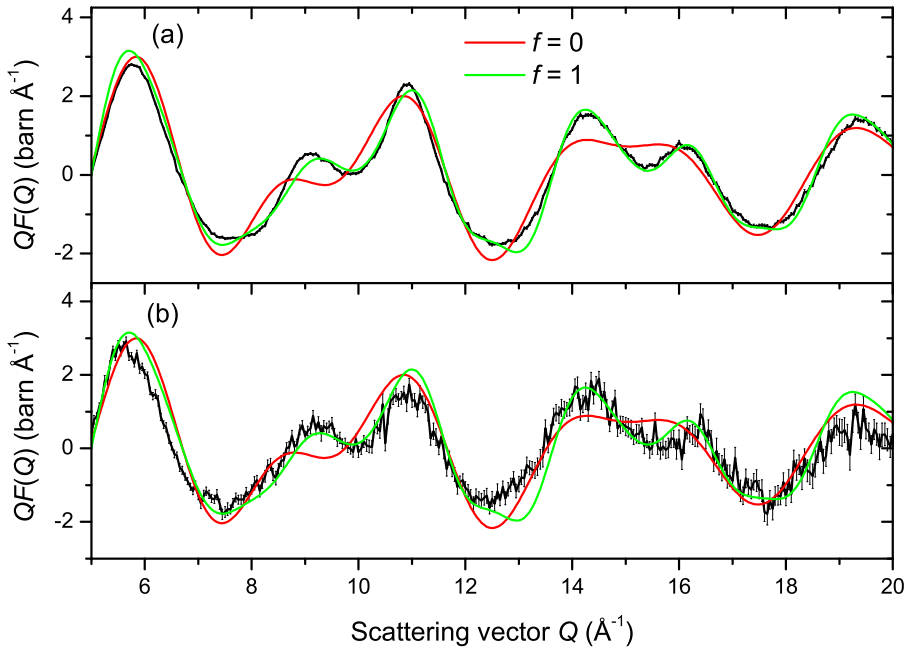

Figure 6-13: The $QF(Q)$ functions measured using D4c (—) at (a) ambient pressure and (b) 8.2 GPa as compared to the calculated $QF(Q)$ functions using the approach described by Hannon *et al.* [14] for a fraction $f = 0$ (—) or $f = 1$ (—) of boron atoms belonging to boroxol rings.

6.6 Conclusions

Accurate neutron total structure factors $F(Q)$ have been measured for glassy B_2O_3 at pressures up to 17.5 GPa using two variants of the Paris-Edinburgh press. The pressure dependence of the first sharp diffraction peak position Q_{FSDP}, the mean nearest neighbour B-O bond distance and the nearest neighbour coordination number $\bar{n}_{\mathrm{B}}^{\mathrm{O}}$ are in agreement with the x-ray diffraction work by Brazkin *et al.* [146] and Lee *et al.* [145] in the pressure range between ambient and $\sim$ 10 GPa. The principal mechanism for the densification of B_2O_3 up to $\sim$ 8 GPa, as seen by both neutron and x-ray diffraction, occurs through rearrangements of the planar BO_3 motifs, which change the intermediate range as manifested by a reduction of the FSDP intensity and a shift towards higher Q values in the measured total structure factors $F(Q)$. This densification mechanism is supported by the *in situ* Raman and Brillouin investigations by Nicolas *et al.* [143] and *in situ* Raman investigations by Grimsditch *et al.* [11] where the network collapse is associated with a break down of boroxol rings in the glass as indicated by the disappearance of the boroxol ring breathing mode in the Raman spectra at a wavenumber of 808 cm^{-1}. At higher pressures ($>$ 8 GPa) the densification of B_2O_3 further proceeds via the appearance of 4-fold coordinated boron atoms which leads to increases in the average coordination number $\bar{n}_{\mathrm{B}}^{\mathrm{O}}$ and the average B-O bond distance r_{BO}. Existing molecular dynamics simulations [146, 148] do not reproduce the measured B-O coordination number change with increasing density due to the difficulty in simulating boroxol rings. Moreover, the available molecular dynamics simulations do not give a sufficiently large fraction of boroxol rings for the ambient pressure glass, and they do not therefore give a realistic description of the changes in the glass structure with increasing density.

To fully understand/ellucidate the role of boroxol rings in the densification of B_2O_3 glass, it is desirable to conduct further *in situ* x-ray diffraction experiments that span the pressure range of the new neutron diffraction measurements, and to make new molecular dynamics studies that give results that are in better agreement with diffraction data.

Chapter 7

Network collapse in amorphous $GeSe_2$ at high pressures

7.1 Introduction

$GeSe_2$ is an archetypal network forming glass that has been long the subject of both experimental and theoretical interest, and has a framework that can be collapsed by the application of pressure [5, 158, 159]. Chalcogenide glasses, in contrast to their much studied oxide counterparts, can be readily made for non-stoichiometric compositions [160] which points to flexibility in character of the network-forming structural motifs (i.e. enhanced structural variability [161, 162]) and flags the potential for different densification mechanisms. A prototype is provided by $GeSe_2$ glass where the ambient pressure network is built from a mixture of corner-sharing (CS) and edge-sharing (ES) tetrahedral units, with a large fraction of homopolar bonds which indicate a departure from perfect chemical ordering [163–167]. This is in stark contrast to archetypical oxide glasses such as GeO_2 and SiO_2 (see also Chapter 4 and 5) where the starting network is chemically ordered and built solely from CS tetrahedra [94, 168]. The nature of the density-driven network collapse in $GeSe_2$ glass is, however, uncertain. Different experimental results at pressures up to ~ 9 GPa were interpreted in terms of either (i) a continuous change in which the Ge-Se coordination number steadily increases with pressure as there is a replacement of corner-sharing tetrahedra by edge-sharing tetrahedra [138, 169] or (ii) no significant structural modification [170]. A semiconductor-glass to metal-crystal transition has also been reported at a pressure $P \simeq 7$ GPa [171]. In the liquid phase, the transformation at $P \sim 2.5$ GPa from a 2-D to 3-D network is inferred from x-ray diffraction data [172].

In this Chapter *in situ* high-pressure neutron diffraction is used to unveil the structure of $GeSe_2$ glass from ambient pressure up to $P \sim 16$ GPa, where enhanced information is accessed by applying the isotope substitution method to simplify the complexity of correlations associated with a single diffraction pattern (see Chapter 4 and reference [173]). The experimental work is complemented by first-principles molecular dynamics (FPMD) [174] simulations, an approach that is necessary for iono-covalently bonded Ge-Se systems in which the different chemical species have comparable electronegativities [167, 175–177]. The combined techniques yield a self-consistent picture in which there is a threshold pressure of $\gtrsim 8.5$ GPa below which there is no change in the mean coordination number $\bar{n}$ but an interplay between the fractions of CS and ES tetrahedra. At pressures beyond this threshold, densification proceeds by the formation of 5- and 6-fold coordinated Ge atoms, leading to larger fractions of ES polyhedra along with 3-, 4- and 5-fold coordinated Se atoms. On initial formation, large proportions of the higher coordinated Ge and Se atoms contain homopolar bonds, i.e. these defects mediate the density-driven structural transformations in $GeSe_2$ glass.

7.1.1 Theory

The total structure factor $F(Q)$ measured in a neutron diffraction experiment on a multicomponent glassy system can be written as:

$$F(Q) = \sum_{\alpha=1}^{n} \sum_{\beta=1}^{n} c_\alpha c_\beta b_\alpha b_\beta [S_{\alpha\beta}(Q) - 1], \tag{7.1}$$

where n is the number of different chemical species α or β, c_α and b_α are the concentration and coherent scattering length of species α, respectively, $S_{\alpha\beta}(Q)$ is a Faber-Ziman partial structure factor, and Q is the magnitude of the scattering vector.

Suppose that diffraction patterns are measured for three samples of $GeSe_2$ glass that are identical in every respect, except for their Ge or Se isotopic enrichments. If the samples are $^{70}Ge^{N}Se_2$, $^{N}Ge^{N}Se_2$ and $^{73}Ge^{76}Se_2$ then the total structure factors ${}^{70}_{N}F(Q)$, ${}^{N}_{N}F(Q)$ and ${}^{73}_{76}F(Q)$ are measured, respectively, where 70 and 73 denote glassy samples with highly enriched Ge isotopes ($\geq 96\%$), 76 denotes a glassy sample with highly enriched ^{76}Se isotope and N denotes the natural isotopic abundance. The total structure factor ${}^{N}_{N}F(Q)$ can, for example, be written as:

$${}^{N}_{N}F(Q) = {}^{N}_{N}A[S_{GeSe}(Q) - 1] + {}^{N}_{N}B[S_{GeGe}(Q) - 1] + {}^{N}_{N}C[S_{SeSe}(Q) - 1], \tag{7.2}$$

where ${}^{N}_{N}A \equiv 2c_{Ge}c_{Se}b_{^{N}Se}b_{^{N}Ge}$, ${}^{N}_{N}B \equiv c^2_{Ge}b^2_{^{N}Ge}$ and ${}^{N}_{N}C \equiv c^2_{Se}b^2_{^{N}Se}$ are weighting factors

whose values are given in table 7.1. The complexity of correlations associated with a single total structure factor can be simplified by forming first difference functions. For example, by taking the two most contrasting total structure factors ${}^{70}_{\rm N}F(Q)$ and ${}^{73}_{76}F(Q)$, the Ge-Ge correlations can be eliminated by forming the first difference function $\Delta F_{\rm Se}(Q)$ defined as:

$$\begin{aligned}\Delta F_{\rm Se}(Q) &\equiv {}^{73}_{76}F(Q) - \frac{b^2_{^{73}\rm Ge}}{b^2_{^{70}\rm Ge}}\ {}^{70}_{\rm N}F(Q) \\ &= D[S_{\rm GeSe}(Q)-1] + E[S_{\rm SeSe}(Q)-1], \end{aligned} \tag{7.3}$$

where $D = 2c_{\rm Ge}c_{\rm Se}[b_{^{73}\rm Ge}b_{^{76}\rm Se} - \frac{b^2_{^{73}\rm Ge}}{b^2_{^{70}\rm Ge}}b_{^{70}\rm Ge}b_{^{\rm N}\rm Se}]$ and $E = c^2_{\rm Se}[b^2_{^{76}\rm Se} - \frac{b^2_{^{73}\rm Ge}}{b^2_{^{70}\rm Ge}}b^2_{^{\rm N}\rm Se}]$. Similarly, the Se-Se correlations can be removed by forming the first difference function $\Delta F_{\rm Ge}(Q)$ defined as:

$$\begin{aligned}\Delta F_{\rm Ge}(Q) &\equiv {}^{70}_{\rm N}F(Q) - \frac{b^2_{^{\rm N}\rm Se}}{b^2_{^{76}\rm Se}}\ {}^{73}_{76}F(Q) \\ &= F[S_{\rm GeSe}(Q)-1] + G[(S_{\rm GeGe}(Q)-1], \end{aligned} \tag{7.4}$$

where $F = 2c_{\rm Ge}c_{\rm Se}[b_{^{70}\rm Ge}b_{^{\rm N}\rm Se} - \frac{b^2_{^{\rm N}\rm Se}}{b^2_{^{76}\rm Se}}\ b_{^{73}\rm Ge}b_{^{76}\rm Se}]$ and $G = c^2_{\rm Ge}[b^2_{^{70}\rm Ge} - \frac{b^2_{^{\rm N}\rm Se}}{b^2_{^{76}\rm Se}}\ b^2_{^{73}\rm Ge}]$. Finally, the Ge-Se correlations can be removed by forming the first difference function $\Delta F_{\rm Se'}(Q)$ defined as:

$$\begin{aligned}\Delta F_{\rm Se'}(Q) &= {}^{73}_{76}F(Q) - \frac{b_{^{73}\rm Ge}b_{^{76}\rm Se}}{b_{^{70}\rm Ge}b_{^{\rm N}\rm Se}}\ {}^{70}_{\rm N}F(Q) \\ &= H[S_{\rm GeGe}(Q)-1] + I[S_{\rm SeSe}(Q)-1], \end{aligned} \tag{7.5}$$

where $H = c^2_{\rm Ge}[b^2_{^{73}\rm Ge} - \frac{b_{^{73}\rm Ge}b_{^{76}\rm Se}}{b_{^{70}\rm Ge}b_{^{\rm N}\rm Se}}\ b^2_{^{70}\rm Ge}]$ and $I = c^2_{\rm Se}[b^2_{^{76}\rm Se} - \frac{b_{^{73}\rm Ge}b_{^{76}\rm Se}}{b_{^{70}\rm Ge}b_{^{\rm N}\rm Se}}\ b^2_{^{\rm N}\rm Se}]$. The weighing coefficients for the $S_{\alpha\beta}(Q)$ are tabulated in table 7.1 and were calculated using coherent scattering length values of $b_{^{70}\rm Ge} = 10.0(1)$, $b_{^{73}\rm Ge} = 5.09(4)$, $b_{^{\rm N}\rm Se} = 7.970(9)$ and $b_{^{76}\rm Se} = 12.2(1)$ fm [86], which correspond to the isotopic enrichments of the samples used. The atomic fractions of Ge and Se are $c_{\rm Ge} = 1/3$ and $c_{\rm Se} = 2/3$, respectively.

The real space functions $G(r)$, $\Delta G_{\rm Ge}(r)$, $\Delta G_{\rm Se}(r)$ and $\Delta G_{\rm Se'}(r)$, where r is a distance in real space, are obtained by using the following Fourier transform relations:

Table 7.1: The weighting factors in units of barns (10^{-28} m^2) for the Ge-Se, Ge-Ge and Se-Se partial structure factors in the measured total and difference functions defined by equations (7.1) to (7.5). The numerical vales take into account the isotopic enrichments of the samples used in the experiments.

	$S_{\mathrm{GeSe}}(Q)$(barns)	$S_{\mathrm{GeGe}}(Q)$(barns)	$S_{\mathrm{SeSe}}(Q)$(barns)
${}^{70}_{\mathrm{N}}F(Q)$	0.354(4)	0.1111(22)	0.2823(6)
${}^{\mathrm{N}}_{\mathrm{N}}F(Q)$	0.2899(8)	0.0744(4)	0.2823(6)
${}^{73}_{76}F(Q)$	0.276(3)	0.0288(5)	0.662(11)
$\Delta F_{\mathrm{Se}}(Q)$	0.184(3)	0.000(6)	0.588(11)
$\Delta F_{\mathrm{Ge}}(Q)$	0.236(4)	0.099(2)	0.000(7)
$\Delta F_{\mathrm{Ge'}}(Q)$	0.000(22)	-0.057(14)	0.442(11)

$$
\begin{aligned}
G(r) &= \frac{1}{2\pi^2 r\rho}\int_0^\infty QF(Q)M(Q)\sin(Qr)dQ \\
\Delta G_{\mathrm{Se}}(r) &= \frac{1}{2\pi^2 r\rho}\int_0^\infty Q\Delta F_{\mathrm{Se}}(Q)M(Q)\sin(Qr)dQ \\
\Delta G_{\mathrm{Ge}}(r) &= \frac{1}{2\pi^2 r\rho}\int_0^\infty Q\Delta F_{\mathrm{Ge}}(Q)M(Q)\sin(Qr)dQ \\
\Delta G_{\mathrm{Se'}}(r) &= \frac{1}{2\pi^2 r\rho}\int_0^\infty Q\Delta F_{\mathrm{Se'}}(Q)M(Q)\sin(Qr)dQ
\end{aligned}
\tag{7.6}
$$

where ρ is the atomic number density and $M(Q)$ is a modification function defined by $M(Q)$=1 for $Q \leq Q_{\max}$, $M(Q) = 0$ for $Q > Q_{\max}$ which is introduced because a diffractometer can measure only over a finite Q range up to maximum value $Q_{\max}$. The relevant $G(r)$ or $\Delta G_{\mathrm{X}}(r)$ functions, with X = {Se, Ge or Se$'$}, are obtained by replacing each $S_{\alpha\beta}(Q)$ by its corresponding partial pair distribution function $g_{\alpha\beta}(r)$ in the equations for $F(Q)$ or $\Delta F_{\mathrm{X}}(Q)$, respectively. In a diffraction experiment the finite maximum scattering vector $Q_{\max}$ leads to peak broadening and unphysical 'truncation ripples' in real space after Fourier transformation. These artifacts can be reduced by applying a damping function prior to Fourier transformation such as a cosine or Lorch [23] modification function.

The theoretical low-r limits for the r-space functions are given by the sum of the weighting coefficients for the $g_{\alpha\beta}(r)$ functions and are presented in table 7.2. The $F(Q)$ functions can also be written in terms of the Bhatia-Thornton [178] number-number (N-

Table 7.2: The theoretical low r limits (in barns) for the $G(r)$ and $\Delta G_{\rm X}(r)$ functions.

${}^{70}_{\rm N}G(r)$	${}^{\rm N}_{\rm N}G(r)$	${}^{73}_{76}G(r)$	$\Delta G_{\rm Ge}(r)$	$\Delta G_{\rm Se}(r)$	$\Delta G_{\rm Se'}$
-0.747(5)	-0.647(1)	-0.966(11)	-0.773(14)	-0.335(7)	-0.384(17)

N), concentration-concentration (C-C) and number-concentration (N-C) partial structure factors i.e. $S^{\rm BT}_{\rm NN}(Q)$, $S^{\rm BT}_{\rm CC}(Q)$ and $S^{\rm BT}_{\rm NC}(Q)$ such that

$$\begin{aligned} F(Q) &= \langle b\rangle^2[S^{\rm BT}_{\rm NN}(Q)-1] + c_{\rm Ge}c_{\rm Se}(b_{\rm Ge}-b_{\rm Se})^2 \times \{[S^{\rm BT}_{\rm CC}(Q)/c_{\rm Ge}c_{\rm Se}-1]\} \\ &+ 2\langle b\rangle(b_{\rm Ge}-b_{\rm Se})S^{\rm BT}_{\rm NC}(Q) \end{aligned} \tag{7.7}$$

where $\langle b\rangle = c_{\rm Ge}b_{\rm Ge}+c_{\rm Se}b_{\rm Se}$ is the average scattering length. The formalism simplifies the expression for the structure factor for ${}^{\rm N}{\rm Ge}^{\rm N}{\rm Se}_2$ glass as measured by neutron diffraction [179] because $b_{\rm Ge} \simeq b_{\rm Se}$, so that $F(Q) \simeq \langle b\rangle^2[S^{\rm BT}_{\rm NN}(Q)-1]$ and $G(r) \simeq \langle b\rangle^2[g^{\rm BT}_{\rm NN}(r)-1]$. The mean coordination number $\bar{n}$ can be extracted from the number-number partial pair-distribution function $g^{\rm BT}_{\rm NN}(r)$ using

$$\bar{n} = 4\pi\rho\int_{r_i}^{r_j} drr^2 g^{\rm BT}_{\rm NN}(r) = c_{\rm Ge}(\bar{n}^{\rm Ge}_{\rm Ge}+\bar{n}^{\rm Se}_{\rm Ge}) + c_{\rm Se}(\bar{n}^{\rm Se}_{\rm Se}+\bar{n}^{\rm Ge}_{\rm Se}) \tag{7.8}$$

and can used to study the evolution of the system topology with pressure.

There are two contrasting models for the ordering in Ge-Se networks under ambient conditions. The first, the random covalent network (RCN) model, assumes a purely statistical distribution of bond types [158, 180] resulting in $\bar{n}^{\rm Ge}_{\rm Ge} = 8c_{\rm Ge}/(1+c_{\rm Ge})$, $\bar{n}^{\rm Se}_{\rm Se} = 2(1-c_{\rm Ge})/(1+c_{\rm Ge})$ and $\bar{n}^{\rm Se}_{\rm Ge} = 4(1-c_{\rm Ge})/(1+c_{\rm Ge})$. The second, the chemically ordered network (CON) model allows for only Ge-Se bands at the stoichiometric composition (i.e. $c_{\rm Ge} = 1/3$) such that $\bar{n}^{\rm Se}_{\rm Ge} = 4$ and $\bar{n}^{\rm Ge}_{\rm Ge} = \bar{n}^{\rm Se}_{\rm Se} = 0$ [158, 181]. Both models give, however, a mean coordination number $\bar{n} = 2.67$ for $GeSe_2$ glass, consistent with the "8-N" rule [179].

7.1.2 Calculating coordination numbers using a Gaussian fitting procedure

The presence of Se-Se and Ge-Ge homopolar bonds in the glassy structure, whose bond lengths are comparable to the Ge-Se nearest-neighbour distance [164], makes it difficult to obtain accurate coordination numbers from the first peak in $G(r)$. Information at the partial pair-distribution function is required in order to solve this problem and

deduce the individual $\bar{n}^{Ge}_{Se}$, $\bar{n}^{Ge}_{Ge}$ or $\bar{n}^{Se}_{Se}$ coordination numbers. To try and tackle this problem, weighted Gaussian functions were fitted to the first peak in the measured total pair distribution or difference functions using the computer program RDFGenie. The protocol is briefly outlined below.

For fitting purposes let us define:

$$D_{\rm exp}(r) = \frac{2}{\pi}\int_0^\infty Q\frac{F(Q)}{|G(0)|}\sin(Qr)M(Q)dQ$$
$$\Delta D_{\rm X,exp}(r) = \frac{2}{\pi}\int_0^\infty Q\frac{\Delta F_{\rm X}(Q)}{|\Delta G_{\rm X}(0)|}\sin(Qr)M(Q)dQ, \tag{7.9}$$

where X = Se, Ge, Se′ and the normalization of the $D_{\rm exp}(r)$ and $\Delta D_{\rm X,exp}(r)$ functions, by $|G(0)|$ and $|\Delta G_{\rm X}(0)|$ respectively, ensures that the weighting factors for the $g_{\alpha\beta}(r)$ sum to unity such that the low-r limit in all cases is given by $-4\pi\rho r$. $M(Q)$ is a modification function which accounts for truncation of the reciprocal data sets at a finite $Q_{\rm max}$ value. By using equations (7.1) and (7.6) $D_{\rm exp}(r)$ can be rewritten as [182]:

$$\begin{aligned} D_{\rm exp}(r) &= 4\pi\rho r\frac{G(r)}{|G(0)|}\otimes P(r) \\ &= 4\pi\rho\sum_{\alpha=1}^{n}\sum_{\beta=1}^{n}\frac{c_\alpha c_\beta b_\alpha b_\beta}{|G(0)|}rg_{\alpha\beta}(r)\otimes P(r) - 4\pi r\rho, \end{aligned} \tag{7.10}$$

where $P(r) = \frac{1}{\pi}\int_0^{Q_{\rm max}}\cos(Qr)dQ = \frac{Q_{\rm max}}{\pi}{\rm sinc}(Q_{\rm max}r)$ is the real-space manifestation of the modification function defined by $M(Q) = 1$ for $Q \leq Q_{\rm max}$, $M(Q) = 0$ for $Q > Q_{\rm max}$.

Each peak in $D_{\rm exp}(r)$, for example, can be represented by a sum of weighted Gaussian functions represented by $D_{\rm fit}(r)$ which is given by:

$$\begin{aligned} D_{\rm fit}(r; r_{\alpha\beta}, \bar{n}^\beta_\alpha, \sigma_{\alpha\beta}) &= \sum_i\left\{w_{\alpha\beta}(i)\frac{\bar{n}^\beta_\alpha(i)}{c_\beta(i)r_{\alpha\beta}(i)}\frac{1}{\sqrt{2\pi}\sigma_{\alpha\beta}(i)}\exp\left[\frac{-(r-r_{\alpha\beta}(i))^2}{2(\sigma_{\alpha\beta}(i))^2}\right]\otimes P(r)\right\} \\ &- 4\pi r\rho, \end{aligned} \tag{7.11}$$

where $w_{\alpha\beta} = 2c_\alpha c_\beta b_\alpha b_\beta/(|G(0)|)$ for $\alpha \neq \beta$ or $w_{\alpha\beta} = c^2_\alpha b^2_\alpha/(|G(0)|)$ for $\alpha = \beta$ and $\sigma_{\alpha\beta}(i)$ defines the width of the i'th Gaussian function. The area of the i'th Gaussian function is proportional to the coordination number $\bar{n}^\beta_\alpha$, e.g. the first peak for $GeSe_2$ can be represented by $i = 3$ Gaussian functions weighted by $\bar{n}^{Se}_{Ge}$, $\bar{n}^{Ge}_{Ge}$ and $\bar{n}^{Se}_{Se}$. The breadth of each fitted Gaussian is affected by $Q_{\rm max}$.

The D_{fit} function is optimised with respect to $\bar{n}_{\alpha}^{\beta}$ or other fitting parameters by minimizing the R_{χ} function which is defined by Grimley *et al.* [50] as:

$$R_{\chi}(r_{\alpha\beta}, \bar{n}_{\alpha}^{\beta}, \sigma_{\alpha\beta}) = \left\{ \frac{\sum_i [D_{\text{exp}}(r_i) - D_{\text{fit}}(r_i; r_{\alpha\beta}, \bar{n}_{\alpha}^{\beta}, \sigma_{\alpha\beta})]^2}{D_{\text{exp}}(r_i)^2} \right\}^{1/2} \tag{7.12}$$

The coordination numbers $\bar{n}_{\text{Ge}}^{\text{Se}}$, $\bar{n}_{\text{Ge}}^{\text{Ge}}$ and $\bar{n}_{\text{Se}}^{\text{Se}}$ for the PE data at ambient pressure was obtained by using the measured values from Petri *et al.* [164] as a starting point. These results were then used as the starting point for fitting the data sets for the first pressure point, yielding results that were, in turn, used as the starting point for the next highest pressure. This process was repeated until the data sets for the maximum pressure were fitted.

7.2 Experimental procedure

7.2.1 The neutron diffraction experiment

The experiments were made at ambient temperature ($T \sim 300$ K) and used the diffractometer D4c at the Institut Laue-Langevin [30]. The high-pressure diffraction experiment employed a VX5/180 type Paris-Edinburgh press (Chapter 3) with cubic BN anvils having a single-toroid profile. Since the sample position changes with piston displacement upon increasing the applied load, the press was mounted on a platform that could be translated vertically (z-axis drive) so that the sample could be centred in the incident beam at each pressure point with the aid of an optical camera.

The background scattering was minimized by optimizing the setup given in Chapter 3. The same samples were used as described in references [164, 183]. The sample pellets for the high-pressure runs were prepared by using an identical procedure as in reference [31] in which finely powdered glass was compacted in a pellet press. The samples were held in gaskets made from a $Ti_{0.676}Zr_{0.324}$ alloy which has a zero coherent neutron scattering length.

The sample masses, as measured at the end of the high-pressure runs, showed that the number of scattering centres for the $^{70}Ge^{N}Se_2$ and $^{73}Ge^{76}Se_2$ were as close as possible to the $^{N}Ge^{N}Se_2$ sample, while the masses of the gaskets were matched to within 0.3% as shown in table 7.3.

Table 7.3: Masses of the recovered $GeSe_2$ glassy pellets and their corresponding Ti-Zr gaskets.

Sample	Sample mass (g)	Gasket mass (g)
$^{N}Ge^{N}Se_2$	0.3400(2)	1.4892(2)
$^{73}Ge^{76}Se_2$	0.3084(2)	1.4913(2)
$^{70}Ge^{N}Se_2$	0.3370(2)	1.4935(2)

The incident neutron wavelength of $\lambda = 0.4961(1)$ Å and zero scattering angle for the detectors were measured using Ni powder contained within an encapsulated $Ti_{0.676}Zr_{0.324}$ gasket [87] mounted in the Paris-Edinburgh press with no applied load. Higher order ($\lambda/2$) scattering was suppressed by placing an Rh filter after the Cu(200) monochromator, upstream of the sample position.

For a given sample, the diffraction pattern for an empty Ti-Zr gasket was first measured with a small applied load. The sample was then mounted in the gasket and the load on the anvils was always increased during the course of a high-pressure run. Diffraction

patterns were also measured for (a) several empty Ti-Zr gaskets that had been recovered from different high pressures in order to estimate the gasket scattering under load, and (b) the empty anvils with different anvil separations in order to help in estimating the background scattering. To assist in the data normalization at different pressures, where the anvils have different separations, additional diffraction patterns were measured at ambient pressure for large and small vanadium pellets contained in unsquashed and recovered (i.e. previously squashed) Ti-Zr gaskets, respectively. The data analysis followed the procedure described in Chapter 3.

The sample pressure P was deduced from the load applied to the anvils of the press by using a calibration curve that has been extensively checked (Chapter 3). Each complete diffraction pattern was built up from the intensities measured for different positions of D4c's group of nine microstrip detectors. These intensities were saved at regular intervals to check the sample and diffractometer stabilities. The data were analysed by using a standard procedure (Chapter 3). The supporting pillars of the Paris-Edinburgh press restrict the maximum accessible scattering angle so the maximum cutoff value $Q_{\max}$ is therefore ~ 21.5 Å^{-1} for an incident neutron wavelength of ~ 0.5 Å.

The pressure P dependence to the number density of $GeSe_2$ glass, as obtained from several *in situ* studies [138], is shown in figure 7-1. Also given is a fit of the data from [138] to a second order Birch-Murnaghan equation of state given by [131]

$$P = \frac{3B_0}{2}\left[\left(\frac{V}{V_0}\right)^{-\frac{7}{3}} - \left(\frac{V}{V_0}\right)^{-\frac{5}{3}}\right], \tag{7.13}$$

where V is the volume at pressure and V_0 is the volume under ambient conditions. The fit parameters were found to be $B_0 = 10.55(30)$ GPa, where B_0 is the bulk modulus under ambient conditions and B_1 is the first pressure derivative at 298 K.

The $^{70}Ge^{N}Se_2$ or $^{73}Ge^{70}Se_2$ samples were measured at ambient pressure and at pressures of 3.0(5), 4.7(5), 6.3(5), 7.1(5) and 8.2(5) GPa which correspond to reduced sample number densities ρ/ρ_0 of 1, 1.119, 1.281, 1.362, 1.404 and 1.464 respectively, where ρ_0 = 0.0334 Å^{-3} is the ambient-pressure value. The structure of $^{N}Ge^{N}Se_2$ was investigated at ambient pressure and at pressure of, 1.7(5), 3.0(5), 3.9(5) and 4.7(5) GPa which correspond to reduced sample number densities ρ/ρ_0 of 1, 1.111, 1.119, 1.186 and 1.281.

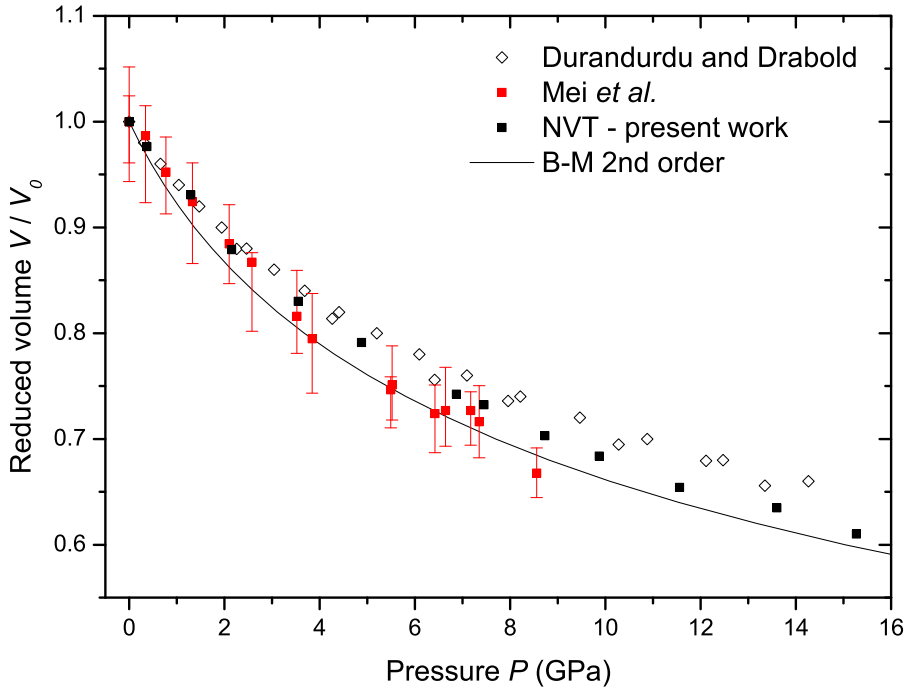

Figure 7-1: The pressure-reduced volume equation of state for $GeSe_2$ glass as measured by Mei *et al.* [138] (■) and as calculated by using first-principles molecular dynamics [174] (■) in the present work and in the work by Durandurdu and Drabold [184] (◇). The measured data is fitted with a second order Birch-Murnaghan equation of state (—).

7.3 Molecular dynamics simulations

The first principles molecular dynamics (FPMD) simulations [174] were performed using the NVT ensemble for $N = 120$ atoms following the approach of reference [167]. The volume V was varied and the pressure computed from the stress tensor. The Becke-Lee-Yang-Parr functional [15, 16] was adopted to describe the electron exchange and correlation, and leads to an accurate representation of the structure-related properties of several liquid and glassy Ge-Se materials at ambient pressure [167, 175–177].

Valence electrons were treated explicitly and were represented by a plane-wave basis set expanded at the Γ point of the simulation cell with an energy cut-off of 20 Ry. The valence-core interactions were described by norm conserving pseudopotentials of the Troullier-Martins type [185]. A fictitious electron mass of 1000 a.u. (i.e. in units of $m_e a_0^2$ where m_e is the electron mass and a_0 is the Bohr radius) and a time step of $\Delta t = 0.24$ fs were used to integrate the equations of motion, ensuring good control of the conserved quantities. The temperature T was controlled by a Nosé-Hoover thermostat [186, 187].

Since the measured and simulated equations of state are not exact, the neutron diffraction and molecular dynamics results will be compared at similar reduced number densities ρ/ρ_0 where ρ and ρ_0 are the values at high and ambient pressure, respectively. The P and ρ values for the simulated data sets are given in table 7.4.

Table 7.4: The pressures P and densities ρ at which first principles molecular dynamics simulations were made for $GeSe_2$ glass. The reduced number density ρ/ρ_0 is also given, where ρ_0 corresponds to the ambient pressure value.

Pressure P(GPa)	Number density ρ (Å^{-3})	Reduced density ρ/ρ_0
0.00	0.0326	1.000
1.58	0.0393	1.206
3.40	0.0393	1.206
4.88	0.0412	1.264
7.25	0.04453	1.366
8.73	0.04639	1.423
9.87	0.04771	1.463

7.4 Results

7.4.1 Total structure factors

The pressure dependence of the total structure factors ${}^{70}_{\mathrm{N}}F(Q)$ and ${}^{73}_{76}F(Q)$ is shown in figures 7-2 and 7-4, respectively, where a comparison is also made with the ambient pressure data of Petri *et al.* [164] and with the FPMD simulations at similar densities (see table 7.4). The corresponding total distribution functions ${}^{70}_{\mathrm{N}}G(r)$ and ${}^{73}_{76}G(r)$ are plotted in figures 7-3 and 7-5. The reciprocal space data sets from the simulations were truncated at the same $Q_{\max}$ as used in experiment before Fourier transformation into r space.

In general there is good agreement in Q-space between the ambient pressure data sets obtained for a vanadium can and in the PE press and the major peak positions Q_1, Q_2 and Q_3 agree to within the experimental error (see table 7.5). The difference in the intensity of the first peak in $G(r)$ between the vanadium can data of Petri *et al.* and the PE press data is due to the different $Q_{\max}$ values used for truncation (21.5 $\mathrm{\AA}^{-1}$ for ambient conditions in the PE press cf. 15.9 $\mathrm{\AA}^{-1}$ for the Petri *et al.* [164] data).

The pressure dependence of the major peak positions in reciprocal and real space for the ${}^{70}\mathrm{Ge}^{\mathrm{N}}\mathrm{Se}_2$ and ${}^{73}\mathrm{Ge}^{76}\mathrm{Se}_2$ glasses is in table 7.5. The density driven changes to the intermediate range order for ${}^{70}_{\mathrm{N}}F(Q)$ are observable as a fast drop in intensity of the first sharp diffraction peak (FSDP) at $Q_1 = 1.0$ $\mathrm{\AA}^{-1}$ as the pressure is increased from ambient to 6.3 GPa. For higher pressures it is hard to quantify the FSDP position but it is estimated to be at $\sim 1.35(2)$ $\mathrm{\AA}^{-1}$ at 8.2 GPa. In contrast, the FSDP in the ${}^{73}_{76}F(Q)$ function has a very small intensity and almost completely vanishes as the pressure is increased to 3.0 GPa. Since the FSDP is primarily due to Ge-Ge correlations [164], these changes are associated with an alteration of the intermediate range order associated with the Ge-Ge correlations [92].

The principal peak (PP), which is associated with extended range order [89, 94], occurs at $Q_2 = 2.05(2)$ $\mathrm{\AA}^{-1}$ in both ${}^{70}_{\mathrm{N}}F(Q)$ and ${}^{73}_{76}F(Q)$ functions at ambient pressure and moves to $Q_2 = 2.22(2)$ $\mathrm{\AA}^{-1}$ as the pressure is increased from ambient to 8.2 GPa, while the height of the peak increases by a factor of 1.15 for ${}^{70}\mathrm{Ge}^{\mathrm{N}}\mathrm{Se}_2$ and by factor of 1.69 for ${}^{73}\mathrm{Ge}^{76}\mathrm{Se}_2$. The third peak position increases from $Q_3 = 3.55(2)$ $\mathrm{\AA}^{-1}$ by 0.20 $\mathrm{\AA}^{-1}$ between ambient pressure and 8.2 GPa. These changes for the FSDP and PP are consistent with a competition between the intermediate and extended range ordering which is won by the latter with increasing density as the glass becomes more fragile [93].

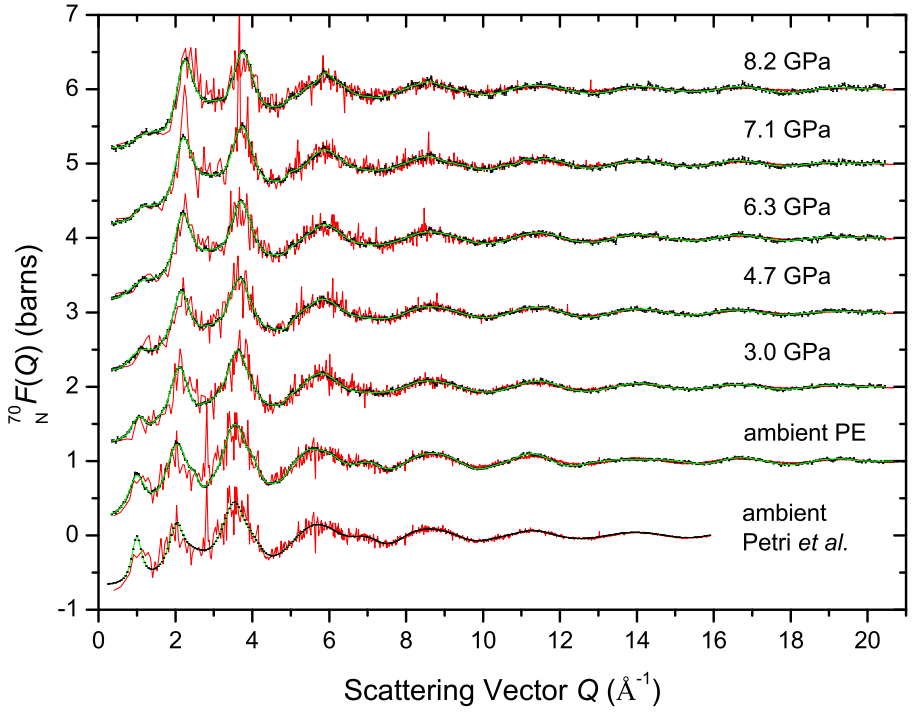

Figure 7-2: The total structure factor $^{70}_{N}F(Q)$ for $^{70}Ge^{N}Se_2$ glass as measured for a sample in a vanadium can by Petri *et al.* [138] and in the PE press at ambient and at pressures up to 8.2 GPa. The solid black curves (—) with vertical error bars represent the unsmoothed total structure factors, the solid green curves (—) represent Harwell spline fitted data sets after a cosine window function has been applied over the Q range from 19.0–21.5 Å^{-1} for ambient or from 19.0–20.5 Å^{-1} for $P \geq 3$ GPa, and the solid green curves represent the Fourier back transforms of the measured $^{70}_{N}G(r)$ functions shown in figure 7-3 after the unphysical oscillations at $r \leq 2.21$ Å have been set to the calculated $^{70}_{N}G(0)$ limit. The experimental data sets are compared to FPMD simulations (—) [174] at similar densities, corresponding to ambient pressure and to pressures of 3.4, 4.88, 7.25, 8.73 and 9.87 GPa (see table 7.4).

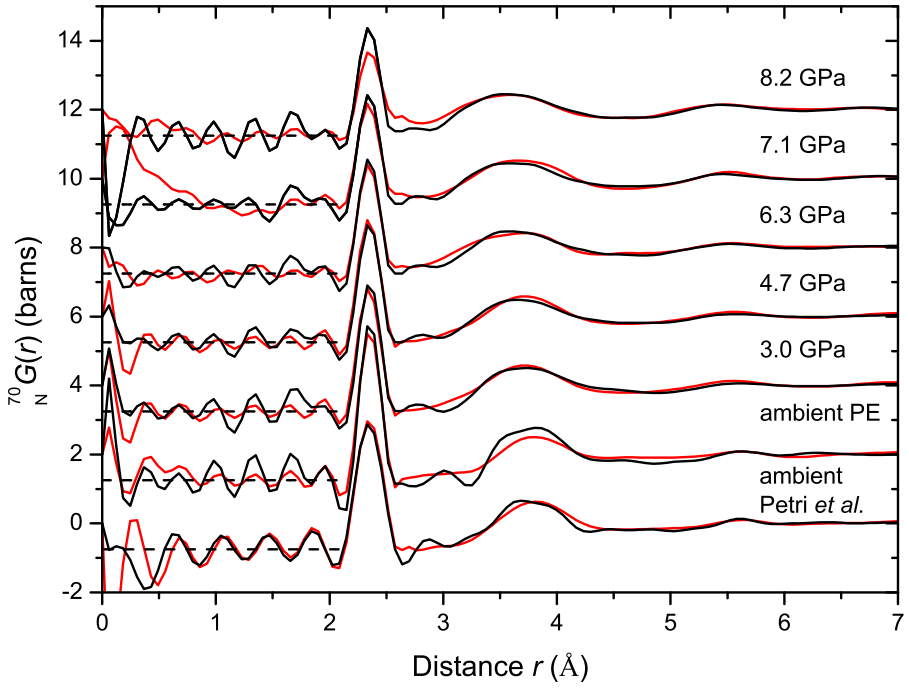

Figure 7-3: The pressure dependence of the total pair distribution functions $^{70}_{N}G(r)$ (——) for $^{70}Ge^{N}Se_2$ glass as obtained by Fourier transforming the total structure factors $^{70}_{N}F(Q)$ shown by the corresponding solid green curves (——) in figure 7-2. The solid black curves (——) show the extent of the low r oscillations while the horizontal black broken curves (- - -) give the calculated $^{70}_{N}G(0)$ limit. The red curves (——) represent the Fourier transforms of the FPMD data sets [174] with a cutoff set at the experimental value of Q_{max}= 21.5 Å^{-1} for ambient and Q_{max}= 20.5 Å^{-1} for $P \geq 3$ GPa.

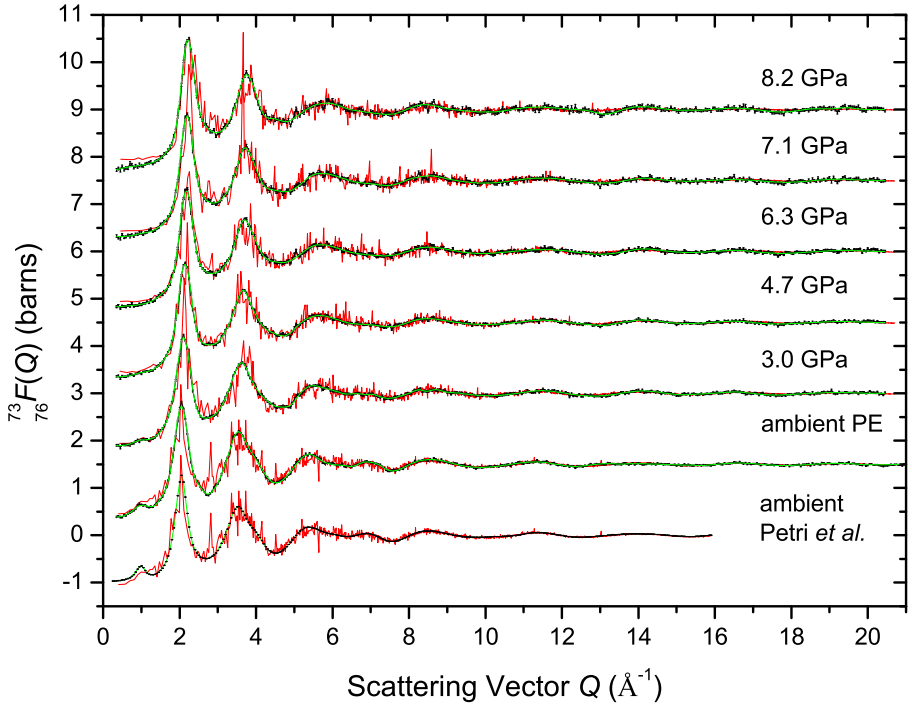

Figure 7-4: The total structure factor $^{73}_{76}F(Q)$ as measured for a sample in a vanadium can by Petri *et al.* [138] and in the PE press at ambient and at pressures up to 8.2 GPa. The solid black curves (—) with vertical error bars represent the unsmoothed total structure factors, the solid green curves (—) represent Harwell spline fitted data sets after a cosine window function has been applied over the Q range from 19.0–21.5 Å^{-1} for ambient or from 19.0–20.5 Å^{-1} for $P \geq 3$ GPa, and the solid green curves represent the Fourier back transforms of the measured $^{73}_{76}G(r)$ functions shown in figure 7-5 after the unphysical oscillations at $r \leq 2.21$ Å have been set to the calculated $^{73}_{76}G(0)$ limit. The experimental data sets are compared to first-principles FPMD simulations (—) [174] at similar densities, corresponding to ambient pressure and to pressures of 3.4, 4.88, 7.25, 8.73 and 9.87 GPa (see table 7.4).

The total pair distribution functions $^{70}_{\mathrm{N}}G(r)$ and $^{76}_{73}G(r)$ have a first peak at $r_1 \sim 2.35$ Å at ambient pressure, which is due predominantly to intra-polyhedral Ge-Se bonds [164, 183]. The first peak does not seem to change position as the pressure is increased up to 8.2 GPa. The mean coordination number $\bar{n}$ (see table 7.5), which was calculated by fitting Gaussian functions to $r[^{70}_{\mathrm{N}}G(r)]$ and $r[^{73}_{76}G(r)]$ as described in § 7.1.2, appears to increase by a small amount from $\bar{n}$ ∼2.6(1) below 7.1 GPa to $\bar{n}$ ∼2.8(1) at 8.2 GPa.

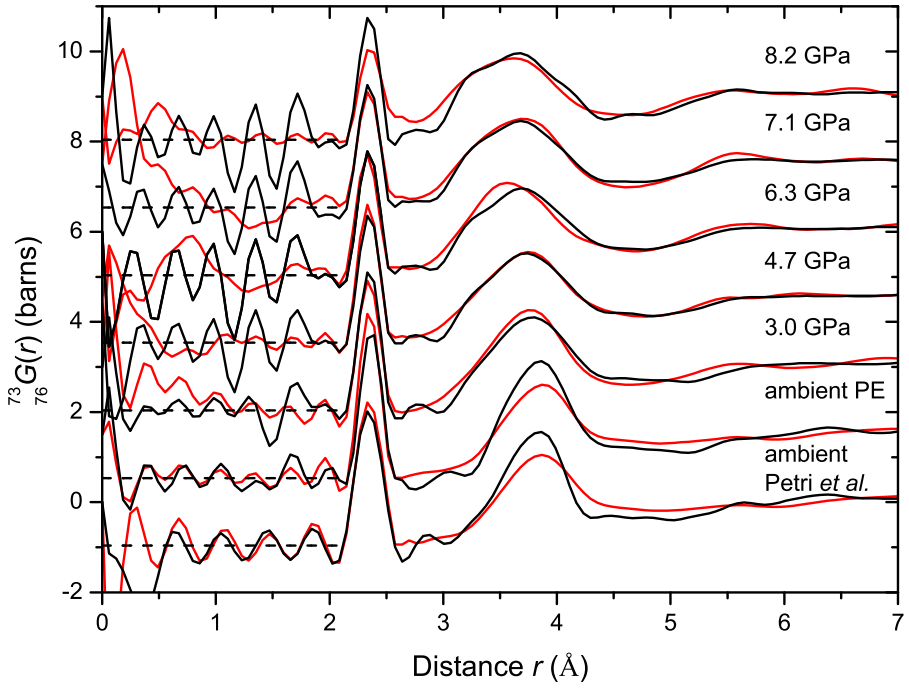

Figure 7-5: The pressure dependence of the total pair distribution functions $^{73}_{76}G(r)$ (——) for $^{73}Ge^{76}Se_2$ glass as obtained by Fourier transforming the total structure factors $^{73}_{76}F(Q)$ shown by the corresponding solid green curves (——) in figure 7-4. The solid black curves (——) show the extent of the low r oscillations while the horizontal black broken curves (- - -) give the calculated $^{73}_{76}G(0)$ limit. The red curves (——) represent the Fourier transforms of the FPMD data sets [174] with a cutoff set at the experimental value of $Q_{\max}$= 21.5 Å^{-1} for ambient or $Q_{\max}$= 20.5 Å^{-1} for $P \geq 3$ GPa.

Table 7.5: The leading peak positions Q_1, Q_2 and Q_3 at pressure P for the measured total structure factors $^{70}_{\mathrm{N}}F(Q)$ and $^{73}_{76}F(Q)$ that are plotted in figures 7-2 and 7-4 for $GeSe_2$ glass. The leading peak position r_1 from the corresponding $^{70}_{\mathrm{N}}G(r)$ functions plotted in figure 7-3, and the first two peak positions r_1 and r_2 from the corresponding $^{73}_{76}G(r)$ functions plotted in figure 7-5 are also listed. The mean coordination numbers $\bar{n}$ as obtained by using a Gaussian fitting method (§ 7.1.2) are also given.

Pressure (GPa)	Number density ρ (Å^{-3})	$^{70}_{\mathrm{N}}F(Q)$ Q_1 (Å^{-1})	Q_2 (Å^{-1})	Q_3 (Å^{-1})	$^{70}_{\mathrm{N}}G(r)$ r_1 (Å)	$\bar{n}$
V can	0.0334(1)	1.05(2)	2.09(2)	3.58(2)	2.35(2)	2.56(10)
0.0	0.0334(1)	1.01(2)	2.05(2)	3.55(2)	2.35(2)	2.55(10)
3.0(5)	0.0396(1)	1.08(2)	2.10(2)	3.62(2)	2.35(2)	2.63(10)
4.7(5)	0.0428(1)	1.15(2)	2.15(2)	3.67(2)	2.35(2)	2.63(10)
6.3(5)	0.0455(1)	1.25(2)	2.20(2)	3.70(2)	2.35(2)	2.63(10)
7.1(5)	0.0469(1)	1.25(2)	2.22(2)	3.73(2)	2.35(2)	2.67(10)
8.2(5)	0.0489(1)	1.35(2)	2.26(2)	3.75(2)	2.34(2)	2.78(10)

Pressure (GPa)	Number density ρ (Å^{-3})	$^{73}_{76}F(Q)$ Q_1 (Å^{-1})	Q_2 (Å^{-1})	Q_3 (Å^{-1})	$^{73}_{76}G(r)$ r_1 (Å)	r_2 (Å)	$\bar{n}$
V can	0.0334(1)	1.04(2)	2.10(2)	3.58(2)	2.36(2)	3.85(2)	2.65(10)
0.0	0.0334(1)	1.03(2)	2.04(2)	3.54(2)	2.37(2)	3.85(2)	2.42(10)
3.0(5)	0.0396(2)	1.05(2)	2.10(2)	3.62(2)	2.35(2)	3.78(2)	2.63(10)
4.7(5)	0.0428(2)	–	2.14(2)	3.67(2)	2.34(2)	3.73(2)	2.64(10)
6.3(5)	0.0455(2)	–	2.18(2)	3.70(2)	2.34(2)	3.69(2)	2.67(10)
7.1(5)	0.0469(2)	–	2.20(2)	3.72(2)	2.34(2)	3.68(2)	2.70(10)
8.2(5)	0.0489(2)	–	2.22(2)	3.76(2)	2.34(2)	3.66(2)	2.77(10)

The pressure dependence of the total structure factor ${}^{\mathrm{N}}_{\mathrm{N}}F(Q)$ is shown in figure 7-6 where a comparison is also made with the ambient pressure data of Petri *et al.* [164] and the FPMD simulations at similar densities (see table 7.4). The reason why the ${}^{\mathrm{N}}\mathrm{Ge}^{\mathrm{N}}\mathrm{Se}_2$ glass sample was measured over a lower pressure range as compared to the isotopically enriched samples is that the gasket failed during compression to 6.3 GPa. Destruction of the Ti-Zr gasket and the damage caused to the anvils ruled out the possibility of making the recovered empty Ti-Zr gasket measurements that are required to correct the data sets at high pressures. Moreover, the background measured after the sample's explosion could not be used to properly correct the data beyond pressures of 4.7 GPa and beyond a $Q_{\max}$ of 18.5 Å^{-1} for ${}^{\mathrm{N}}_{\mathrm{N}}F(Q)$ as compared to a $Q_{\max}$ of 20.5 Å^{-1} for ${}^{70}_{\mathrm{N}}F(Q)$ and ${}^{73}_{76}F(Q)$.

The mean coordination number $\bar{n}$ was calculated by fitting the first peak in $r[{}^{\mathrm{N}}_{\mathrm{N}}G(r)]$ and the values are given in table 7.6. Integrating over the first peak in $g_{\mathrm{NN}}(r) = {}^{\mathrm{N}}_{\mathrm{N}}G(r)/|G(0)| + 1$ gives the same $\bar{n}$ values as obtained from the fitting procedure.

Table 7.6: The leading peak positions Q_1, Q_2 and Q_3 at pressure P for the measured total structure factors ${}^{\mathrm{N}}_{\mathrm{N}}F(Q)$ that are plotted in figure 7-6 for $GeSe_2$ glass. The positions r_1 and r_2 of the first two peaks in the corresponding ${}^{\mathrm{N}}_{\mathrm{N}}G(r)$ functions plotted in figure 7-7 are also shown, together with the mean coordination numbers $\bar{n}$ obtained by fitting a Gaussian the first peak in $r[{}^{\mathrm{N}}_{\mathrm{N}}G(r)]$.

Pressure (GPa)	Number density ρ (Å^{-3})	${}^{\mathrm{N}}_{\mathrm{N}}F(Q)$ Q_1 (Å^{-1})	Q_2 (Å^{-1})	Q_3 (Å^{-1})	${}^{\mathrm{N}}_{\mathrm{N}}G(r)$ r_1 (Å)	r_2 (Å)	$\bar{n}$
V can	0.0334(1)	1.04(2)	2.10(2)	3.58(2)	2.36(2)	3.85(2)	2.58(10)
0.0	0.0334(1)	0.99(2)	2.07(2)	3.54(2)	2.35(2)	3.81(2)	2.58(10)
1.7(5)	0.0371(1)	1.04(2)	2.11(2)	3.62(2)	2.35(2)	3.79(2)	2.58(10)
3.0(5)	0.0396(1)	1.10(2)	2.11(2)	3.62(2)	2.35(2)	3.78(2)	2.58(10)
3.9(5)	0.0412(1)	1.08(2)	2.14(2)	3.62(2)	2.35(2)	3.73(2)	2.58(10)
4.7(5)	0.0428(1)	1.17(2)	2.16(2)	3.67(2)	2.35(2)	3.66(2)	2.60(10)

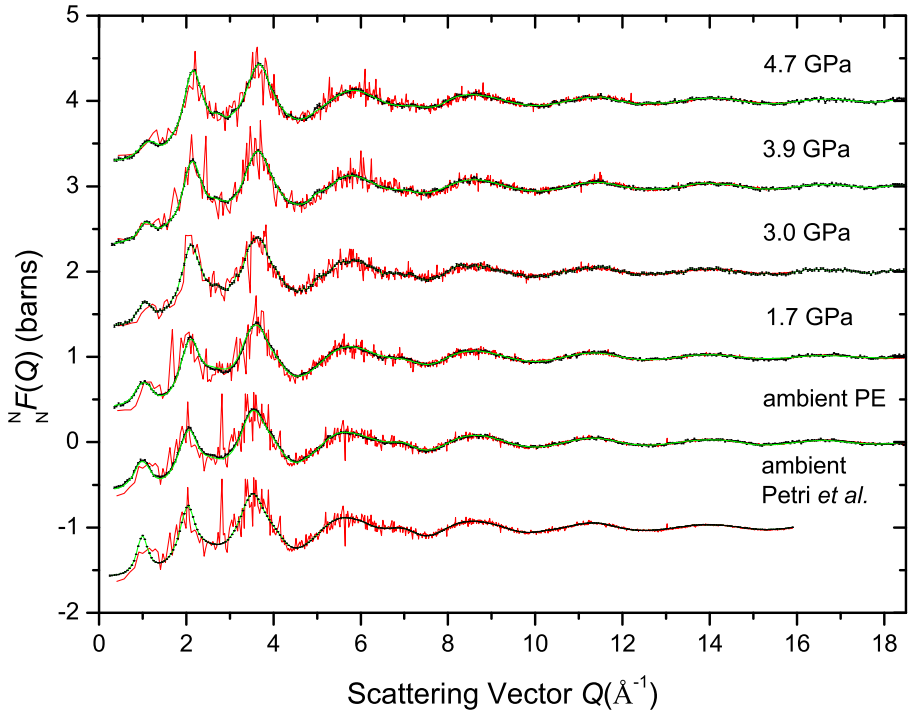

Figure 7-6: The total structure factor $^{N}_{N}F(Q)$ as measured for a sample in a vanadium can by Petri *et al.* [138] and in the PE press at ambient and at pressures up to 4.7 GPa. The solid black curves (—) with vertical error bars represent the unsmoothed total structure factors, the solid green curves (—) represent Harwell spline fitted data sets after a cosine window function has been applied over the Q range from 19.0–21.5 Å^{-1} for ambient or from 19.0–20.5 Å^{-1} for $P \geq 3$ GPa, and the solid green curves represent the Fourier back transforms of the $^{N}_{N}G(r)$ functions shown in figure 7-7 after the unphysical oscillations at $r \leq 2.21$ Å have been set to the calculated $^{N}_{N}G(0)$ limit. The experimental data sets are compared to FPMD simulations (—) at similar densities, corresponding to ambient pressure and to pressures of 1.59, 3.40, 3.70 and 4.88 GPa (see table 7.4).

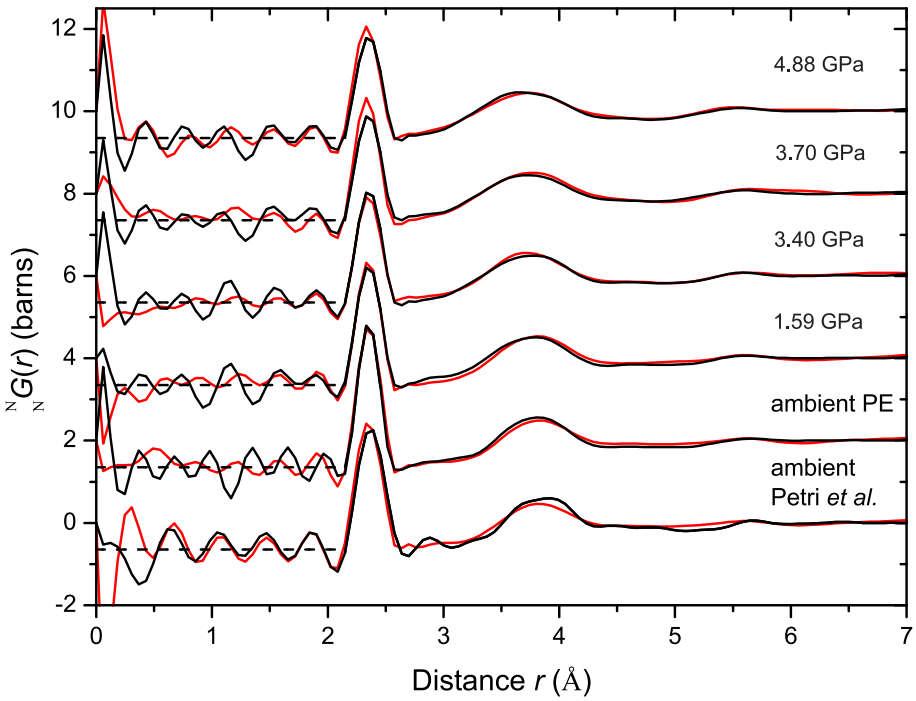

Figure 7-7: The pressure dependence of the total pair distribution functions ${}^{\mathrm{N}}_{\mathrm{N}}G(r)$ (——) as obtained by Fourier transforming the total structure factors ${}^{\mathrm{N}}_{\mathrm{N}}F(Q)$ shown by the corresponding solid green curves (——) in figure 7-6. The solid black curves (——) show the extent of the low r oscillations while the horizontal black broken curves (- - -) give the calculated ${}^{\mathrm{N}}_{\mathrm{N}}G(0)$ limit. The red curves (——) represent the Fourier transforms of the FPMD data sets with a cutoff value set at $Q_{\max} = 19.5$ Å^{-1} for ambient or at $Q_{\max}$ =18.5 Å^{-1} for $P \geq 1.59$ GPa.

7.4.2 Difference functions

The pressure dependence of the first difference function $\Delta F_{\mathrm{Se}}(Q)$ is plotted in figure 7-8 for the ambient – 8.2 GPa pressure range. By contrast to ${}^{70}_{\mathrm{N}}F(Q)$ and ${}^{73}_{76}F(Q)$, the intensity of the FSDP in $\Delta F_{\mathrm{Se}}(Q)$ at $Q_1 \sim 1.0$ Å^{-1} is relatively small at ambient and the peak completely vanishes when $P \geq 3.0$ GPa. The position of the PP is $Q_2 = 2.05$ Å^{-1} at ambient and shifts to $Q_2 = 2.22$ Å^{-1} for $P = 8.2$ GPa. For this pressure range, its height increases by a factor of 1.14, while the third peak also shifts towards higher Q values by 0.26 Å^{-1}. The broad double peak in the range $4.5 \leq Q(\text{Å})^{-1} \leq 7.6$ seen in the ambient diffraction pattern changes to a single broad peak at $\simeq 5.8$ Å^{-1} for $P = 8.2$ GPa.

The first peak in $\Delta G_{\mathrm{Se}}(r)$ is at $r_1 = 2.36(2)$ Å for ambient pressure in the PE press. It arises primarily from Ge-Se correlations, but also contains a non-negligible contribution from $g_{\mathrm{SeSe}}(r)$ (see figure 7-10). It does not appear to change its average position as the pressure is increased to 8.2 GPa. More prominent changes are seen for the broad second peak in $\Delta G_{\mathrm{Se}}(r)$ that is attributable mainly to Se-Se correlations (figure 7-10) and spreads over the range $2.95 \leq r(\text{Å}) \leq 4.39$ at ambient. The Se-Se peak maximum at $r_2 = 3.85(3)$ Å for ambient shifts to $r_2 = 3.68(2)$ Å at $P = 8.2$ GPa. The ratio of the distances r_2/r_1 is 1.65(2) at ambient, and is comparable to the value of $\sqrt{8/3} = 1.633$ expected for a perfect tetrahedron i.e. the data are consistent with the formation of tetrahedral structural units.

The difference functions $\Delta F_{\mathrm{Ge}}(Q)$ are plotted in figure 7-11 for the ambient–8.2 GPa pressure range. At ambient there is, in general, very good agreement with the data measured by Petri *et al.* [164].

The FSDP at $Q_1 \sim 1.0$ Å^{-1} arises mainly from Ge-Ge correlations (see table 7.1). This peak shifts to $Q_1 = 1.27$ Å^{-1} and its height is almost completely extinguished as the pressure is increased to $P = 8.2$ GPa. Interestingly, and excluding the FSDP, the changes in the $\Delta F_{\mathrm{Ge}}(Q)$ function in the measured pressure range are quite small suggesting that the biggest structural changes in the glass result from Se-Se rearrangements.

The real space difference functions $\Delta G_{\mathrm{Ge}}(r)$ are plotted in figure 7-12, while the low and high pressure r-space data sets are compared to the weighted partials in figure 7-13. The first peak position at $\sim 2.35(2)$ Å does not appear to change over the whole ambient–8.2 GPa pressure range. Figure 7-13 indicates that the second low intensity peak at $r \sim 3.5$ Å results predominantly from corner sharing Ge-Ge correlations suggesting that the nearest neighbour Ge-Ge distance can be reliably extracted from the $\Delta G_{\mathrm{Ge}}(r)$ functions. Unfortunately it is not possible to determine the Ge-Ge distance arising from edge sharing units due to the small intensity of this peak [164].

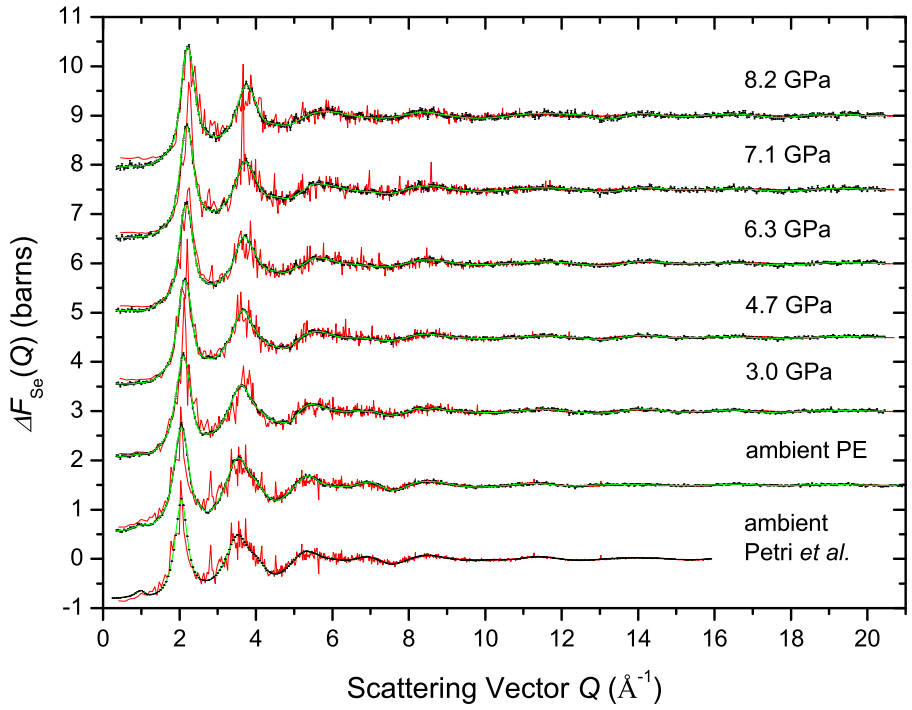

Figure 7-8: The difference functions $\Delta F_{\mathrm{Se}}(Q)$ as measured for samples in a vanadium can by Petri *et al.* [138] and in the PE press at ambient and at pressures up to 8.2 GPa. The solid black curves (—) with vertical error bars represent the unsmoothed difference functions, the solid green curves (—) represent Harwell spline fitted data sets after a cosine window function has been applied over the Q range from 19.0–21.5 Å^{-1} for ambient or from 19.0–20.5 Å^{-1} for $P \geq 3$ GPa, and the solid green curves represent the Fourier back transforms of the $\Delta G_{\mathrm{Se}}(r)$ functions shown in figure 7-9 after the unphysical oscillations at $r \leq 2.21$ Å have been set to the calculated $\Delta G_{\mathrm{Se}}(0)$ limit. The experimental data sets are compared to FPMD simulations (—) at similar densities corresponding to ambient pressure and to pressures of 3.4, 4.88, 7.25, 8.73 and 9.87 GPa (see table 7.4).

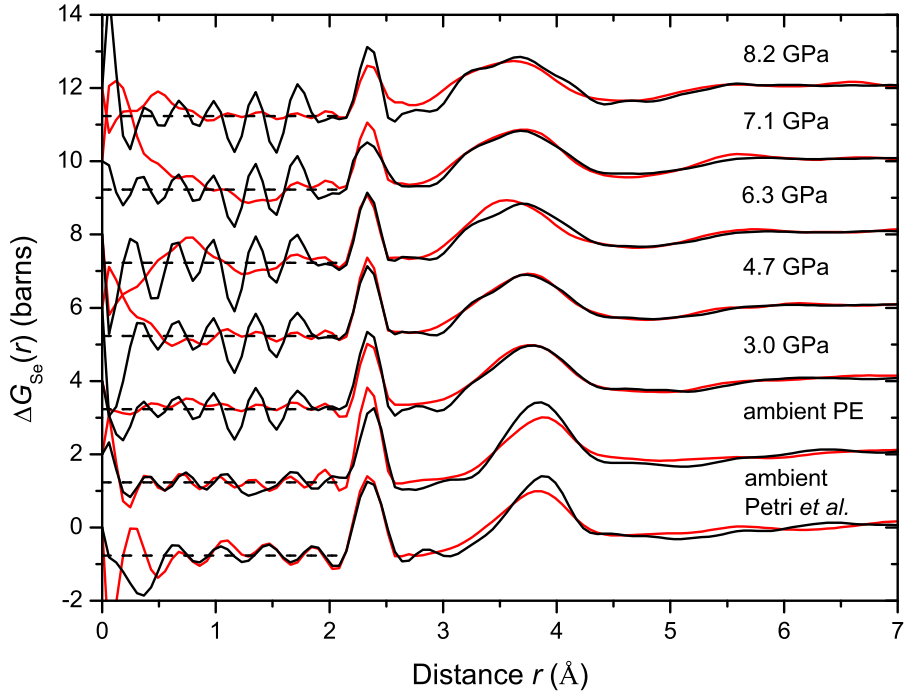

Figure 7-9: The pressure dependence of the difference functions $\Delta G_{\mathrm{Se}}(r)$ (——) as obtained by Fourier transforming the difference functions $\Delta F_{\mathrm{Se}}(Q)$ shown in figure 7-8 by the solid green curves (——). The solid black curves (——) show the extent of the low r oscillations while the horizontal black broken curves (- - -) give the calculated $\Delta G_{\mathrm{Se}}(0)$ limit. The red curves (——) represent the Fourier transforms of the FPMD data set with a cutoff value sets at the experimental value of Q_{max}= 21.5 Å^{-1} for ambient or Q_{max}= 20.5 Å^{-1} for $P \geq 3$ GPa.

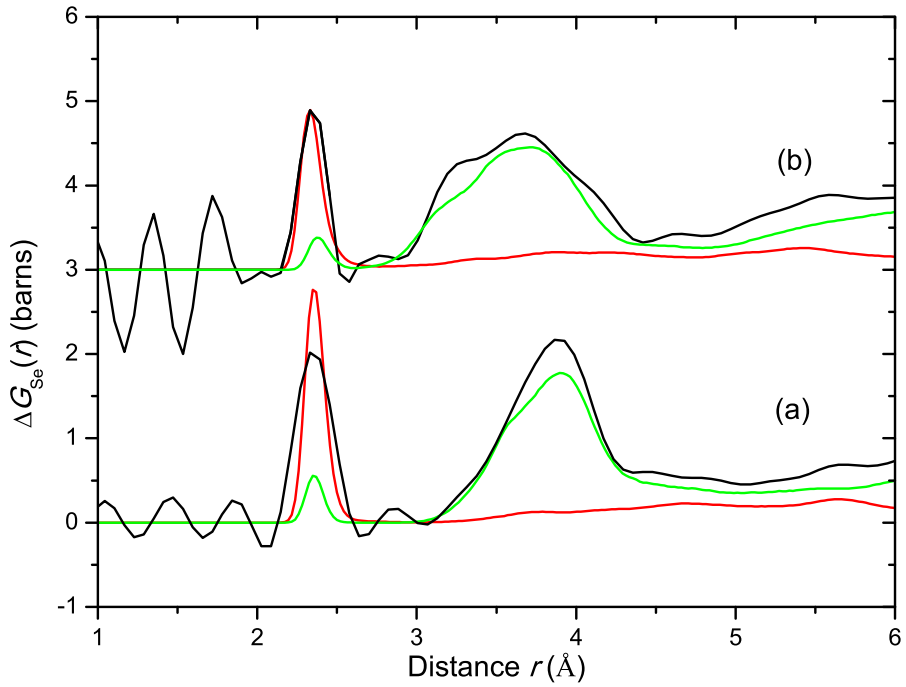

Figure 7-10: A comparison of: (a) $\Delta G_{\mathrm{Se}}(r)$-$\Delta G_{\mathrm{Se}}(0)$ (—) at ambient pressure from neutron diffraction with the weighted partial pair distribution functions $0.184(3)g_{\mathrm{GeSe}}(r)$(—) and $0.588(11)g_{\mathrm{SeSe}}(r)$(—) obtained from the FPMD simulation; (b) $\Delta G_{\mathrm{Se}}(r)$ - $\Delta G_{\mathrm{Se}}(0)$ + 3 barns (—) at 8.2 GPa from neutron diffraction with the weighted partial pair distribution functions $0.184g_{\mathrm{GeSe}}(r) + 3$barns (—) and $0.588g_{\mathrm{SeSe}}(r)$+ 3 barns(—) obtained from the FPMD simulation at 7.98 GPa.

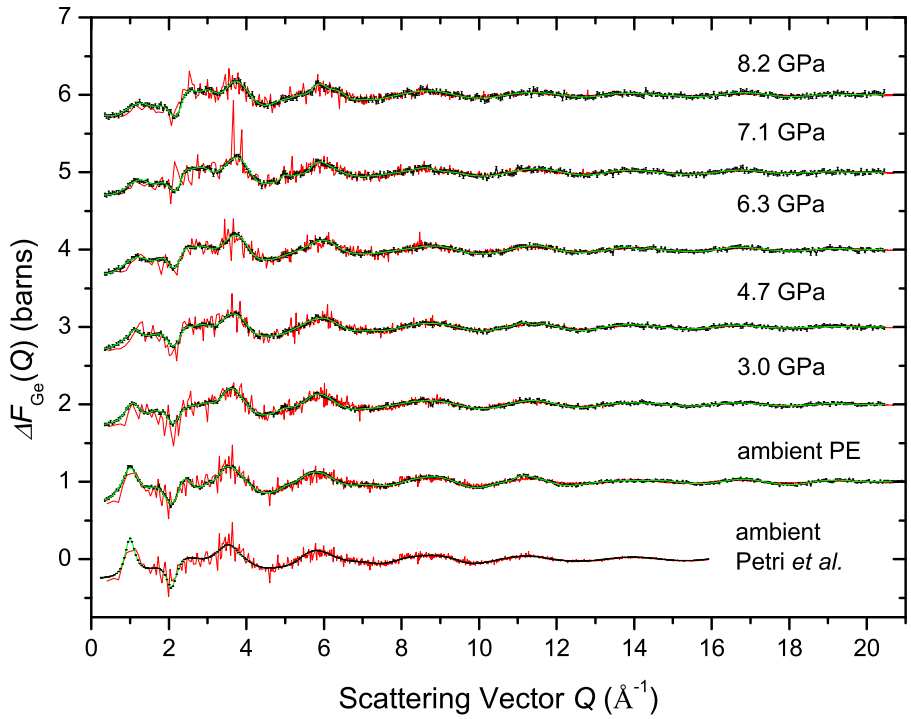

Figure 7-11: The pressure dependence on the difference functions $\Delta F_{\mathrm{Ge}}(Q)$ as measured for samples in a vanadium can by Petri *et al.* [138] and in the PE press at ambient and at pressures up to 8.2 GPa. The solid black curves (—) with vertical error bars represent the unsmoothed difference functions, the solid green curves (—) represent Harwell spline fitted data sets after a cosine window function has been applied over the Q range from 19.0–21.5 $\mathrm{Å}^{-1}$ for ambient or from 19.0–20.5 $\mathrm{Å}^{-1}$ for $P \geq 3$ GPa, and the solid green curves represent the Fourier back transforms of the measured $\Delta G(r)$ functions shown in figure 7-12 after the unphysical oscillations at $r \leq 2.21$ Å have been set to the calculated $\Delta G_{\mathrm{Ge}}(0)$ limit. The experimental data sets are compared to FPMD simulations (—) at similar densities corresponding to ambient pressure and to pressures of 3.4, 4.88, 7.25, 8.73 and 9.87 GPa (see table 7.4).

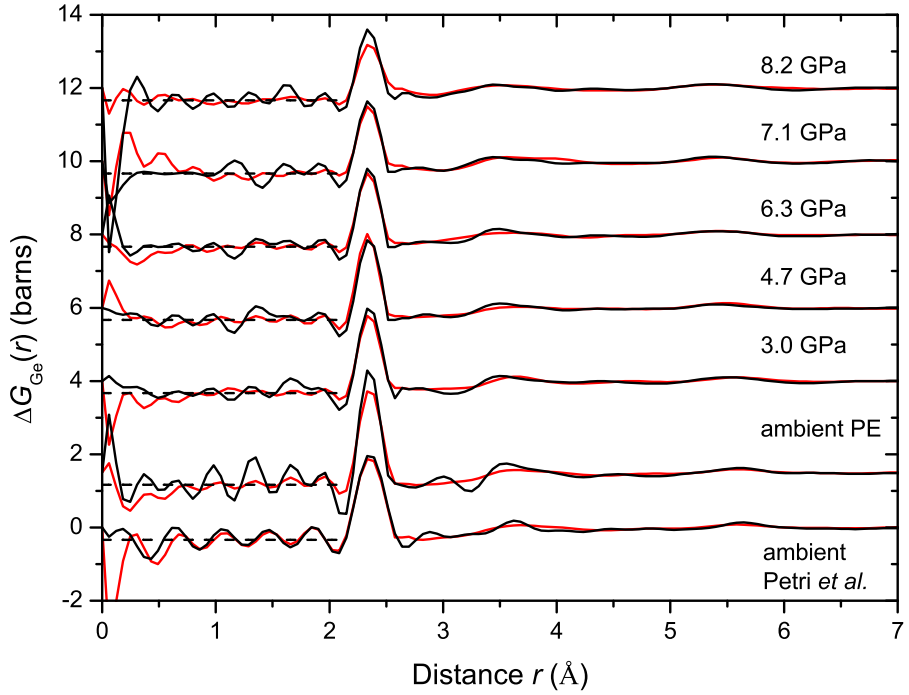

Figure 7-12: The pressure dependence of the difference functions $\Delta G_{\mathrm{Ge}}(r)$ (—) as obtained by Fourier transforming the corresponding difference functions $\Delta F_{\mathrm{Ge}}(Q)$ shown in figure 7-11 by the solid green curves (—). The solid black curves (—) show the extent of the low r oscillations while the horizontal black broken curves (- - -) give the calculated $\Delta G_{\mathrm{Ge}}(0)$ limit. The red curves (—) represent the Fourier transforms of the FPMD data sets with a cutoff value set at the experimental value of Q_{max}= 21.5 Å^{-1} for ambient or Q_{max}= 20.5 Å^{-1} for $P \geq 3$ GPa.

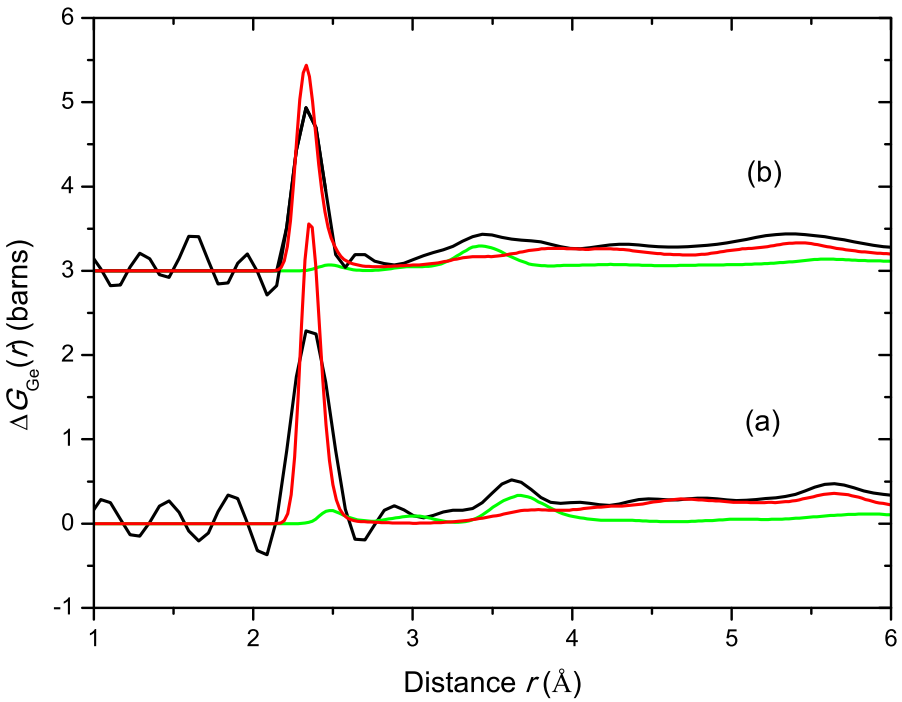

Figure 7-13: A comparison of: (a) $\Delta G_{\mathrm{Ge}}(r)$ + $\Delta G_{\mathrm{Ge}}(0)$ (—) at ambient pressure from neutron diffraction with the weighted partial pair distribution functions $0.237(4)g_{\mathrm{GeSe}}(r)$ (—) and $0.099(2)g_{\mathrm{GeGe}}(r)$ (—) obtained from the FPMD simulation; (b) $\Delta G_{\mathrm{Ge}}(r)$ + $\Delta G_{\mathrm{Ge}}(0)$ + 3 barns(—) at 8.2 GPa from neutron diffraction with the weighted pair distribution functions $0.237(4)g_{\mathrm{GeSe}}(r)$ + 3 barns (—) and $0.099(2)g_{\mathrm{GeGe}}(r)+3$ barns (—) obtained from the FPMD simulation at 7.98 GPa.

The last set of difference functions $\Delta F_{\mathrm{Se}'}(Q)$ are plotted in figure 7-14 for the ambient to 8.2 GPa pressure range, while the corresponding real space difference functions $\Delta G_{\mathrm{Se}'}(r)$ are shown in figure 7-15. A FSDP at $Q_1 \sim 1.0$ Å^{-1} is not found in the $\Delta F_{\mathrm{Se}'}(Q)$ functions. At ambient pressure, the PP is at $Q_2 \sim 2.04(2)$ Å^{-1}, the third peak is at $Q_3 \sim 3.50(2)$ Å^{-1} and the fourth peak is at $Q \sim 5.30(2)$ Å^{-1}. These peaks shift towards higher Q values by approximately 0.20(2) Å as the pressure is increased to 8.2 GPa, and the oscillations beyond the fourth peak are heavily dampened above a pressure of 3 GPa.

The low and high pressure $\Delta G_{\mathrm{Se}'}(r)$ functions from experiment are compared to the calculated weighted partial pair distribution functions from FPMD in figure 7-16. Although the first Ge-Se peak is completely removed, it is difficult to discriminate any features that arise from homopolar Ge-Ge or Se-Se bonds from the small r oscillations at high pressure. The second peak shift from $r_2 = 3.90(2)$ Å at ambient pressure to $r_2 = 3.63(2)$ Å at $P = 8.2$ GPa is consistent with the behaviour of the second peak in $\Delta G_{\mathrm{Se}}(r)$.

The major peak positions in Q and r space as measured for the $\Delta F_{\mathrm{X}}(Q)$ and $\Delta G_{\mathrm{X}}(r)$ functions, with X = Se, Ge, Se$'$, are summarised in table 7.7.

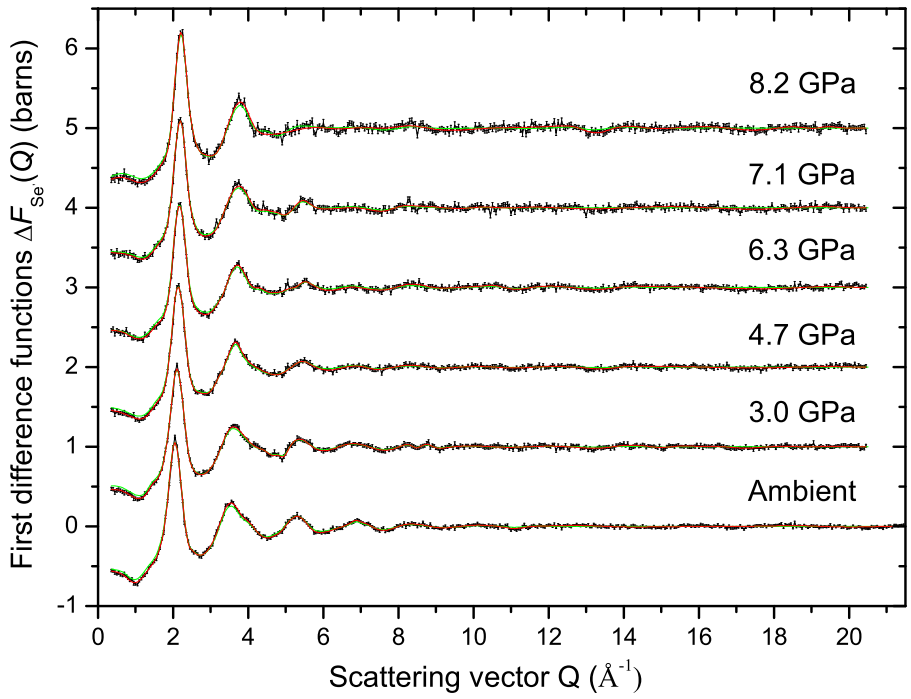

Figure 7-14: The difference functions $\Delta F_{\mathrm{Se}'}(Q)$ as measured for samples in a vanadium can by Petri *et al.* [138] and in the PE press at ambient and pressures up to 8.2 GPa. The solid black curves (—) with vertical error bars represent the unsmoothed difference functions, the solid green curves (—) represent Harwell spline fitted data sets after a cosine window function has been applied over the Q range from 19.0–21.5 Å^{-1} for ambient or from 19.0–20.5 Å^{-1} for $P \geq 3$ GPa, and the solid green curves represent the Fourier back transforms of the $\Delta G_{\mathrm{Se}'}(r)$ functions shown in figure 7-12 after the unphysical oscillations at $r \leq 2.21$ Å have been set to the calculated $\Delta G_{\mathrm{Se}'}(0)$ limit. The experimental data sets are compared to FPMD simulations (—) at similar densities corresponding to ambient pressure and to pressures of 3.4, 4.88, 7.25, 8.73 and 9.87 GPa (see table 7.4).

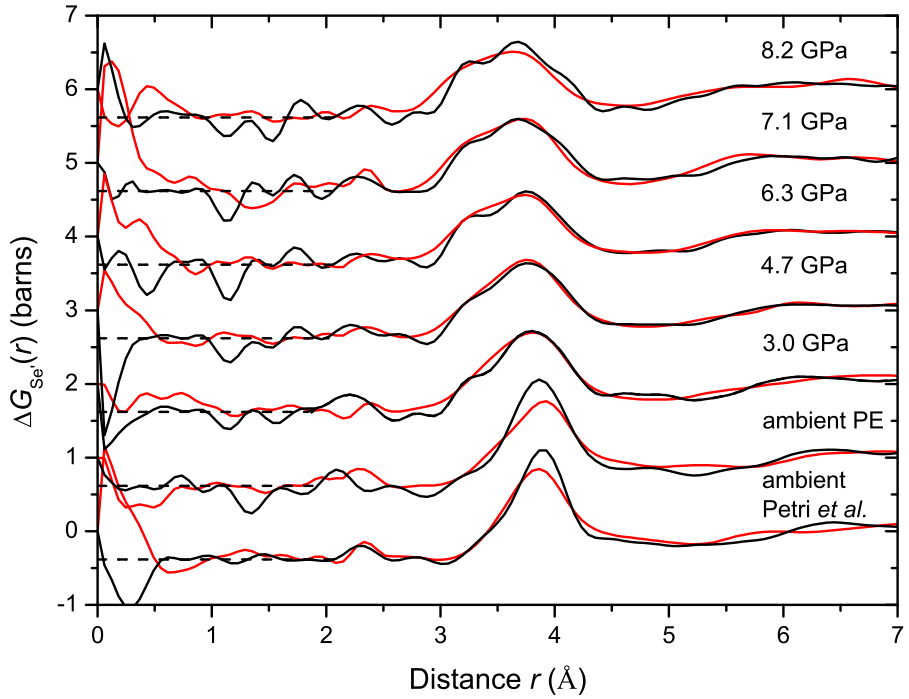

Figure 7-15: The pressure dependence of the difference functions $\Delta G_{\mathrm{Se}'}(r)$ (——) as obtained by Fourier transforming the difference functions $\Delta F_{\mathrm{Se}'}(Q)$ shown in figure 7-14 by the solid green curves (——). The solid black curves (——) show the extent of the low r oscillations while the horizontal black broken curves (- - -) give the calculated $\Delta G_{\mathrm{Se}'}(0)$ limit. The red curves (——) represent the Fourier transforms of the FPMD data sets with a cutoff value of experimental value of Q_{max}= 21.5 Å^{-1} for ambient or Q_{max}= 20.5 Å^{-1} for $P \geq 3$ GPa.

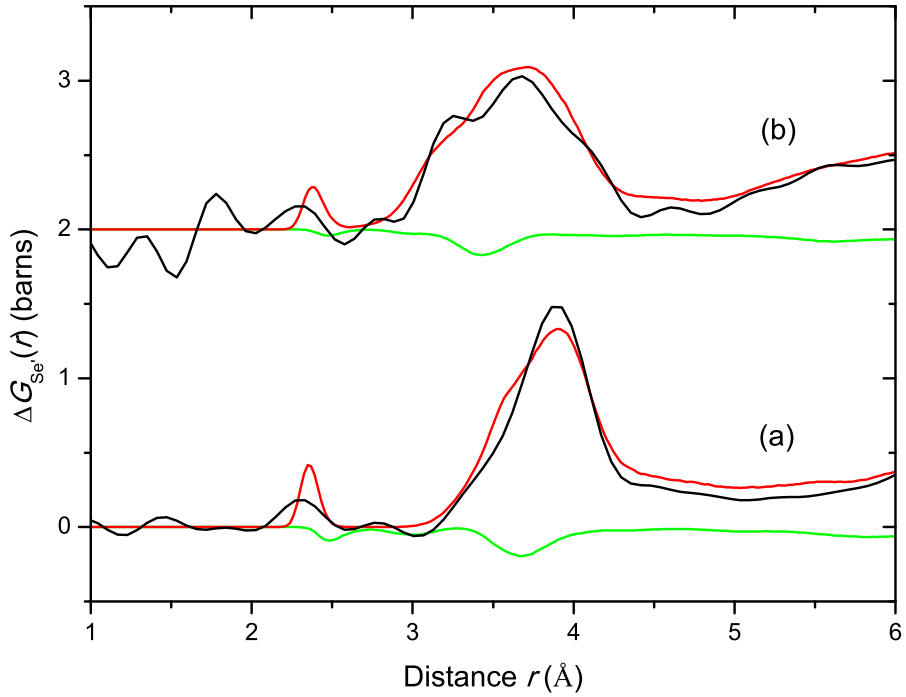

Figure 7-16: A comparison of: (a) $\Delta G_{Se'}(r)$-$\Delta G_{Se'}(0)$ (—) at ambient pressure from neutron diffraction with the weighted pair distribution functions -0.057(14)$g_{GeGe}(r)$ (—)and 0.442(11)$g_{SeSe}(r)$(—) obtained from the FPMD simulation; (b) $\Delta G_{Se'}(r)$-$\Delta G_{Se'}(0)$ + 2 barns (—) at 8.2 GPa from neutron diffraction with the weighted pair distribution functions -0.057(14)$g_{GeGe}(r)$(—) and 0.442(11)$g_{SeSe}(r)$(—) obtained from the FPMD simulation at 7.98 GPa.

Table 7.7: The leading peak positions Q_1 Q_2 and Q_3 in the measured difference functions $\Delta F_X(Q)$ {X = Se, Ge or Se′} plotted in figures 7-8, 7-11 and 7-14 for $GeSe_2$ glass for pressures of 0–8.2 GPa. The leading peak positions r_1 and r_2 from the corresponding $\Delta G_X(r)$ functions plotted in figures 7-9, 7-12, 7-15 are also given, together with the Se-Ge-Se and Ge-Se-Ge bond angles as obtained by using the cosine rule.

P	Number density ρ	$\Delta F_{Se}(Q)$			$\Delta G_{Se}(r)$			
(GPa)	(Å^{-3})	Q_1(Å^{-1})	Q_2(Å^{-1})	Q_3(Å^{-1})	r_1(Å)	r_2(Å)	r_2/r_1	Se-$\widehat{\text{Ge}}$-Se (°)
V can	0.0334(1)	1.05(2)	2.05(2)	3.53(2)	2.35(2)	3.89(2)	1.66(2)	108(2)
0.0(5)	0.0334(1)	1.01(2)	2.05(2)	3.54(2)	2.38(2)	3.85(2)	1.62(2)	111(2)
3.0(5)	0.0396(2)	1.08(2)	2.10(2)	3.61(2)	2.35(2)	3.78(2)	1.61(2)	108(2)
4.7(5)	0.0428(2)	1.15(2)	2.13(2)	3.66(2)	2.34(2)	3.73(2)	1.59(2)	104(2)
6.3(5)	0.0455(2)	1.25(2)	2.18(2)	3.70(2)	2.34(2)	3.69(2)	1.58(2)	104(2)
7.1(5)	0.0469(2)	1.25(2)	2.19(2)	3.72(2)	2.35(2)	3.68(2)	1.57(2)	103(2)
8.2(5)	0.0489(2)	1.35(2)	2.21(2)	3.79(2)	2.35(2)	3.66(2)	1.56(2)	102(2)

P	Number density ρ	$\Delta F_{Ge}(Q)$			$\Delta G_{Ge}(r)$			
(GPa)	(Å^{-3})	Q_1(Å^{-1})	Q_2(Å^{-1})	Q_3(Å^{-1})	r_1(Å)	r_2(Å)	r_2/r_1	Ge-$\widehat{\text{Se}}$-Ge (°)
V can	0.0334(1)	1.00(2)	–	3.53(2)	2.36(2)	3.63(2)	1.54	101(2)
0.0(5)	0.0334(1)	1.01(2)	–	3.55(2)	2.35(2)	3.55(2)	1.48	95(2)
3.0(5)	0.0396(2)	1.08(2)	–	3.61(2)	2.35(2)	3.51(2)	1.47	95(2)
4.7(5)	0.0428(2)	1.13(2)	–	3.67(2)	2.35(2)	3.51(2)	1.48	95(2)
6.3(5)	0.0455(2)	1.23(2)	–	3.73(2)	2.35(2)	3.48(2)	1.47	94(2)
7.1(5)	0.0469(2)	1.26(2)	–	3.75(2)	2.34(2)	3.45(2)	1.46	94(2)
8.2(5)	0.0489(2)	1.27(2)	–	3.73(2)	2.34(2)	3.45(2)	1.46	94(2)

P	Number density ρ	$\Delta F_{Se'}(Q)$			$\Delta G_{Se'}(r)$	
(GPa)	(Å^{-3})	Q_1 (Å^{-1})	Q_2 (Å^{-1})	Q_3 (Å^{-1})	r_1 (Å)	r_2(Å)
V can	0.0334(1)	–	2.05(3)	3.53(5)	–	3.90(3)
0.0(5)	0.0334(1)	–	2.05(3)	3.54(4)	–	3.87(3)
3.0(5)	0.0396(2)	–	2.10(3)	3.61(4)	–	3.80(3)
4.7(5)	0.0428(2)	–	2.13(3)	3.66(4)	–	3.69(3)
6.3(5)	0.0455(2)	–	2.18(3)	3.70(4)	–	3.74(3)
7.1(5)	0.0469(2)	–	2.19(3)	3.72(4)	–	3.74(3)
8.2(5)	0.0489(2)	–	2.21(3)	3.79(4)	–	3.63(3)

7.5 Discussion

FPMD gives an excellent account of the measured total structure factors, as shown in figures 7-2, 7-4 and 7-6, and of the measured difference functions, as shown in figures 7-8, 7-11 and 7-14.

The mean nearest-neighbour peak positions r_1 and coordination numbers $\bar{n}$ from the NDIS experiment (see figure 7-17((a)-(b))) and the FPMD simulations are in agreement within the experimental error for pressures up to $\sim$ 8 GPa. At higher pressures, the results obtained from PEARL diffraction experiments [188] and from FPMD both show an increase in $\bar{n}$ as the first coordination shell expands in order to accommodate a larger number of nearest neighbours. This process starts at $\sim$ 8.5 GPa from the FPMD results ($\rho/\rho_0 \sim 1.42$) as compared to $\sim$ 12 GPa ($\rho/\rho_0 \sim 1.55$) from the PEARL experiment [188]. The measured r_1 values are in agreement with x-ray diffraction data, although the x-ray value for $\bar{n}$ at the highest pressure of 9.3 GPa is larger than found in the PEARL diffraction work [188]. However, these $\bar{n}$ values can be brought into agreement by removing an unphysical slope on the x-ray total structure factors and renormalising (see Appendix).

The density dependence of the fractions of n-fold coordinated Ge and Se atoms (n = 2, 3, 4, 5 or 6) is given in figure 7-17((c)-(d)), and is broken down in figure 7-17((e)-(f)) into the fractions of these n-fold species that contain homopolar bonds. As the density is increased to $\rho/\rho_0 \sim 1.55$, there is no obvious tendency for a suppression of chemical disorder as suggested by previous work [184]. The intra-polyhedral Se-Ge-Se and inter-polyhedral Ge-Se-Ge bond angle distribution are shown in figures 7-18((a)-(b)), and the fractions of Ge atoms that are involved either in CS or ES motifs are given in figure 7-18(c). The CS motifs are denoted by Ge_0 while the ES motifs are broken down into their contributions from Ge_l (l = 1, 2, 3/4) centred polyhedra, where the l-value indicates the number of ES connections to other polyhedra. The following picture thereby emerges from the FPMD results for the different stages in the density-driven structural transformations of $GeSe_2$ glass.

In the first stage, as the density is increased from ambient to $\rho/\rho_0 = 1.42$, $\bar{n}$ remains constant but there are subtle changes in the CS to ES ratio of tetrahedral units. The mean inter-tetrahedral Ge-Se-Ge bond angle decreases from $\sim 103^\circ$ to $\sim 97^\circ$ for CS units but remains invariant for ES units at $\sim 79^\circ$ (figure 7-18(b)). This behavior is in contrast to the crystalline phase, where transitions are observed from an ambient pressure 2-D structure in which layers are formed from equal numbers of ES and CS tetrahedra [190], to 3-D structures of densely-packed CS tetrahedra [191, 192] (see figure 7-19). Higher

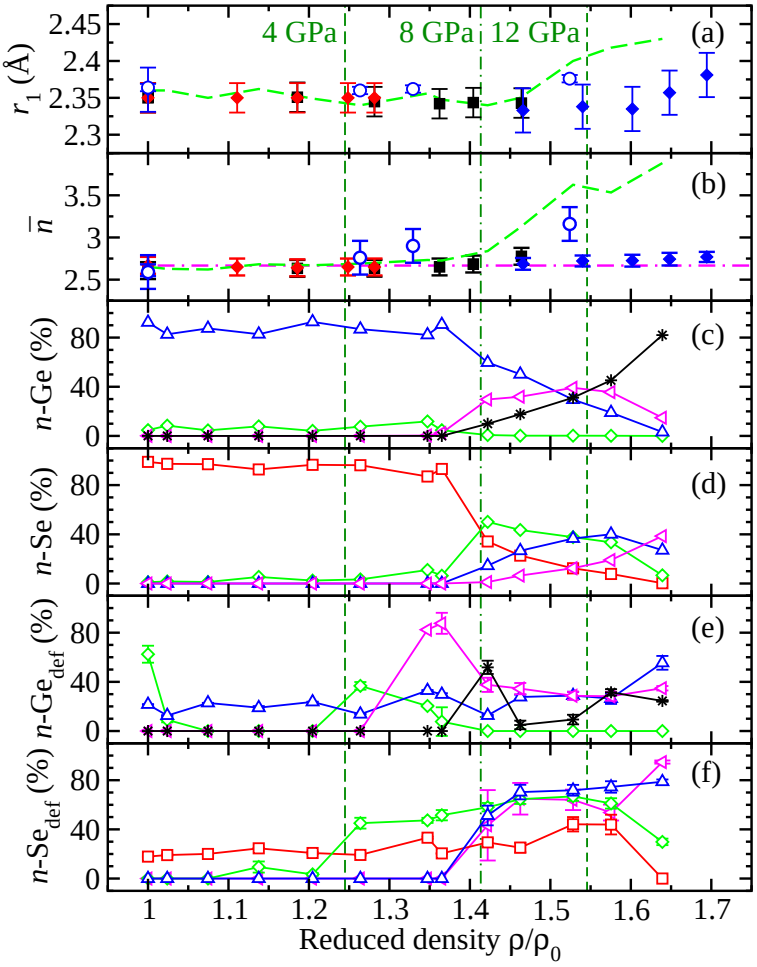

Figure 7-17: The ρ/ρ_0 dependence of the mean nearest-neighbor (a) bond distance r_1 and (b) mean coordination number $\bar{n}$ as obtained from (i) neutron diffraction with a $^{N}Ge^{N}Se_2$ sample and either the D4c (♦) or PEARL (♦) diffractometer [188], or with $^{70}Ge^{N}Se_2$ and $^{73}Ge^{76}Se_2$ samples measured on D4c and averaging the results (■); (ii) x-ray diffraction [138] (○); or (iii) molecular dynamics simulations by integrating the $g_{\alpha\beta}(r)$ functions to the first minimum in the total pair-distribution function (- - -). In (b) the horizontal chained line (-·-·-) gives the "8-N" rule expectation of $\bar{n} = 2.67$ (see §7.1.1). From the simulations, the ρ/ρ_0 dependence is also given for the fractions of n-fold coordinated (c) Ge atoms and (d) Se atoms, along with the fractions of these n-fold coordinated (e) Ge and (f) Se atoms that contain homopolar bonding defects. In (c)-(f) the symbols denote 2-fold (□), 3-fold (◇), 4-fold (△), 5-fold (◁) or 6-fold (∗) coordinated species, and the error bars, calculated using the method described in reference [189], are usually smaller than the symbol size. The vertical broken lines correspond to pressures of ∼ 4, 8 and 12 GPa.

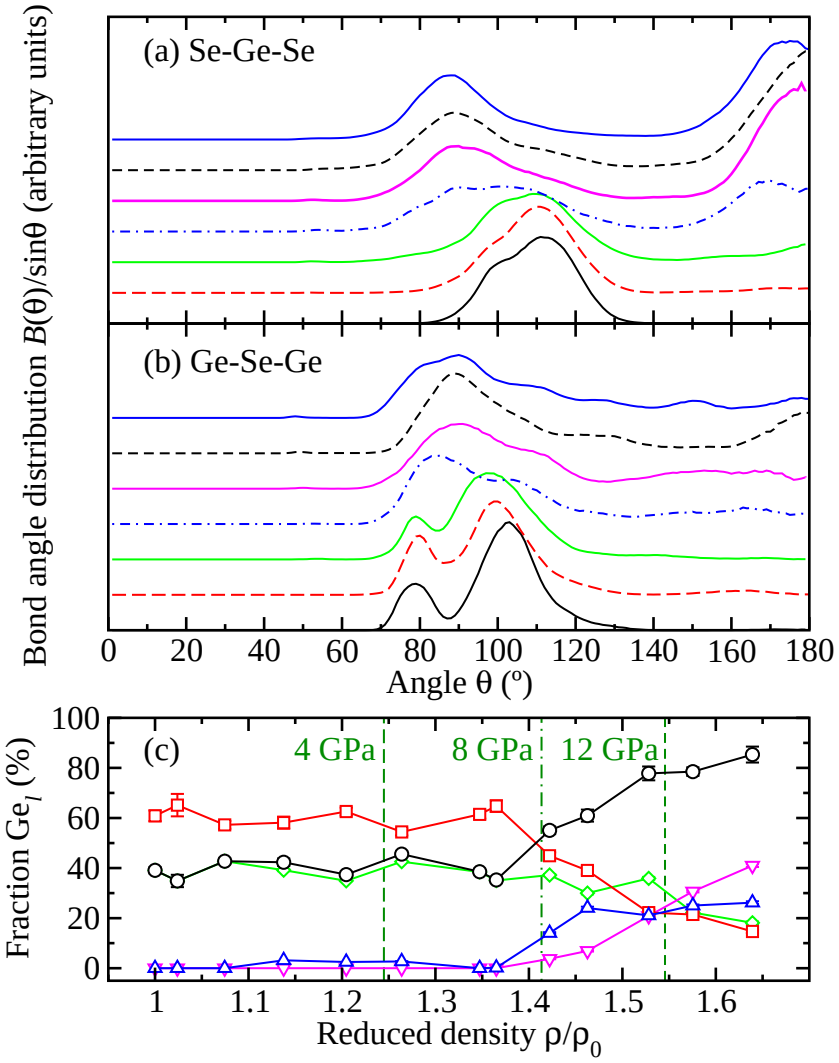

Figure 7-18: The ρ/ρ_0 dependence of (a) the intra-polyhedral Se-Ge-Se and (b) inter-polyhedral Ge-Se-Ge bond angle distributions where, from bottom to top in each panel, ρ/ρ_0 = 1, 1.204, 1.365, 1.423, 1.463, 1.528, 1.575 or 1.639. In (c) the corresponding ρ/ρ_0 dependence of the fractions of CS Ge atoms G_0, (□) and ES Ge atoms (○) is given together with a breakdown of the latter into their contributions from Ge_1 (◇), Ge_2 (△) and $Ge_{3/4}$ (▽) units. In (c) the error bars were calculated using the method described in reference [189] and are usually smaller than the symbol size, and the vertical broken lines corresponds to pressures of ∼ 4, 8 and 12 GPa.

temperatures are usually required to facilitate these transitions [191–193].

In the second stage, as the density is increased beyond $\rho/\rho_0 = 1.42$, $\bar{n}$ increases with r_1 and there is a monotonic reduction in the CS to ES ratio (figure 7-18(c)). Four-fold coordinated Ge atoms make way for 5-fold and 6-fold coordinated Ge atoms and, in order to maintain glass stoichiometry, 2-fold coordinated Se atoms make way for higher coordinated Se atoms (figure 7-17(c)), many of which form homopolar bonds (figure 7-17(f)).

Antao *et al.* [111] found a change in the elastic properties of $GeSe_2$ glass around $\rho/\rho_0 \simeq 1.24$ ($P = 4$ GPa) from *in situ* acoustic experiments. A minimum was inferred for the network rigidity at $\simeq 4$ GPa, originating from a competition between two densification mechanisms: a conversion from ES to CS tetrahedra which initially enhances the network flexibility versus an increase in $\bar{n}$ which stiffens the network [111]. An increase in the CS to ES ratio from 1.3 to 1.7 in the range $\rho/\rho_0 \sim 1.07$–1.20 (P 1.29–3.55 GPa), consistent with the trend observed by Raman spectroscopy [169], is found from the FPMD results. However, since the present work shows that $\bar{n}$ does not increase until $\rho/\rho_0 \gtrsim 1.42$ ($P \sim 8.5$ GPa), the stiffening mechanism is most likely related to more subtle changes in the network connectivity e.g. to an adjustment of the CS to ES ratio at $\rho/\rho_0 \sim 1.24$ ($P \sim 4$ GPa) (figure 7-18(c)).

Figure 7-20 shows typical atomistic configurations for different points in the densification process. When ρ/ρ_0 increases beyond 1.42, the Se atoms in Ge_0 motifs make additional bonds with their neighboring Ge_1 motifs, transforming the latter to 5-fold coordinated Ge_2 units having a distorted square pyramidal geometry. As these Ge_0 tetrahedra are removed, there is a broadening of the Se-Ge-Se bond angle distribution and a shift in its maximum from $\sim 111^\circ$ towards smaller angles, accompanied by a merger of the twin peaks in the Ge-Se-Ge bond angle distribution (figures 7-18(a)-(b)). Around $\rho/\rho_0 \sim 1.53$, the fraction of Ge_0 units continues to decrease rapidly to make way for more Ge_2 and a few $Ge_{3/4}$ type configurations, where many of the latter correspond to 6-fold coordinated Ge atoms. Accordingly, the main peak in the Se-Ge-Se bond angle distribution shifts to around 90° and a second peak appears near 180°. Eventually, the network develops a pseudo-cubic arrangement of Ge-centered units for which the main peak in the Ge-Se-Ge bond angle distribution is at $\sim 90^\circ$. In all of this, the fractions of defected 5-fold and 6-fold coordinated Ge atoms peak at densities around which these species first start to emerge (figure 7-17(e)) i.e. homopolar bonds mediate in the initial development of the higher-coordinated Ge-centered polyhedra.

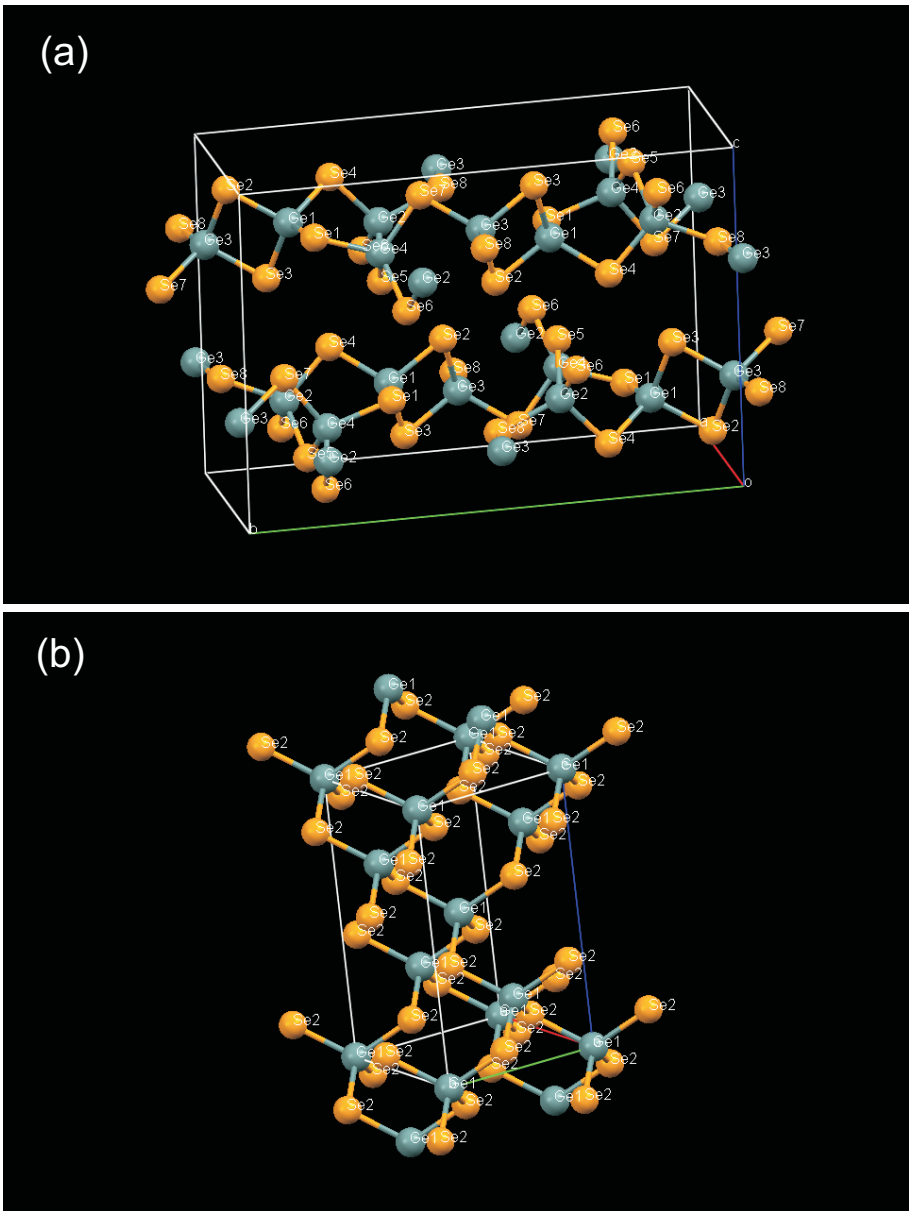

Figure 7-19: (a) The structure of crystalline $GeSe_2$ under ambient conditions as measured using x-ray diffraction by Dittmar and Schäfer [190]. (b) The structure of high pressure (6 GPa) and high temperature (741 °C) crystalline $GeSe_2$ as measured using *in situ* x-ray diffraction by Grzechnik *et al.* [191].

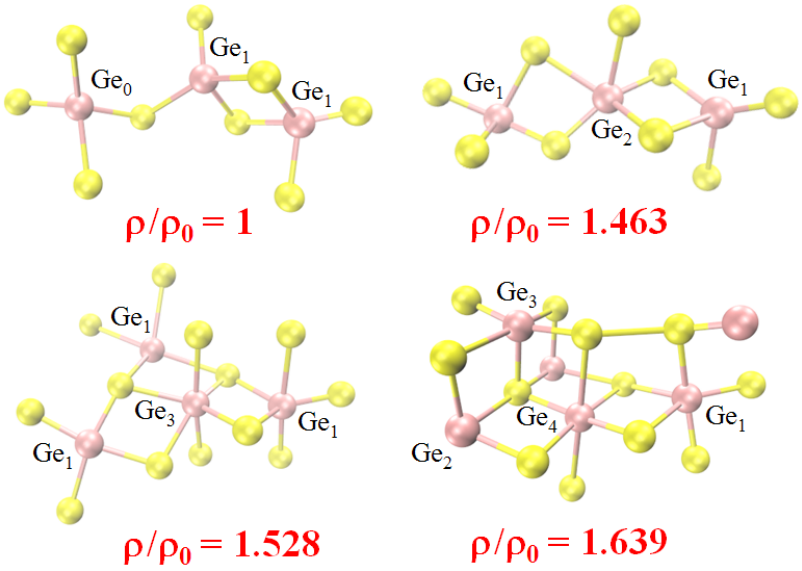

Figure 7-20: Atomistic configurations taken from the FPMD models for $GeSe_2$ glass at different reduced densities. Ge atoms are dark (•) and Se atoms are light (•). Bonds are drawn when two atoms are separated by a cutoff distance given by the position of the first minimum in $g_{GeSe}(r)$.

7.6 Conclusions

In summary, the density-driven structural transformations in $GeSe_2$ glass differ substantially from those observed in common oxide glasses such as GeO_2 (Chapter 4), SiO_2 (Chapter 5) and B_2O_3 (Chapter 6). For example, in $GeSe_2$ glass ES motifs remain numerous over the density range for which the chemical species retain their ambient pressure coordination numbers, in contrast to oxide glasses where CS conformations dominate (Chapter 4) [85, 116, 194, 195]. At larger pressures, in $GeSe_2$ glass 5- and 6-fold coordinated Ge atoms start to form at a similar density, unlike MO_2 glasses (M = Si or Ge) where densification proceeds first by the formation of MO_5 units and then by the formation of MO_6 units [173] (or see Chapter 4) [85, 116]. Also in $GeSe_2$ glass homopolar bonds play an intimate role in the formation of higher coordinated polyhedra, in contrast to oxide glasses where the chemical order is retained [173] (and Chapter 4) [85, 116, 194, 195]. The stability under load of ES conformations, which promote the fragility of glass forming materials [62], and the importance of homopolar bonding defects in mediating the transformations to higher-coordinated polyhedra, are likely to be common features in the density-driven network collapse for the class of e.g. chalcogenide glass-forming materials where ES motifs and homopolar bonds are prevalent in

the ambient pressure network [5, 158, 159].

7.7 Appendix

7.7.1 X-ray data before and after slope removal

The comparison in figure 7-21 between the x-ray [138] and neutron total structure factors, denoted by $S_X(Q)$ and $S_N(Q)$ respectively, shows that the X-ray data sets have a residual slope, a feature that also manifests itself in r-space at low r (figure 7-22). The slope was removed by setting the few first large amplitude low r oscillations to $G_X(0)$= -1 and back Fourier transforming.

The slope corrected reciprocal data sets denoted by $S^*_X(Q)$ (see figure 7-23) were then scaled and Fourier transformed in order to ensure that the low r wriggles oscillate symmetrically around the $G_X(0)$= -1 limit, resulting in functions denoted by $G^*_X(r)$ (see figure 7-24). The lowest r wriggles in the $G^*_X(r)$ functions were then set to the $G_X(0)$ limit and back Fourier transformed to check for agreement with the slope corrected $S^*_X(Q)$ functions. The first peak r_1 and coordination number $\bar{n}$, before and after the slope correction are summarised in table 7.8.

Table 7.8: The pressures P and densities ρ at which x-ray diffraction measurements on $GeSe_2$ glass were made by Mei *et al* [138]. The distance r_1 and coordination number $\bar{n}$ at each pressure points are given (I) before and (II) after slope correction.

(I)				
Pressure	Number density	Reduced density	Distance	Coordination number
P(GPa)	ρ (Å^{-3})	ρ/ρ_0	$r_1 G_X(r)$(Å)	$\bar{n}$
0	0.0334	1.000	2.36(2)	2.59(2)
3.9	0.0422	1.263	2.36(2)	2.76(2)
5.3	0.0444	1.329	2.36(2)	2.90(2)
9.3	0.0509	1.523	2.38(2)	3.16(2)
(II)				
Pressure	Number density	Reduced density	Distance	Coordination number
P(GPa)	ρ (Å^{-3})	ρ/ρ_0	$r_1 G_X(r))$(Å)	$\bar{n}$
Ambient	0.0334	1.000	2.35(2)	2.65(10)
3.9	0.0422	1.263	2.39(2)	2.65(10)
5.3	0.0444	1.329	2.37(2)	2.68(10)
9.3	0.0509	1.523	2.38(2)	2.87(10)

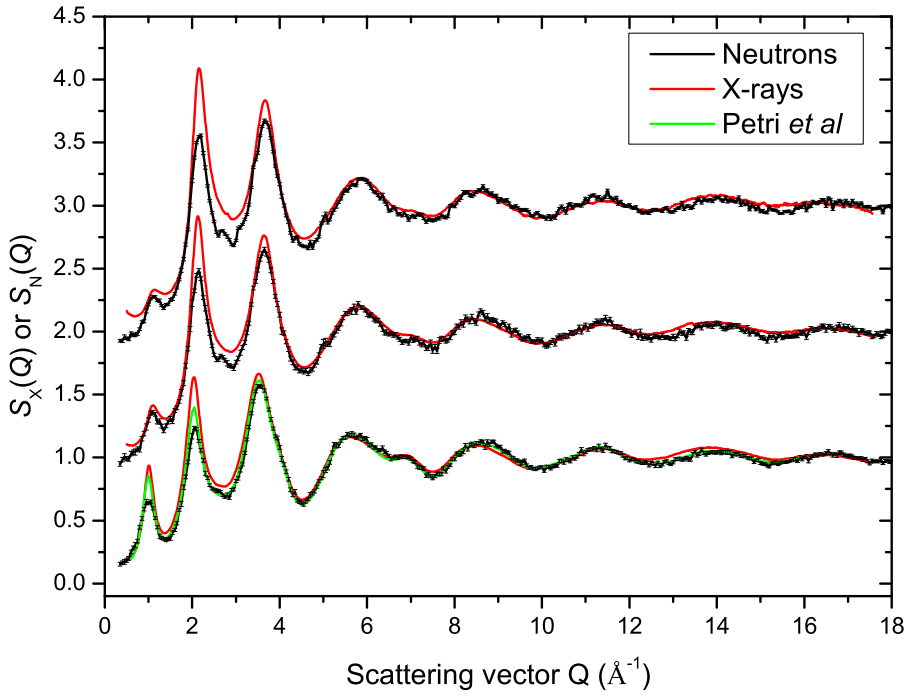

Figure 7-21: A comparison between the total x-ray structure factors $S_X(Q)$ of Mei *et al.* [138] (——) and the total neutron structure factors $S_N(Q)$ (——) taken from the PE experiment and from the ambient pressure work by Petri *et al.* [164] (——). The comparisons are made between data sets measured (a) under ambient conditions, (b) at 3.9 GPa and (c) at 5.3 GPa(——) versus 4.7 GPa (——).

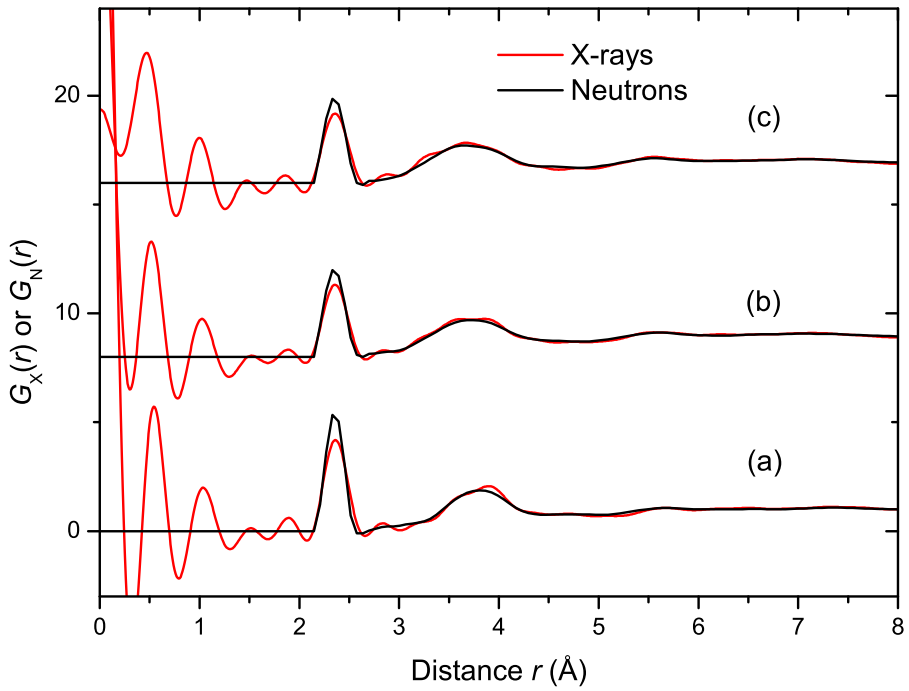

Figure 7-22: Comparison between the total x-ray pair distribution functions $S_X(Q)$ of Mei *et al.* [138] (—) and the total neutron pair distribution functions $G_N(r)$ (—) from the PE experiments. The comparisons are made between data sets measured (a) under ambient conditions, (b) at 3.9 GPa and (c) at 5.3 GPa(—) versus 4.7 GPa (—).

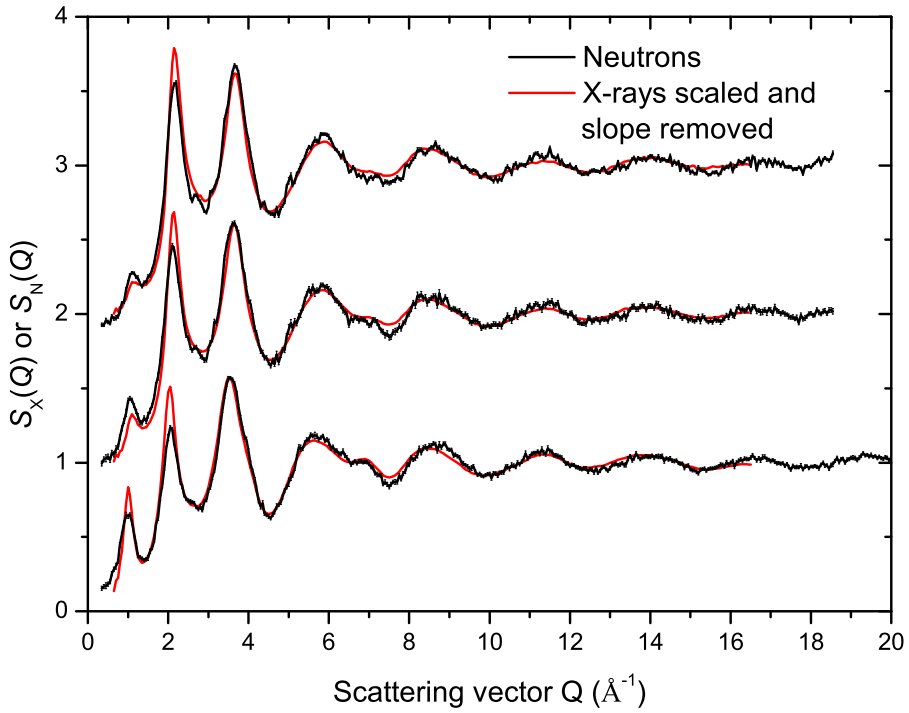

Figure 7-23: Comparison between the slope corrected total x-ray structure factors $S^{*}_{\mathrm{X}}(Q)$ (——) and the neutron total structure factors $S_{\mathrm{N}}(Q)$ (——) from the PE experiment. The comparisons shown are made between data sets measured (a) under ambient conditions, (b) at 3.9 GPa and (c) at 5.3 GPa (——) versus 4.7 GPa (——).

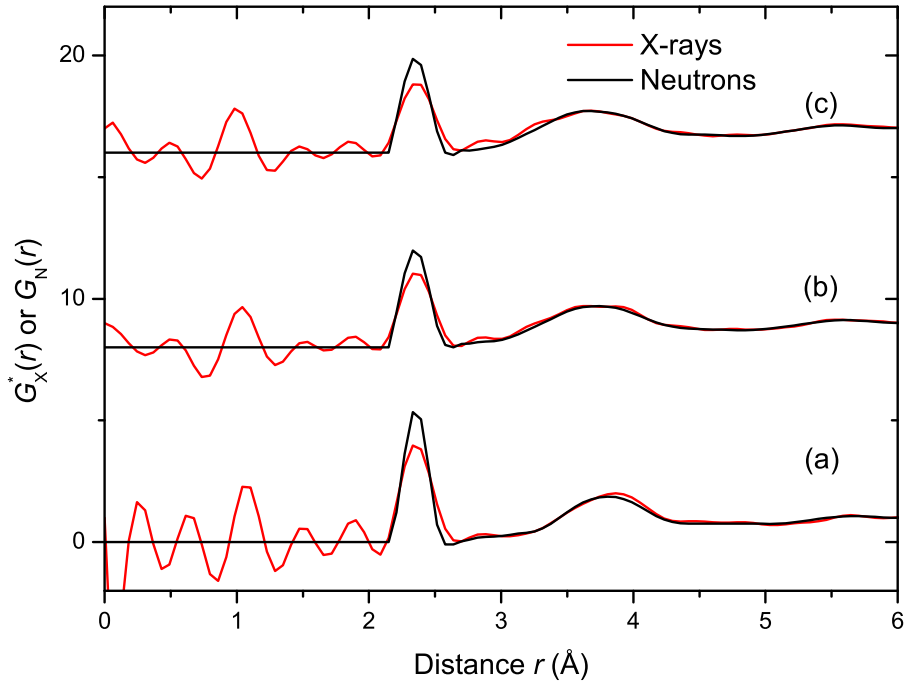

Figure 7-24: Comparison between the slope corrected total x-ray pair distribution functions $G^*_X(r)$ (—) and the total neutron pair distribution functions $G_N(r)$ (—) from the PE experiment. The comparisons are made between data sets measured (a) under ambient conditions, (b) at 3.9 GPa and (c) at 5.3 GPa (—) versus 4.7 GPa (—).

Chapter 8

Overall Conclusions

In this thesis *in situ* neutron diffraction was employed to provide new information on the mechanisms of density-driven structural transformation in the glassy materials GeO_2, $GeSe_2$, SiO_2 and B_2O_3. The majority of the neutron diffraction work employed the diffractometer D4c at the ILL with a Paris-Edinburgh press which enabled the pressure range from ambient to 8 GPa to be accessed. The pressure range was extended to 17.5 GPa by using the PEARL diffractometer at ISIS following measurements and data analysis protocols reported in the reference [13]. In the cases of GeO_2 and $GeSe_2$ glass, the NDIS method was developed to provide benchmark experimental results to test the results obtained from various molecular dynamics simulations using different theoretical schemes. The main results from this thesis are summarised as following.

In Chapter 4, the diffraction patterns for isotopically enriched samples of GeO_2 glass were measured. The NDIS method was used, for the first time, to help disentangle the structural complexity of GeO_2 glass under *in situ* high-pressure conditions up to 8 GPa. The experimental information that was obtained from the NDIS method provided a strong foundation to test several computer simulation models for the structure of this material [12, 79–84, 100]. It was found that excellent overall agreement with the experimental results was obtained by using the DIPPIM interaction potentials [12] which led to a reproduction of the measured nearest neighbour Ge-O bond distances and coordination numbers, the nearest neighbour O-O distance and coordination number, the nearest neighbour Ge-Ge distance and the peaks in the Ge-O-Ge and O-Ge-O bond angle distributions. The combined diffraction and DIPPIM results show that the density increase initially occurs through a reorganisation of corner-shared GeO_4 tetrahedra on an intermediate length scale as the pressure is increased from ambient to 5 GPa. At higher pressures, there is a progression from a tetrahedral to an octahedral glass, via the

formation of 5-fold coordinated Ge-atoms which have a predominantly square pyramidal geometry.

In Chapter 5, accurate neutron total structure factors $F(Q)$ were presented for glassy SiO_2. Pressures up to ~ 8 GPa were accessed by using the D4c instrument and pressures up to 14.5 GPa were accessed by using the PEARL diffractometer. Parameters such as the FSDP position Q_{FSDP}, the mean nearest neighbour Si-O bond distance r_{SiO} and coordination number $\bar{n}^{\mathrm{O}}_{\mathrm{Si}}$ were found to be in agreement with those obtained from the x-ray diffraction work by Benmore *et al.* [121] within the measured pressure range. Both sets of experimental results reveal a self consistent story where the principal mechanism for the densification of SiO_2 glass at pressures up to ~ 15 GPa occurs through a change in the intermediate range ordering of SiO_4 tetrahedra. This is manifested by a shift of the FSDP towards larger Q values and a decrease in its height. Recent molecular dynamics simulations by Wilson [135] will help to illuminate the densification processes in SiO_2 glass for the low-pressure region of constant network topology and beyond. All of this will help to distinguish the mechanisms of structural collapse in SiO_2 and related glasses to those found in other network glass-forming materials.

In Chapter 6, the results from *in situ* high pressure neutron diffraction experiments on B_2O_3 glass up to 17.5 GPa were presented. Accurate total structure factors $F(Q)$ were measured using the D4c diffractometer at pressures up to 8 GPa and the PEARL diffractometer at pressures of 17.5 GPa. Parameters such as the FSDP position Q_{FSDP}, the mean nearest neighbour B-O bond distance r_{BO} and the coordination number $\bar{n}^{\mathrm{O}}_{\mathrm{B}}$ were found to be in agreement with those obtained from the x-ray diffraction work by Brazhkin *et al.* [146] and the inelastic x-ray scattering work by Lee *et al.* [145] within measured pressure range. The principal mechanism for the densification of B_2O_3 at pressures up to ~ 8 GPa occurs through changes in the IRO as manifested by a reduction in height of the FSDP and a shift in its position towards higher Q values in the measured total structure factors $F(Q)$. The *in situ* Raman and Brillouin investigation by Nicolas *et al.* [143] and the *in situ* Raman investigation by Grimsditch *et al.* [11] show that these changes in the IRO are associated with the removal of boroxyl rings with increasing pressure. The breakdown of boroxol rings is indicated by the disappearance of the boroxol ring breathing mode in the Raman spectra at a wavenumber of 808 cm^{-1}. At higher pressures (> 8 GPa) the densification of B_2O_3 proceeds via the appearance of 4-fold coordinated boron atoms which leads to an increase in the average B-O bond distance r_{BO} and coordination number $\bar{n}^{\mathrm{O}}_{\mathrm{B}}$. Existing molecular dynamics simulations [146, 148] do not reproduce the measured B-O coordination number change with increasing density due to the difficulty in simulating boroxol rings. Indeed, the available

molecular dynamics simulations do not give a sufficiently large fraction of boroxol rings for the ambient pressure glass, and they are not therefore expected to give a realistic description of the changes that occur in the glass structure with increasing density. To fully understand/ellucidate the role of boroxol rings in the densification of B_2O_3 glass, it is desirable to conduct further *in situ* x-ray diffraction experiments that span the pressure range of the new neutron diffraction measurements, and to make new molecular dynamics studies to give results that are in better agreement with experiment.

In Chapter 7, the chalcogenide glass $GeSe_2$ was investigated at pressures up to 8.2 GPa using the *in situ* high-pressure NDIS method, and the results were augmented by data from the PEARL diffractometer for pressure up to 16.1 GPa. The experimental work was complemented by first-principles molecular dynamics simulations which employed the Becke-Lee-Yang-Parr functional [15, 16]. The combined experimental and molecular dynamics approach provides new insights into the nature of the density-driven network collapse. For example, edge sharing (ES) motifs remain numerous as the pressure is increased from ambient up to ~ 8 GPa and structural changes are manifested by a reorganisation of edge and corner-sharing $GeSe_4$ tetrahedra on an intermediate range order length scale. Above this pressure threshold, 5- and 6-fold coordinated Ge atoms start to form at a similar density and homopolar bonds play an intimate role in the formation of these higher coordinated polyhedra. The stability under load of ES conformations, which promote the fragility of glass-forming materials [62], and the importance of homopolar bonding defects in mediating the transformations to higher-coordinated polyhedra, are likely to be common features in the density-driven network collapse for the class of e.g. chalcogenide glass-forming materials where ES motifs and homopolar bonds are prevalent in the ambient pressure network [5, 158, 159]. The densification mechanisms for $GeSe_2$ glass differ substantially from those observed in common oxide glasses such as GeO_2, SiO_2 and B_2O_3.

The results presented in this thesis show that the *in situ* high pressure neutron diffraction method can be used to successfully measure the detailed structure of glassy materials at pressure up to 8 GPa and beyond. In particular, the results show that it is possible to apply the NDIS method to simplify the complexity of correlations associated with the measurement of a single diffraction pattern. This paves the way for future investigations of other glassy (e.g. different compositions of Ge_xSe_{1-x} glass where $0 \leqslant x \leqslant 1$) and indeed liquid materials under high pressure conditions, where interesting materials include water and ionic-solutions.

Bibliography

[1] P. W. Bridgman and I. Simon. Effects of very high pressures on glass. *Journal of Applied Physics*, 24(4):405, 1953.

[2] S. Minomura, editor. *Solid State Physics under Pressure: Recent Advances with Anvil Devices*. KTK Scientific Publishers, Japan, 1985.

[3] Wilfried B. Holzapfel and Neil S. Isaacs, editors. *High-Pressure Techniques in Chemistry and Physics: A Practical Approach*. Oxford University Press, New York, 1997.

[4] Stefan Klotz. *Techniques in High Pressure Neutron Scattering*. CRC Press, Boca Raton, 2013.

[5] G. N. Greaves and S. Sen. Inorganic glasses, glass-forming liquids and amorphizing solids. *Advances in Physics*, 56:1–166, 2007.

[6] C. A. Angell. Formation of glasses from liquids and biopolymers. *Science*, 267(5206):1924, 1995.

[7] V. V. Brazhkin and A. G. Lyapin. High-pressure phase transformations in liquids and amorphous solids. *Journal of Physics: Condened Matter*, 15:6059, 2003.

[8] M. C. Wilding, M. Wilson, and P. F. McMillan. Structural studies and polymorphism in amorphous solids and liquids at high pressure. *Chemical Society Reviews*, 35:964, 2006.

[9] G. Parthasarathy and E. S. R Gopal. Effect of high pressure on chalcogenide glasses. *Bulletin of Materials Science*, 7:271, 1985.

[10] H. E. Fischer, A. C. Barnes, and P. S. Salmon. Neutron and x-ray diffraction studies of liquids and glasses. *Reports on Progress in Physics*, 69:233, 2006.

[11] M. Grimsditch, A. Polian, and A. C. Wright. Irreversible structural changes in vitreous B_2O_3 under pressure. *Physical Review B*, 54:152, 1996.

[12] D. Marrocchelli, M. Salanne, P. A. Madden, C. Simon, and P. Turq. The construction of a reliable potential for GeO_2 from first principles. *Molecular Physics*, 107(4-6):443, 2009.

[13] P. S. Salmon, J. W. E. Drewitt, D. A. J. Whittaker, A. Zeidler, K. Wezka, C. L. Bull, M. G. Tucker, M. C. Wilding, M. Guthrie, and D. Marrocchelli. High pressure neutron diffraction study of GeO_2 glass up to 17.5 GPa. *Journal of Physics: Condensed Matter*, 24:415102, 2012.

[14] A. C. Hannon, D. I. Grimley, R. A. Hulme, A. C. Wright, and R. N. Sinclair. Boroxol groups in viterous boron oxide: new evidence from neutron diffraction and inelastic neutron scattering studies. *Journal of Non-Crystalline Solids*, 177:299, 1994.

[15] A. D. Becke. Density-functional exchange-energy approximation with correct asymptotic behavior. *Physical Review A*, 38:3098, 1988.

[16] C. Lee, W. Yang, and R. G. Parr. Development of the Colle-Salvetti correlation-energy formula into a functional of the electron density. *Physical Review B*, 37:785, 1988.

[17] D. S. Sivia. *Elementary Scattering Theory For X-ray and Neutron Users*. Oxford University Press, New York, 2011.

[18] G. L. Squires. *An Introduction to the Theory of Thermal Neutron Scattering*. Cambridge University Press, Cambridge, 1978.

[19] G. E. Bacon. *Neutron Diffraction*. Clarendon, Oxford, 1975.

[20] V. F. Sears. Neutron scattering lengths and cross sections. *Neutron News*, 3(3):26–37, 1992.

[21] J. L. Yarnell, M. J. Katz, R. G. Wenzel, and S. H. Koenig. Structure Factor and Radial Distribution Function for Liquid Argon at 85 °K. *Physical Review A*, 7:2130, 1973.

[22] T. E. Faber and J. M. Ziman. A theory of the electrical properties of liquid metals. *Philosophical Magazine*, 11(109):153–173, 1965.

[23] E. Lorch. Neutron diffraction by germania, silica and radiation-damaged silica glasses. *Journal of Physics C: Solid State Physics*, 2:229, 1969.

[24] J. E. Enderby, D. M. North, and P. A. Egelstaff. The partial structure factors of liquid Cu-Sn. *Philosophical Magazine*, 14(131):961, 1966.

[25] D. L. Price and A. Pasquarello. Number of independent partial structure factors for a disordered n-component system. *Physical Review B*, 59:5–7, 1999.

[26] J. R. Westlake. *A Handbook of Numerical Matrix Inversion and Solution of Linear Equations*. New York: Wiley, 1968.

[27] D. A. Keen. A comparison of various commonly used correlation functions for describing total scattering. *Journal of Applied Crystallography*, 34(2):172–177, 2001.

[28] J. H. Hubbell, Wm. J. Veigele, E. A. Briggs, R. T. Brown, D. T. Cromer, and R. J. Howerton. Atomic form factors, incoherent scattering functions, and photon scattering cross sections. *Journal of Physical and Chemical Reference Data*, 4:471–538, 1975.

[29] Giovanna Cicognani, editor. *The Yellow Book 2008: Guide to Neutron Research Facilities*. Institut Laue-Langevin, Grenoble, 2008.

[30] H. E. Fischer, G. J. Guello, P. Palleau, D. Feltin, A.C. Barnes, Y. S. Badyal, and J. M. Simonson. D4c: A very high precision diffractometer for disordered materials. *Applied Physics A*, 74:S160, 2002.

[31] J. W. E. Drewitt, P. S. Salmon, A. C. Barnes, S. Klotz, H. E. Fischer, and W. A. Crichton. Structure of GeO_2 glass at pressures up to 8.6 GPa. *Physical Review B*, 81:014202, 2010.

[32] J. M. Besson, R. J. Nelmes, G. Hamel, J. S. Loveday, G. Weill, and S. Hull. Neutron powder diffraction above 10 GPa. *Physica B: Condensed Matter*, 180 - 181(2):907, 1992.

[33] S. Klotz, J. M. Besson, G. Hamel, R. J. Nelmes, J. S. Loveday, W. G. Marshall, and R. M. Wilson. Neutron powder diffraction at pressures beyond 25 GPa. *Applied Physics Letters*, 66(14):1735, 1995.

[34] S. Klotz, G. Hamel, and J. Frelat. A new type of compact large-capacity press for neutron and X-ray scattering. *High Pressure Research*, 24(1):219, 2004.

[35] C. L. Bull, M. Guthrie, S. Klotz, J. Philippe, T. Strässle, R. J. Nelmes, J. S. Loveday, and G. Hamel. Toroidal anvils for single-crystal neutron studies. *High Pressure Research*, 25(4):229, 2005.

[36] J. M. Brown. The NaCl pressure standard. *Journal of Applied Physics*, 86:5801, 1999.

[37] R. J. Hemley, A. P. Jephcoat, H. K. Mao, C. S. Zha, L. W. Finger, and D. E. Cox. Static compression of H_2O-ice to 128 GPa (1.28 Mbar). *Nature*, 330:737, 1987.

[38] Y. K. Vohra and P. T. Spencer. Novel γ-Phase of Titanium Metal at Megabar Pressures. *Physical Review Letters*, 86:3068, 2001.

[39] Y. Akahama, H. Kawamura, and T. Le Bihan. A new distorted body-centred cubic phase of titanium (δ-Ti) at pressures up to 220 GPa. *Journal of Physics: Condensed Matter*, 14:10583, 2002.

[40] H. Xia, S. J. Duclos, A. L. Ruoff, and Y .K. Vohra. New high-pressure phase transition in zirconium metal. *Physical Review Letters*, 64:204, 1990.

[41] Y. Akahama, M. Kobayashi, and H. Kawamura. High-Pressure X-Ray Diffraction Study on Electronic s-d Transition in Zirconium. *Journal of Physical Society of Japan*, 60:3211, 1991.

[42] C. W. Greeff. Phase changes and the equation of state of Zr. *Modelling and Simulation in Materials Science*, 13:1015, 2005.

[43] J. Zhao, Y. Zhang, C. Pantea, J. Qian, L. L. Daemen, P. A. Rigg, R. S. Hixson, G. T. Gray, Y. Yang, L. Wang, Y. Wang, and T. Uchida. Thermal equations of state of the α, β, and ω phases of zirconium. *Physical Review B*, 71:184119, 2005.

[44] I. O. Bashkin, V. K. Fedotov, M. V. Nefedova, V. G. Tissen, G. Ponyatovsky, A. Schiwek, and W. B. Holzapfel. Crystal structure and superconductivity of TiZr up to 57 GPa. *Physical Review B*, 68:054401, 2003.

[45] V. P. Dmitriev, L. Dubrovinsky, T. Le Bihan, A. Kuznetsov, H.-J. Weber, and E. G. Poniatovsky. Collapsed hexagonal ω phase in a compressed TiZr alloy: Angle-dispersive synchrotron-radiation x-ray diffraction study. *Physical Review B*, 73:094114, 2006.

[46] H. H. Paalman and C. J. Pings. Numerical Evaluation of X-Ray Absorption Factors for Cylindrical Samples and Annular Sample Cells. *Journal of Applied Physics*, 33(8):2635, 1962.

[47] D. M. North, J. E. Enderby, and P. A. Egelstaff. The structure factor for liquid metals I. The application of neutron diffraction techniques. *Journal of Physics C: Solid State Physics*, 1(3):784, 1968.

[48] A. K. Soper and P. A. Egelstaff. Multiple scattering and attenuation of neutrons in concentric cylinders. *Nuclear Instruments and Methods*, 178(2-3):415, 1980.

[49] http://www.isis.stfc.ac.uk/groups/disordered-materials/people/workshop-2010-gudrun-si-310472.pdf.

[50] D. I. Grimley, A. C. Wright, and R. N. Sinclair. Neutron scattering from vitreous silica IV. Time-of-flight diffraction. *Journal of Non-Crystalline Solids*, 119:49, 1990.

[51] Wilson A. Crichton, 2010. Private communication.

[52] M. J. Hooper. UK Atomic Energy Authority Report AERE. *Harwell: UK Atomic Energy Authority*, R. 7477, 1973.

[53] P. S. Salmon, S. Xin, and H. E. Fischer. Structure of the glassy fast-ion conductor $AgPS_3$ by neutron diffraction. *Physical Review B*, 58:6115, 1998.

[54] A. C. Barnes, L. B. Skinner, P. S. Salmon, A. Bytchkov, I. Pozdnyakova, T. O. Farmer, and H. E. Fischer. Liquid-Liquid Phase Transition in Supercooled Yttria-Alumina. *Physical Review Letters*, 103:225702, 2009.

[55] D. Daisenberger, T. Deschamps, B. Champagnon, M. Mezouar, R. Q. Cabrera, M. Wilson, and P. F. McMillan. Polyamorphic Amorphous Silicon at High Pressure: Raman and Spatially Resolved X-ray Scattering and Molecular Dynamics Studies. *Journal of Physical Chemistry*, 115:14246, 2011.

[56] N. E. Cusack. *The Physics of Structurally Disordered Matter: An Introduction.* IOP Publishing, Bristol, 1987.

[57] M. Guthrie, C. A. Tulk, C. J. Benmore, J. Xu, J. L. Yarger, D. D. Klug, J. S. Tse, H-K. Mao, and R. J. Hemley. Formation and structure of a dense octahedral glass. *Physical Review Letters*, 93(11):115502, 2004.

[58] M. Wilding, M. Guthrie, C. L. Bull, M. G. Tucker, and P. F. McMillan. Feasibility of *in situ* neutron diffraction studies of non-crystalline silicates up to pressures of 25 GPa. *Journal of Physics: Condensed Matter*, 20:244122, 2008.

[59] E. Soignard, C. J. Benmore, and J. L. Yarger. A perforated diamond anvil cell for high-energy x-ray diffraction of liquids and amorphous solids at high pressure. *Review of Scientific Instruments*, 81(3):035110, 2010.

[60] D. L. Price. *High-Temperature Levitated Materials*. Cambridge: Cambridge University Press, 2010.

[61] S. Klotz. *Techniques in High Pressure Neutron Scattering*. Boca Raton, FL: CRC Press, 2012.

[62] M. Wilson and P. S. Salmon. Network topology and the fragility of tetrahedral glass-forming liquids. *Physical Review Letters*, 103:157801, 2009.

[63] J. P. Itié, A. Polian, G. Calas, J. Petiau, A. Fontaine, and H. Tolentino. Pressure-induced coordination changes in crystalline and vitreous GeO_2. *Physical Review Letters*, 63:398, 1989.

[64] D. J. Durben and G. H. Wolf. Raman spectroscopic study of the pressure-induced coordination change in GeO_2 glass. *Physical Review B*, 43:2355, 1991.

[65] K. H. Smith, E. Shero, A. Chizmeshya, and G. H. Wolf. The equation of state of polyamorphic germania glass - a 2-domain description of the viscoelastic response. *Journal of Chemical Physics*, 102(17):6851, 1995.

[66] O. B. Tsiok, V. V. Brazhkin, A. G. Lyapin, and L. G. Khvostantsev. Logarithmic kinetics of the amorphous-amorphous transformations in SiO_2 and GeO_2 glasses under high pressure. *Physical Review Letters*, 80(5):999, 1998.

[67] M. Micoulaut, L. Cormier, and G. S. Henderson. The structure of amorphous, crystalline and liquid GeO_2. *Journal of Physics: Condensed Matter*, 18:R753, 2006.

[68] M. Vaccari, G. Aquilanti, S. Pascarelli, and O. Mathon. A new EXAFS investigation of local structural changes in amorphous and crystalline GeO_2 at high pressure. *Journal of Physics: Condensed Matter*, 21(14):145403, 2009.

[69] Q. Mei, S. Sinogeikin, G. Shen, S. Amin, C. J. Benmore, and K. Ding. High-pressure X-ray diffraction measurements on vitreous GeO_2 under hydrostatic conditions. *Physical Review B*, 81(17):174113, 2010.

[70] M. Baldini, G. Aquilanti, H-k. Mao, W. Yang, G. Shen, S. Pascarelli, and W. L. Mao. High-pressure EXAFS study of vitreous GeO_2 up to 44 GPa. *Physical Review B*, 81:024201, 2010.

[71] C. H. Polsky, K. H. Smith, and G. H. Wolf. Effect of pressure on the absolute Raman scattering cross section of SiO_2 and GeO_2 glasses. *Journal of Non-Crystalline Solids*, 248(2-3):159, 1999.

[72] S. Sampath, C. J. Benmore, K. M. Lantzky, J. Neuefeind, K. Leinenweber, D. L. Price, and J. L. Yarger. Intermediate-range order in permanently densified GeO_2 glass. *Physical Review Letters*, 90(11):115502, 2003.

[73] A. E. Ringwood. The system Mg_2SiO_4 -Mg_2GeO_4. *American Journal of Science*, 254:707, 1956.

[74] N. L. Ross and A. Navrotsky. The Mg_2GeO_4 olivine - spinel phase transition. Physics and Chemistry of Minerals. 14:473, 1987.

[75] P. C. Burnley, H. W. Green II, and D. J. Prior. Faulting associated with the olivine to spinel transformation in Mg_2GeO_4 and its implications for deep-focus earthquakes. *Journal of Geophysical Research*, 96:425, 1991.

[76] B. Reynard, P-E. Petit, F. Guyot, and P. Gillet. Pressure-induced structural modifications in Mg_2GeO_4-olivine - A Raman-spectroscopic study. *Physics and Chemistry of Minerals*, 20:556, 1994.

[77] P. C. Burnley. Investigation of martensitic-like transformation from Mg_2GeO_4 olivine to its spinel structure polymorph. *American Mineralogist*, 90:1315, 2005.

[78] J. V. Walther. *Essentials of Geochemistry*. Sudbury MA: Jones and Bartlett, 2005.

[79] M. Micoulaut. Structure of densified amorphous gemanium dioxide. *Journal of Physics: Condensed Matter*, 16:L131, 2004.

[80] M. Micoulaut, Y. Guissani, and B. Guillot. Simulated structural and thermal properties of glassy and liquid germania. *Physical Review E*, 73(3):031504, 2006.

[81] K. V. Shanavas, N. Garg, and S. M. Sharma. Classical molecular dynamics simulations of behavior of GeO_2 under high pressures and at high temperatures. *Physical Review B*, 73(9):094120, 2006.

[82] M. Micoulaut, X. Yuan, and L. W. Hobbs. Co-ordination and intermediate-range order alterations in densified germania. *Journal on Non-Crystalline Solids*, 353(18 - 21):1961, 2007.

[83] T. Li, S. Huang, and J. Zhu. The structure and void analysis of pressure-induced amorphous GeO_2: Molecular dynamics simulation. *Chemical Physics Letters*, 471:253, 2009.

[84] X. F. Zhu and L. F. Chen. First-principles molecular dynamics simulations of the structure of germanium dioxide under pressures. *Physica B*, 404:4178, 2009.

[85] D. Marrocchelli, M. Salanne, and P. A Madden. High-pressure behaviour of GeO_2: a simulation study. *Journal of Physics: Condensed Matter*, 22(15):152102, 2010.

[86] V. F. Sears. Neutron scattering lengths and cross sections. *Neutron News*, 3(3):27, 1992.

[87] W. G. Marshall and D. J. Francis. Attainment of near-hydrostatic compression conditions using the Paris-Edinburgh cell. *Journal of Applied Crystallography*, 32:122, 2002.

[88] X. Hong, G. Shen, V. B. Prakapenka, M. Newville, M. L. Rivers, and S. R. Sutton. Intermediate states of GeO_2 glass under pressures up to 35 GPa. *Physical Review B*, 75:104201, 2007.

[89] P. S. Salmon. Decay of the pair correlations and small-angle scattering for binary liquids and glasses. *Journal of Physics: Condensed Matter*, 18:11443, 2006.

[90] P. S. Salmon. The structure of tetrahedral network glass forming systems at intermediate and extended length scales. *Journal of Physics: Condensed Matter*, 19:455208, 2007.

[91] Y. Liang, C. R. Miranda, and S. Scandolo. Temperature-induced densification of compressed SiO_2 glass: A molecular dynamics study. *High Pressure Research*, 28:35, 2008.

[92] P. S. Salmon. Real space manifestation of the first sharp diffraction peak in the structure factor of liquid and glassy materials. *Proceedings of the Royal Society of London A*, 445:351, 1994.

[93] P. S. Salmon, A. C. Barnes, R. A. Martin, and G. J. Cuello. Glass fragility and atomic ordering on the intermediate and extended range. *Physical Review Letters*, 96:235502, 2006.

[94] P. S Salmon, A. C. Barnes, R. A. Martin, and G. J. Cuello. Structure of glassy GeO_2. *Journal of Physics: Condensed Matter*, 19(41):415110, 2007.

[95] G. Shen, Q. Mei, V. B. Prakapenka, P. Lazor, S. Singogeikin, Y. Meng, and C. Park. Effect of helium on structure and compression behavior of SiO_2 glass. *Proceedings of the National Academy of Sciences*, 108:6004, 2011.

[96] T. Sato, N. Funamori, and T. Yagi. Helium penetrates into silica glass and reduces its compressibility. *Nature Communications*, 2:345, 2011.

[97] G. Lelong, L. Cormier, G. Ferlat, G. S. Henderson, A. Shukla, and G. Calas. Evidence of fivefold-coordinated Ge atoms in amorphous GeO_2 under pressure using inelastic x-ray scattering. *Physical Review B*, 85:134202, 2012.

[98] J. D. Jorgensen. Compression mechanisms in alpha-quartz structures—SiO_2 and GeO_2. *Journal of Applied Physics*, 49(11):5473, 1978.

[99] J. Glinnemann, H. E. Jr. King, H. Schulz, Th. Hahn, S. J. La Placa, and F. Dacol. Crystal structures of the low-temperature quartz-type phases of SiO_2 and GeO_2 at elevated pressure. *Zeitschrift für Kristallographie*, 198:177, 1992.

[100] R. D. Oeffner and S. R. Elliott. Interatomic potential for germanium dioxide empirically fitted to an ab initio energy surface. *Physical Review B*, 58(22):14791, 1998.

[101] J. Haines, J. M Léger, and C. Chateau. Transition to a crystalline high-pressure phase in a-GeO_2 at room temperature. *Physics Review B*, 61:8701, 2000.

[102] A. Pasquarello, I. Petri, P. S. Salmon, O. Parisel, R Car, É. Tóth, D. H. Powell, H. E. Fischer, L. Helm, and A. E. Merbach. First solvation shell of the Cu(II) aqua ion: Evidence for fivefold coordination. *Science*, 291:856, 2001.

[103] S. Le Roux and P. Jund. Ring statistics analysis of topological networks: new approach and application to amorphous GeS_2 and SiO_2 systems. *Computational Materials Science*, 49:70, 2010.

[104] S. Le Roux and P. Jund. *Computational Materials Science*, 50:1217, 2011.

[105] L. Giacomazzi, P. Umari, and A. Pasquarello. Vibrational spectra of vitreous germania from first-principles. *Physical Review B*, 74(15):155208, 2006.

[106] L. Giacomazzi, P. Umari, and A. Pasquarello. Medium-range structural properties of vitreous germania obtained through first-principles analysis of vibrational spectra. *Physical Review Letters*, 95(7):075505, 2005.

[107] Q. Mei, C. J. Benmore, S. Sen, R. Sharma, and J. L. Yarger. Intermediate range order in vitreous silica from a partial structure factor analysis. *Physical Review B*, 78:144204, 2008.

[108] A. C. Wright and R. N. Sinclair. Neutron scattering from vitreous silica: III. Elastic diffraction. *Journal of Non-Crystalline Solids*, 76(2-3):351, 1985.

[109] A. Polian, D. Vo-Thanh, and P. Richet. Elastic properties of a-SiO_2 up to 2300 K from Brillouin scattering measurements. *Europhysics Letters*, 57:375, 2002.

[110] T. Rouxel. Elastic Properties and Short-to Medium-Range Order in Glasses. *Journal of American Ceramic Society*, 90:3019, 2007.

[111] S. M. Antao, C. J. Benmore, B. Li, L. Wang, E. Bychkov, and J. B. Parise. Network Rigidity in $GeSe_2$ Glass at High Pressure. *Physical Review Letters*, 100:115501, 2008.

[112] J. Schroeder, T. G. Bilodeau, and X. Zhao. Brillouin and Raman scattering from glasses under high pressure. *High Pressure Research*, 4(1-6):531, 1990.

[113] C. Weigel, A. Polian, M. Kint, B. Rufflé, M. Foret, and R. Vacher. Vitreous Silica Distends in Helium Gas: Acoustic Versus Static Compressibilities. *Physical Review Letters*, 24:245504, 2012.

[114] J. A. Walker, L. A. Sullivan, K. Trachenko, R. P. Bruin, T. O. H. White, M. T. Dove, R. P. Tyer, I. T. Todorov, and S. A. Wells. The origin of the compressibility anomaly in amorphous silica: a molecular dynamics study. *Journal of Physics: Condensed Matter*, 19:275210, 2007.

[115] L. Huang and J. Kieffer. Amorphous-amorphous transitions in silica glass. I. Reversible transitions and thermomechanical anomalies. *Physical Review B*, 69:224203, 2004.

[116] Y. Liang, C. R. Miranda, and S. Scandolo. Mechanical strength and coordination defects in compressed silica glass: Molecular dynamics simulations. *Physical Review B*, 75:024205, 2007.

[117] M. Grimsditch. Polymorphism in Amorphous SiO_2. *Physical Review Letters*, 52:2379, 1984.

[118] C. S. Zha, R. J. Hemley, H. K. Mao, T. S. Duffy, and C. Meade. Acoustic velocities and refractive index of SiO_2 glass to 57.5 GPa by Brillouin scattering. *Physical Review B*, 50:13105, 1994.

[119] T. Rouxel, H. Ji, T. Hammouda, and A. Moréac. Poisson's Ratio and the Densification of Glass under High Pressure. *Physical Review Letters*, 100:225501, 2008.

[120] Y. Inamura, Y. Katayama, W. Utsumi, and K. Funakoshi. Transformations in the intermediate-range structure of SiO_2 glass under high pressure and temperature. *Physical Review Letters*, 93:015501, 2004.

[121] C. J. Benmore, E. Soignard, S. A. Amin, M. Guthrie, S. D. Shastri, P. L. Lee, and J. L. Yarger. Structural and topological changes in silica glass at pressure. *Physical Review B*, 81:054105, 2010.

[122] R. J. Hemley, H. K. Mao, P. M. Bell, and B. O. Mysen. Raman spectroscopy of SiO_2 glass at high pressure. *Physical Review Letters*, 57:747, 1986.

[123] P. F. McMillan. Structural studies of silicate glasses and melts: applications and limitations of Raman spectroscopy. *American Mineralogist*, 69(7-8):622, 1984.

[124] G. E. Walrafen and P. N. Krishnan. Raman spectrum of pressure compacted fused silica. *Journal of Chemical Physics*, 81:5328, 1981.

[125] R. A. B. Devine, R. Dupree, I. Farnan, and J. J. Capponi. Pressure-induced bond-angle variation in amorphous SiO_2. *Physical Review B*, 35:2560, 1987.

[126] A. Zeidler, J. W. E. Drewitt, P. S. Salmon, A. C. Barnes, W. A. Crichton, S. Klotz, H. E. Fischer, C. J. Benmore, S. Ramos, and A. C. Hannon. Establishing the structure of GeS_2 at high pressures and temperatures: a combined approach using

x-ray and neutron diffraction. *Journal of Physics: Condensed Matter*, 21:474217, 2009.

[127] http://www.isis.stfc.ac.uk/instruments/pearl/.

[128] D. A. J. Whittaker. *The Structure and Dynamics of Fundamental Glasses by Neutron Scattering Techniques*. PhD thesis, University of Bath, 2012.

[129] C. Meade and R. Jeanloz. Frequency-dependent equation of state of fused silica to 10 GPa. *Physical Review B*, 35:236, 1987.

[130] T. Sato and N. Funamori. Sixfold-coordinated amorphous polymorph of SiO_2 under high pressure. *Physical Review Letters*, 101:255502, 2008.

[131] F. Birch. Finite elastic strain of cubic crystals. *Physical Review*, 71:809, 1947.

[132] S. Klotz, Th. Strässle, G. Rousse, G. Hamel, and V. Pomjakushin. Angle-dispersive neutron diffraction under high pressure to 10 GPa. *Applied Physics Letters*, 86(3):031917, 2005.

[133] T. Sato and N. Funamori. High-pressure structural transformation of SiO_2 glass up to 100 GPa. *Physical Review B*, 82:184102, 2010.

[134] C. Meade, R. J. Hemley, and H. K. Mao. High-pressure x-ray diffraction of SiO_2 glass. *Physical Review Letters*, 69:1387, 1992.

[135] M. Wilson, March 2012. Private Communication.

[136] P. Tangney and S. Scandolo. An *ab initio* parametrized interatomic force field for silica. *Journal of Chemical Physics*, 117:8898, 2002.

[137] L. Huang and J. Kieffer. Molecular dynamics study of cristobalite silica using a charge transfer three-body potential: Phase transformation and structural disorder. *Journal of Chemical Physics*, 118:1487, 2003.

[138] Q. Mei, C. J. Benmore, R. T. Hart, E. Bychkov, P. S. Salmon, C. D. Martin, F. M. Michel, S. M. Antao, P. J. Chupas, P. L. Lee, S. D. Shastri, J. B. Parise, K. Leinenweber, S. Amin, and J. L. Yarger. Topological changes in glassy $GeSe_2$ at pressures up to 9.3 GPa determined by high-energy X-ray and neutron diffraction measurements. *Physical Review B*, 74(1):014203, 2006.

[139] P. S. Salmon, R. A. Martin, P. E. Mason, and G. J. Cuello. Topological versus chemical ordering in network glasses at intermediate and extended length scales. *Nature*, 435:75, 2005.

[140] J. S. Tse, D. D. Klug, and Y. L. Page. High-pressure densification of amorphous silica. *Physical Review B*, 46(10):5933, 1992.

[141] M. Grimsditch, R. Bhadra, and Y. Meng. Brillouin scattering from amorphous materials at high pressures. *Physical Review B*, 38:7836, 1988.

[142] A. C. Hannon, A. C. Wright, J. A. Blackman, and R. N. Sinclair. The vibrational modes of vitreous B_2O_3: inelastic neutron scattering and modelling studies. *Journal of Non-Crystalline Solids*, 182:78, 1995.

[143] J. Nicholas, S. Sinogeikin, J. Kieffer, and J. Bass. Spectroscopic Evidence of Polymorphism in Vitreous B_2O_3. *Physical Review Letters*, 92(21):215701, 2004.

[144] P. Umari and A. Pasquarello. Fraction of Boroxol Rings in Vitreous Boron Oxide from a First-Principles Analysis of Raman and NMR Spectra. *Physical Review Letters*, 95:137401, 2005.

[145] S. K. Lee, P. J. Eng, H-K Mao, Y. Meng, M. Newville, M. Y. Hiu, and J. Shu. Probing of Bonding Changes in B_2O_3 Glasses at High Pressures with Inelastic X-ray Scattering. *Nature Materials*, 4:851, 2005.

[146] V. V. Brazhkin, Y. Katayama, K. Trachenko, O. B. Tsiok, A. G. Lyapin, E. Artacho, M. Dove, G. Ferlat, Y. Inamura, and H. Saitoh. Nature of the Structural Transformations in B_2O_3 Glass under High Pressure. *Physical Review Letters*, 101:035702, 2008.

[147] G. Ferlat, T Charpentier, A. P. Seitsonen, A. Takada, M. Lazzeri, L. Cormier, G. Calas, and F. Mauri. Boroxol Rings in Liquid and Vitreous B_2O_3 from First Principles. *Physical Review Letters*, 101:065504, 2008.

[148] A. Takada. Molecular dynamics study of pressure induced structural changes in B_2O_3. *Physics and Chemistry of Glasses*, 45:156, 2004.

[149] L. Huang, J. Nicholas, J. Kieffer, and J. Bass. Polyamorphic transitions in vitreous B_2O_3 under pressure. *Journal of Physics: Condensed Matter*, 20:075107, 2008.

[150] R. L. Mozzi and B. E. Warren. The Structure of Boron Oxide. *Journal of Applied Crystallography*, 3:251, 1970.

[151] A. H. Silver and P. J. Bray. Nuclear Magnetic Resonance Absorption in Glass. I. Nuclear Quadrupole Effects in Boron Oxide, Soda-Boric Oxide, and Borosilicate Glasses. *Journal of Chemical Physics*, 29:984, 1958.

[152] P. A. V. Johnson, A. C. Wright, and R. N. Sinclair. A neutron diffraction investigation of the structure of viterous boron trioxide. *Journal of Non-Crystalline Solids*, 50:281, 1982.

[153] A. C. Wright, C. E. Stone, R. N. Sinclair, N. Umesaki, N. Kitamura, K. Ura, N. Ohtori, and A. C. Hannon. Structure of pressure compacted vitreous boron oxide. *Physics and Chemistry of Glasses*, 41 (5):296, 2000.

[154] A. Zeidler, P. S. Salmon, R. A. Martin, T. Usuki, P. E. Mason, G. J. Cuello, S. Kohara, and H. E. Fischer. Structure of liquid and glassy $ZnCl_2$. *Physical Review B*, 82:104208, 2010.

[155] V. V. Brazhkin, Y. Katayama, Y. Inamura, M. V. Kondrin, A. G. Lyapin, S. V. Popova, and R. N. Voloshin. Structural transformation in liquid, crystalline and glassy B_2O_3 under high pressure. *Journal of Experimental and Theoretical Physics*, 78:845, 2003.

[156] V. V. Brazhkin, Y. Katayama, Y. Inamura, M. V. Kondrin, A. G. Lyapin, S. V. Popova, and R. N. Voloshin. Erratum: "Structural transformations in Liqid, Crystal and Glassy B_2O_3 under High Pressure" [JETP Lett. 78(6), 393-397 (2003)]. *Journal of Experimental and Theoretical Physics*, 79:308, 2004.

[157] C. T. Prewitt and R. D. Shannon. Crystal Structure of a High-Pressure Form of B_2O_3. *Acta Crystallographica*, 24:869, 1968.

[158] S. R. Elliott. *Physics of Amorphous Materials*. Longman Group UK, Essex, 2nd. edition, 1990.

[159] A. Feltz. *Amorphous Inorganic Materials and Glasses*. Wiley-VCH, Weinheim, New York, 1993.

[160] Z. U. Borisova. *Glassy Semiconductors*. Plenum, New York, 1981.

[161] A. Sartbaeva, S. A. Wells, A. Huerta, and M. F. Thorpe. Local structural variability and the intermediate phase window in network glasses. *Physical Review B*, 75:224204, 2007.

[162] C. Massobrio, M. Celino, P. S. Salmon, R. A. Martin, M. Micoulaut, and A. Pasquarello. Atomic structure of the two intermediate phase glasses $SiSe_4$ and $GeSe_4$. *Physical Review B*, 79(17):174201, 2009.

[163] P. Boolchand, J. Grothaus, W. J. Bresser, and P. Suranyi. Structural origin of broken chemical order in a $GeSe_2$ glass. *Physical Review B*, 25:2975, 1982.

[164] I. Petri, P. S. Salmon, and H.E. Fischer. Defects in a disordered world: The structure of glassy $GeSe_2$. *Physical Review Letters*, 84(11):2413, 2000.

[165] P. Boolchand. *Insulating and Semiconducting Glasses*. World Scientific, Singapore, 2000.

[166] X. Zhang and D. A. Drabold. Structural and electronic properties of glassy $GeSe_2$ surfaces. *Physics Review B*, 62:15695, 2000.

[167] A. Bouzid and C. Massobrio. Note: Accounting for pressure effects on the calculated equilibrium structure of glassy $GeSe_2$. *Journal of Chemical Physics*, 137:046101, 2012.

[168] A. C. Wright. Neutron scattering from vitreous silica. V. The structure of vitreous silica: What have we learned from 60 years of diffraction studies? *Journal of Non-Crystalline Solids*, 179:84, 1994.

[169] F. Wang, S. Mamedov, and P. Boolchand. Pressure Raman effects and internal stress in network glasses. *Physical Review B*, 71:174201, 2005.

[170] P. V. Terededai. High pressure Raman spectroscopy of $GeSe_2$ glass. *Journal of Chemical Physics*, 127:046101, 2012.

[171] S. Asokan, M. V. N. Prasad, G. Parthasarathy, and E. S. R Gopal. Mechanical and Chemical Thresholds in IV-VI Chalcogenide Glasses. *Physical Review Letters*, 62:808, 1989.

[172] W. A Crichton, M. Mezouar, T. Grande, S. Stølen, and A. Grzechnik. Breakdown of intermediate-range order in liquid $GeSe_2$ at high pressure. *Nature*, 414:622–625, 2001.

[173] K. Wezka, P. S. Salmon, A. Zeidler, D. A. J. Whittaker, J. W. E. Drewitt, S. Klotz, H. E. Fischer, and D. Marrocchelli. Mechanisms of network collapse in GeO_2 glass: high-pressure neutron diffraction with isotope substitution as arbitrator of competing models. *Journal of Physics: Condensed Matter*, 24:502101, 2012.

[174] A. Bouzid and C. Massobrio. Private Communication.

[175] M. Micoulaut, R. Vuilleumier, and C. Massobrio. Improved modeling of liquid $GeSe_2$: Impact of the exchange-correlation functional. *Physical Review B*, 79(21):214205, 2009.

[176] S. Le Roux, A. Zeidler, P. S. Salmon, M. Boero, M. Micoulaut, and C. Massobrio. Structural properties of liquid Ge_2Se_3: A first-principles study. *Physical Review B*, 84:134203, 2011.

[177] S. Le Roux, A. Bouzid, M. Boero, and C. Massobrio. Structural properties of glassy Ge_2Se_3 from first-principles molecular dynamics. *Physical Review B*, 86:224201, 2012.

[178] A. B. Bhatia and D. E. Thornton. Structural aspects of the electrical resistivity of binary alloys. *Physical Review B*, 2(8):3004–3012, 1970.

[179] P. S. Salmon. Structure of liquids and glasses in the Ge-Se binary system. *Journal of Non-Crystalline Solids*, 353(32-40):2959, 2007.

[180] K. S. Liang, A. Bienenstock, and C. W. Bates. *Physical Review B*, 10:1528, 1974.

[181] R. M. White. *Journal of Non-Crystalline Solids*, 16:387, 1974.

[182] R. A. Martin, P. S. Salmon, H. E. Fischer, and G. J. Cuello. Structure of dysprosium and holmium phosphate glasses by the method of isomorphic substitution in neutron diffraction. *Journal of Physics: Condensed Matter*, 15:8235–8252, 2003.

[183] P. S. Salmon and I. Petri. Structure of glassy and liquid $GeSe_2$. *Journal of Physics: Condensed Matter*, 15:S1509, 2003.

[184] M. Durandurdu and D. A. Drabold. Simulation of pressure-induced polyamorphism in a chalcogenide glass $GeSe_2$. *Physical Review B*, 65:104208, 2002.

[185] N. Troullier and J. L. Martins. Efficient pseudopotentials for plane-wave calculations. *Physical Review B*, 43:1993, 1991.

[186] S. Nosé. A molecular dynamics method for simulations in the canonical ensemble. *Molecular Physics*, 52:255, 1984.

[187] W. G. Hoover. Canonical dynamics: Equilibrium phase-space distributions. *Physical Review A*, 31:1695, 1985.

[188] K. J. Pizzey and P. S. Salmon, 2013. Private communication.

[189] C. Massobrio and A. Pasquarello. Short and intermediate range order in amorphous $GeSe_2$. *Physical Review B*, 77(14):144207, 2008.

[190] G. Dittmar and H. Schäfer. Die Kristallstruktur von Germaniumdiselenid. *Acta Crystallographica Section B*, 32(9):2726–2728, Sep 1976.

[191] A. Grzechnik, S. Stølen, E. Bakken, T. Grande, and M. Mezouar. Structural transformations in three-dimensional crystalline $GeSe_2$. *Journal of Solid State Chemistry*, 150:121–127, 2000.

[192] T. Grande, M. Ishii, S. Akaishi, M. Aasland, H. Fjellvåg, and S. Stølen. Structural Properties of $GeSe_2$ at High Pressures. *Journal of Solid State Chemistry*, 145:167, 1999.

[193] M. Shimada and F. Dachille. Crystallisation of amorphous GeS_2 and $GeSe_2$ under pressure. *Inorganic Chemistry*, 16:2094, 1977.

[194] L. P. Dávilá, M. J. Caturla, A. Kubota, B. Sadigh, T. D. de la Rubia, J. F. Shackelford, S. H. Risbud, and S. H. Garofalini. *Physical Review Letters*, 91:205501, 2003.

[195] S. K. Lee, K. Mibe, Y. Fei, G. D. Cody, and B. O. Mysen. Structure of B_2O_3 Glass at High Pressure: A ^{11}B Solid-State NMR Study. *Physical Review Letters*, 94:165507, 2005.